ISSN 2074-272X

науково-практичний журнал 2026/2

Електротехніка і Електромеханіка

Electrical Engineering & Electromechanics

Електричні машини та апарати
Електротехнічні комплекси та системи
Промислова електроніка
Електроізоляційна та кабельна техніка
Електричні станції, мережі і системи

Журнал включено до найвищої категорії «А» Переліку фахових видань України

З 2019 р. журнал індексується у Scopus

З 2005 р. журнал індексується у Web of Science Core Collection: Emerging Sources Citation Index

Electrical Engineering & Electromechanics

Scientific Journal was founded in 2002
Co-founders: National Technical University «Kharkiv Polytechnic Institute» (Kharkiv, Ukraine);
Anatolii Pidhornyi Institute of Power Machines and Systems of NAS of Ukraine (Kharkiv, Ukraine)

From no. 1 2019 Journal «Electrical Engineering & Electromechanics» is indexing in **Scopus** and from no. 1 2005 Journal is indexing in **Web of Science Core Collection: Emerging Sources Citation Index (ESCI)**

Also included in DOAJ (Directory of Open Access Journals), in EBSCO's database, in ProQuest's databases – Advanced Technologies & Aerospace Database and Materials Science & Engineering Database, in Gale/Cengage Learning databases.

Editorial office address:
National Technical University «Kharkiv Polytechnic Institute», Kyrpychova Str., 2, Kharkiv, 61002, Ukraine
phone: +380 67 3594696, **e-mail:** a.m.grechko@gmail.com (**Grechko O.M.)**
ISSN (print) 2074-272X
ISSN (online) 2309-3404

Approved for printing on 27 February 2026. Format 60 × 90 ⅛. Paper – offset. Laser printing. Edition 50 copies.
Printed by Printing house «Madrid Ltd» (18, Gudanova Str., Kharkiv, 61024, Ukraine)

Electrical Engineering & Electromechanics
Scientific Journal

no. 2, 2026

Table of Contents

Electrical Machines and Apparatus

Electrotechnical Complexes and Systems

Industrial Electronics

Electrical Insulation and Cable Engineering

Power Stations, Grids and Systems

UDC 621.316 https://doi.org/10.20998/2074-272X.2026.2.01

V.V. Kozyrskyi, T. Nurek, J. Sloma, V.Ya. Bunko, M.V. Goncharuk

The use of shape memory alloys in fuses for the protection of electrical installations

***Problem**. The degree of damage to electrical installations during short circuits depends on the response time of the protection. An effective way to enhance the current-limiting effect in electrical fuses (reducing their response time) may be the use of shape memory alloy (SMA) elements. However, this requires careful study and research. The **goal** of the work is to establish the patterns of strengthening the current-limiting effect of a fuse (reducing the response time) when using thermosensitive elements made of shape memory alloys. The achievement of this goal is based on the analysis of experimental studies conducted by the authors and mathematical models of the characteristics of a fuse containing an SMA element. **Methodology**. The article presents mathematical modelling of the parameters and characteristics of fuses with thermomechanical destruction of the fuse element, as well as a thermophysical model of a fuse with a thermosensitive SMA element. The article presents the **results** of experimental studies of a traditional fuse and a fuse equipped with a thermosensitive SMA element. For each current, the response time of the modified fuse was shorter than that of the traditional fuse. The use of a thermosensitive element reduced the response time by more than 20 times for a current of 10 A and approximately 10 times (from 0.257 s to 0.0244 s) for a current of 20 A. For the highest tested current (90 A), the fuse response time was half that of a traditional fuse. The article also presents the results of calculations of fuse characteristics using a mathematical model and a comparison with the results of experimental studies. **Scientific novelty**. The developed mathematical models of the characteristics of electrical fuses containing SMA elements made it possible for the first time to substantiate the interrelationships between the parameters (geometric dimensions and characteristics of SMA elements, fuse links) with current loads of electrical installations. The **practical value** of the work lies in the proposed use of thermosensitive elements made of functional materials to increase the current-limiting effect of electrical fuses for protecting electrical installations during short circuits.* References 19, tables 2, figures 7.
Key words: **functional materials, fuse, shape memory alloy, thermosensitive element**.

***Проблема.** Ступінь пошкодження електроустановок при коротких замиканнях залежить від часу спрацювання захисту. Ефективним способом покращення струмообмежуючого ефекту в електричних запобіжниках (зменшення часу їх спрацювання) може бути застосування елементів із сплавів з ефектом пам'яті форми. Проте, це потребує ретельного вивчення та дослідження. **Метою** роботи є встановлення закономірностей покращення струмообмежувального ефекту запобіжника (зменшення часу спрацьовування) при застосуванні термочутливих елементів із сплаву з пам'яттю форми (SMA – shape memory alloy). Досягнення мети базується на аналізі проведених авторами експериментальних досліджень і побудованих математичних моделях характеристик запобіжника, що містить елемент SMA. **Методика.** У статті представлено математичне моделювання параметрів і характеристик запобіжників з термомеханічним руйнуванням запобіжного елемента, а також теплофізичну модель запобіжника з термочутливим елементом SMA. У статті представлені **результати** експериментальних досліджень традиційного запобіжника та запобіжника, оснащеного термочутливим елементом SMA. Для кожного струму час спрацьовування модифікованого запобіжника був коротшим, ніж у традиційного запобіжника. Використання термочутливого елемента скоротило час спрацьовування більш ніж у 20 разів для струму 10 А і приблизно в 10 разів (з 0,257 с до 0,0244 с) для струму 20 А. Для найбільшого випробуваного струму (90 А) час спрацьовування запобіжника був удвічі меншим, ніж у традиційного запобіжника. Наведено результати розрахунків характеристик запобіжника за допомогою математичної моделі та порівняння з результатами експериментальних досліджень. **Наукова новизна.** Розроблені математичні моделі характеристик запобіжників, що містять елементи SMA, дозволили вперше обґрунтувати взаємозв'язки параметрів (геометричних розмірів і характеристик елементів SMA, плавких вставок запобіжників) зі струмовими навантаженнями електроустановок. **Практична значимість** роботи полягає у пропонованому використанні термочутливих елементів з функціональних матеріалів для підвищення струмообмежувальної дії запобіжників для захисту електроустановок при коротких замиканнях.* Бібл. 19, табл. 2, рис. 7.
Ключові слова: **функціональні матеріали, запобіжник, сплав з пам'яттю форми, термочутливий елемент.**

Introduction. A number of electrical devices are particularly sensitive to overload (for example, voltage transformers [1] in automatic reserve input and sectioning devices [2]), respectively, fuses with a current-limiting effect are used for their protection. The current-limiting effect in modern fuses is created by dissolving more refractory metals in less refractory ones, using an alloy of fusible inserts, pointwise reduction of the cross-sectional area of fusible inserts, accelerated extinguishing of the electric arc with a quartz filler, etc.

An effective way to improve the current-limiting effect can be the use of elements made of shape memory alloys (SMA) [3]. The basic physical essence of the shape memory effect can be interpreted as the property of a technical element made of an alloy containing thermoelastic martensite in its structure to restore its original shape when heated (Fig. 1).

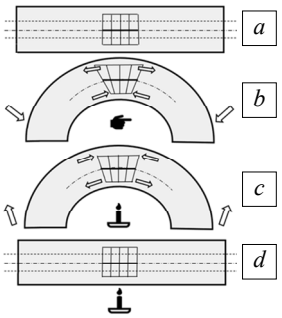

Fig. 1. Interpretation of the properties of a product made of an alloy with a shape memory effect: *a* – the initial shape of the product; *b* – forced deformation of the product (deformation of the martensite structure); *c* – heating of the product and the beginning of the recovery of the shape (thermoelastic reverse deformation of the martensite structure); *d* – completion of the recovery of the shape to the initial state

The SMA alloy element can perform the functions of both a sensor and an actuator [3, 4].

The two most common SMAs in terms of application and research are Ni-Ti, also known as Nitinol, and copper-based alloys such as Cu-Al-Mn [4–6]. One variant of copper-based SMA is Camital [7].

The shape recovery of SMA products can be achieved by indirect heating with a heat source and directly by the action of an electric current. A SMA product can convert thermal energy into mechanical work, the value of which depends mainly on the alloy composition and the geometry of the product [3, 8, 9].

The shape memory process involves two types of martensitic transformations: direct and reverse. Each of them manifests itself in a certain temperature range: M_S and M_F – the initial and final temperatures of the martensitic transformation during cooling; A_S and A_F – the initial and final temperatures of the reverse martensitic transformation during heating, respectively. The martensitic transformation temperatures are a function of the alloy grade (alloy system) and its chemical composition. Minor changes in the chemical composition of the alloy (intentional or due to defects) cause a change in the characteristic transformation temperatures. This leads to the need to maintain the exact chemical composition for the functional manifestation of the shape memory effect with programmed parameters and characteristics, which puts the metallurgical production of SMA in the field of high technology [3, 4].

Experimental studies of SMA products have shown [3, 10, 11] that from the point of view of economic indicators, as well as physical properties and characteristics, the copper-based alloy Cu (83 %)-Al (12 %)-Mn (5 %) is the most suitable for solving various engineering problems, for example, in electrical installations and other areas. Of great importance is its cost, which is almost 20 times lower compared to Ni-Ti Nitinol.

A unique physical feature of SMA is the time-dependent characteristic of shape recovery during direct heating of products with electric current, which allows creating highly sensitive electrical devices for protecting electrical installations from overloads and short circuits [9, 12].

The indicators obtained by the authors during previous experimental studies of the shape recovery time of a thermosensitive element heated directly by electric current, as well as the reactive power and its behavior during an increase in electric current, confirm the possibility of designing protection and control devices [3].

There are two classical principles of fuse design: a fusible type with thermal destruction of the fuse element and a multiple contact type with a bimetallic thermosensitive element [13].

Based on the electrothermomechanical properties of the SMA application, a new principle of fuse design was implemented in this study (Fig. 2). The operation of this fuse is based on the forced mechanical destruction of the fuse element by a thermosensitive tension element at a given current value [14].

The current flowing through the fuse element and the thermal element heats them. The thermal element 1 changes (restores) its shape under the influence of temperature, causing mechanical tension in the fuse element 2. If the tension reaches the mechanical strength limit, the fuse element first breaks mechanically and then thermally due to the electric arc that stretches between the parts of the torn fuse element, which reduces the fuse response time.

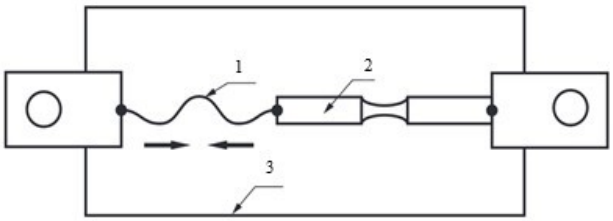

Fig. 2. Schematic representation of a fuse with forced destruction of the fuse element: 1 – SMA thermosensitive element; 2 – fuse element; 3 – housing [14]

Therefore, **the goal of the work** is to establish the patterns of strengthening the current-limiting effect of a fuse (reducing the response time) when using thermosensitive elements made of shape memory alloys. The achievement of the goal is based on the analysis of the experimental studies conducted by the authors and the mathematical models of the characteristics of the fuse containing the SMA element.

Mathematical modelling of parameters and characteristics of fuses with thermomechanical destruction of the fuse element. Let us assume that the thermosensitive element is located in a homogeneous confined medium with low thermal resistance in such a way that the temperature gradient in the middle of this element is very small, and there is an ideal thermal contact between the thermosensitive element and its medium. The heat transfer coefficient does not depend on temperature [15, 16]. When current flows, the heat produced in the thermosensitive element is spent on heating both this element and its contact medium. In this case, the heat balance equation has the form [17, 18]:

$$\left(c_1 m_1 + c_2 m_2\right)\frac{\mathrm{d}\theta}{\mathrm{d}t} + \alpha S\left(\Theta - \Theta_0\right) = I^2 R_0\left(1 + \beta\Theta\right), \quad (1)$$

where θ is the temperature of the thermosensitive element, °C; c_1 is the specific heat capacity of the alloy of the thermosensitive element, J/(kg·K); c_2 is the specific heat capacity of the medium in which the thermosensitive element is located, J/(kg·K); m_1 is the mass of the thermosensitive element, kg; m_2 is the mass of the medium, kg; R_0 is the electrical resistance of the thermosensitive element at 0 °C; S is the cooling surface, m^2; I is the current flowing through the thermosensitive element, A; β is the coefficient of temperature resistance, K^{-1}; α is the heat transfer coefficient, W/(m^2·K); θ_0 is the ambient temperature, °C.

Under these conditions, the solution of the differential equation (1) for a direct current I and the initial condition $\theta|_{t=0} = \theta_0$ is as follows [3]:

$$\theta = \frac{\dfrac{I^2 R_0}{\alpha S} + \theta_0}{1 - \dfrac{I^2 R_0}{\alpha S}\beta} - \frac{\dfrac{I^2 R_0}{\alpha S}\left(1 + \beta\theta_0\right)}{1 - \dfrac{I^2 R_0}{\alpha S}\beta} \exp\left[-\frac{t\left(1 - \dfrac{I^2 R_0}{\alpha S}\beta\right)\alpha S}{c_1 m_1 + c_2 m_2}\right]. \quad (2)$$

Fuse characteristics in steady state if $\frac{I^2R_0}{\alpha S}\beta < 1$, then according to (2), when $t \to \infty$, the temperature of the thermosensitive element will approach the value θ_{es}, which is expressed as:

$$\theta_{es} = \left(\frac{I^2R_0}{\alpha S} + \theta_0\right) \Bigg/ \left(1 - \frac{I^2R_0}{\alpha S}\beta\right). \quad (3)$$

If in (3) the temperature coefficient of resistance $\beta = 0$, then the dependence of the given temperature on the current will be determined by the expression:

$$\theta_{es} = \frac{I^2R_0}{\alpha S} + \theta_0 . \quad (4)$$

The rated fuse current I_N is determined from (3) provided that:

$$\theta_{es} = A_S, \quad (5)$$

where A_S is the temperature at which the thermosensitive element begins to recover its shape, °C.

Therefore, the rated current of the fuse is:

$$I_N = \sqrt{\frac{\alpha S(A_s - \theta_0)}{R_0(1+\beta A_s)}} . \quad (6)$$

The limit current ($I_{\lim}$) for this type of fuse will be determined by the critical temperature level θ_{kr} at which the condition will be fulfilled:

$$\sigma_{ad} = \sigma_{in}, \quad (7)$$

where σ_{ad} is the ultimate mechanical tensile stress of the fuse element, Pa; σ_{in} is the mechanical stress in the fuse element when the therm0sensitive element is heated, Pa:

$$I_{\lim} = \sqrt{\frac{\alpha S(\theta_{kr} - \theta_0)}{(R_0(1+\beta\theta_{kr})}} . \quad (8)$$

The ratio of the limiting current to the rated current will be determined by the critical temperature and the shape recovery temperature of the SMA thermosensitive element.

$$I_{\lim} / I_N = \sqrt{\frac{(\theta_{kr} - \theta_0)(1+\beta A_s)}{(A_s - \theta_0)(1+\beta A_{kr})}} . \quad (9)$$

Fuse characteristics in unstable mode. The differential equation describing the cooling process of the thermosensitive element has the form:

$$(c_1m_1 + c_2m_2)\frac{\mathrm{d}\theta}{\mathrm{d}t} + \alpha S(\theta - \theta_0) = 0 , \quad (10)$$

and its solution for the initial condition $\theta|_{t=0} = \theta_{es}$ is [3]:

$$\theta - \theta_0 = (\theta_{es} - \theta_0)e^{-t/\left[\frac{(c_1m_1+c_2m_2)}{\alpha S}\right]}. \quad (11)$$

Since formula (2) shows the dependence of the temperature of a thermosensitive element on the time of current flow, it can be transformed to determine the time required to heat the element to a given temperature and, in particular, to the critical temperature:

$$t_{kr} = \frac{c_1m_1 + c_2m_2}{\alpha S\left(\frac{I^2R_0}{\alpha S}\beta - 1\right)} \ln\left[\frac{1+\beta\theta_{kr}}{1+\beta\theta_0} - \frac{\theta_{kr} - \theta_0}{\frac{I^2R_0}{\alpha S}(1+\beta\theta_0)}\right]. \quad (12)$$

The formula for the time-current characteristic of a fuse with any SMA thermosensitive element is:

$$\frac{t_{kr}}{\tau} = \frac{I_{\lim}^2(1+\beta\Theta_{kr})}{I^2(\theta_{kr} - \theta_0) - I_{\lim}^2(1+\beta\theta_{kr})} \ln\left[\frac{1+\beta\theta_{kr}}{1+\beta\theta_0}\left(1 - \frac{I_{\lim}^2}{I^2}\right)\right], \quad (13)$$

where the time constant is:

$$\tau = \frac{c_1m_1 + c_2m_2}{\alpha S} .$$

The thermomechanical characteristics of the thermosensitive SMA element and the mechanical strength characteristics of the fuse, the protective characteristics of the fuse with thermomechanical fuse failure can be obtained by fulfilling condition (7).

Since the fuse uses the principle of mechanical failure of the fuse element, the equation of the maximum mechanical strength limit of the fuse element will be as follows:

$$F_{ad} = \sigma_{AD}\pi\frac{d_{fe}^2}{4}, \quad (14)$$

where d_{fe} is the diameter of the fuse element, m.

Accordingly, the force generated in the thermosensitive element (SMA) of the fuse is equal to:

$$F_{te}(t, I) = ab\sigma_{te}(t, I) , \quad (15)$$

where a, b are the width and thickness of SMA, respectively, m; $\sigma_{te}(t, I)$ is the thermomechanical stress arising in the thermosensitive element during direct heating (function of time t and current I), Pa.

Then the balance equation of the mechanical strength limit will be as follows:

$$\sigma_{te}(t, I)ab - \sigma_{ad}\pi\frac{d_{fe}^2}{4} = 0 . \quad (16)$$

Modelling of thermomechanical strength in a SMA thermosensitive element can be performed using the following equations:

$$\sigma_{te}(t) = \mathrm{if}\left[\theta(t) \geq 90, M_{te}(t), K_{te}(t)\right]; \quad (17)$$

$$M_{te}(t) = (1 - e^{-\theta(t)A_1})A_2L_0 - A_3L_0 ; \quad (18)$$

$$K_{te}(t) = A_4\theta(t)^4L , \quad (19)$$

where σ_{te} is the thermomechanical stress, Pa; t is the time, s; θ is the temperature, °C; A_1 – A_4, L_0, L are the coefficients calculated based on experimental measurements of thermomechanical characteristics of SMA samples. Dimensions of coefficients: L – [Pa/K^4]; L_0 – [Pa]; A_1 – [1/K]; A_2 – A_4 – dimensionless quantities.

The dependence of the temperature of the thermosensitive element on the current and its flow time is based on the well-known dependence [3, 9]:

$$\theta = \frac{\rho}{C}10^6(I/q)^2t , \quad (20)$$

where ρ is the specific electrical resistance of the SMA, Ω·m; C is the specific volumetric heat capacity of the conductor material, J/(m^3·K); I is the current, kA; q is the cross-sectional area of the conductor, m^2; t is the time, s.

For the Camital alloy, the change in the temperature of the SMA over time when heated by a short-circuit current can be represented by the expression [3]:

$$\theta(t,I)=5{,}328\cdot10^{-7}\frac{W(t)}{q^2}+1{,}28\cdot10^{-18}\frac{W(t)^2}{q^4}+ \\ +4{,}014\cdot10^{-29}\frac{W(t)^4}{q^6}+\theta_0 \quad , \quad (21)$$

where $W(t)$ is the thermal impulse, $A^2\cdot s$; q is the cross-sectional area of the thermally sensitive element, m^2.

The thermal impulse generated in the thermosensitive element during the flow of a short-circuit current is calculated by the formula [3, 9]:

$$W(t)=\int_0^t\left[I_{pm}\sin(\omega t)+I_{am}e^{-t/T_a}\right]^2 \mathrm{d}t\,, \quad (22)$$

where I_{pm}, I_{am} are the periodic and aperiodic components of the short-circuit current, respectively, kA; T_a is the time constant of the decay of the aperiodic component of the short-circuit current, s.

To obtain a generalized equation of the protective characteristics of the fuse, the relationship between the heating temperature of the thermosensitive element and the current and its flow time is approximated by the following polynomial (based on experimental measurement data):

$$\theta(t,I)=5{,}328\cdot10^{-7}I^2\frac{t}{q^2}+1{,}28\cdot10^{-18}I^4\frac{t^2}{q^4}+ \\ +4{,}014\cdot10^{-29}I^6\frac{t^4}{q^6}+\theta_0. \quad (23)$$

Since the second and third terms in (23) take values close to zero, we can use a simplified dependence with an error of <1 %:

$$\theta(t,I)=5{,}328\cdot10^{-7}I^2\frac{t}{q^2}+\theta_0\,. \quad (24)$$

Then the model of thermomechanical characteristics takes the following form:

$$\sigma_{te}(t,I)=\mathrm{if}\left[\theta(t,I)\geq 90, M_{te}(t,I), K_{te}(t,I)\right]; \quad (25)$$

$$M_{te}(t,I)=\left[1-e^{-(5{,}328\cdot10^{-7}I^2\frac{t}{q^2}+\theta_0)A_1}\right]A_2L_0-A_3L_0\,; \quad (26)$$

$$K_{te}(t,I)=A_4(5{,}328\cdot10^{-7}I^2\frac{t}{q^2}+\Theta_0)^4L\,. \quad (27)$$

After transforming (24) with respect to time t and taking into account the equation of thermomechanical characteristics of the thermosensitive element, we obtain the ampere-second characteristic (mathematical model) of a fuse with a tension element made of a shape memory alloy:

$$t(I)=1{,}87\cdot10^6\frac{q_{te}^2}{I^2}\left[\sqrt[4]{\pi\sigma_{fe}\frac{d_{fe}^2}{ALq}}-\theta_0\right], \quad (28)$$

where $A=4\cdot A_4$ is the dimensionless quantity.

In the case of SMA in the form of a coiled spring, we obtain:

$$t(I)=1{,}87\cdot10^6\frac{q_{te}^2}{I^2}\left[\sqrt{d_{fe}d_{te}\sqrt{\sigma_{fe}\pi\frac{D_{te}}{2A_4LL_{te}\ln(1+\varepsilon)}}}-\Theta_0\pi^2d_{te}\right], \quad (29)$$

where d_{te} is the diameter of the SMA wire, m; L_{te} is the length of the SMA wire, m; D_{te} is the diameter of the SMA spring, m; ε is the relative deformation of the spring, a dimensionless quantity; $C/\rho=1.87\cdot10^6$ [$A^2\cdot s/(m^4\cdot K)$].

Test bench design. A special test bench was created to conduct tests to verify the developed mathematical model. Its functional diagram is shown in Fig. 3; Fig. 4 shows the measuring unit, and Fig. 5 shows the general view.

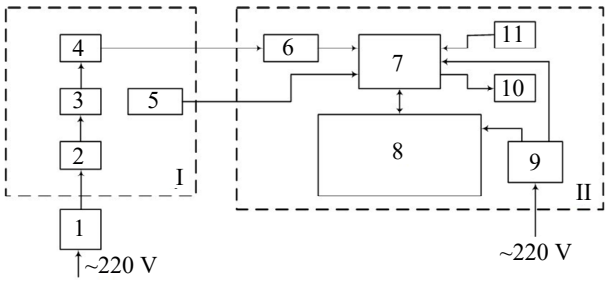

Fig. 3. Functional diagram of the test bench: I – measuring device; II – information display and storage unit; 1 – regulated power supply; 2 – fuse; 3 – strain gauge; 4 – current sensor; 5, 6 – analog-to-digital converters; 7 – microcontroller; 8 – touch screen; 9 – power supply; 10 – information storage device; 11 – ambient temperature sensor

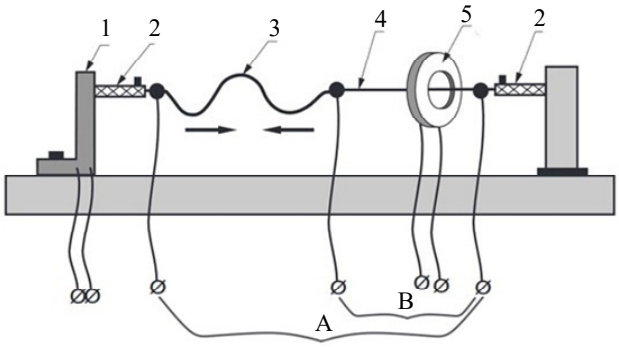

Fig. 4. Measuring unit of the test bench: 1 – strain gauge mounting; 2 – insulating mountings; 3 – SMA thermosensitive element; 4 – fuse element; 5 – induction coil, current measuring element; A – power supply circuit when testing a fuse with a SMA thermosensitive element; B – power supply circuit when testing a traditional fuse

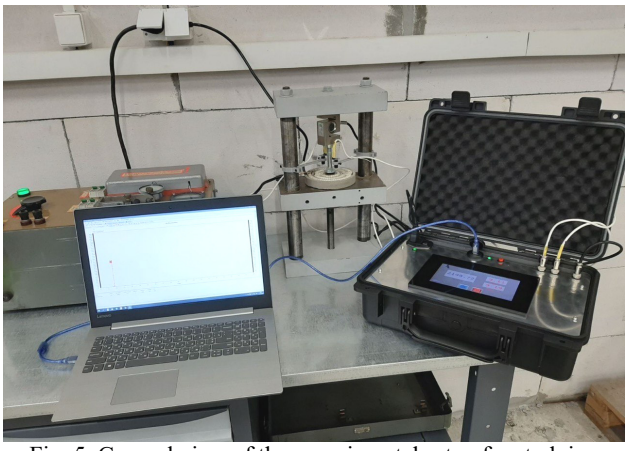

Fig. 5. General view of the experimental setup for studying thermosensitive elements with shape memory and fuses [19]

The stand can be used to test both traditional fuses and fuses with an SMA element. In the first case, voltage is applied to circuit B, and current flows only through element 4. In the second case, voltage is applied to circuit A, and current flows through both the traditional fuse element 4 and the thermosensitive element 3. The thermosensitive element heats up and, changing its shape, increases the mechanical load on part 4 of the fuse. The strain gauge system measures the increase in tensile force until the tensile strength is exceeded and the fuse element breaks. The current is measured using an inductive sensor YTT-6M2 with an accuracy class of 0.2 (5) and a control and measurement system. The accuracy of the breaking force measurement is 2 %.

The characteristics of a fuse with a rated current of 7 A, which assume thermomechanical destruction of the safety element, can be analyzed using an example with the following initial data: geometry of the thermosensitive element a = 0.005 m (width), b = 0.00035 m (thickness); copper safety element – wire with a diameter of d = 0.0002 m; mechanical tensile strength limit of the safety element σ_{fe} =2·10^8 Pa (tensile strength 6.28 N); current I = 40 A; A_4 = 5.8·10^{-5}; L = 2·10^5 Pa/K^4. The results of the calculations are shown in Fig. 6, 7.

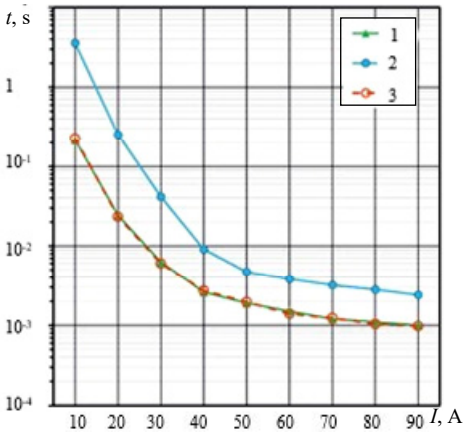

Fig. 6. Ampere-second characteristics of fuses: 1 – thermomechanical destruction of the fuse element (calculated); 2 – experimental protective characteristics of a traditional fuse; 3 – experimental protective characteristics of a fuse with a thermosensitive SMA element

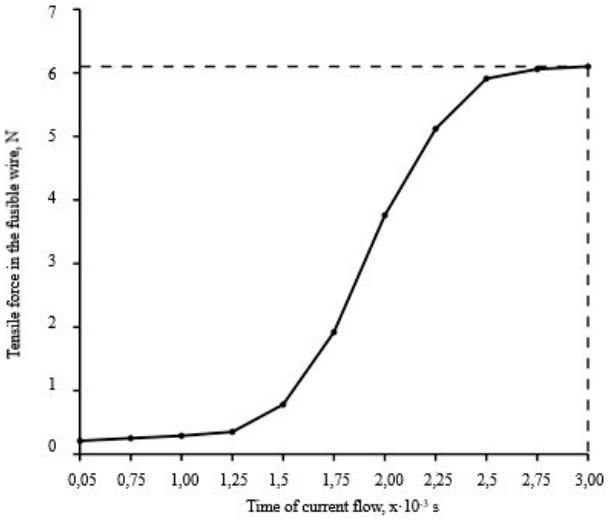

Fig. 7. Dynamics of change in the tensile force acting on the fuse element (copper wire)

Results and discussion. Table 1 shows the measurement results for a conventional fuse and an SMA fuse equipped with a thermally sensitive element. For each current value, the responce time of the modified fuse was shorter than that of the conventional fuse. The use of a thermosensitive element reduced the response time by more than 20 times for a current of 10 A and by about 10 times (from 0.257 s to 0.0244 s) for a current of 20 A. The reduction in response time decreased with increasing current. For the highest current tested (90 A), the response time of the fuse was less than half that of the conventional fuse.

Table 1

Fuse response time for different current values (SD – standard deviation)

Current, A	Traditional fuse	Fuse with SMA element	Values calculated for a fuse with an SMA element
	Safety element destruction time, average value (±SD), s		
10	3,579 (±0,0224)	0,2158 (±0,0041)	0,2266
20	0,254 (±0,0044)	0,0244 (±0,0005)	0,02338
30	0,0416 (±0,0003)	0,0063 (±0,0002)	0,00602
40	0,0091 (±0,0002)	0,0026 (±0,0001)	0,00272
50	0,0047 (±0,0003)	0,0022 (±0,0001)	0,00196
60	0,0038 (±0,0001)	0,0015 (±0,0001)	0,00139
70	0,0032 (±0,0003)	0,0012 (±0,0002)	0,00104
80	0,0028 (±0,0001)	0,0011 (±0,0001)	0,00104
90	0,0024 (±0,0001)	0,0010 (±0,00002)	0,00098

Table 2 contains calculated values from the mathematical model described in the research methodology, which are close to the measurement results. The dependencies of the fuse response time for different current values in three variants are shown in Fig. 6.

Table 2

Dynamics of changes in the tensile force acting on the fusible wire (SD – standard deviation)

Current flow time, ms	Force acting on the fusible wire
	Average value (±SD), N
0,5	0,21 (±0,006)
0	0,25 (±0,002)
1	0,29 (±0,002)
1,25	0,35 (±0,002)
1,5	0,78 (±0,004)
1,75	1,92 (±0,003)
2	3,76 (±0,004)
2,25	5,12 (±0,004)
2,5	5,91 (±0,004)
2,75	6,06 (±0,013)
3	6,12 (±0,000)

In experimental studies, the same fuse element (copper wire with a diameter d = 0.0002 m) was used. The positions of the characteristics obtained from calculations and experiments in the coordinate grid (Fig. 6) confirm the

positive effect of the SMA thermosensitive element on the fuse sensitivity and the increase in the current-limiting effect. The discrepancy between the calculated (1) and experimental results (3) in Fig. 6, estimated by the least squares method, does not exceed 5 % on average.

According to the research methodology, measurements of the change in the tensile force at different currents were carried out. The results are given in Table 2 and shown in Fig. 7. Under these conditions, at a current I = 40 A, the tensile force reached the limit value after ≈3 ms. Such a fuse response time is achieved due to the use of the SMA thermally sensitive element and significantly increases the current protection class, ensuring satisfactory safety for most electrical equipment. The tensile strength of the safety element was ≈6 N and was slightly lower than the calculated tensile strength given above (6.28 N). This difference is due to the heating of the safety element and the change in its mechanical characteristics.

Conclusions.

1. Using a thermosensitive shape memory alloy (SMA) element to ensure thermomechanical destruction of the fuse element is a highly effective way to improve its current-limiting effect. It is experimentally proven that the modified fuse exhibits a significantly shorter response time compared to the traditional one: the response time reduction was more than 20 times for a current of 10 A and about 10 times for a current of 20 A.

2. The developed mathematical model adequately describes thermal, electrical and thermomechanical processes in a fuse with an SMA element; the discrepancy between the calculated and experimental ampere-second characteristics does not exceed 5 %, which confirms the possibility of its use for engineering design and optimization of fuse parameters.

3. To implement the new fuse design principle, it is advisable to use a functional copper-based alloy, for example Cu-Al-Mn (Camital). This choice is due not only to its suitable physical properties and characteristics, but also to its significantly lower cost compared to Ni-Ti Nitinol, which increases the practical significance of the proposed solution.

Conflict of interest. The authors declare no conflict of interest.

REFERENCES

1. Grechko O., Baida Y., Sereda O., Sereda O., Pantelyat M., Dryvetskyi S. Improvement of Fuses to Increase the Efficiency of Medium Voltage Instrument Transformers Protection. *2025 IEEE 6th KhPI Week on Advanced Technology (KhPIWeek)*, 2025, pp. 1-4. doi: https://doi.org/10.1109/KhPIWeek61436.2025.11288696.

2. Kozyrskyi V., Gay O., Synyavskyi O., Savchenko V., Makarevyth S. Optimization of sectionalisation parameters of distributive electric networks. *Handbook of Research on Smart Computing for Renewable Energy and Agro-Engineering*, 2020, pp. 78-105. doi: https://doi.org/10.4018/978-1-7998-1216-6.ch004.

3. Kozyrsky V., Kaplun V., Firstov G., Likhachov O. *Monograph. Electrical equipment based on functional materials*. Kyiv, NUBIP Publ., 2014. 409 p. (Ukr).

4. Sharma N., Jangra K., Raj T. Applications of Nickel-Titanium Alloy. *Journal of Engineering and Technology*, 2015, vol. 5, no. 1, pp. 1-7. doi: https://doi.org/10.4103/0976-8580.149472.

5. Bubley I.R., Koval Y.N., Likhachev A.A., Sych T.G., Zatsarnaya A.V. Investigation at Aging of Functional Properties of Alloy of Cu–Al–Mn System Alloyed with Co. *Metallofizika i Noveishie Tekhnologii*, 2021, vol. 43, no. 12, pp. 1627-1637. doi: https://doi.org/10.15407/mfint.43.12.1627.

6. Sun S., Yu J., Chang Y., Zheng Y., Wang C. Effect of Al content and quenching on the microstructure and mechanical properties of as-cast Cu–Al–Mn shape memory alloy. *Materials Chemistry and Physics*, 2025, vol. 345, art. no. 131282. doi: https://doi.org/10.1016/j.matchemphys.2025.131282.

7. CAMITAL brand registration certificate no. 163545. Available at: https://alotek.international/uploads/230/1jgmO5anW3WCOVP22n2bZsx7RSeMc9-metaQ2FtaXRhbCDQodCy0LjQtNC10YLQtdC70YHRgtCy0L4r0LfQsCvRgNC10LPQuNGB0YLRgNCw0YbQuNGPLnBkZg==-.pdf (Accessed 20 May 2025).

8. Theren B., Schmelter T., Chromik P., Kuhlenkötter B. Investigations Regarding the Longterm Behaviour of Electrically Heated SMA Wires Using Alternating Current. *Proceedings of ASME 2021 Conference on Smart Materials, Adaptive Structures and Intelligent Systems, SMASIS 2021*, art. no. V001T06A003. doi: https://doi.org/10.1115/SMASIS2021-67649.

9. Panciroli R. Influence of electric current on the thermo-mechanical static and fatigue properties of shape memory NiTi wires. *Smart Materials and Structures*, 2020, vol. 29, no. 11, art. no. 115046. doi: https://doi.org/10.1088/1361-665X/abb986.

10. Kozyrskyi V., Bunko V. Experimental Studies of Elements from the Functional Intermetallic Cu-Al-Mn for Construction of a Heat Engine and Power Plant. *Problems of the Regional Energetics*, 2025, vol. 3, no. 67, pp. 162-173. doi: https://doi.org/10.52254/1857-0070.2025.3-67.14.

11. Bunko V.Ya., Kozyrskyi V.V. Research of elements with shape memory effect and determination of their thermo-mechanical characteristics at different hardening temperatures. *Collection of Scientific Papers of Admiral Makarov National University of Shipbuilding*, 2024, no. 1 (494), pp. 69-73. (Ukr).

12. Gorges T., Seelecke S., Motzki P. Alternating current activation of SMA wires. *GMM-Fachberichte*, 2021, vol. 2021-February, no. 98, pp. 149-151.

13. *EATON. High speed fuse application guide*. 2016. 44 p. Available at: https://www.eaton.com/content/dam/eaton/products/electrical-circuit-protection/bussmann-iec-high-speed-semi-conductors-fuses/eaton-bussmann-series-high-speed-fuses-application-guide-br132015en-en-us.pdf (Accessed 20 May 2025).

14. Kravets A.V., Kozyrskyi V.V. *Fuse. Patent USSR no. 1707646*, 1992, bulletin no. 3. 14 p. (Rus).

15. Chiriac G. Thermal analysis of fuses with variable cross-section fuselinks. *Electric Power Systems Research*, 2012, vol. 92, pp. 73-80. doi: https://doi.org/10.1016/j.epsr.2012.06.010.

16. Todorov G., Kamberov K. EV fuse design cost reduction based on Thermal-Electric Conduction analyses. *Case Studies in Thermal Engineering*, 2020, vol. 21, art. no. 100692. doi: https://doi.org/10.1016/j.csite.2020.100692.

17. Fernandez E., Torres E., Zamora I., Mazon A.J., Albizu I. Thermal model for current limiting fuses installed in vertical position. *Electric Power Systems Research*, 2014, vol. 107, pp. 167-174. doi: https://doi.org/10.1016/j.epsr.2013.10.004.

18. Torres E., Mazón A.J., Fernández E., Zamora I., Pérez J.C. Thermal performance of back-up current-limiting fuses. *Electric Power Systems Research*, 2010, vol. 80, no. 12, pp. 1469-1476. doi: https://doi.org/10.1016/j.epsr.2010.06.010.

19. *Thermal relay. Alotek Technology*. Available at: https://alotek.international/components/termorele_vid_alotek_technology (Accessed 20 May 2025).

Received 17.10.2025
Accepted 30.11.2025
Published 02.03.2026

V.V. Kozyrskyi[1], *Doctor of Technical Science, Professor,*
T. Nurek[2], *Full Professor,*
J. Sloma[2], *PhD,*
V.Ya. Bunko[3], *PhD, Associate Professor,*
M.V. Goncharuk[4], *Master Student,*
[1] ALOTEK Technology sp.z.o.o.,
Zadabrowie 311, Krakowska 11, 37-716, Orly, Poland.
[2] Department of Biosystem Engineering,
Institute of Mechanical Engineering,
Warsaw University of Life Sciences,
Nowoursynowska 166, 02-787, Warsaw, Poland.
[3] Separated Subdivision of National University
of Life and Environmental Sciences of Ukraine
«Berezhany Agrotechnical Institute»,
20, Akademichna Str., Berezhany, Ternopil region, Ukraine, 47501.
e-mail: vbunko@gmail.com (Corresponding Author)
[4] National University of Life and Environmental Sciences of Ukraine,
15, Heroyiv Oborony Str., Kyiv, Ukraine, 03041.

The use of shape memory alloys in fuses for the protection of electrical installations.

Problem. *The degree of damage to electrical installations during short circuits depends on the response time of the protection. An effective way to enhance the current-limiting effect in electrical fuses (reducing their response time) may be the use of shape memory alloy (SMA) elements. However, this requires careful study and research. The* ***goal*** *of the work is to establish the patterns of strengthening the current-limiting effect of a fuse (reducing the response time) when using thermosensitive elements made of shape memory alloys. The achievement of this goal is based on the analysis of experimental studies conducted by the authors and mathematical models of the characteristics of a fuse containing an SMA element.* ***Methodology***. *The article presents mathematical modelling of the parameters and characteristics of fuses with thermomechanical destruction of the fuse element, as well as a thermophysical model of a fuse with a thermosensitive SMA element. The article presents the* ***results*** *of experimental studies of a traditional fuse and a fuse equipped with a thermosensitive SMA element. For each current, the response time of the modified fuse was shorter than that of the traditional fuse. The use of a thermosensitive element reduced the response time by more than 20 times for a current of 10 A and approximately 10 times (from 0.257 s to 0.0244 s) for a current of 20 A. For the highest tested current (90 A), the fuse response time was half that of a traditional fuse. The article also presents the results of calculations of fuse characteristics using a mathematical model and a comparison with the results of experimental studies.* ***Scientific novelty***. *The developed mathematical models of the characteristics of electrical fuses containing SMA elements made it possible for the first time to substantiate the interrelationships between the parameters (geometric dimensions and characteristics of SMA elements, fuse links) with current loads of electrical installations. The* ***practical value*** *of the work lies in the proposed use of thermosensitive elements made of functional materials to increase the current-limiting effect of electrical fuses for protecting electrical installations during short circuits.* References 19, tables 2, figures 7.

Key words: **functional materials, fuse, shape memory alloy, thermosensitive element**.

How to cite this article:
Kozyrskyi V.V., Nurek T., Sloma J., Bunko V.Ya., Goncharuk M.V. The use of shape memory alloys in fuses for the protection of electrical installations. *Electrical Engineering & Electromechanics*, 2026, no. 2, pp. 3-9. doi: https://doi.org/10.20998/2074-272X.2026.2.01

UDC 621.313 https://doi.org/10.20998/2074-272X.2026.2.02

A.N. Patel, T.H. Panchal

Mitigation of cogging torque in surface permanent magnet brushless DC motor using slot opening shift

Introduction. *Cogging torque deteriorates the torque quality of surface permanent magnet brushless DC (PMBLDC) motors.* ***Problem.*** *Reducing cogging torque is indispensable for performance upgradation of PMBLDC motors; hence, it is an important issue for motor designers.* ***Goal.*** *This paper presents a slot opening shift approach to reduce the cogging torque of radial flux surface PMBLDC motors.* ***Methodology.*** *A 200 W, 1000 rpm radial flux surface PMBLDC motor is first designed based on different assumed design variables and is treated as a reference model. The parallel stator teeth are uniformly distributed along the stator periphery, and the slot opening is considered in the middle position in the reference design. The cogging torque of the reference design is obtained from simulation and electromagnetic analysis.* ***Results.*** *A series of finite element simulations are performed to examine the impact of design upgradation on the cogging torque of the surface PMBLDC motor. It is observed that the peak-to-peak cogging torque is reduced by 44.5 %.* ***Scientific novelty.*** *The design is enhanced by applying slot opening shift to stator slots. The slot opening is shifted in an anticlockwise direction, and subsequently, the cogging torque waveform is determined for the upgraded motor from finite element modelling and analysis.* ***Practical value****. Research has revealed that this technique is effective in reducing cogging torque, and it can also be applied to other topologies of permanent magnet motors.* References 23, tables 2, figures 12.

Key words: **brushless motor, finite element analysis, slot opening shift, cogging torque.**

Вступ. *Пульсація крутного моменту погіршує його якість у безщіткових двигунах постійного струму з постійними магнітами (PMBLDC).* ***Проблема****. Зниження пульсації крутного моменту є необхідною умовою підвищення продуктивності PMBLDC двигунів, тому це є важливим завданням для проєктувальників двигунів.* ***Мета****. У статті представлений підхід, заснований на зміщенні пазів для зниження пульсації крутного моменту PMBLDC двигунів з радіальними поверхневими магнітними потоками.* ***Методологія****. Спочатку проєктується PMBLDC двигун з радіальними поверхневими магнітними потоками потужністю 200 Вт та частотою обертання 1000 об/хв на основі різних передбачуваних проєктних змінних, що розглядається як еталонна модель. Паралельні зубці статора рівномірно розподілені по периферії статора, а паз еталонної конструкції розташований посередині. Пульсація крутного моменту еталонної конструкції отримана з моделювання та електромагнітного аналізу.* ***Результати****. Проведено ряд скінченно-елементних моделювань для вивчення впливу вдосконаленої конструкції на пульсацію крутного моменту PMBLDC двигуна з поверхневими магнітами. Встановлено, що пікова пульсація крутного моменту знижується на 44,5 %.* ***Наукова новизна****. Конструкція вдосконалена за рахунок застосування усунення відкриття пазів статора. Відкриття паза зміщується проти годинникової стрілки, і згодом форма пульсації моменту модернізованого двигуна визначається за допомогою скінченно-елементного моделювання та аналізу.* ***Практична значимість****. Дослідження показали, що цей метод є ефективним для зниження пульсації крутного моменту, і його також можна застосовувати до інших топологій двигунів з постійними магнітами.* Бібл. 23, табл. 2, рис. 12.

Ключові слова: **безщітковий двигун, аналіз методом скінченних елементів, зсув відкриття пазу, крутний момент зубчатого обертання.**

Introduction. Brushless DC motors offer better operational efficiency, a high power-to-volume ratio, a varied speed range, and rapid dynamic response. Due to these characteristics, it has gained widespread acceptance in various residential and industrial applications. Progress in material technology in permanent magnet (PM) and semi-conductor switches has accelerated the development of brushless DC motors. Apparent torque ripple is one of the biggest problems in permanent magnet brushless DC (PMBLDC) motors. Torque ripple produces vibration and unwanted audible noise which may deteriorate the overall performance of the motor. The development of smooth torque in brushless DC motors is a prime objective that needs thorough attention to all aspects of motor design. Torque ripple is inherent in brushless DC motors due to cogging torque (CT), distorted back electromotive force (EMF) waveform, non-ideal exciting current waveform, and time delay in excitation pattern [1–3]. The torque ripple of brushless DC motors can be reduced by either decreasing the CT or improving the quality of back EMF and exciting current waveforms. Reducing CT is a design issue, while improving the quality of back EMF and exciting current waveforms is a control issue. Any variation in control techniques results in reduced operational efficiency of brushless DC motor drives. CT is the major cause in brushless DC motors for producing torque ripple. CT is inherent because of the existence of PMs and a slotted stator structure. The combination of the number of rotor poles and the number of stator slots significantly affects the torque quality and output of the PMBLDC motor. Inappropriate combination of number of rotor poles and stator slots results in a high CT and torque ripple [4]. The CT of PM motors cannot be eliminated, but can be decreased with design improvements. The reduction of torque ripple is indispensable for applications that require smooth running. Ideally, the torque ripple reduction technique should only improve torque quality without affecting other performance parameters of the motor. The average CT value is zero, and its variation is achieved by unexcited stator windings. CT is large for a more compact motor, having a smaller air gap and stronger PM. CT reduction is a significant concern while designing the PMBLDC motor and is considered an important criterion for the quality of motor design. Reduction of CT is a difficult task and it cannot be eliminated but can be reduced to a certain extent [5].

In literature different techniques are available to decrease the CT from a design perspective. Skewing, shaping of PM, displacing magnets, inclusion of dummy slots, variation of magnet pole arc, dual notching, slot displacement and use of fractional number of slots are a few methods used to mitigate CT of PM motors [6–21]. The length of the stator conductor and hence copper losses increase with the application of skewing of the stator slot. One of the most popular approaches for mitigating CT is the skewing of PM. However, the stray losses and leakage inductance increase, and the useful magnetic flux linking with the stator winding decreases. It also produces unbalanced axial electromagnetic force which produces vibration and acoustic noise besides damaging the bearing system. Shaping of PM reduces CT but it adversely affects the back EMF waveform. Displacing magnets and rotors cause the rotor's center of mass to shift away from the rotating axis. The use of

dummy slots or teeth reduces the amplitude and increases the frequency of CT. But an important drawback of this method is manufacturing difficulties which results in increased cost of motor. In the fractional number of slots, each magnet has a different placement compared to stator slots. Therefore, CT components due to individual PM poles are out of phase relative to each other. Hence, the resulting CT is decreased due to the mutual cancellation of the sub-components of CT.

Goal. This paper presents a slot opening shift approach to reduce the cogging torque of radial flux surface PMBLDC motors.

Cogging torque. The slot opening shift method's influence on surface PMBLDC motor performance is examined and presented. Extensive simulations utilizing finite element (FE) modelling and analysis [22] are conducted to arrive at a result. CT and its associated equations are explained. A detailed explanation of the reference PMBLDC motor model is provided. An enhanced design is introduced that utilizes a slot opening shift mechanism to reduce the CT of the reference BLDC motor.

CT is immanent in PM motors due to the association between air-gap permeability changes and rotor magnetomotive force. CT exists without stator current and is periodic in nature. The subsequent equation represents the CT generated in PMBLDC motors in the absence of skewing [23]:

$$T_{cog} = \sum_{k=1}^{\infty} T_{N_{pk}} \sin\left(N_{pk}\alpha\right), \tag{1}$$

where k is the order of harmonics; N_p is the number of CT cycles in one mechanical rotation; it is determined by LCM of the number of stator slots (N_s), and the number of rotor poles (p); α is the angular difference between the stator's and the rotor's teeth; T_{Npk} is the coefficient resulting from the fast Fourier transform (FFT) of the CT profile.

Equation (1) is used for each stator tooth of the motor to calculate the total CT. The total CT is the cumulative effect of the CTs produced by each stator tooth. The N_{pk} in (1) must be a multiple of the rotor pole numbers p. The CT produced can be shown as the ratio of N_{pk} to p, denoted by i, for any given teeth represented by j (where $1 \le j \le N_s$):

$$T_{scj} = \sum_{i=1}^{\infty} T_{sci} \sin pi\left(\alpha + \phi_j\right), \tag{2}$$

where T_{sci} is the Fourier coefficient; ϕ_j is the positioning of tooth number j of the stator, with respect to tooth number 1 of the reference stator.

Hence,

$$\phi_j = 2\pi\left(j-1\right)/N_s \,.$$

By adding together, the CT contributions from each of the N_s stator teeth, the total CT can be calculated as:

$$T_{cog} = \sum_{j=1}^{N_s} \sum_{i=1}^{\infty} T_{sci} \sin pi\left(\alpha + \frac{2\pi}{N_s}\left(j-1\right)\right). \tag{3}$$

From (3), when p/N_s is a whole number, then regardless of teeth number j:

$$\sin pi\left(\alpha + \frac{2\pi}{N_s}\left(j-1\right)\right) = \sin pi\alpha \,.$$

This indicates that the CT produced by each stator tooth and the total CT are in phase with each other. Therefore, the total CT is equal to the product of N_s and individual CT, and can be represented as:

$$T_{cog} = N_s \sum_{i=1}^{\infty} T_{sci} \sin pi\alpha \,. \tag{4}$$

The CT produced by dissimilar tooth is out of phase if the ratio p/N_s is not a whole number. Consequently, equation (3) poses a challenge in terms of simplification. A set of a specific number of adjacent slots can be arranged to find the solution. The groups are selected such that the CT generated by different groups is always in phase. As a result, there is a direct correlation among the total CT and the CT of each group [23].

Taking into account λ neighbouring slots (tooth) as a single group, $\lambda = N_p/p$. Using the formula $n = N_s p/N_p$, the number of groups (n), can be calculated. The CT for a specific tooth j is represented by (2), which can be reformulated as:

$$T_{scj} = \sum_{i=1}^{\infty} T_{sci} \sin pi\left[\alpha + \frac{2\pi}{N_s}\left(j-1\right)\right]. \tag{5}$$

The CT produced by a specific group of λ teeth is determined by adding up the CTs created by individual tooth within this group. This can be expressed as:

$$T_{cog} = \sum_{j=1}^{\lambda} \sum_{i=1}^{\infty} T_{sci} \sin\left[pi\left(\alpha + \frac{2\pi}{N_s}\left(j-1\right)\right)\right]. \tag{6}$$

Equation (6) can be simplified as:

$$T_{cog} = \sum_{i=1}^{\infty} T_{sci} \frac{\sin\left(p\lambda\pi i/N_s\right)}{\sin\left(p\pi i/N_s\right)} \sin\left[pi\alpha + \frac{p\lambda\pi i}{N_s} - \frac{p\pi i}{N_s}\right]. \tag{7}$$

Since $p\lambda i/N_s$ in (7) is an integer number, value of $\sin(p\lambda\pi i/N_s)$ is zero. Therefore, just the CT component will be present for a specific harmonic index i. Equation (7) can be shortened to these values of i and is expressed as:

$$T_{cog} = \sum_{i=1}^{\infty} T_{sci} \lambda \sin pi\alpha \,. \tag{8}$$

To get total CT, multiply the CT of a single group, as provided by (8), by the number of groups n:

$$T_{cog} = n \sum_{i=1}^{\infty} T_{sci} \lambda \sin pi\alpha \,. \tag{9}$$

Design of reference motor. The first motor designed for the analysis is a 200 W, 1000 rpm surface mounted PMBLDC motor, which serves as a reference motor. Figure 1 displays the reference motor's cross-sectional view.

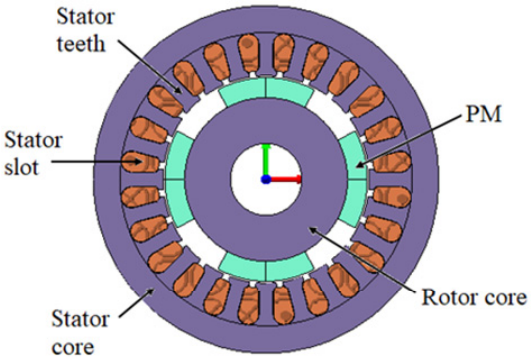

Fig. 1. Reference radial flux PMBLDC motor

The motor is designed by selecting suitable values of various design variables viz., specific magnetic and electric loadings, slot fill factor, distribution factor and pitch factor of winding, stacking factor of laminations, conductor current density etc. The FE model of the reference PMBLDC motor is created in accordance with the design calculations, and appropriate materials are assigned in respective sections. The neodymium iron-

boron (NdFeB) material is used as PM material for better performance. PMs are fixed on the periphery of the rotor. NdFeB holds the maximum energy product of all commercially available magnets at room temperature. High flux density in air gap due to the application of NdFeB leads to remarkable reductions in motor frame size for the same rating. The laminations of stator and rotor are allocated M19 silicon steel material. The specific iron loss of M19 silicon steel material at 1.4 T and 50 Hz frequency is 2 W/kg. The design particulars of the reference BLDC motor are given in Table 1.

Table 1

Design details of reference BLDC motor

Stator's outer diameter, mm	87
Rotor's outer diameter, mm	51
Stack length, mm	50
Stator's inner diameter, mm	52
Width of stator teeth, mm	3.5
Slot opening, mm	1.7
Magnet pole arc, degree	57
Number of slots	24
Number of phases/poles	3/4
Magnet's thickness, mm	5
Air gap length, mm	0.5
Type of PM	NdFeB
Stator and rotor core material	M19, 29 Ga

The FE model of reference surface mounted BLDC motor is devised using commercially available FE software and an appropriate boundary condition is assigned. The solver creates meshing and the model is divided into triangular elements [22]. Several simulation exercises were performed to acquire the CT waveform of reference motor. With the stator winding unenergized, the rotor is mechanically rotated by 1° increments up to 15°. The torque value obtained for each degree of rotation of the rotor is noted and the curve is plotted between torque values and rotor positions.

It has been analyzed that the reference PMBLDC motor has a peak-to-peak CT of 1.1 N·m. The CT profile is shown in Fig. 2.

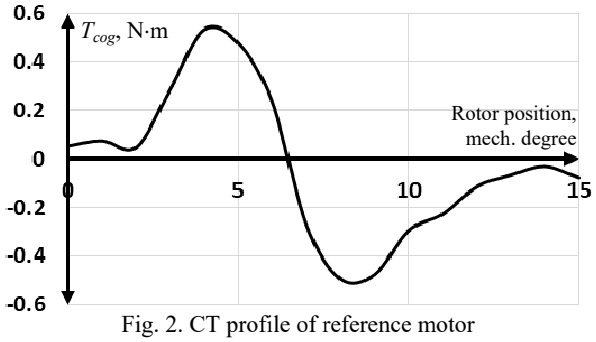

Fig. 2. CT profile of reference motor

The average torque output of the motor is calculated using 2D FE analysis. The rotor is created as a motion component in this analysis, and rotated at the rated speed of 1000 rpm. The correct operation of the inverter energizes stator winding. The torque at distinct rotor positions is calculated and shown against them. Figure 3 depicts the torque waveform of the reference motor. The average torque derived from FE analysis is 1.91 N·m.

Upgraded design using slot-opening shift approach. The CT profile is periodic because of the symmetrical structure of PM motors. The magnitude of harmonics of CT should be reduced to mitigate vibration. Conventional skew of slots and slot openings result in to decentralization of winding function and deterioration of

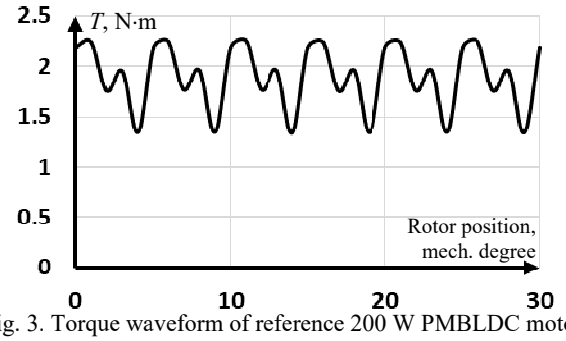

Fig. 3. Torque waveform of reference 200 W PMBLDC motor

back EMF waveform. The air-gap reluctance variation is due to slot openings hence shifting of only slot openings smoothies the air-gap reluctance variation without adversely affecting back EMF waveform. This can be considered as an apparent advantage of slot opening shifting in comparison to slot skewing. Slot openings are in the middle in the reference design of the 200 W PMBLDC motor. The upgraded design accomplishes the slot openings shifted in an anticlockwise direction by 3.75° mechanical. Stator stampings of reference design and upgraded design are illustrated respectively in Fig. 4.

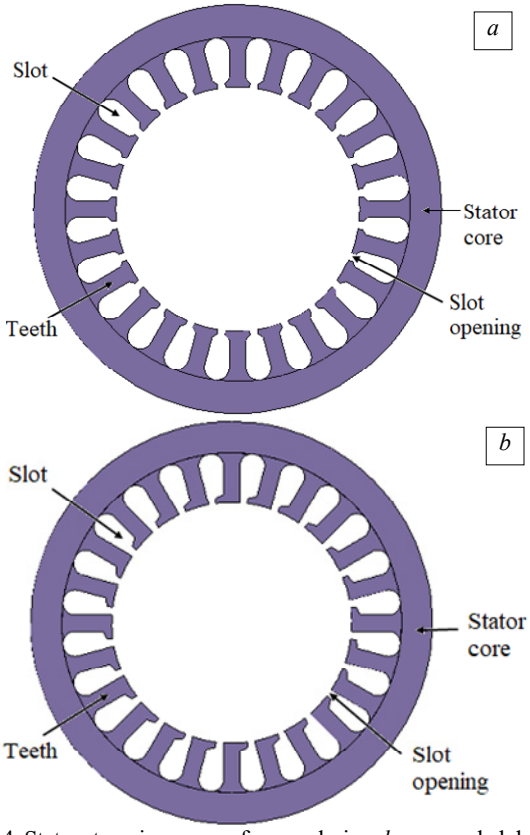

Fig. 4. Stator stampings: *a* – reference design; *b* – upgraded design

An upgraded model with shifted stator slot openings in an anticlockwise direction is shown in Fig. 5. All other design details of the upgraded model are the same as the reference model.

Figure 6 depicts a comparison of the reference and modified motors' CT patterns. It is analyzed that the reference design has a CT (peak-to-peak) of 1.1 N·m. When the slot opening of all slots is shifted in an anticlockwise direction, the CT (peak-to-peak) obtained is 0.61 N·m. The CT (peak-to-peak) decreases from 1.1 N·m to 0.61 N·m as slot openings shift anticlockwise.

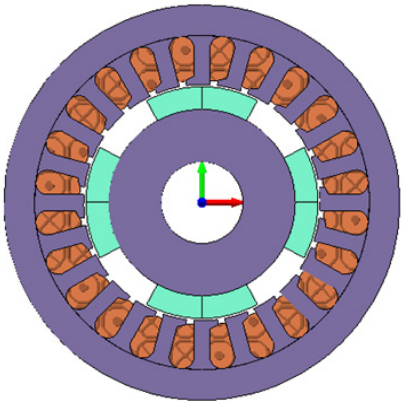

Fig. 5. Radial flux PMBLDC motor with the shifted slot opening

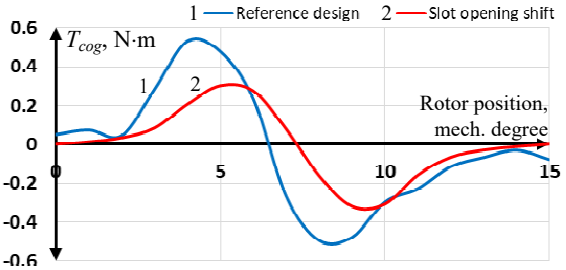

Fig. 6. Comparison of CT profiles

Table 2 depicts variation in CT with slot-opening shift methods. Slot openings are shifted in the anticlockwise direction. It is observed that a 44.5 % reduction in CT (peak-to-peak) is attained with a borderline drop in average torque.

Table 2

Comparison between reference and upgraded design

Design details	CT (peak-to-peak), N·m	Average torque, N·m
Reference design	1.1	1.91
Upgraded design with slot-opening shift in the anticlockwise direction	0.61	1.86

Figure 7 depicts FFT analysis of CT waveforms of reference design and upgraded design. The fundamental, 2nd order and 3rd order components of CT are significantly reduced on the application of the slot opening shift approach.

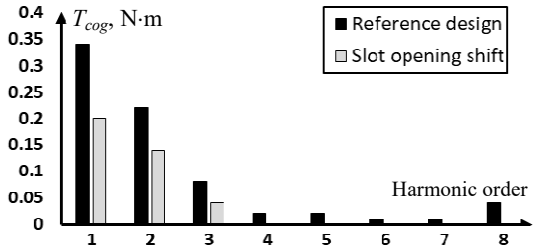

Fig. 7. Comparison of FFT analysis of CT

Figure 8 shows a comparison of the reference design's average torque and that of an upgraded design employing the slot opening shift method. The reference design produces an average torque of 1.91 N·m. When the slot opening of all slots is shifted in an anticlockwise direction, the average torque attained is 1.86 N·m. Thus, using the slot opening modification approach, the CT of the surface PM motor is substantially reduced while average torque is marginally reduced.

Figure 9 shows back EMF profiles for reference and upgraded designs. The amplitude of the back EMF waveform is marginally lowered in the modified design compared to the reference design.

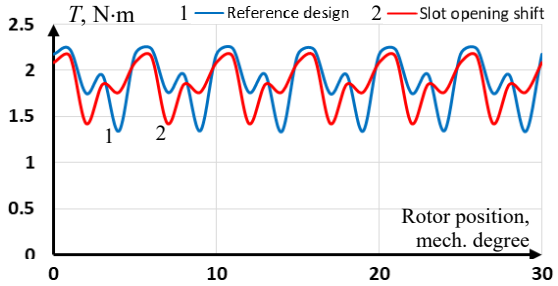

Fig. 8. Comparison of torque profiles of reference design and upgraded design

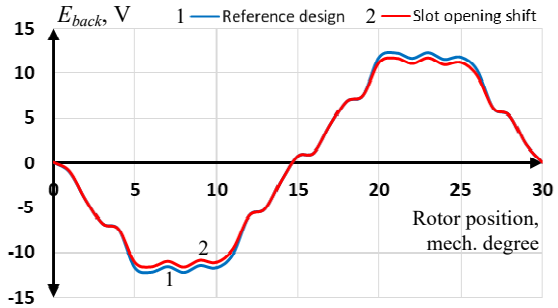

Fig. 9. Comparison of back EMF profile of reference design and upgraded design

Figure 10 shows the back EMF's harmonic spectrum for both the reference and upgraded designs. The total harmonic distortion (THD) of the reference design is 8.03 % while the THD of the upgraded design is 6.9 %. Hence, it is analyzed that the quality of back EMF waveform is improved with a reduction in THD.

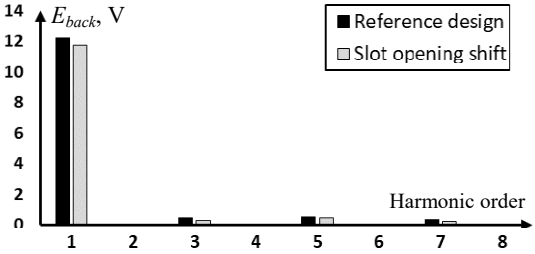

Fig. 10. Comparison of FFT analysis of back EMF

Flux densities are assessed in different motor sections using electromagnetic field analysis. This helps to demonstrate the correctness of improved and reference designs. Figures 11, 12 show the flux density distributions for the reference design and the upgraded designs.

Conclusions. This research presents a slot opening shift technique to reduce the CT of a surface PMBLDC motor.

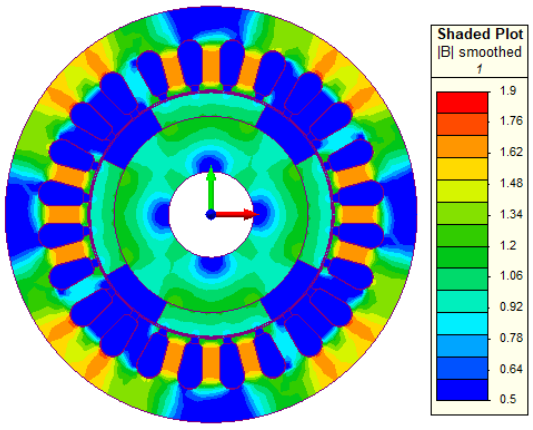

Fig. 11. Distribution of flux density in the reference design

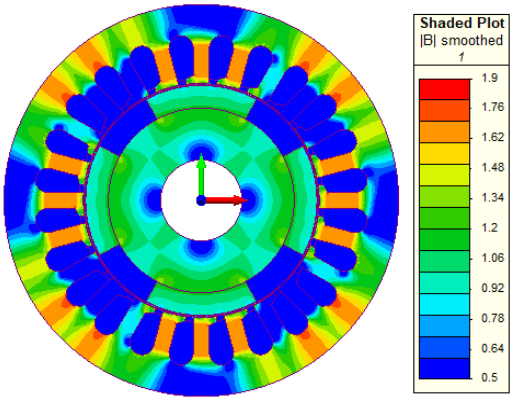

Fig. 12. Distribution of flux density in upgraded design having slot-opening shifted anticlockwise

The reference design for a 200 W, 1000 rpm surface-mounted BLDC motor does not include any shifting of slot opening. The design is upgraded with the slot opening of all slots shifted in an anticlockwise direction by 3.75° mechanical keeping the center line of slots unchanged. The CT waveform of reference and upgraded designs is obtained from FE modelling and analysis. It is observed that with the application of the slot opening shift approach peak-to-peak CT of the surface PMBLDC motor is reduced by 44.5 % with a borderline reduction in average torque. The slot opening shift approach is a practically implementable approach without any extra manufacturing difficulty and cost. The slot opening shift is an effective and practical method for reducing the CT of a surface PMBLDC motor.

Conflict of interest. The authors declare that they have no conflicts of interest.

REFERENCES

1. Hanselman D.C. *Brushless Permanent Magnet Motor Design*. Magna Physics Publ., Ohio, 2006. 411 p.

2. Hendershot J.R., Miller T.J.E. *Design of Brushless Permanent Magnet Motors*. Oxford, Magna Physics & Clarendon Press, 1995. 580 p.

3. Chen Y., Fang Z., Chen K., Luo J., Pan J.F. Design and Co-Simulation of High-Speed Permanent Magnet Brushless DC Motor. *2022 IEEE 9th International Conference on Power Electronics Systems and Applications (PESA)*, 2022, pp. 1-4. doi: https://doi.org/10.1109/PESA55501.2022.10038434.

4. Diao C., Zhao W., Wang N., Wang X. Analysis of a High-Speed Axial Flux Permanent Magnet Motor With Hybrid Magnets for Low Cost. *2022 IEEE 20th Biennial Conference on Electromagnetic Field Computation (CEFC)*, 2022, pp. 1-2. doi: https://doi.org/10.1109/CEFC55061.2022.9940827.

5. Panchal T.H., Patel A.N., Patel R.M. Reduction of cogging torque of radial flux permanent magnet brushless DC motor by magnet shifting technique. *Electrical Engineering & Electromechanics*, 2022, no. 3, pp. 15-20. doi: https://doi.org/10.20998/2074-272X.2022.3.03.

6. Patel A.N., Doshi P.J., Mahagoakar S.C., Panchal T.H. Optimization of cogging torque in interior permanent magnet synchronous motor using optimum magnet v-angle. *Electrical Engineering & Electromechanics*, 2023, no. 6, pp. 16-20. doi: https://doi.org/10.20998/2074-272X.2023.6.03.

7. Athira R.S., Binu L.S. Techniques for Torque Ripple Reduction in BLDC Motor for EV. *2023 International Conference on Circuit Power and Computing Technologies (ICCPCT)*, 2023, pp. 1008-1014. doi: https://doi.org/10.1109/ICCPCT58313.2023.10245720.

8. Tsunata R., Takemoto M. Skewing Technology for Permanent Magnet Synchronous Motors: A Comprehensive Review and Recent Trends. *IEEE Open Journal of the Industrial Electronics Society*, 2024, vol. 5, pp. 1251-1273. doi: https://doi.org/10.1109/OJIES.2024.3491295.

9. Hua T., Wang A., Jiang Y., Gu L. Study on the Weakening of Cogging Torque by Stator Structure Optimization of Permanent Magnet Synchronous Motor. *2024 IEEE International Conference on Electrical Energy Conversion Systems and Control (IEECSC)*, 2024, pp. 53-57. doi: https://doi.org/10.1109/IEECSC62814.2024.10913732.

10. Kim K., Hwang M., Cha H. Cogging Reduction Method for Axial Flux Permanent Magnet Motor Utilizing Skew-Shaped Slot Rotor. *2024 IEEE 6th Eurasia Conference on Biomedical Engineering, Healthcare and Sustainability (ECBIOS)*, 2024, pp. 504-509. doi: https://doi.org/10.1109/ECBIOS61468.2024.10885473.

11. Lee S.-W., Yang I.-J., Kim W.-H. A Study on Reducing Cogging Torque of IPMSM Applying Rotating Tapering. *IEEE Transactions on Magnetics*, 2022, vol. 58, no. 8, pp. 1-5. doi: https://doi.org/10.1109/TMAG.2022.3179126.

12. Dai L., Niu S., Gao J., Liu K., Huang S., Chan W.L. Diverse Slot-Opening Designs for Cogging Torque and Performance Optimization in PM Machines. *IEEE Transactions on Transportation Electrification*, 2025, vol. 11, no. 3, pp. 8414-8426. doi: https://doi.org/10.1109/TTE.2025.3540837.

13. Banchhor D.K., Jain A.K., Dalal A. Effect of Eccentric Tooth Tip Arc on Cogging Torque of PM Machines. *2023 IEEE 2nd Industrial Electronics Society Annual On-Line Conference (ONCON)*, 2023, pp. 1-6. doi: https://doi.org/10.1109/ONCON60463.2023.10431049.

14. Kobayashi M., Morimoto S., Sanada M., Inoue Y. A Novel Design for Notch on Rotor Surface of Double-Layered Interior Permanent Magnet Synchronous Motor for Reducing Cogging Torque. *2020 International Conference on Electrical Machines (ICEM)*, 2020, pp. 39-44. doi: https://doi.org/10.1109/ICEM49940.2020.9270972.

15. Imanuddin N., Furqani J., Rizqiawan A. Effects of Radial Divided Magnet Shifting on Cogging Torque of Axial Flux Permanent Magnet Generator for Small Scale Wind Turbine. *2023 4th International Conference on High Voltage Engineering and Power Systems (ICHVEPS)*, 2023, pp. 555-560. doi: https://doi.org/10.1109/ICHVEPS58902.2023.10257501.

16. Wan X., Yang S., Li Y., Shi Y., Lou J. Minimization of Cogging Torque for V-Type IPMSM by the Asymmetric Auxiliary Slots on the Rotor. *IEEE Access*, 2022, vol. 10, pp. 89428-89436. doi: https://doi.org/10.1109/ACCESS.2022.3201246.

17. Wang B., Wang D., Peng C., Wang C., Xu C., Wang X. Interior Permanent Magnet Synchronous Machines With Composed T-Shaped Notching Rotor. *IEEE Transactions on Industrial Electronics*, 2024, vol. 71, no. 6, pp. 5519-5529. doi: https://doi.org/10.1109/TIE.2023.3292854.

18. Yuan B., Li H., Xiang X., Zhou T., Zhou H., Jiang P. Investigation of Cogging Torque Comprehensive Reduction Method in High Precision Servo Permanent Magnet Motor. *2022 25th International Conference on Electrical Machines and Systems (ICEMS)*, 2022, pp. 1-4. https://doi.org/10.1109/ICEMS56177.2022.9983382.

19. Ding J., Jiang W. Effect of Stator Auxiliary Groove on the Vibration and Noise of Permanent Magnet Synchronous Motor. *2024 IEEE International Conference on Electrical Energy Conversion Systems and Control (IEECSC)*, 2024, pp. 32-36. doi: https://doi.org/10.1109/IEECSC62814.2024.10913734.

20. Zon B., Wegiel T. Analysis of Cogging Torque Reduction Method Effectiveness on the Example of a Surface Mounted Permanent Magnet Synchronous Motor Model. *2018 International Symposium on Electrical Machines (SME)*, 2018, pp. 1-5. doi: https://doi.org/10.1109/ISEM.2018.8442778.

21. Ocak O., Aydin M. An Innovative Semi-FEA Based, Variable Magnet-Step-Skew to Minimize Cogging Torque and Torque Pulsations in Permanent Magnet Synchronous Motors. *IEEE Access*, 2020, vol. 8, pp. 210775-210783. doi: https://doi.org/10.1109/ACCESS.2020.3038340.

22. Grechko O.M. Influence of the poles shape of DC electromagnetic actuator on its thrust characteristic. *Technical Electrodynamics*, 2024, no. 1, pp. 38-45. doi: https://doi.org/10.15407/techned2024.01.038.

23. Liu T., Huang S., Gao J., Lu K. Cogging Torque Reduction by Slot-Opening Shift for Permanent Magnet Machines. *IEEE Transactions on Magnetics*, 2013, vol. 49, no. 7, pp. 4028-4031. doi: https://doi.org/10.1109/TMAG.2013.2239977.

Received 11.08.2025
Accepted 23.11.2025
Published 02.03.2026

A.N. Patel[1], *PhD, Associate Professor,*
T.H. Panchal[1], *PhD, Assistant Professor,*
[1] Department of Electrical Engineering, Institute of Technology, Nirma University, Ahmedabad, Gujarat, India,
e-mail: amit.patel@nirmauni.ac.in;
tejas.panchal@nirmauni.ac.in (Corresponding Author)

How to cite this article:
Patel A.N., Panchal T.H. Mitigation of cogging torque in surface permanent magnet brushless DC motor using slot opening shift. *Electrical Engineering & Electromechanics*, 2026, no. 2, pp. 10-14. doi: https://doi.org/10.20998/2074-272X.2026.2.02

UDC 621.311 https://doi.org/10.20998/2074-272X.2026.2.03

S.A. Alomari, A. Smerat, O.P. Malik, M. Dehghani, Z. Montazeri

Efficient and reliable scheduling of power generating units in the unit commitment problem using the Tardigrade optimization algorithm

Introduction. *The unit commitment (UC) problem is a critical operational task in power systems, involving the optimal scheduling of generating units while meeting demand, satisfying technical constraints, and minimizing operating costs. Due to its combinatorial nature, nonlinear characteristics, and numerous interdependent constraints, UC poses a highly complex optimization challenge. Metaheuristic algorithms have demonstrated strong potential in addressing such large-scale problems; however, many existing methods struggle to maintain a proper exploration–exploitation balance, limiting their performance in dynamic UC environments.* ***Problem.*** *Traditional metaheuristic algorithms often suffer from premature convergence, inadequate local refinement, or dependency on control parameters that require tuning. Such limitations reduce robustness and adaptability when dealing with UC's intricate search landscape. Therefore, there is a need for a parameter-free, self-adaptive optimization algorithm capable of reliably solving UC with high efficiency and convergence stability. The* ***goal*** *of this study is to develop an efficient and reliable scheduling framework for power generating units in the UC problem by employing the tardigrade optimization algorithm (TOA) and to demonstrate its effectiveness compared with established optimization techniques.* ***Methodology.*** *TOA is inspired by the active and cryptobiotic survival behaviors of tardigrades. The exploration phase imitates active adaptive locomotion to broaden global search, while the exploitation phase abstracts cryptobiotic stability to refine solutions locally. These mechanisms are formulated through adaptive state-transition operators that adjust search behavior automatically without external parameters. TOA is applied to a 24-hour UC problem consisting of 10 generating units under realistic load and operational constraints. Its performance is benchmarked against 6 widely used metaheuristic algorithms.* ***Results.*** *The proposed TOA achieves the lowest total operating cost, exhibits strong convergence behavior, and demonstrates high consistency across independent runs, outperforming all comparative methods. The* ***scientific novelty*** *lies in introducing a biologically inspired, parameter-free, self-adaptive metaheuristic algorithm. Its* ***practical value*** *is validated through superior performance in UC scheduling, indicating strong potential for broader power system optimization tasks.* References 21, tables 3, figures 3.

Key words: **tardigrade optimization algorithm, unit commitment problem, metaheuristic algorithm, power system optimization, power generating unit.**

Вступ*. Проблема зобов'язань за потужністю одиниць (UC) є критично важливим операційним завданням в енергетичних системах, що включає оптимальне планування генеруючих блоків з одночасним задоволенням попиту, технічних обмежень та мінімізацією експлуатаційних витрат. Через свою комбінаторну природу, нелінійні характеристики та численні взаємозалежні обмеження, UC створює дуже складну задачу оптимізації. Метаевристичні алгоритми продемонстрували значний потенціал у вирішенні таких масштабних проблем, однак багато існуючих методів мають труднощі з підтримкою належного балансу між розвідкою та експлуатацією, що обмежує їхню продуктивність у динамічних середовищах UC.* ***Проблема****. Традиційні метаевристичні алгоритми часто страждають від передчасної збіжності, недостатнього локального уточнення або залежності від параметрів керування, які потребують налаштування. Такі обмеження знижують стійкість та адаптивність при роботі зі складним ландшафтом пошуку UC. Тому існує потреба в безпараметричному, самоадаптивному алгоритмі оптимізації, здатному надійно вирішувати UC з високою ефективністю та стабільністю збіжності.* ***Метою*** *роботи є розробка ефективної та надійної системи планування роботи енергоблоків у задачі оптимізації енергосистеми з використанням алгоритму оптимізації тихоходок (TOA) та демонстрація її ефективності порівняно з існуючими методами оптимізації.* ***Методика****. TOA натхненний активною та криптобіотичною поведінкою тихоходок, спрямованою на виживання. Фаза дослідження імітує активне адаптивне пересування для розширення глобального пошуку, тоді як фаза експлуатації абстрагує криптобіотичну стабільність для локального уточнення рішень. Ці механізми формулюються за допомогою адаптивних операторів переходу станів, які автоматично коригують поведінку пошуку без зовнішніх параметрів. TOA застосовується до 24-годинної задачі UC, що складається з 10 генеруючих блоків за реальних обмежень навантаження та експлуатації. Його продуктивність порівнюється з 6 широко використовуваними метаевристичними алгоритмами.* ***Результати****. Запропонований TOA досягає найнижчих загальних експлуатаційних витрат, демонструє значну поведінку збіжності та демонструє високу узгодженість у незалежних запусках, перевершуючи всі порівняльні методи.* ***Наукова новизна*** *полягає у впровадженні біологічно натхненного, безпараметричного, самоадаптивного метаевристичного алгоритму. Його* ***практична цінність*** *підтверджена високою продуктивністю у плануванні UC, що вказує на значний потенціал для ширших завдань оптимізації енергосистеми.* Бібл. 21, табл. 3, рис. 3.

Ключові слова: **алгоритм оптимізації тихоходки, завдання планування роботи енергоблоків, метаевристичний алгоритм, оптимізація енергосистеми, енергогенеруюча установка.**

Introduction. The unit commitment (UC) problem is a fundamental optimization task in power system operation, aimed at determining the on/off status of generating units and the optimal allocation of their output power over multiple time intervals [1]. The primary objective is to satisfy system load demand while minimizing the total generation cost, subject to the operational constraints of power units. Due to its economic and operational significance, UC mathematical models play a central role in planning and decision-making for power system operators [2].

The UC problem is inherently combinatorial and nonlinear, as it involves both discrete decision variables (unit status) and continuous variables (generation levels). Efficient solution methods are therefore crucial for achieving optimal system performance while respecting physical and operational constraints [3]. Metaheuristic algorithms have shown effective applications in solving the UC problem, providing near-optimal solutions within reasonable computational effort and successfully handling its nonlinearity and combinatorial complexity [4, 5].

Metaheuristic algorithms are stochastic, population-based optimization techniques inspired by natural, biological, social or physical processes. Their key strength lies in their ability to handle multimodal, nonlinear, high-dimensional and derivative-free problems with reasonable computational effort [6]. Metaheuristics

are capable of escaping local optima through probabilistic exploration mechanisms while providing high-quality near-optimal solutions, making them highly suitable for UC scheduling and similar engineering challenges [7–11]. Numerous well-known metaheuristic methods – genetic algorithm (GA) [12], particle swarm optimization (PSO) [13], gravitational search algorithm (GSA) [14], and many recently developed nature-inspired algorithms – have demonstrated notable success in improving UC solution quality compared to deterministic approaches.

However, despite their effectiveness, metaheuristics inherently rely on stochastic operators and therefore can not guarantee convergence to the global optimum [15]. Their performance critically depends on maintaining an appropriate balance between exploration (searching new regions) and exploitation (refining existing promising solutions) [16, 17]. According to the no free lunch theorem [18], no single metaheuristic can outperform all others across every optimization scenario, motivating continuous research into new algorithms capable of offering improved performance, adaptability, and robustness for specific classes of problems such as UC.

In this context, biological systems exhibiting exceptional adaptability and resilience provide a rich source of inspiration for designing new optimization methods. One such organism is the tardigrade (Tardigrada), a microscopic extremophile renowned for its unmatched survival strategies, including cryptobiosis, adaptive locomotion, and reactive environmental exploration. These behaviors naturally align with the fundamental principles of optimization – particularly the dynamic interplay between global exploration and local exploitation.

Motivated by these unique biological characteristics, this study introduces a novel population-based metaheuristic method called the Tardigrade Optimization Algorithm (TOA). In TOA, the exploration mechanism models the tardigrade's adaptive roaming across micro-environments in search of favorable conditions, while the exploitation mechanism mimics its cryptobiotic stability and localized reactivation behavior under improved environmental conditions. This biologically inspired modeling enables TOA to achieve a dynamic and efficient balance between wide-range search and precise local refinement.

The **goal** of this study is to develop an efficient and reliable scheduling framework for power generating units in the UC problem by employing the tardigrade optimization algorithm (TOA) and to demonstrate its effectiveness compared with established optimization techniques.

The major contributions of this study are as follows:

- development of the TOA, inspired by the unique adaptive and cryptobiotic behavior of tardigrades;
- formulation of a mathematical search model capturing both large-scale exploration and small-scale exploitation through biologically inspired mechanisms;
- application of TOA to the UC scheduling problem and comprehensive simulation studies validating its effectiveness;
- comparative performance assessment against modern metaheuristic algorithms, demonstrating superior robustness, convergence ability, and solution accuracy.

Problem definition. UC problem. In this section, the mathematical formulation of the UC problem is presented, which serves as the basis for optimization using the proposed TOA.

Mathematical formulation. The UC problem involves determining the operational schedule of generating units over a predefined time horizon while satisfying demand and operational constraints, with the ultimate objective of minimizing total generation cost. This mathematical representation provides a rigorous framework for modeling the complex interactions between unit statuses, generation levels and system requirements.

Objective function. The primary objective of the UC problem is to minimize the total generation cost across all units and time periods. The cost is typically represented as a quadratic function of the generated power for each unit, reflecting fuel and operational expenditures:

$$\min C_t = \sum_{i=1}^{N_G} \left(a_i + b_i P_{i,t} + c_i P_{i,t}^2 \right), \tag{1}$$

where C_t is the total generation cost at time period t; N_G is the total number of generating units; $P_{i,t}$ is the power output of unit i at time t; a_i, b_i, c_i are the fuel cost coefficients of unit i, capturing the fixed, linear and quadratic components of the generation cost function.

This objective function accurately models the relationship between unit generation levels and operational costs, allowing the evaluation of alternative commitment strategies in a quantitative manner.

Decision variables. The UC problem involves two types of decision variables:

1. Unit status (binary variable). The binary decision variable $u_{i,t}$ is indicating the ON/OFF status of unit i at time t ($u_{i,t} = 1$ if the unit is ON, and $u_{i,t} = 0$ otherwise):

$$u_{i,t} = \begin{cases} 1, \text{ if unit } i \text{ is ON at time } t; \\ 0, \text{ if unit } i \text{ is OFF at time } t. \end{cases} \tag{2}$$

2. Unit generation level (continuous variable):

$$P_{i,t} \geq 0. \tag{3}$$

These two variables are interdependent, as a unit can generate power only when it is switched ON.

Constraints. The UC problem is subject to a set of operational and system constraints, which ensure feasibility, reliability, and safety of power system operation. Each constraint is explained in detail below:

1. Power balance constraint. The total generated power must exactly meet the system load demand at each time interval:

$$\sum_{i=1}^{N_G} u_{i,t} P_{i,t} = P_t^D , \tag{4}$$

where P_t^D is the system load demand at time t. This constraint guarantees that electricity supply matches demand continuously, preventing shortages or surpluses.

2. Generation limits of units. Each unit must operate within its minimum and maximum generation capacities when it is ON:

$$u_{i,t} P_i^{\min} \leq P_{i,t} \leq u_{i,t} P_i^{\max}, \tag{5}$$

where $P_i^{\min}$, $P_i^{\max}$ are the minimum and maximum generation limits of unit i. This constraint ensures operational feasibility by restricting generation to allowable ranges and enforcing that units produce zero output when they are OFF.

Introducing and mathematical modeling of the TOA. This section introduces the proposed TOA, a novel bio-inspired metaheuristic designed to simulate the adaptive, survival-oriented behaviors of Tardigrades (water bears) in natural environments. The algorithm is mathematically modeled to be applicable across a wide variety of optimization problems in engineering, science and artificial intelligence. The TOA models 3 essential biological processes of tardigrades (free aquatic motion, local feeding and survival behavior, and the tun mechanism for revival) each corresponding to exploration, exploitation and adaptive switching between these 2 main phases.

Behavioral analysis of tardigrades and core design concept of TOA. Tardigrades are microscopic invertebrates known for their extraordinary ability to survive under extreme environmental conditions, including desiccation, freezing, radiation and vacuum. Their adaptability originates from a series of behaviors that allow them to explore, exploit, and survive in fluctuating environments. These behaviors are abstracted and mapped into three computational phases in the proposed algorithm:

- **Exploration phase** corresponds to the *free locomotion and foraging behavior* of tardigrades in aquatic environments. In this state, tardigrades move freely to discover new regions containing food or suitable conditions. This inspires wide, randomized search movements across the problem space.
- **Exploitation phase** corresponds to *localized feeding behavior* in nutrient-rich microenvironments. Once a tardigrade identifies a favorable area, it remains locally active with small and precise movements to optimize feeding. This is analogous to local fine-tuning around promising solutions.
- **Switching phase (tun mechanism)** corresponds to *cryptobiosis (tun state)*, a survival response when the environment becomes hostile. The tardigrade dehydrates, halts metabolism, and later revives with renewed energy. In the algorithm, this mechanism controls the transition between exploitation and exploration, allowing the population to escape stagnation and restore diversity.

Through this behavioral mapping, TOA achieves a biologically motivated balance between global exploration, local exploitation, and adaptive restarts, resulting in efficient convergence while preventing premature stagnation.

Initialization process of the TOA. At the beginning of the optimization process, the TOA initializes a population of tardigrades with N member, each representing a candidate solution in the m-dimensional search space. The population matrix X is defined as:

$$X = \begin{bmatrix} x_{1,1} & \cdots & x_{1,d} & \cdots & x_{1,m} \\ \vdots & \ddots & \vdots & \iddots & \vdots \\ x_{i,1} & \cdots & x_{i,d} & \cdots & x_{i,m} \\ \vdots & \iddots & \vdots & \ddots & \vdots \\ x_{N,1} & \cdots & x_{N,d} & \cdots & x_{N,m} \end{bmatrix}_{N\times m}, \quad (6)$$

where each element $x_{i,d}$ is the position of tardigrade i in dimension d.

The initial positions are randomly generated within the problem's lower and upper bounds:

$$x_{i,d} = lb_d + r\cdot(ub_d - lb_d), \quad (7)$$

where lb_d, ub_d are the lower and upper bounds of the d^{th} dimension; $r \sim U(0, 1)$ is the uniformly distributed random number.

The fitness of each tardigrade is evaluated using the objective function F:

$$F = \begin{bmatrix} F_1 \\ \vdots \\ F_i \\ \vdots \\ F_N \end{bmatrix}_{N\times 1} = \begin{bmatrix} F(X_1) \\ \vdots \\ F(X_i) \\ \vdots \\ F(X_N) \end{bmatrix}_{N\times 1}. \quad (8)$$

Exploration phase. The exploration phase models the *free aquatic movement* of tardigrades as they search for new sources of nutrients. This behavior corresponds to global exploration in the search space – large stochastic movements toward promising regions. Each tardigrade identifies potential food locations among members with better fitness values, including the global best position:

$$Food_i = \in \{X_k \,|\, F_k < F_i \cup X_{best}\}. \quad (9)$$

Then, each tardigrade updates its position according to:

$$X_i^{P1} = X_i + I_1\cdot r_1\cdot(Food_i - I_2\cdot X_i) + \Delta X_\varepsilon^{P1}(t), \quad (10)$$

where $I_i\in \{1, 2\}$ are integer control parameters determining interaction intensity; $r_i \sim U(0, 1)$ is a random coefficient controlling stochastic motion. The perturbation term $\Delta X_\varepsilon^{P1}(t)$ is a random hydrodynamic disturbances:

$$\Delta X_\varepsilon^{P1}(t) = P_\varepsilon \cdot \frac{(1-2r_2)}{(t+1)^{1+r_3}} \cdot |ub - lb|, \quad (11)$$

where $P_\varepsilon\in \{0, 1\}$ determines the presence of noise, and $r_i \sim U(0, 1)$.

The updated position is accepted if it improves the fitness:

$$X_i = \begin{cases} X_i^{P1}, \text{ if } F_i^{P1} < F_i; \\ X_i, \text{ else.} \end{cases} \quad (12)$$

This formulation allows each tardigrade to move dynamically toward better regions while maintaining stochastic diversity, thus effectively performing wide exploration.

Exploitation phase. Once a tardigrade finds a resource-rich region, it limits its movement to fine adjustments in the local area. This behavior corresponds to the exploitation phase of optimization.

The local search is expressed as:

$$X_i^{P2} = X_i + \sigma\cdot r_4\cdot(Food_i - I_3\cdot X_i) + \Delta X_\varepsilon^{P2}(t), \quad (13)$$

The local random perturbation term $\Delta X_\varepsilon^{P2}(t)$ is defined as:

$$\Delta X_\varepsilon^{P2}(t) = P_\varepsilon \cdot \frac{r_5}{(t+1)^{1+r_6}} \cdot (X_{best} - I_4 \cdot X_i), \quad (14)$$

where $r_i \sim U(0, 1)$ and $I_i\in \{1, 2\}$.

The adaptive coefficient σ controls the intensity of local movement and gradually decreases with iterations, ensuring convergence:

$$\sigma = 1 - (t / T)^{1+r_7}. \quad (15)$$

Finally, the updated position is accepted if it improves the fitness value:

$$X_i = \begin{cases} X_i^{P2}, \text{ if } F_i^{P2} < F_i; \\ X_i, \text{ else.} \end{cases} \quad (16)$$

This phase simulates precise micro-movements of tardigrades near favorable food sources, analogous to local refinement around optima.

Tun mechanism: adaptive switching between phases. Tardigrades enter the *tun state* when exposed to unfavorable conditions and later revive once the environment becomes suitable again. In TOA, this phenomenon is abstracted to govern the switching between exploitation and exploration.

If a tardigrade's position does not improve for several consecutive iterations (TS_i), or if the food location becomes less favorable, the algorithm triggers the tun mechanism and reactivates exploration.

The phase update rule is defined as:

Update phase for member i :

$$\begin{cases} \text{switch to exploration, } TS_i > \tau; \\ \text{switch to exploration, } F_i < F_{Food_i}; \\ \text{stay in exploitation, else.} \end{cases} \tag{17}$$

where τ is the maximum allowable stagnation duration.

The counter TS_i is updated in each iteration as:

$$TS_i = 0;$$

$$TS_i = \begin{cases} 0, \text{ if } F_i^{t+1} < F_i^t; \\ TS_i + 1, \text{ else.} \end{cases} \tag{18}$$

When the tun mechanism is activated, the tardigrade regenerates its energy and re-enters the exploration phase from an improved position close to the global best:

$$X_i^{TM} = X_i + r_7 \cdot (X_{best} - I_5 \cdot X_i); \tag{19}$$

$$X_i = \begin{cases} X_i^{TM}, \text{ if } F_i^{TM} < F_i; \\ X_i, \text{ else.} \end{cases} \tag{20}$$

where X_i^{TM} is the newly calculated position for the i-th individual based on the tun mechanism; F_i^{TM} is the corresponding objective function value.

This mechanism helps the algorithm recover diversity, escape local optima and maintain global search ability throughout the optimization process.

Simulation studies and experimental analysis of the UC problem. This section presents a comprehensive analysis of the performance of the proposed TOA in solving the UC problem.

Case study. To evaluate the effectiveness of the proposed TOA in solving the UC problem, a comprehensive case study is designed. The case study considers a power system comprising 10 generating units, with diverse operational characteristics and cost parameters. The detailed specifications of each generating unit including maximum and minimum generation capacities ($P_i^{\max}$ and $P_i^{\min}$) and fuel cost coefficients (a_i, b_i, c_i) are summarized in Table 1. These parameters provide a realistic basis for simulating operational costs and constraints.

The planning horizon for this study is set to 24 hours, representing a typical daily operation schedule. The hourly system load demand (P^D) over the 24-hour period is defined as follows: P^D = (700, 750, 850, 950, 1000, 1100, 1150, 1200, 1300, 1400, 1450, 1500, 1400, 1300, 1200, 1050, 1000, 1100, 1200, 1400, 1300, 1100, 900, 800) MW. This load profile captures variations in electricity demand throughout a typical day, reflecting peak and off-peak periods that challenge the scheduling and dispatch of generating units.

Table 1

Generators data

Unit	$P^{\max}$, MW	$P^{\min}$, MW	a, \$	b, \$/MW	c, \$/MW^2
1	455	150	1000	16.19	0.00048
2	455	150	970	17.26	0.00031
3	130	20	700	16.6	0.002
4	130	20	680	16.5	0.00211
5	162	25	450	19.7	0.00398
6	80	20	370	22.26	0.00712
7	85	25	480	27.74	0.00079
8	55	10	660	25.92	0.00413
9	55	10	665	27.27	0.00222
10	55	10	670	27.79	0.00173

The selected network configuration provides a realistic test bed for evaluating TOA performance, incorporating units with a wide range of generation capacities, fuel costs, and operational constraints. The case study network is modeled as a simplified system with a single-bus load representation, allowing focus on the commitment and dispatch problem without the additional complexity of transmission constraints. Each generating unit is assumed to operate independently, but the total generation must satisfy the system demand in every hour while respecting minimum and maximum generation limits, as well as the binary commitment status of each unit.

By employing this case study, the proposed TOA algorithm is tested under practical operational conditions, enabling assessment of its ability to generate cost-effective, feasible schedules and to balance exploration and exploitation effectively in a real-world power system scenario. This approach provides a robust framework for comparative analysis against other state-of-the-art metaheuristic methods.

Simulation results. The TOA is implemented for the 24-hour planning horizon described in the case study, and the results are summarized in Table 2, which details the hourly generation schedule of each unit alongside the corresponding hourly generation cost.

Table 2 provides the optimal power output for each generating unit across all 24 hours, ensuring that the system demand is met while respecting unit-specific constraints such as minimum and maximum generation limits. The hourly cost of supplying energy is also reported, allowing for an assessment of cost variations throughout the day.

From the results, it is observed that the minimum hourly generation cost occurs at hour 1, with a value of \$13,683.13, while the maximum hourly generation cost is recorded at hour 12, amounting to \$33,932.85. The total generation cost for the entire 24-hour period is calculated to be \$560,497.99, demonstrating the efficiency of TOA in minimizing operational costs under realistic operational conditions.

The generation schedules shown in Table 2 indicate that TOA successfully allocates power outputs in a manner that meets the hourly system demand while maintaining operational feasibility for all units.

Table 2

Results obtained from TOA in optimizing the UC problem

Hour	Cost, $	G1, MW	G2, MW	G3, MW	G4, MW	G5, MW	G6, MW	G7, MW	G8, MW	G9, MW	G10, MW
1	13683.13	455	245	0	0	0	0	0	0	0	0
2	14554.31	455	294.9892	0	0	0	0	0	0	0	0
3	16892.93	454.0284	265.973	0	129.9987	0	0	0	0	0	0
4	19261.7	454.7526	235.2669	129.9902	129.9902	0	0	0	0	0	0
5	20132.57	454.9878	285.0178	129.9972	129.9972	0	0	0	0	0	0
6	22396.72	452.8644	363.8085	125.8501	129.8987	27.57826	0	0	0	0	0
7	23267.58	454.996	423.1044	117.084	129.804	25.01165	0	0	0	0	0
8	24150.11	455	455	130	130	29.98856	0	0	0	0	0
9	27320.34	450.3331	450.3272	127.845	123.1917	100.5967	22.34973	25.35662	0	0	0
10	30154.94	454.3235	454.3237	129.8694	128.3279	136.2574	54.2766	27.12575	15.49565	0	0
11	32042.39	454.9642	454.9642	129.3439	128.417	161.1025	44.04084	25.06252	30.86957	21.2352	0
12	33932.85	454.9856	454.9858	129.9251	129.9251	161.9093	74.2046	38.19795	32.77667	13.07466	10.01527
13	30324.48	453.9498	453.8795	129.5039	129.5039	106.284	65.80941	51.03695	10.03235	0	0
14	27444.02	452.5941	452.5941	129.9926	129.9926	28.77119	79.78389	26.27156	0	0	0
15	24151.93	454.7145	454.7145	130	130	30.569	0	0	0	0	0
16	21005.99	454.0312	335.9734	129.9977	129.9977	0	0	0	0	0	0
17	20132.99	454.4689	285.532	129.9996	129.9996	0	0	0	0	0	0
18	22397.25	454.868	383.3131	106.697	129.9719	25.14999	0	0	0	0	0
19	24147.18	455	455	130	130	29.84141	0	0	0	0	0
20	30232.79	454.9843	454.9886	129.7335	129.9606	105.9667	79.93328	34.41234	10.02059	0	0
21	27277.48	454.8961	454.8964	129.9839	124.2223	90.04006	20.15884	25.80241	0	0	0
22	22400.55	454.1909	381.7471	129.9388	108.2244	25.89879	0	0	0	0	0
23	17765.08	453.8843	316.1406	0	129.9752	0	0	0	0	0	0
24	15428.68	453.5143	346.4857	0	0	0	0	0	0	0	0

The results reflect the algorithm's capability to manage both peak and off-peak demand periods, effectively balancing high-demand hours with cost-efficient generation from multiple units.

Figure 1 shows the hourly load demand versus the total generation output. It can be seen that the scheduled generation closely follows the system demand, ensuring full compliance with the power balance constraint. This confirms that the TOA can generate feasible UC schedules while satisfying demand at all times.

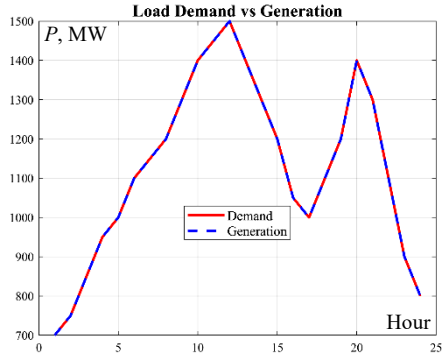

Fig. 1. Hourly generation and demand curves of the power plants over the study period

Figure 2 shows the hourly generation cost curve, highlighting the variation in cost throughout the 24-hour horizon. As observed, the highest hourly generation cost occurs at hour 12, while the lowest cost corresponds to hour 1. This trend is consistent with the system load profile, as periods of higher demand generally lead to increased generation costs due to the dispatch of higher-cost units.

Overall, the simulation results demonstrate that TOA is capable of producing cost-effective and feasible UC schedules across all hours of the day, handling the complexity of multiple units with diverse operational characteristics. The results confirm that TOA is a robust and reliable optimization tool for real-world UC problems.

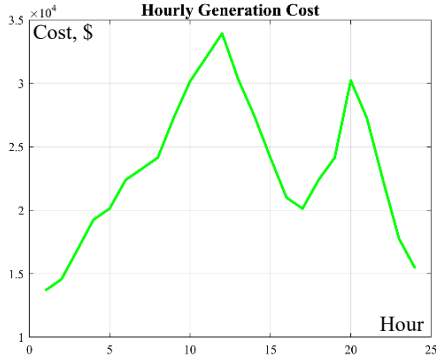

Fig. 2. Hourly generation cost over the study period

Comparison with metaheuristic algorithms. In this subsection, the performance of the proposed TOA is rigorously compared with 6 well-known metaheuristic algorithms, namely: genetic algorithm (GA) [12], particle swarm optimization (PSO) [13], gravitational search algorithm (GSA) [14], whale optimization algorithm (WOA) [19], multi-verse optimizer (MVO) [20] and reptile search algorithm (RSA) [21]. To ensure a fair and statistically significant comparison, TOA and each competitor algorithm were independently executed ten times on the same UC problem instance. The outcomes of these runs were evaluated using 6 statistical indicators: mean, best, worst, median, standard deviation and rank, with results presented in Table 3. The cost metric considered is the average cost per MWh, calculated as:

$$\text{Average cost per MWh} = \text{total cost} / \sum P^D. \quad (21)$$

Table 3 highlights the statistical performance of all algorithms across multiple runs. The results clearly demonstrate that TOA achieves the lowest mean cost (20.70201 $/MWh) among all algorithms, reflecting

superior economic efficiency in the generation scheduling problem. Furthermore, TOA attains the best recorded cost (20.68258 $/MWh) and maintains a small standard deviation (0.0118), indicating high solution reliability and robustness against stochastic variations inherent to metaheuristic optimization.

Table 3

Statistical results of the optimization algorithms for the UC problem

Algorithm	Mean	Best	Worst	Median	Std	Rank
TOA	**20.70201**	**20.68258**	**20.71869**	**20.7**	**0.0118**	**1**
GA	20.70768	20.68936	20.72181	20.7	0.01232	2
PSO	20.90376	20.84684	20.93963	20.9	0.03007	3
GSA	21.00885	20.99178	21.02262	21	0.009	7
MVO	20.95189	20.88262	21.02085	20.9	0.04207	5
WOA	20.95449	20.90798	21.0091	21	0.03107	6
RSA	20.95109	20.90124	20.99329	21	0.03373	4

The statistical comparison reveals several key insights:

1. **Superior performance of TOA.** TOA consistently outperforms all other algorithms in terms of both mean and best cost, establishing it as the most effective optimization method for the considered UC problem.

2. **Stability and robustness.** The relatively low standard deviation of TOA indicates high consistency across multiple runs, reducing the likelihood of suboptimal solutions.

3. **Competitor analysis.** GA exhibits competitive performance with slightly higher mean cost and rank 2, while PSO and RSA show moderate performance. The other algorithms (GSA, MVO, WOA) display higher mean costs and greater variability, suggesting less efficient exploration-exploitation balance for this UC instance.

In addition to numerical analysis, Fig. 3 presents boxplots of the cost distributions for TOA and competitor algorithms. The boxplots visually confirm that TOA not only achieves lower median and quartile values but also exhibits a narrower interquartile range, reflecting both high-quality solutions and reduced variability. The boxplots of other algorithms, particularly GSA, WOA, and MVO, indicate larger spread and occasional higher-cost outliers, further emphasizing TOA's superiority in achieving both optimal and reliable solutions.

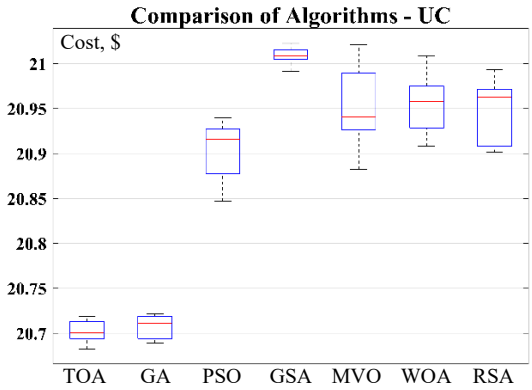

Fig. 3. Boxplot diagrams obtained from TOA and competing algorithms on UC problems

Overall, the comparative analysis demonstrates that TOA provides a robust, cost-effective, and highly reliable optimization framework for the UC problem, outperforming well-established metaheuristic algorithms in both solution quality and stability.

Conclusions. This study presented an efficient and reliable solution framework for the UC problem using the TOA. The UC problem, as a fundamental operational task in power systems, requires optimization methods capable of handling mixed-integer decision variables, nonlinear cost structures, and a wide range of operational constraints. In this work, TOA was employed to schedule ten generating units over a 24-hour horizon while satisfying realistic operating limits and load balance requirements.

The scientific contribution of this study lies in the development and application of a biologically inspired, parameter-free, and self-adaptive optimization mechanism. TOA models the unique survival strategies of tardigrades (active mobility, localized adjustment, and cryptobiotic stabilization) and translates these into adaptive exploration-exploitation operators. This design enables the algorithm to dynamically adjust its search behavior without external parameter tuning, effectively overcoming challenges such as premature convergence and insufficient local refinement that commonly affect traditional metaheuristics in UC applications.

The performance evaluation against six well-established algorithms demonstrated that TOA consistently achieves lower operating costs, stronger convergence stability, and higher robustness across multiple runs. The algorithm maintained feasibility with respect to all UC constraints and produced reliable schedules with minimal variability. These findings validate the practical suitability of TOA for modern power system operations and confirm its superiority in balancing global search efficiency and local optimization accuracy.

Future extensions of this research can further enhance the applicability of TOA. First, TOA may be expanded to large-scale UC systems, multi-area networks, and transmission-constrained environments. Second, integrating renewable energy sources, energy storage systems, and uncertainty modeling would allow TOA to address emerging challenges in future power grids. Third, hybrid TOA variants combining machine learning or local search strategies could improve convergence speed and precision. Additionally, multi-objective UC formulations involving cost, emissions, and reliability merit investigation. Finally, applying TOA to real-time UC, stochastic scheduling, and other energy management problems represents a promising direction for broader power system optimization.

Acknowledgment. The authors are grateful to the Deanship of Scientific Research at Jadara University for providing financial support for this publication.

Conflict of interest. The authors declare that they have no conflicts of interest.

REFERENCES

1. Manikandan K., Sasikumar S., Arulraj R. A novelty approach to solve an economic dispatch problem for a renewable integrated micro-grid using optimization techniques. *Electrical Engineering & Electromechanics*, 2023, no. 4, pp. 83-89. doi: https://doi.org/10.20998/2074-272X.2023.4.12.

2. Qin J., Yu N. Solve Large-Scale Unit Commitment Problems by Physics-Informed Graph Learning. *IEEE Transactions on Power Systems*, 2025, vol. 40, no. 6, pp. 4439-4451. doi: https://doi.org/10.1109/TPWRS.2025.3562886.

3. Greenough R., Murakami K., Davidson M.R., Kleissl J., Khurram A. Wildfire Resilient Unit Commitment Under

Uncertain Demand. *IEEE Transactions on Power Systems*, 2025, vol. 40, no. 4, pp. 3131-3143. doi: https://doi.org/10.1109/TPWRS.2025.3527879.
4. Ali A., Shah A., Keerio M.U., Mugheri N.H., Abbas G., Touti E., Hatatah M., Yousef A., Bouzguenda M. Multi-Objective Security Constrained Unit Commitment via Hybrid Evolutionary Algorithms. *IEEE Access*, 2024, vol. 12, pp. 6698-6718. doi: https://doi.org/10.1109/ACCESS.2024.3351710.
5. Bouhadouza B., Sadaoui F. Optimal power flow analysis under photovoltaic and wind power uncertainties using the blood-sucking leech optimizer. *Electrical Engineering & Electromechanics*, 2025, no. 6, pp. 15-26. doi: https://doi.org/10.20998/2074-272X.2025.6.03.
6. Mozhdehi A.T., Khodadadi N., Aboutalebi M., El-Kenawy E.-S.M., Hussien A.G., Zhao W., Nadimi-Shahraki M.H., Mirjalili S. Divine Religions Algorithm: a novel social-inspired metaheuristic algorithm for engineering and continuous optimization problems. *Cluster Computing*, 2025, vol. 28, no. 4, art. no. 253. doi: https://doi.org/10.1007/s10586-024-04954-x.
7. Zalzala A.M., Jawad R.K., AL-Salih A.A.M.M., Ahmed M.A., Ibraheem I.K. Application of Spider-Tailed Horned Viper Optimization for Unit Commitment Problem in Power Systems. *INASS Express*, 2025, vol. 1, no. 1, pp. 10-18. doi: https://doi.org/10.22266/inassexpress.2025.002.
8. Hamadneh T., Batiha B., Gharib G.M., Aribowo W. Application of Orangutan Optimization Algorithm for Feature Selection Problems. *INASS Express*, 2025, vol. 1, no. 1, pp. 1-9. doi: https://doi.org/10.22266/inassexpress.2025.001.
9. Hamadneh T., Batiha B., Gharib G.M. Enhanced Distributed Generation Placement Using Carpet Weaver Optimization: A Comparative Metaheuristic Approach. *INASS Express*, 2025, vol. 1, no. 1, pp. 19-28. doi: https://doi.org/10.22266/inassexpress.2025.003.
10. Laouafi F. Improved grey wolf optimizer for optimal reactive power dispatch with integration of wind and solar energy. *Electrical Engineering & Electromechanics*, 2025, no. 1, pp. 23-30. doi: https://doi.org/10.20998/2074-272X.2025.1.04.
11. Jeridi A., Moulahi M.H., Khaterchi H., Zaafouri A. Maximum power point tracking improving of photovoltaic systems based on hybrid triangulation topology aggregation optimizer and incremental conductance algorithm. *Electrical Engineering & Electromechanics*, 2025, no. 5, pp. 17-26. doi: https://doi.org/10.20998/2074-272X.2025.5.03.
12. Holland J.H. Genetic Algorithms. *Scientific American*, 1992, vol. 267, no. 1, pp. 66-73.
13. Kennedy J., Eberhart R. Particle swarm optimization. *Proceedings of ICNN'95 – International Conference on Neural Networks*, 1995, vol. 4, pp. 1942-1948. doi: https://doi.org/10.1109/ICNN.1995.488968.
14. Rashedi E., Nezamabadi-pour H., Saryazdi S. GSA: A Gravitational Search Algorithm. *Information Sciences*, 2009, vol. 179, no. 13, pp. 2232-2248. doi: https://doi.org/10.1016/j.ins.2009.03.004.
15. Dinler Ö.B., Bektemyssova G., Ahmed M.A., Ibraheem I.K., Smerat A., Montazeri Z., Dehghani M., Malik O.P., Şahin C.B., Al-Salih A.A.M.M., Eguchi K. Blue-eared Hedgehog Optimization (BEHO): A Nature-inspired Metaheuristic for Robust and Efficient Global Optimization. *International Journal of Intelligent Engineering and Systems*, 2025, vol. 18, no. 11, pp. 133-148. doi: https://doi.org/10.22266/ijies2025.1231.08.
16. Dinler Ö.B., Bektemyssova G., Şahin C.B., Montazeri Z., Dehghani M., Smerat A., Werner F., Eguchi K. Carpenter Optimization Algorithm: A Human-inspired Metaheuristic for Robust and Efficient Constrained Optimization. *International Journal of Intelligent Engineering and Systems*, 2025, vol. 18, no. 11, pp. 344-357. doi: https://doi.org/10.22266/ijies2025.1231.21.
17. Xiao Y., Cui H., Khurma R.A., Castillo P.A. Artificial lemming algorithm: a novel bionic meta-heuristic technique for solving real-world engineering optimization problems. *Artificial Intelligence Review*, 2025, vol. 58, no. 3, art. no. 84. doi: https://doi.org/10.1007/s10462-024-11023-7.
18. Wolpert D.H., Macready W.G. No free lunch theorems for optimization. *IEEE Transactions on Evolutionary Computation*, 1997, vol. 1, no. 1, pp. 67-82. doi: https://doi.org/10.1109/4235.585893.
19. Mirjalili S., Lewis A. The Whale Optimization Algorithm. *Advances in Engineering Software*, 2016, vol. 95, pp. 51-67. doi: https://doi.org/10.1016/j.advengsoft.2016.01.008.
20. Mirjalili S., Mirjalili S.M., Hatamlou A. Multi-Verse Optimizer: a nature-inspired algorithm for global optimization. *Neural Computing and Applications*, 2016, vol. 27, no. 2, pp. 495-513. doi: https://doi.org/10.1007/s00521-015-1870-7.
21. Abualigah L., Elaziz M.A., Sumari P., Geem Z.W., Gandomi A.H. Reptile Search Algorithm (RSA): A nature-inspired meta-heuristic optimizer. *Expert Systems with Applications*, 2022, vol. 191, art. no. 116158. doi: https://doi.org/10.1016/j.eswa.2021.116158.

Received 04.09.2025
Accepted 09.11.2025
Published 02.03.2026

S.A. Alomari [1], *PhD, Associate Professor,*
A. Smerat [2], *Candidate PhD, Lecturer,*
O.P. Malik[3], *PhD, Professor,*
M. Dehghani[4], *PhD,*
Z. Montazeri[4], *PhD Student,*
[1] Computer Science Department, Faculty of Information Technology, Jadara University, Irbid 21110, Jordan.
[2] Hourani Center for Applied Scientific Research, Al-Ahliyya Amman University, Amman 19328, Jordan.
[3] Department of Electrical and Software Engineering, University of Calgary, Canada.
[4] Department of Electrical and Electronics Engineering, Shiraz University of Technology, Iran,
e-mail: adanbax@gmail.com (Corresponding Author)

How to cite this article:
Alomari S.A., Smerat A., Malik O.P., Dehghani M., Montazeri Z. Efficient and reliable scheduling of power generating units in the unit commitment problem using the Tardigrade optimization algorithm. *Electrical Engineering & Electromechanics*, 2026, no. 2, pp. 15-21. doi: https://doi.org/10.20998/2074-272X.2026.2.03

UDC 621.316 https://doi.org/10.20998/2074-272X.2026.2.04

S. Belakehal, M.L. Srief

Comparative performance analysis of backstepping and sliding mode control for static synchronous compensators based on flying capacitor multicell converters

Introduction. *The integration of a static synchronous compensator (STATCOM) based on a flying capacitor multicell converter (FCMC) provides an effective solution for dynamic reactive power compensation and voltage quality improvement. The adoption of nonlinear control strategies, such as sliding mode control (SMC) and backstepping (BSC), enhances system robustness and ensures precise tracking of variables despite network nonlinearities and disturbances.* ***Problem.*** *Reactive, inductive or capacitive loads cause network imbalances leading to voltage sags, swells and fluctuations at the point of common coupling (PCC). These disturbances degrade power quality, reduce the power factor and place excessive stress on equipment. Moreover, high reactive power flow increases losses and decreases the overall system efficiency.* ***Goal.*** *This study compares the performance of SMC and BSC controllers applied to a STATCOM for PCC voltage regulation aiming to improve the power factor, effectively control reactive power and overcome the limitations of conventional controllers under network nonlinearities and voltage disturbances caused by reactive loads.* ***Methodology.*** *The SMC uses a sliding surface based on current errors to achieve fast and precise tracking even in the presence of disturbances. The BSC control employs Lyapunov functions to decompose the nonlinear system into controllable subsystems, ensuring overall stability. Both strategies are simulated on a 5-level flying capacitor multicell STATCOM using MATLAB/Simulink. Simulation* ***results*** *confirm the effectiveness of both controllers in maintaining the PCC voltage at its reference value with a very short response time (1 ms), even under reactive load variations. Precise reactive power control enables rapid compensation of fluctuations, improves the power factor and reduces harmonic distortion. The* ***scientific novelty*** *of this work lies in the comparative performance analysis of the nonlinear SMC and BSC controllers applied to a STATCOM based on a FCMC converter, considering network disturbances caused by reactive loads.* ***Practical value.*** *These nonlinear control strategies significantly enhance the stability, voltage quality, and power factor of low-voltage networks equipped with STATCOMs.* References 36, tables 4, figures 18.

Key words: **flying capacitor multicell converter, static synchronous compensator, sliding mode control, PI controller.**

Вступ. *Інтеграція статичного синхронного компенсатора (STATCOM) на основі багатоелементного перетворювача з літаючим конденсатором (FCMC) забезпечує ефективне рішення для динамічної компенсації реактивної потужності та покращення якості напруги. Впровадження нелінійних стратегій керування, таких як ковзне керування (SMC) та зворотний крок (BSC), підвищує стійкість системи та забезпечує точне відстеження змінних, незважаючи на нелінійність та збурення мережі.* ***Проблема***. *Реактивні, індуктивні або ємнісні навантаження викликають дисбаланс мережі, що призводить до знижень, збільшень та коливань напруги в точці спільного підключення (PCC). Ці збурення погіршують якість електроенергії, знижують коефіцієнт потужності та створюють надмірне навантаження на обладнання. Крім того, високий потік реактивної потужності збільшує втрати та знижує загальну ефективність системи.* ***Мета***. *У цьому дослідженні порівнюється продуктивність контролерів SMC та BSC, що застосовуються до STATCOM для регулювання напруги PCC, з метою покращення коефіцієнта потужності, ефективного керування реактивною потужністю та подолання обмежень традиційних контролерів за умов нелінійності мережі та збурень напруги, спричинених реактивними навантаженнями.* ***Методика***. *SMC використовує ковзну поверхню на основі похибок струму для досягнення швидкого та точного відстеження навіть за наявності збурень. Керування BSC використовує функції Ляпунова для розкладання нелінійної системи на керовані підсистеми, забезпечуючи загальну стабільність. Обидві стратегії моделюються на п'ятирівневому багатоелементному STATCOM з літаючим конденсатором за допомогою MATLAB/Simulink.* ***Результати*** *моделювання підтверджують ефективність обох контролерів у підтримці напруги PCC на її опорному значенні з дуже коротким часом відгуку (1 мс), навіть за коливань реактивного навантаження. Точне керування реактивною потужністю дозволяє швидко компенсувати коливання, покращує коефіцієнт потужності та зменшує гармонійні спотворення.* ***Наукова новизна*** *роботи полягає в порівняльному аналізі продуктивності нелінійних контролерів SMC та BSC, застосованих до STATCOM на основі перетворювача FCMC, з урахуванням мережевих збурень, спричинених реактивними навантаженнями.* ***Практична значимість***. *Ці нелінійні стратегії керування значно покращують стабільність, якість напруги та коефіцієнт потужності низьковольтних мереж, оснащених STATCOM.* Бібл. 36, табл. 4, рис. 18.

Ключові слова: **багатоелементний перетворювач з літаючим конденсатором, статичний синхронний компенсатор, керування ковзним режимом, ПІ-регулятор.**

Introduction. Flexible AC transmission systems (FACTS) have been widely adopted in modern power networks to enable efficient control of power flow, enhance the maximum transferable power, regulate voltage profiles, improve power factor, and strengthen overall system stability. In addition, certain FACTS devices contribute to network frequency management, thereby supporting reliable and flexible operation of the electrical grid [1, 2]. Within the wide range of FACTS devices, the static synchronous compensator (STATCOM) has received considerable attention due to its robustness and capability to provide dynamic reactive power with rapid response [3]. It is widely regarded as one of the most effective FACTS devices. When connected in parallel with the power grid, the STATCOM operates via voltage source converters integrated into the transmission network. Its operating principle relies on controlling the reactive power exchanged between the converter and the grid, analogous to the behavior of a rotating synchronous machine [4, 5]. This exchange is accomplished through 3-phase voltages of adjustable amplitude and frequency, which are synchronized with the grid and generated from a DC voltage source maintained by charged capacitors [6].

The implementation of a STATCOM can be achieved using a conventional 2-level voltage source converter, as reported in earlier studies [5]. Such converters offer several advantages, including a reduced component count, the use of at most two DC voltage sources, and relatively straightforward control strategies. However, they exhibit significant limitations, such as poor output voltage quality, high harmonic distortion, and applicability restricted to low-voltage and low-to medium-power systems. In recent years, 2-level converter-based STATCOMs have increasingly been supplanted by multilevel converter technologies. Multilevel converters provide numerous benefits, including an increased number of output voltage levels, superior harmonic performance, higher efficiency,

improved power quality, reduced total converter losses, and lower electromagnetic interference due to decreased d*v*/d*t* stresses in the system [7–9]. Accordingly, considerable research efforts are currently directed toward the design, optimization and control of STATCOM topologies based on multilevel converters.

As demonstrated in several studies [7–12], 3 main multilevel converter structures are commonly identified:

1) cascaded H-bridge converters;
2) neutral-point clamped converters;
3) flying capacitor multicell converters (FCMCs).

The FCMC offers several compelling advantages for medium voltage applications. Notably, it can operate without a transformer, requires no clamping diodes, and inherently maintains its floating-capacitor voltages at their nominal values. This natural self-balancing property enables the design of converters with a large number of voltage levels [13, 14].

However, one of the main control challenges in FCMCs lies in maintaining stable and balanced voltages across all floating capacitors. In the absence of an effective balancing mechanism, the voltages of these capacitors can drift from their nominal values, thereby increasing the electrical stress on the power switches. To ensure reliable voltage balancing, these structures generally rely on advanced modulation techniques, notably phase-shifted pulse width modulation (PS-PWM) [15, 16].

The interleaved carrier modulation technique, widely known as PS-PWM, is the conventional control strategy employed in flying-capacitor converters. This method is particularly effective because the phase-shifted switching patterns naturally distribute the charge among the floating capacitors, thereby maintaining their voltage balance without requiring additional control loops. By preserving the inherent self-balancing property of the capacitor voltages, PS-PWM ensures reliable operation of the switching devices and enhances the overall stability of the converter [17, 18].

Recent research efforts have been directed towards enhancing the performance of multilevel STATCOM systems through PWM-based control approaches. In [19], the authors studied a 5-level half-bridge modular multilevel converter (MMC) for D-STATCOM applications, employing phase disposition modulation and a PI controller to effectively balance the capacitor voltages. The authors in [20] proposed a flexible modeling approach for a delta-connected MMC STATCOM with embedded energy storage, aiming to optimize reactive power compensation and system interface control. Finally, the authors of [21] developed a variable DC voltage control strategy for MMC-STATCOMs, which improves the reactive power response and stabilizes capacitor voltages under various operating conditions.

The goal of the work. This study compares the performance of sliding mode control (SMC) and backstepping (BSC) controllers applied to a STATCOM for point of common coupling (PCC) voltage regulation aiming to improve the power factor, effectively control reactive power and overcome the limitations of conventional controllers under network nonlinearities and voltage disturbances caused by reactive loads. The BSC provides stable and precise regulation of voltage and reactive current, while the SMC offers high robustness and a fast dynamic response, with a minor chattering effect. Both methods outperform linear controllers such as PID and linear quadratic regulator in STATCOM applications by effectively handling nonlinearities and network disturbances, while enabling precise balancing of floating capacitors and optimization of reactive power flow, thereby ensuring improved overall stability and performance.

System under study. The studied system (Fig. 1) consists of a 3-phase voltage source and 2 types of balanced 3 phase loads: a fixed active load and 2 dynamic reactive loads. The setup also includes a multilevel STATCOM comprising a DC energy source typically provided by high-capacity capacitors coupled with a 5-level FCMC. The compensator is connected to the PCC through a 3-phase filter inductor, enabling effective voltage regulation and mitigation of network disturbances. The control subsystem, which includes the reference signal generator and the controller, ensures dynamic voltage regulation while maintaining the desired power factor. The exchange of reactive power between the grid and the STATCOM is controlled by adjusting the compensator's output voltage V_c.

When the STATCOM voltage exceeds the grid voltage at the point of PCC, reactive power is injected into the grid. Conversely, if the grid voltage is higher than the STATCOM voltage, reactive power flows from the grid to the compensator. When the two voltages are equal, there is no exchange of reactive power [22, 23].

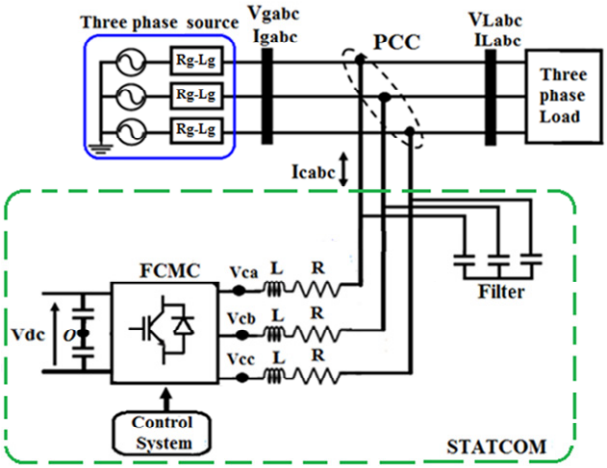

Fig. 1. Equivalent circuit of STATCOM

Mathematical modeling of the STATCOM. The circuit of a distribution system controlled by a STATCOM is shown in Fig. 1. In this system, V_{gabc} denote the 3-phase grid voltages at the PCC, V_{cabc} represent the 3-phase output voltages of the converter, and I_{cabc} are the corresponding STATCOM output currents. Moreover, L denotes the coupling filter inductance per phase, while R represents the series resistance, which accounts for both the winding resistance of the coupling filter and the conduction losses of the converter.

The instantaneous phase voltages at the PCC are:

$$V_{ga} = V_m \cos \omega t \; ; \tag{1}$$

$$V_{gb} = V_m \cos(\omega t - 2\pi/3) \; ; \tag{2}$$

$$V_{sc} = V_m \cos(\omega t - 4\pi/3) \; . \tag{3}$$

According to Kirchhoff's law of voltages, the relationship between the voltage at the PCC, the converter output voltage and the currents is as follows [24–26]:

$$V_{gabc} = V_{cabc} + RI_{cabc} + L\frac{\mathrm{d}I_{cabc}}{\mathrm{d}t} \; . \tag{4}$$

Using the Park transformation (*abc-dq*), the equation (4) can be rewritten as follows:

$$V_d = V_{cd} + RI_d + L\frac{\mathrm{d}I_d}{\mathrm{d}t} - L\omega I_q\,; \tag{5}$$

$$V_q = V_{cq} + RI_q + L\frac{\mathrm{d}I_q}{\mathrm{d}t} + L\omega I_d\,, \tag{6}$$

where I_d, I_q are the d and q axis currents corresponding to I_{ca}, I_{cb}, I_{cc}; ω is the synchronized angular velocity of rotation of the voltage vector; V_{cd}, V_{cq} are the d and q axis voltages corresponding to V_{ca}, V_{cb}, V_{cc}.

According to the theory of instantaneous power, the active and reactive power exchanged between the network and the STATCOM can be calculated in the dq frame as:

$$P = \frac{3}{2}(V_d I_d + V_q I_q)\,; \tag{7}$$

$$Q = \frac{3}{2}(V_q I_d - V_d I_q)\,. \tag{8}$$

In the synchronized rotary reference frame $V_g = V_d$ and $V_q = 0$, the instantaneous active and reactive powers can be written as follows:

$$P = \frac{3}{2}V_d I_d\,; \tag{9}$$

$$Q = -\frac{3}{2}V_d I_q\,. \tag{10}$$

FCMC model. FCMC is based on the series connection of multiple switching cells, which allows the generation of high voltages with low harmonic distortion. Each phase of the converter consists of a set of p cells, interleaved with (p–1) floating capacitors. Each cell comprises 2 bidirectional switches (IGBTs), operated complementarily to prevent short circuits between voltage sources [16, 27, 28]. The binary state S_{ki} of switching cell (i =1, 2, 3,..., p) in phase (k = a, b, c) corresponds to the state of the upper switch of the cell: S_{ki} = 1 when the switch is closed, and S_{ki} = 0 when it is open.

The converter output voltage V_{kO} can then be expressed as a function of the switching states S_{ki} according to the following relationship:

$$V_{kO} = \frac{V_{dc}}{p}\left(\sum_{i=1}^{p} S_{ki} - p/2\right). \tag{11}$$

In a state of equilibrium, the voltages of the cells are equal:

$$V_{Ccellki} = V_{dc} / p\,. \tag{12}$$

Under these conditions, the voltages of the capacitors are given by:

$$V_{Cki} = \frac{i \cdot V_{dc}}{p}\,. \tag{13}$$

For a converter with p cells, the number of levels that the converter is capable of generating at the output is p+1. The characteristic values per phase of the combination of p switching cells are defined in Table 1.

Table 1

Definition of the per phase characteristic parameters of FCMC

Number of cells	p
Number of active switches	$2p$
Number of flying capacitors	p–1
Number of combinations	2^p
Number of generated output voltage levels	p+1
Main supply voltage value	V_{dc}
Voltage source of each cell i	$i \cdot V_{dc} / p$

In the specific case where the converter consists of 4 cells, it is referred to as a 5-level series multicell converter. Figure 2 illustrates the structure of one arm of this converter, which is composed of 8 switches forming 4 switching cells connected in series, along with 3 floating capacitors. The DC bus, in turn, consists of 2 capacitors, denoted C1 and C2.

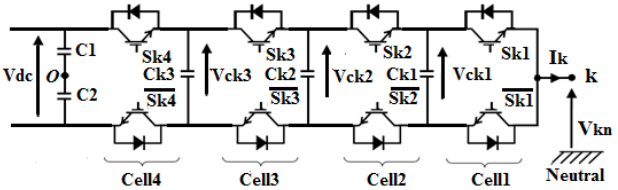

Fig. 2. Per-leg circuit configurations of the 5-level FCMC

The output voltages of the converter, measured with respect to the negative terminal O of the DC bus, are expressed as follows [29]:

$$V_{kO} = (S_{k4} - 0.5)\cdot V_{dc} + (S_{k3} - S_{k4})\cdot V_{ck3} + \\ + (S_{k2} - S_{k3})\cdot V_{ck2} + (S_{k1} - S_{k2})\cdot V_{ck1}. \tag{14}$$

The switches states of 4-cell 5-level FCM converter are demonstrated in Table 2.

Table 2

States of switches in the 4-cell-5-level FCMC

Output voltage level	States of (S_{k1}, S_{k2}, S_{k3}, S_{k4})	Number of state
V_{dc}/2	(1, 1, 1, 1)	1
V_{dc}/4	(1, 1, 1, 0) (1, 1, 1, 1) (1, 1, 0, 1) (0, 1, 1, 1)	4
0	(1, 1, 0, 0) (1, 0, 0, 1) (0, 0, 1, 1) (0, 1, 1, 0)	4
–V_{dc}/4	(0, 0, 0, 1) (0, 0, 1, 0) (0, 1, 0, 0) (1, 0, 0, 0)	4
–V_{dc}/2	(0, 0, 0, 0)	1

For a balanced 3-phase system, the sum of the 3 phase voltages is zero:

$$V_{an} + V_{bn} + V_{cn} = 0\,. \tag{15}$$

The relationship between the converter output voltages V_{kn} (k = a, b, c) and the voltage V_{nO} is:

$$V_{kn} = V_{kO} - V_{nO}\,, \tag{16}$$

where $V_{nO} = (V_{aO} + V_{bO} + V_{cO}) / 3$.

Starting from (16), we express V_{an}, V_{bn} and V_{cn} in terms of V_{aO}, V_{bO} and V_{cO}:

$$V_{an} = (2/3)\cdot V_{aO} - (1/3)\cdot V_{bO} - (1/3)\cdot V_{cO}\,; \tag{17}$$

$$V_{bn} = -(1/3)\cdot V_{aO} + (2/3)\cdot V_{bO} - (1/3)\cdot V_{cO}\,; \tag{18}$$

$$V_{cn} = -(1/3)\cdot V_{aO} - (1/3)\cdot V_{bO} + (2/3)\cdot V_{cO}\,, \tag{19}$$

where V_{aO}, V_{bO}, V_{cO} are determined by (11).

STATCOM control strategy. The block diagram of the control strategy is shown in Fig. 3. This diagram consists of a dual-loop control structure: an inner current control loop and an outer current reference generation loop. In the outer loop, the DC voltage control loop is designed to maintain the DC-link voltage at its reference value.

The measured DC voltage is compared with the reference value, and the resulting error is processed by a PI controller. This controller generates the active current reference component I_{dref}, as shown in Fig. 3. Similarly, in the AC voltage regulation loop, the RMS value of the AC voltage measured at PCC is compared with a predefined reference voltage. The resulting error is processed by another PI controller, in which the proportional term provides a fast dynamic response to voltage variations,

while the integral term eliminates the steady-state error. The control signal produced by the controller is then converted into reactive current references I_{qref}, enabling the adjustment of the reactive power exchanged by the STATCOM, thereby ensuring effective voltage regulation at the PCC and enhancing the overall stability of the power system [7, 22]. The quantity V_{rms} denotes the measured value of the AC voltage, calculated from the components d and q of the 3-phase voltage vector:

$$V_{rms} = \sqrt{V_d^2 + V_q^2}\ . \tag{20}$$

The inner current control loop, implementing either SMC or the backstepping approach, subsequently computes the converter reference output voltages required for the modulation process.

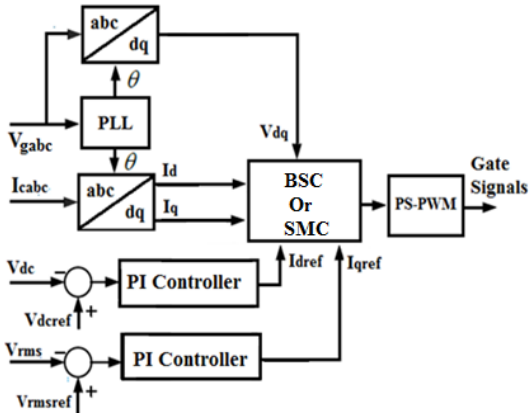

Fig. 3. STATCOM control block diagram

Sliding mode controller. In the control strategy, STATCOM is driven using SMC to regulate the STATCOM currents (I_d and I_q) [30, 31]. The equations of state (5) and (6) are expressed as follows:

$$\frac{\mathrm{d}I_d}{\mathrm{d}t} = -\frac{R}{L}I_d - \frac{1}{L}V_{cd} + \omega I_q + \frac{1}{L}V_d\ ; \tag{21}$$

$$\frac{\mathrm{d}I_q}{\mathrm{d}t} = -\frac{R}{L}I_q - \frac{1}{L}V_{cq} - \omega I_d + \frac{1}{L}V_q\ , \tag{22}$$

with:

$$V_d = V_{d\_eq} + V_{dcr}\ ; \tag{23}$$

$$V_q = V_{q\_eq} + V_{qcr}\ . \tag{24}$$

The implementation of SMC is initiated by the selection of sliding surfaces:

$$S_d = I_{dref} - I_d\ ; \tag{25}$$

$$S_q = I_{qref} - I_q\ . \tag{26}$$

After derivation, we obtain:

$$\dot{S}_d = \dot{I}_{dref} - \dot{I}_d\ ; \tag{27}$$

$$\dot{S}_q = \dot{I}_{qref} - \dot{I}_q\ . \tag{28}$$

Then, by substituting (21) into (27) and (22) into (28), we obtain:

$$\dot{S}_d = \dot{I}_{dref} - \dot{I}_d = \dot{I}_{dref} + \frac{R}{L}I_d - \omega I_q + \frac{1}{L}V_{cd} - \frac{1}{L}V_d\ ; \tag{29}$$

$$\dot{S}_q = \dot{I}_{qref} - \dot{I}_q = \dot{I}_{qref} + \frac{R}{L}I_q + \omega I_d + \frac{1}{L}V_{cq} - \frac{1}{L}V_q\ . \tag{30}$$

And to check Lyapunov stability criterion $\dot{S}_i \times S_i < 0$ we must have:

$$\dot{S}_d = -k_d \cdot \mathrm{sign}(S_d)\ ; \tag{31}$$

$$\dot{S}_q = -k_q \cdot \mathrm{sign}(S_q)\ , \tag{32}$$

where k_d, k_q are the design parameters chosen according to the desired performance in closed loop.

By substituting $\dot{S}_d$ and $\dot{S}_q$ with their expressions from (29), (30) into (31), (32), respectively, we obtain:

$$\dot{I}_{dref} + \frac{R}{L}I_d - \omega I_q + \frac{1}{L}V_{cd} - \frac{1}{L}V_d = -k_d \cdot \mathrm{sign}(S_d)\ , \tag{33}$$

$$\dot{I}_{qref} + \frac{R}{L}I_q + \omega I_d + \frac{1}{L}V_{cq} - \frac{1}{L}V_q = -k_q \cdot \mathrm{sign}(S_q)\ . \tag{34}$$

Consequently, the V_d and V_q control commands can be expressed as follows:

$$V_d = L\dot{I}_{dref} + RI_d - \omega L I_q + V_{cd} + L \cdot k_d \cdot \mathrm{sign}(S_d) = \\ = V_{d\_eq} + V_{dcr};\tag{35}$$

$$V_q = L\dot{I}_{qref} + RI_q + \omega L I_d + V_{cq} + L \cdot k_q \cdot \mathrm{sign}(S_q) = \\ = V_{q\_eq} + V_{qcr}.\tag{36}$$

The following control and correction terms are obtained:

- equivalent commands terms:

$$V_{d\_eq} = L\dot{I}_{dref} + RI_d - \omega L I_q + V_{cd}\ ; \tag{37}$$

$$V_{q\_eq} = L\dot{I}_{qref} + RI_q + \omega L I_d + V_{cq}\ ; \tag{38}$$

- correction terms:

$$V_{dcr} = L \cdot k_d \cdot \mathrm{sign}(S_d)\ ; \tag{39}$$

$$V_{qcr} = L \cdot k_q \cdot \mathrm{sign}(S_q)\ . \tag{40}$$

In MATLAB/Simulink implementation, the chattering phenomenon was alleviated by replacing the discontinuous sign(S) function with a Saturation block. This adjustment results in a smoother control behavior near the sliding surface while retaining the robustness and stability of the sliding mode controller.

Backstepping current controller. The backstepping approach is a robust nonlinear control strategy based on Lyapunov's stability theory, which enables a systematic linearization of nonlinear systems. The method consists in progressively constructing the control law by defining some state variables as virtual control inputs and designing intermediate control laws for each stage [32, 33]. The purpose of the BSC applied to the active and reactive currents is to guarantee that the active and reactive current components (I_d and I_q), accurately track their respective reference values I_{dref} and I_{qref}.

The tracking errors of these currents are defined by:

$$z_1 = I_{dref} - I_d\ ; \tag{41}$$

$$z_2 = I_{qref} - I_q\ . \tag{42}$$

Their derivatives are given by:

$$\dot{z}_1 = \dot{I}_{dref} - \dot{I}_d\ ; \tag{43}$$

$$\dot{z}_2 = \dot{I}_{qref} - \dot{I}_q\ . \tag{44}$$

Substituting (21) into (43) and (22) into (44), we obtain:

$$\dot{z}_1 = \dot{I}_{dref} + \frac{R}{L}I_d - \omega I_q - \frac{V_d - V_{cd}}{L}\ ; \tag{45}$$

$$\dot{z}_2 = \dot{I}_{qref} + \frac{R}{L}I_q + \omega I_d - \frac{V_q - V_{cq}}{L}\ . \tag{46}$$

Lyapunov candidate functions are defined by:

$$V_1 = \frac{1}{2} z_1^2 ; \quad (47)$$

$$V_2 = \frac{1}{2} z_2^2 . \quad (48)$$

The derivation of these functions leads to:

$$\dot{V}_1 = z_1 \dot{z}_1 = z_1 \left(\dot{I}_{dref} + \frac{R}{L} I_d - \omega I_q - \frac{V_d - V_{cd}}{L} \right); \quad (49)$$

$$\dot{V}_2 = z_2 \dot{z}_2 = z_2 \left(\dot{I}_{qref} + \frac{R}{L} I_q + \omega I_d - \frac{V_q - V_{cq}}{L} \right). \quad (50)$$

To ensure the stability of the Lyapunov function, its derivative must always be negative. To achieve this, we choose:

$$\dot{z}_1 = -k_1 z_1 ; \quad (51)$$

$$\dot{z}_2 = -k_2 z_2 . \quad (52)$$

Replacing the expression for $\dot{z}_1$ in (45) and the expression for $\dot{z}_2$ in (46), we obtain:

$$\dot{I}_{dref} + \frac{R}{L} I_d - \omega I_q - \frac{V_d - V_{cd}}{L} = -k_1 z_1 ; \quad (53)$$

$$\dot{I}_{qref} + \frac{R}{L} I_q + \omega I_d - \frac{V_q - V_{cq}}{L} = -k_2 z_2 . \quad (54)$$

The commands V_{cd} and V_{cq} can then be defined by:

$$V_{cd} = L \left(-k_1 z_1 - \dot{I}_{dref} - \frac{R}{L} I_d + \omega I_q \right) + V_d ; \quad (55)$$

$$V_{cq} = L \left(-k_2 z_2 - \dot{I}_{qref} - \frac{R}{L} I_q - \omega I_d \right) + V_q , \quad (56)$$

where k_1 and k_2 are the positive constants.

The reference voltages in the dq frame, obtained from the output of the inner current control loop (whether based on SMC or the backstepping method), are transformed into the stationary (a, b, c) reference frame. These voltages are then compared with triangular carrier signals to generate the corresponding switching signals for the power switches. Several capacitor voltage balancing techniques have been proposed in the literature. Among these methods, the PS-PWM technique stands out for its ease of implementation and its superior performance in terms of total harmonic distortion (THD) compared to other techniques. It is based on the use of multiple triangular carrier signals with identical peak-to-peak amplitude and frequency, each phase-shifted relative to the previous one, with the phase shift expressed as $\varphi = 360°/p$ [34, 35].

Figure 4 shows the reference and carrier signals used in conventional PS-PWM modulation for a 4-cell, 5-level FCMC. In this topology, the PS-PWM method employs 4 carrier signals of identical amplitude and frequency, each phase-shifted by 90° relative to the preceding one (Fig. 5). A sinusoidal reference signal, varying within the interval [–1, 1] in the linear modulation region, is compared with all 4 carriers to generate the switching control signals. Each comparison generates a binary output: 1 if the reference signal is greater than or equal to the carrier, and 0 otherwise (Fig. 4).

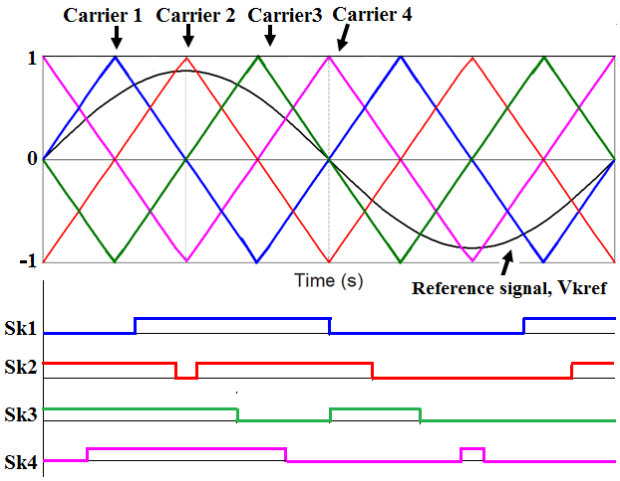

Fig. 4. PS-PWM technique for the 5-level FCMC

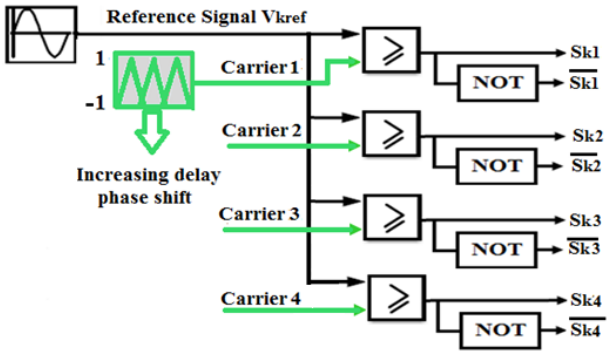

Fig. 5. Schematic diagram of the PS-PWM control

Simulation results and analysis. The complete electrical system, shown in Fig. 1, along with the proposed control strategy, illustrated in Fig. 3, was simulated in MATLAB/Simulink (SimPowerSystems) with a reactive power compensation capacity of ±100 kVAr, under various reactive load conditions, based on the main parameters summarized in Table 3. In the simulation scenario, load L1 is applied continuously from 0 to 8 s. At t = 0.4 s, an inductive load L2 is added, and at t = 0.6 s, a capacitive load L3 is applied while L2 is disconnected.

Table 3

Parameters of simulated system [36]

Component	Parameters	Value
AC source	Line-to-line RMS voltage	381 V
	Frequency	50 Hz
	Source resistance	7 mΩ
	Source inductance	0.23 mH
STATCOM	DC-link voltage	750 V
	L filter inductance	0.7 mH
Load	Fixed load L1	100 kW
	Dynamic load L2	10 kW / +50 kVAr
	load L3	10 kW / –50 kVAr

Figure 6 shows the effective per-phase voltage at the PCC, with and without STATCOM compensation, during the connection of reactive loads (inductive and capacitive). The red curve represents the PCC voltage without STATCOM operation. As observed, the voltage amplitude increases relative to the desired value between 0.2 s and 0.4 s due to the connection of capacitive loads, which inject additional reactive power into the network, causing an overvoltage. It then decreases between 0.4 s and 0.6 s relative to the nominal voltage due to the connection of

inductive loads, which absorb more reactive power, resulting in voltage sag. Conversely, the green curve illustrates the PCC voltage with the STATCOM operating under SMC. It is clearly observed that the voltage is accurately maintained at its reference value, exhibiting a very fast response time of approximately 1 ms, even during the connection of reactive loads. The blue curve shows the PCC voltage with the STATCOM controlled using the backstepping method, demonstrating its effectiveness in maintaining the voltage at the desired value, with a very fast response time and fewer fluctuations compared to the STATCOM under SMC.

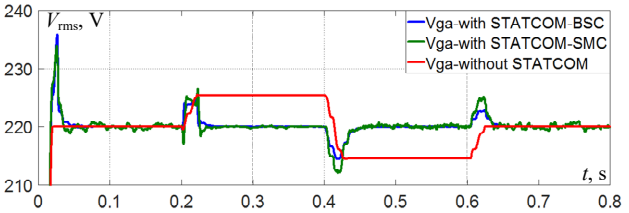

Fig. 6. RMS phase voltage at PCC without and with STATCOM

Figure 7 shows the 3-phase voltages at the PCC without the STATCOM during the connection of reactive loads. Overvoltages caused by capacitive loads can be observed between 0.2 s and 0.4 s, and voltage sags resulting from inductive loads appear between 0.4 s and 0.6 s.

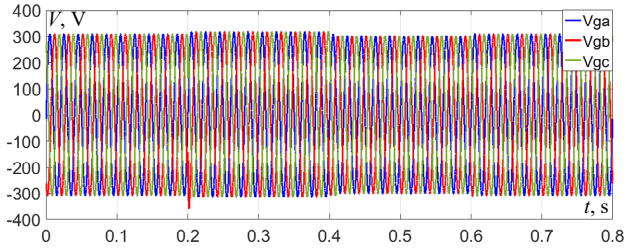

Fig. 7. 3-phase voltage (abc) at PCC without STATCOM

Figure 8 illustrates the 3-phase voltages at the PCC under STATCOM operation. The voltage waveforms clearly reach the desired values, demonstrating the responsiveness and effectiveness of the proposed controllers.

Figure 9 presents the dynamic response of the reactive power exchanged between the compensator and the AC network for the 2 proposed structures (SMC STATCOM and BSC STATCOM). It is clearly observed that both structures respond effectively to voltage disturbances caused by reactive loads at the PCC through the injection and absorption of reactive power. This figure confirms that the network remains in a steady state during the periods from 0 s to 0.2 s and from 0.6 s to 0.8 s, during which no reactive power is exchanged between the STATCOM and the network. In the interval 0.2 s to 0.4 s, the network experiences a voltage increase due to the connection of the capacitive load, and the STATCOM intervenes by absorbing the necessary reactive power to compensate for the excess, meaning that the STATCOM operates in inductive mode. In the interval from 0.4 s to 0.6 s, the network experiences voltage sag due to the connection of the inductive load, and the STATCOM intervenes by injecting the necessary reactive power to compensate for the loss, meaning that the STATCOM operates in capacitive mode.

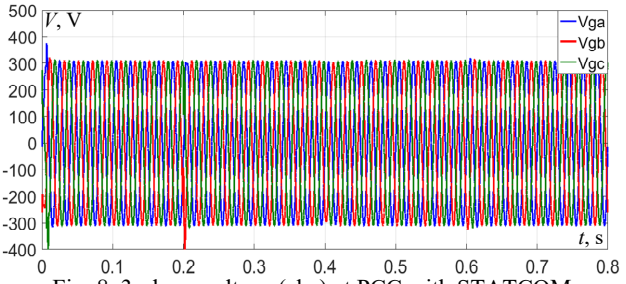

Fig. 8. 3-phase voltage (abc) at PCC with STATCOM

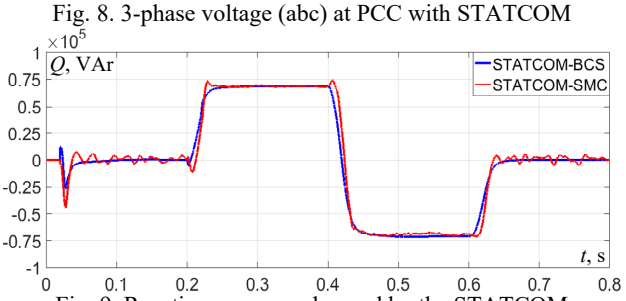

Fig. 9. Reactive power exchanged by the STATCOM

In Fig. 10, the phase voltage at the PCC and the phase current of the STATCOM compensator are shown. As observed, during the intervals from 0 to 0.2 s and from 0.6 s to 0.8 s, no disturbances affect the source, and no reactive power is supplied or absorbed by the compensator, resulting in zero current. Conversely, during the interval from 0.2 s to 0.3 s, the compensator operates in inductive mode: the STATCOM current lags the voltage by 90°. Finally, during the interval from 0.3 s to 0.4 s, the compensator operates in capacitive mode: the STATCOM current leads the voltage by 90°.

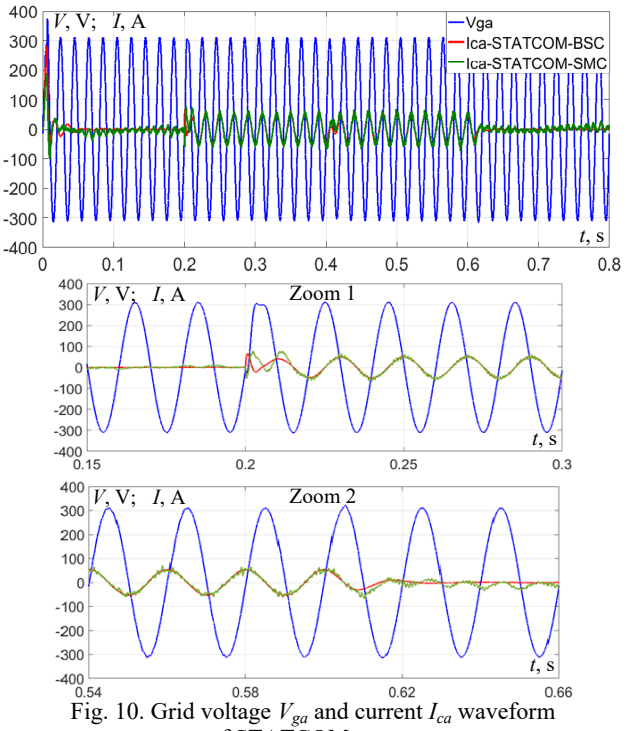

Fig. 10. Grid voltage V_{ga} and current I_{ca} waveform of STATCOM output

Figure 11 shows the evolution of the STATCOM DC bus voltage. This voltage stabilizes around 750 V, with minor fluctuations not exceeding 4 % for both structures (SMC STATCOM and BSC STATCOM) during the voltage sag and overvoltage intervals caused by reactive loads. It is also observed that the fluctuations are slightly smaller for the SMC STATCOM compared to the BSC STATCOM.

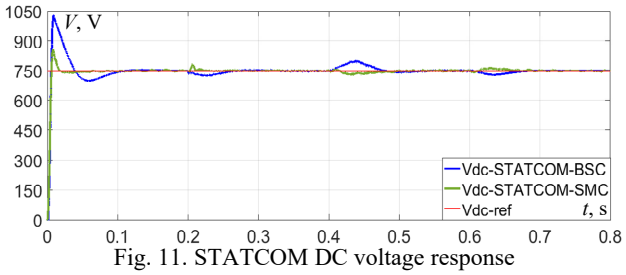

Fig. 11. STATCOM DC voltage response

Figure 12 shows the network phase voltage (V_{ga}) and the corresponding phase current (I_{ga}) at the PCC in the absence of the STATCOM. It can be observed that the current leads the source voltage (capacitive behavior) during the interval 0.2 s to 0.4 s, and lags behind it (inductive behavior) during the interval 0.4 s to 0.6 s. These phase shifts between the network voltage and current, caused by the presence of capacitive and inductive loads, disturb the stability of reactive power and deteriorate the power quality within the electrical system.

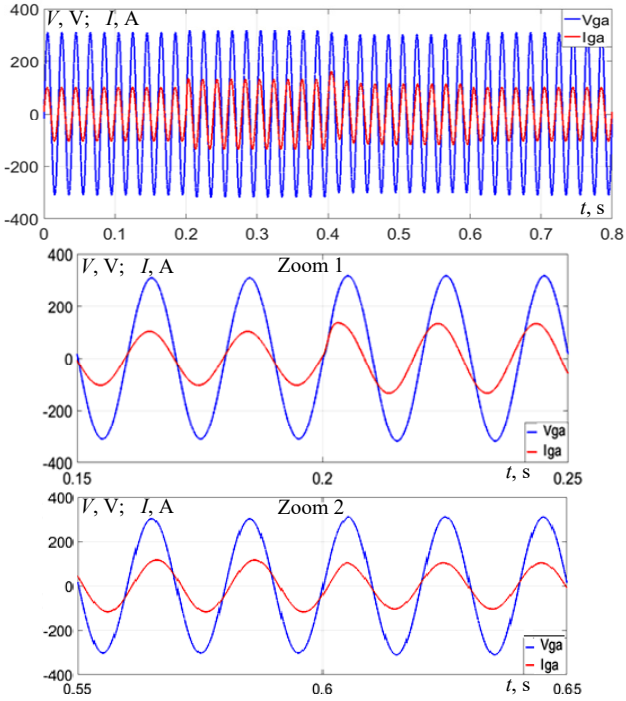

Fig. 12. Grid voltage V_{ga} and current I_{ga} without STATCOM

Figure 13 shows the voltage and current waveforms of phase A at the point of PCC during STATCOM operation. It can be observed that the current and voltage are nearly in phase, with the STATCOM effectively compensating the reactive power supplied by the capacitive loads between 0.2 s and 0.4 s, and the reactive power absorbed by the inductive loads between 0.4 s and 0.6 s, thereby achieving a unity power factor. These results confirm the STATCOM's capability to maintain a sinusoidal current aligned with the grid voltage at the PCC, irrespective of load variations.

Figures 14, 15 show the voltage between phase A and the neutral point O (V_{caO}) at the converter output for both STATCOM-BSC and STATCOM-SMC structures. It is clearly observed that this voltage exhibits 5 distinct and symmetrical levels: $\pm V_{dc}/2$, $\pm V_{dc}/4$ and 0.

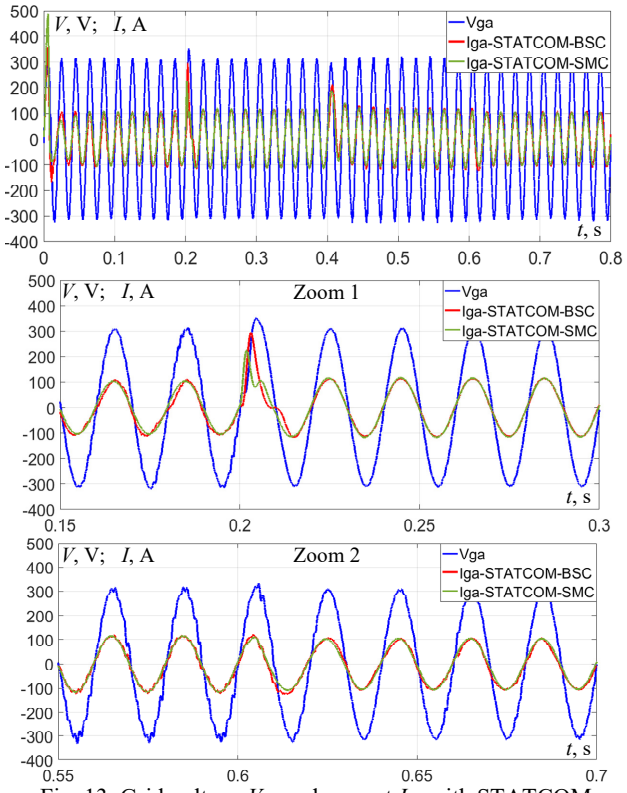

Fig. 13. Grid voltage V_{ga} and current I_{ga} with STATCOM

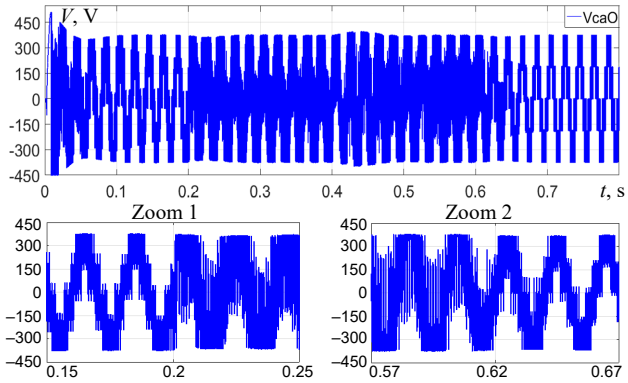

Fig. 14. Output phase voltage V_{caO} of the STATCOM-BSC converter

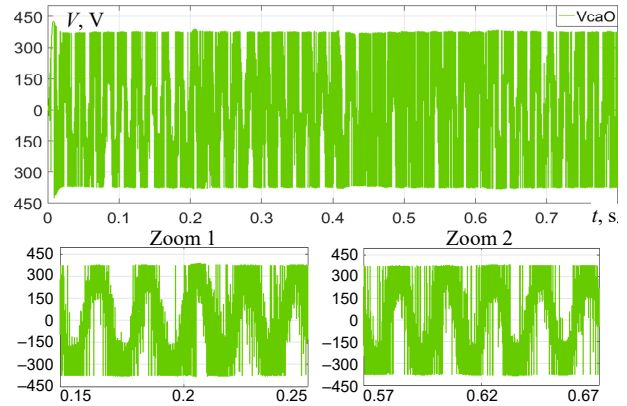

Fig. 15. Output phase voltage V_{caO} of the STATCOM-SMC converter

Figures 16, 17 illustrate the line-to-line voltage (V_{cab}) between phases A and B at the converter output for the same structures, in which the voltage displays 9 levels: $-V_{dc}$; $-3V_{dc}/4$; $-V_{dc}/2$; $-V_{dc}/4$; 0; $V_{dc}/4$; $V_{dc}/2$; $3V_{dc}/4$; V_{dc} thereby confirming the proper operation of the multilevel converter and the accuracy of the applied modulation.

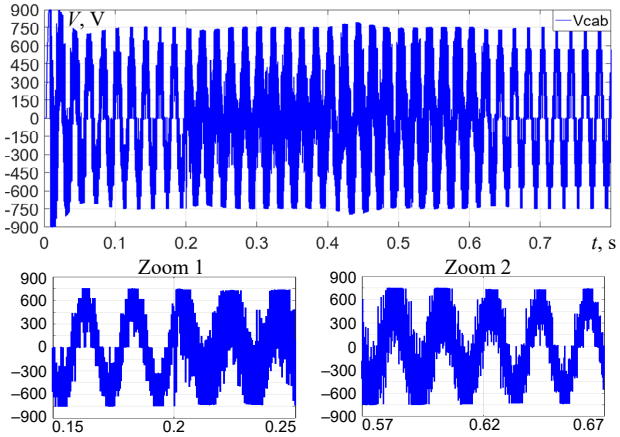

Fig. 16. Line-to-line output voltage V_{cab} of the STATCOM-BSC converter

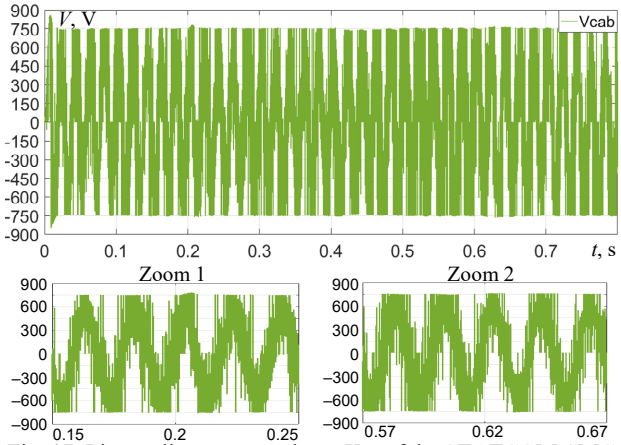

Fig. 17. Line-to-line output voltage V_{cab} of the STATCOM-SMC converter

Figure 18 illustrates the evolution of the internal flying capacitor voltages of the converter for phase of the STATCOM during the connection of reactive loads. A natural balancing of the flying capacitor voltages is also observed, achieved through the PS-PWM control technique. The voltage variations of the capacitors become more pronounced during the time interval between 0.2 s and 0.6 s, due to the reactive power supplied to or absorbed by the reactive loads.

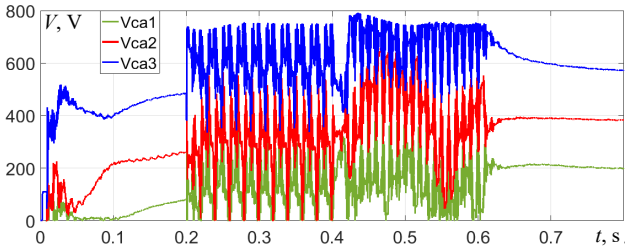

Fig. 18. Voltages of the flying capacitors in the FCMC

A harmonic analysis of the phase voltage V_{sa} at the PCC was performed using the FFT (fast Fourier transform) block in MATLAB for the two STATCOM structures, controlled respectively by SMC and BSC, under voltage sags and swells caused by reactive loads. As shown in Table 4, both structures exhibit almost identical fundamental voltage values. However, the backstepping mode-controlled STATCOM demonstrates better performance in terms of THD. Nevertheless, the THD values for both structures remain within the limits of the IEEE Std. 519-1992.

Table 4

Comparison of performance of SMC and BSC

	THD of V_{sa} at PCC, %	Fundamental V_{sa} at PCC, V
STATCOM SMC	3.13	310.1
STATCOM BSC	4.44	310

Conclusions. This paper presented a comparative analysis of the performance of two nonlinear control strategies, namely backstepping and sliding mode, applied to a STATCOM based on a 5-level series multicell flying-capacitor converter, for dynamic reactive power compensation, voltage regulation, and power factor improvement in a low-voltage network. The control strategies were implemented to ensure accurate tracking of active and reactive currents as well as stable voltage regulation. The study showed that the connection or disconnection of inductive and capacitive loads, causing voltage sags or swells, can be effectively compensated by the STATCOM.

The STATCOM model and the two control strategies were implemented in MATLAB/Simulink. The simulation results demonstrated that both controllers can maintain a stable voltage at the PCC with a fast dynamic response of approximately 1 ms, due to the almost instantaneous injection or absorption of reactive power, even under network disturbances such as load variations, voltage sags, and swells. In addition, the THD of the PCC voltage remains well below the 5 % limit specified by the IEEE-519 standard, with values of 3.13 % for BSC and 4.44 % for SMC, showing that the BSC strategy achieves superior harmonic performance.

Future works should focus on experimental validation of these control strategies under real operating conditions, as well as on further optimization of dynamic performance and capacitor-voltage balancing.

Conflict of interest. The authors declare that they have no conflicts of interest.

REFERENCES

1. Asoodar M., Nahalparvari M., Zhang Y., Danielsson C., Nee H.-P., Blaabjerg F. Accurate Condition Monitoring of Semiconductor Devices in Cascaded H-Bridge Modular Multilevel Converters. *IEEE Transactions on Power Electronics*, 2023, vol. 38, no. 3, pp. 3870-3884. doi: https://doi.org/10.1109/TPEL.2022.3221285.

2. Carbonara A., Dambone Sessa S., L'Abbate A., Sanniti F., Chiumeo R. Comparison of Advanced Flexible Alternating Current Transmission System (FACTS) Devices with Conventional Technologies for Power System Stability Enhancement: An Updated Review. *Electronics*, 2024, vol. 13, no. 21, art. no. 4262. doi: https://doi.org/10.3390/electronics13214262.

3. Pires V.F., Cordeiro A., Foito D., Silva J.F. A Multilevel Converter Topology for a STATCOM System Based on Four-Leg Two-Level Inverters and Cascaded Scott Transformers. *IEEE Transactions on Power Delivery*, 2022, vol. 37, no. 3, pp. 1391-1402. doi: https://doi.org/10.1109/TPWRD.2021.3086399.

4. Sharma S., Gupta S., Zuhaib M., Bhuria V., Malik H., Almutairi A., Afthanorhan A., Hossaini M.A. A Comprehensive Review on STATCOM: Paradigm of Modeling, Control, Stability, Optimal Location, Integration, Application, and Installation. *IEEE Access*, 2024, vol. 12, pp. 2701-2729. doi: https://doi.org/10.1109/ACCESS.2023.3345216.

5. He C., Yang B., Luo Z., Liu G. Research on a New Topology and Reactive Power Compensation Application of Reinjection Multilevel Voltage Source Converter. *Applied Sciences*, 2024, vol. 14, no. 21, art. no. 9998. doi: https://doi.org/10.3390/app14219998.

6. Sharma H., Nanda H., Yadav A. Novel nine level switched capacitor multi-level inverter based STATCOM for distribution system. *Computers and Electrical Engineering*, 2024, vol. 120, art. no. 109647. doi: https://doi.org/10.1016/j.compeleceng.2024.109647.

7. Atanalian S., Sebaaly F., Zgheib R., Al-Haddad K. Z Packed U-Cell Modular Multilevel Converter for STATCOM Applications. *IEEE*

Access, 2025, vol. 13, pp. 78795-78807. doi: https://doi.org/10.1109/ACCESS.2025.3566015.
8. Heidari M., Kovsarian A., Seifossadat S.Gh. Power quality improvement with cascaded multilevel converter based STATCOM. *IIUM Engineering Journal*, 2018, vol. 19, no. 1, pp. 91-103. doi: https://doi.org/10.31436/iiumej.v19i1.873.
9. Hassan R.F., Shyaa S.S. Design and Analysis of the STATCOM Based on Diode Clamped Multilevel Converter Using Model Predictive Current Control Strategy. *European Journal of Electrical Engineering*, 2021, vol. 23, no. 3, pp. 221-228. doi: https://doi.org/10.18280/ejee.230306.
10. Neyshabouri Y., Chaudhary S.K., Teodorescu R., Sajadi R., Iman-Eini H. Improving the Reactive Current Compensation Capability of Cascaded H-Bridge Based STATCOM Under Unbalanced Grid Voltage. *IEEE Journal of Emerging and Selected Topics in Power Electronics*, 2020, vol. 8, no. 2, pp. 1466-1476. doi: https://doi.org/10.1109/JESTPE.2019.2916571.
11. Hasanzadeh S., Shojaeian H., Mohsenzadeh M.M., Heydarian-Forushani E., Alhelou H.H., Siano P. Power Quality Enhancement of the Distribution Network by Multilevel STATCOM-Compensated Based on Improved One-Cycle Controller. *IEEE Access*, 2022, vol. 10, pp. 50578-50588. doi: https://doi.org/10.1109/ACCESS.2022.3172144.
12. Cheng Q., Wang C., Chen Z. A Dual Modulation Waveform PWM Combined With Phase-Shifted Carriers in Stacked Multicell Converter. *IEEE Transactions on Power Electronics*, 2021, vol. 36, no. 12, pp. 14456-14465. doi: https://doi.org/10.1109/TPEL.2021.3088463.
13. Tebaldi D. An Approach to Control Multilevel Flying-Capacitor Converters Using Optimal Dynamic Programming Benchmark. *Electronics*, 2025, vol. 14, no. 5, art. no. 948. doi: https://doi.org/10.3390/electronics14050948.
14. Mersche S.C., Schwendemann R., Hiller M. Validation of the Quasi-Two-Level Operation for a Flying Capacitor Converter in Medium-Voltage Applications. *Energies*, 2023, vol. 16, no. 6, art. no. 2797. doi: https://doi.org/10.3390/en16062797.
15. Ebrahimi J., Esfahani F.N., Eren S., Bakhshai A. An Active Capacitor Voltage Balancing Method for a Four-Level Single Flying Capacitor Converter. *IECON 2024 - 50th Annual Conference of the IEEE Industrial Electronics Society*, 2024, pp. 1-6. doi: https://doi.org/10.1109/IECON55916.2024.10905229.
16. Laamiri S., Ghanes M., Santomenna G. Observer based direct control strategy for a multi-level three phase flying-capacitor inverter. *Control Engineering Practice*, 2019, vol. 86, pp. 155-165. doi: https://doi.org/10.1016/j.conengprac.2019.03.011.
17. Redouane A., Saou R., Oukaour A. Flying Capacitor Voltage Balancing Control Strategy Based on Logic-equations in Five Level ANPC Inverter. *Periodica Polytechnica Electrical Engineering and Computer Science*, 2023, vol. 67, no. 4, pp. 438-448. doi: https://doi.org/10.3311/PPee.21879.
18. Buso S., Rossetto L. Damping of Flying Capacitor Dynamics in Multi-Level Boost DC-DC Converters. *Electronics*, 2024, vol. 13, no. 24, art. no. 4883. doi: https://doi.org/10.3390/electronics13244883.
19. Ramakrishna E., Gadhamappagari J., Sujatha P. Auto tuning of PI Gains using Cuttlefish Optimization for DC Link Voltage Control in a 5-level HB MMC D-STATCOM. *Engineering, Technology & Applied Science Research*, 2023, vol. 13, no. 6, pp. 12086-12091. doi: https://doi.org/10.48084/etasr.6413.
20. Stepanov A., Saad H., Mahseredjian J. Modeling of MMC-based STATCOM with embedded energy storage for the simulation of electromagnetic transients. *Electric Power Systems Research*, 2023, vol. 220, art. no. 109316. doi: https://doi.org/10.1016/j.epsr.2023.109316.
21. Yu L., Wang G., Wu T., Zhu J., Booth C.D. Variable DC voltage based reactive power enhancement scheme for MMC-STATCOM. *IET Smart Grid*, 2024, vol. 7, no. 4, pp. 427-441. doi: https://doi.org/10.1049/stg2.12147.
22. Ahmed T., Waqar A., Elavarasan R.M., Imtiaz J., Premkumar M., Subramaniam U. Analysis of Fractional Order Sliding Mode Control in a D-STATCOM Integrated Power Distribution System. *IEEE Access*, 2021, vol. 9, pp. 70337-70352. doi: https://doi.org/10.1109/ACCESS.2021.3078608.
23. Boghdady T.A., Mohamed Y.A. Reactive power compensation using STATCOM in a PV grid connected system with a modified MPPT method. *Ain Shams Engineering Journal*, 2023, vol. 14, no. 8, art. no. 102060. doi: https://doi.org/10.1016/j.asej.2022.102060.
24. Freire D.F.M., Caseiro L.M.A., Mendes A.M.S. Model Predictive Control of a five-level Neutral-Point-Clamped STATCOM. *2019 IEEE International Conference on Industrial Technology (ICIT)*, 2019, pp. 1482-1487. doi: https://doi.org/10.1109/ICIT.2019.8755208.
25. Jin Y., Xiao Q., Jia H., Mu Y., Ji Y., Teodorescu R., Dragicevic T. A Dual-Layer Back-Stepping Control Method for Lyapunov Stability in Modular Multilevel Converter Based STATCOM. *IEEE Transactions on Industrial Electronics*, 2022, vol. 69, no. 3, pp. 2166-2179. doi: https://doi.org/10.1109/TIE.2021.3063973.
26. Djellad A., Belakehal S., Chenni R., Dekhane A. Reliability Improvement in Serial Multicellular Converters Based on STATCOM Control. *Journal Europeen des Systemes Automatises*, 2021, vol. 54, no. 4, pp. 519-528. doi: https://doi.org/10.18280/jesa.540401.
27. Bressan M.V., Rech C., Batschauer A.L. Design of flying capacitors for n-level FC and n-level SMC. *International Journal of Electrical Power & Energy Systems*, 2019, vol. 113, pp. 220-228. doi: https://doi.org/10.1016/j.ijepes.2019.05.030.
28. El Khlifi Y., El Magri A., Lajouad R., Bouattane O., Giri F. Output-feedback control of a grid-connected photovoltaic system based on a multilevel flying-capacitor inverter with power smoothing capability. *ISA Transactions*, 2024, vol. 147, pp. 360-381. doi: https://doi.org/10.1016/j.isatra.2024.02.007.
29. El Khlif Y., El Magri A., Lajouad R., Bouattane O. Hybrid feedback control of PMSG-based WECS with multilevel flying-capacitor inverter enhanced by fractional order extremum seeking. *E-Prime - Advances in Electrical Engineering, Electronics and Energy*, 2024, vol. 10, art. no. 100760. doi: https://doi.org/10.1016/j.prime.2024.100760.
30. Kerrouche K.D.E., Lodhi E., Kerrouche M.B., Wang L., Zhu F., Xiong G. Modeling and design of the improved D-STATCOM control for power distribution grid. *SN Applied Sciences*, 2020, vol. 2, no. 9, art. no. 1519. doi: https://doi.org/10.1007/s42452-020-03315-8.
31. Belila H., Boudjerda N., Boubakir A., Bahri I. Improved STATCOM efficiency using a hybrid technique based on sliding mode control and proportional integral control. *Przegląd Elektrotechniczny*, 2020, vol. 96, no. 10, pp. 156-162. doi: https://doi.org/10.15199/48.2020.10.29.
32. Mazouz F., Belkacem S., Boukhalfa G., Colak I. Backstepping Approach Based on Direct Power Control of a DFIG in WECS. *2021 10th International Conference on Renewable Energy Research and Application (ICRERA)*, 2021, pp. 198-202. doi: https://doi.org/10.1109/ICRERA52334.2021.9598599.
33. El Ouanjli N., Derouich A., El Ghzizal A., Bouchnaif J., El Mourabit Y., Taoussi M., Bossoufi B. Real-time implementation in dSPACE of DTC-backstepping for a doubly fed induction motor. *The European Physical Journal Plus*, 2019, vol. 134, no. 11, art. no. 566. doi: https://doi.org/10.1140/epjp/i2019-12961-x.
34. Vijaya Sambhavi Y., Vijayapriya R. Phase disposition PWM control topology based: A novel multilevel inverter with reduced switch for power electronics applications. *Heliyon*, 2024, vol. 10, no. 21, art. no. e39856. doi: https://doi.org/10.1016/j.heliyon.2024.e39856.
35. Oghorada O.J.K., Zhang L., Esan B.A., Dickson E. Carrier-based sinusoidal pulse-width modulation techniques for flying capacitor modular multi-level cascaded converter. *Heliyon*, 2019, vol. 5, no. 12, art. no. e03022. doi: https://doi.org/10.1016/j.heliyon.2019.e03022.
36. Deniz E., Tuncer S., Gençoglu M.T. Voltage regulation in a distribution system by using STATCOM with three-level diode clamped inverter. *Proceedings of the 5th International Advanced Technologies Symposium*, 2009, pp. 1036-1042.

Received 24.10.2025
Accepted 28.11.2025
Published 02.03.2026

S. Belakehal [1]*, PhD, Associate Professor,*
M.L. Srief [1]*, PhD Student,*
[1] Laboratory of Electrical Engineering – Constantine LGEC, Department of Electrical Engineering,
Mentouri Brothers University, Constantine, 25000, Algeria,
e-mail: belakehal.soltane@umc.edu.dz (Corresponding Author); mohamedlaminesrief@gmail.com

How to cite this article:
Belakehal S., Srief M.L. Comparative performance analysis of backstepping and sliding mode control for static synchronous compensators based on flying capacitor multicell converters. *Electrical Engineering & Electromechanics*, 2026, no. 2, pp. 22-30. doi: https://doi.org/10.20998/2074-272X.2026.2.04

UDC 621.311 https://doi.org/10.20998/2074-272X.2026.2.05

M. Kamal, M.F. Ullah, N. Anwar, A.I. Hussein

Optimizing residential energy usage patterns in smart grids using hybrid metaheuristic techniques

Introduction. *This study applies hybrid metaheuristic optimization techniques to intelligently schedule household loads, ensuring a balance between cost reduction, comfort and grid stability in smart homes.* ***Problem.*** *The growing gap between energy demand and supply leads to high electricity costs, increased appliance waiting times, a higher peak-to-average ratio (PAR) and reduced user comfort. Efficient management of residential energy consumption remains a major challenge for sustainable smart grid operation.* ***Goal.*** *This study aims to minimize electricity costs, reduce PAR and enhance user comfort by optimally scheduling household appliances and shifting loads from peak hours to off-peak hours.* ***Methodology.*** *A demand-side management approach is implemented using 5 metaheuristic optimization algorithms: harmony search algorithm (HSA), flower pollination algorithm (FPA), hybrid harmony flower pollination algorithm (HFPA), multiverse optimization algorithm (MVO) and cuckoo search algorithm (CSA). Real-time pricing is employed as the pricing model. MATLAB simulations were conducted for 10, 30 and 50 smart homes, each comprising 15 residential loads categorized as controllable or base appliances.* ***Results.*** *Simulation results demonstrate that the proposed HFPA consistently outperforms HSA, FPA, MVO and CSA across all tested scenarios, achieving notable reductions in electricity cost and PAR while minimizing appliance waiting times.* ***Scientific novelty****. The hybrid HFPA effectively combines the strengths of HSA and FPA, balancing exploration and exploitation to deliver superior performance in multi-objective optimization for home energy management systems.* ***Practical value.*** *The proposed HFPA achieved up to 19.86 % reduction in electricity cost and 81.03 % minimization in PAR, significantly enhancing user comfort and operational efficiency. The method can be further extended for integration with renewable energy sources and machine learning-based predictive control systems.* References 32, tables 6, figures 5.

Key words: **home energy management system, energy consumption pattern, meta-heuristic optimization, hybrid optimization technique, demand side management.**

Вступ*. У роботі застосовуються гібридні метаевристичні методи оптимізації для інтелектуального планування навантаження побутових приладів, що забезпечують баланс між зниженням витрат, комфортом та стабільністю мережі у «розумних» будинках.* ***Проблема****. Зростання розриву між попитом і пропозицією енергії призводить до високих витрат на електроенергію, збільшення часу очікування приладів, підвищення відношення пікового навантаження до середнього (PAR) і зниження комфорту користувачів. Ефективне управління споживанням енергії у житлових будинках залишається серйозною проблемою для сталої роботи «розумної» мережі.* ***Мета****. Дане дослідження спрямоване на мінімізацію витрат на електроенергію, зниження PAR та підвищення комфорту користувачів шляхом оптимального планування роботи побутових приладів та перенесення навантаження з пікових годинників на непікові.* ***Методика****. Реалізовано підхід до управління попитом з використанням 5 метаевристичних алгоритмів оптимізації: алгоритму пошуку гармонії (HSA), алгоритму квіткового запилення (FPA), гібридного гармонійного алгоритму квіткового запилення (HFPA), алгоритму оптимізації мультивсесвіту (MVO) та алгоритму пошуку зозулі (CSA). У якості моделі ціноутворення використовується ціноутворення у режимі реального часу. Проведено симуляції у MATLAB для 10, 30 та 50 «розумних будинків», кожен з яких включав 15 побутових навантажень, класифікованих як керовані чи базові прилади.* ***Результати*** *моделювання показують, що запропонований HFPA перевершує HSA, FPA, MVO та CSA у всіх протестованих сценаріях, досягаючи помітного зниження витрат на електроенергію та PAR за мінімізації часу очікування приладів.* ***Наукова новизна****. Гібридний HFPA ефективно поєднує у собі переваги HSA та FPA, балансуючи дослідження та використання для забезпечення високої продуктивності у багатоцільовій оптимізації систем управління енергоспоживанням у будинку.* ***Практична значимість****. Запропонований HFPA дозволяє знизити витрати на електроенергію до 19,86 % та мінімізувати PAR на 81,03 %, значно підвищивши комфорт користувача та ефективність роботи. Метод може бути додатково розширено для інтеграції з відновлюваними джерелами енергії та системами прогнозуючого керування на основі машинного навчання.* Бібл. 32, табл. 6, рис. 5.

Ключові слова: **система керування енергоспоживанням у будинку, структура енергоспоживання, метаевристична оптимізація, гібридний метод оптимізації, керування попитом.**

Introduction. The rapid growth in global power demand, driven by technological advancements, highlights the urgent need for efficient energy management. Traditional electricity networks are increasingly unable to meet these growing needs, prompting the development of a new concept known as the Smart Grid. Smart Grid integrates cutting-edge components such as smart devices, clean energy sources, smart meters, and energy-saving appliances. Smart meters, for example, are used to monitor energy flow importing, exporting, or both. They are also critical in ensuring communication between customers and utilities, offering efficient, reliable, cost-effective, and dynamically controllable energy solutions [1, 2].

Many demand-side management (DSM) solutions have been suggested in the literature to optimize power consumption patterns by shifting loads on a priority basis, reducing loads to off-peak levels, and filling valleys by utilizing energy during low-demand periods. These approaches help balance supply and demand effectively [3]. The objectives of DSM techniques are to minimize electricity cost, energy consumption, and the peak-to-average ratio (PAR). Demand response programs, which play a pivotal role in DSM, encourage customers to modify their power consumption habits depending on price signals. Demand response is typically classified into 2 types: price-based and incentive-based programs, both aiming to induce energy-efficient behaviors [3, 4]. For example, users shifting their loads during off-peak hours benefit from lower power bills, increasing user satisfaction.

The major objectives of electricity management include lowering PAR, electricity costs, and energy use, along with the integration of renewable energy sources. To fulfill these objectives, several DSM strategies have been devised; some involving scheduling algorithms that optimize demand through demand response programs. These initiatives use smart appliances, smart metering infrastructure, and two-way communication to ensure effective energy use in multiple load sectors such as homes, plazas, towns, cities, and industries. Dynamic pricing systems also play a vital role: real-time pricing (RTP) provides current data and prices; variable peak pricing manages multiple peak periods; and time-of-use pricing accounts for devices operating at different times [4, 5].

Given that residential areas contribute significantly to overall energy consumption, this research focuses on optimizing the usage of smart appliances in single and multiple homes. Appliances are categorized as controllable or base appliances to facilitate effective scheduling.

The main challenges in Smart Grid include minimization of energy consumption, electricity bill reduction, PAR reduction, minimization of waiting time (equivalent to maximizing user comfort), and renewable energy source integration. Several heuristic and mathematical approaches have been proposed to address these optimization challenges. Most crucially, waiting time – used as a proxy for user comfort is often overlooked in efforts to mitigate rising power expenses. Furthermore, the unpredictable nature of consumer demand complicates optimal scheduling at the residential level. DSM also faces challenges such as communication, load shifting, security and privacy, and fairness. To address these limitations, various meta-heuristic optimization strategies have been applied. Previous studies have employed binary particle swarm optimization (BPSO), genetic algorithm (GA), bacterial foraging optimization (BFOA), wind-driven optimization (WDO) and hybrid methods such as GA–BPSO.

This study **aims** to minimize electricity costs, reduce PAR, and enhance user comfort by optimally scheduling household appliances and shifting loads from peak hours to off-peak hours. To accomplish these aims, 5 metaheuristic optimization algorithms are implemented to optimally shift household loads from peak hours to off-peak hours within a smart grid environment: harmony search algorithm (HSA), flower pollination algorithm (FPA), hybrid harmony flower pollination algorithm (HFPA), multiverse optimization algorithm (MVO) and cuckoo search algorithm (CSA).

Analysis of the related work. In recent years, a variety of optimization strategies have been presented to enhance Smart Grid optimization utilizing DSM and demand response. Cost minimization, PAR reduction, and load optimization have always been the primary objectives for achieving an ideal solution. In this part, a literature review on various optimization strategies is presented. In [6], the authors proposed an empirical pattern and real-time mutli-period artificial bee colony (MABC) technique type cardinal electrical power management scheme for home microgrids to maximize system overall performance and decrease power expenditures. To regulate unit pricing in real time, this system employs real-time scheduling in conjunction with day-ahead scheduling points, as well as a localized energy marketplace structure based on single-side auctioneer. The recommended approach's performance is compared to that of the mixed integer non-linear programming (MINLP) method. The results show a considerable increase in efficiency and accuracy across a variety of circumstances. An experimental approach to energy management systems (EnMS), focusing on reducing energy consumption through advanced techniques is discussed in [7].

EnMS is a technique created by UNIDO that is used to minimize greenhouse gas emissions [8] into the environment by conserving energy. This strategy would be used for commercial and office buildings that utilize a lot of power on a regular basis. Simulation and results indicate that installing EnMS can cut power usage by up to 30 %. The distributed optimization algorithm for microgrids energy management (MEM-DOA) was first put out in [9]. The authors of this paper contend that the contributions of distributed energy generation and distributed energy storage to DSM cannot be overestimated. A DSM-connected grid consists of large-scale central energy storage, electric vehicles, and a variety of smart consumers, both active and passive. MEM-DOA is being implemented by the authors according to the type of customer. According to the results, the suggested approach is more successful in reducing PAR, power costs, and user comfort. The authors [10] presented a hybrid method for residential area load scheduling called teaching learning genetic optimization (TLGO), which blends the teaching learning-based optimization (TLBO) algorithm with GA.

In [11] was proposed a metaheuristic optimization strategy for residential areas. This study work employs 3 metaheuristic optimization techniques: tabu search algorithm, particle swarm optimization (PSO) and simulated annealing. The authors of [12] describe a home energy management system (HEMS) that is based on 4 heuristic algorithms: WDO, GA, BFOA and BPSO. Additionally, a hybrid method called genetic BPSO (GBPSO) is suggested. The RTP model is used to get updated time base prices of energy units for load optimization. The simulation and findings illustrate that GA out runs in PAR, BPSO outruns in cost minimization, and GBPSO out runs in cost and PAR reduction. Based on the RTP price structure, work [13] suggests a simple DSM model for residential clients. It seeks to lower electricity bills, PAR and appliance wait times. The GA heuristic technique is used in this study. The authors explore 2 test systems for validation of simulation results, one is of one user or home and other one is 20 users. The results show that the proposed system perform well in both cases. A heuristic-based evolutionary method has been developed in [14] with the primary goal to minimize electricity costs and PAR. In this research, the authors look at 3 sorts of users: residential load, industrial load and commercial load. The results demonstrate that the suggested method can handle several types of devices and achieves the desired PAR and cost.

The authors proposed a successful DSM paradigm for residential areas in [15]. The authors employ 2 pricing methods, time-of-use and inclining block rate and 3 optimization approaches: GA, ant colony optimization (ACO) algorithm and BPSO. The results of the study illustrated that GA outperform from ACO and BPSO in cost and PAR minimization. In [16], employs consumer demand response with dynamic price rates. The goal of this strategy is to enhance the user experience by shift the loads from high demand period to low demand period. The authors provide self-organizing home energy networks that are controlled by appliance control interfaces and interact with smart appliances. In [17], the authors provide a real-time information-based energy management system for balancing the household load in microgrid. For this objective, the authors employ GA to reduce power costs while increasing user comfort. In this study, daily utilizing loads are divided into 5 categories: elastic, inelastic, thermostatically controlled, user aware, and normally used loads. The results reveal that the proposed algorithms lowered costs by up to 22.63 % and reduced PAR by up to 22.77 %. The authors employ RTP to encourage consumers to engage in load scheduling [18]. The authors employ an intelligent decision support system (IDSS) for load scheduling. High-performance scheduling is used to establish time of use pricing, on/off peak pricing, RTP, two-tier pricing and combinations of the above.

In [19], a multi-objective optimization framework is suggested for the optimized operation of a stand-alone combined cooling, heating, and power microgrid. The study employs a modified chaos particle swarm optimization (MCPSO) algorithm to enhance convergence speed and search performance for complex optimization

problems. In [20] was proposed a strategy to tackle global warming and increasing carbon emissions. The authors assess their goal by utilizing GA, effective differential evolution (EDE), the suggested improved differential teaching learning algorithm, and the TLBO method to control energy usage and user comfort. The authors of this study utilize RTP. For the HEMS in DSM, the authors [21] proposed a heuristic optimization method. For residential load control, this study employs the conventional dynamic programming approach in addition to 2 heuristic optimization techniques: GA and BPSO. In [22], the authors suggest a realistic scheduling mechanism (RSM) to cut power costs and achieve equilibrium amongst appliance utilities. In this study, the authors suggest a BPSO-based optimization approach to cut power costs and improve user pleasure. PAR is ignored in this article. Table 1 gives a summary of the most recent study, including the research purpose, recommended methodology, and constraints.

Table 1

Review of the most recent research

References	Techniques	Objectives	Limitations
Energy management systems for smart hybrid home [6]	MABC, MINLP	Cost, PAR reduction, user comfort	Increased system complexity
Energy management system on energy efficiency [7]	EnMS	Cost reduction and maximize user comfort	PAR is neglected
Distributed optimization algorithm for DSM [9]	MEM-DOA	Cost, PAR reduction	User comfort is ignored
Intelligent hybrid heuristic approach for smart metering [10]	GA, TLBO, TLGO	Cost and user comfort	PAR not considered, Increased complexity
Metaheuristic optimization techniques for residential energy management [11]	PSO, simulated annealing, tabu search	Cost, PAR reduction, user comfort	Increased system complexity
Heuristic algorithm based HEMS [12]	GA, BPSO, BFOA, WDO, GBPSO	Cost and PAR reduction	Increased system complexity
An improved system architecture for optimal DSM [13]	GA	Cost reduction	PAR is ignored
DSM of smart grid [14]	Heuristic based evolutionary algorithm	Cost reduction and minimization of PAR	Waiting time is ignored
Using heuristic methods to optimize energy management [15]	GA, BPSO, ACO	Reduce cost, PAR, execution time, and improve user comfort.	Increased system complexity
An intelligent HEMS to improve demand response [16]	ANFIS predictor	Energy consumption	User comfort is ignored
Real-time information-driven energy management [17]	GA	Minimize power costs while increasing user comfort	PAR not considered, increased complexity
Heuristic optimization of consumer electricity costs [18]	IDSS	Minimize electricity cost and execution time	PAR and user comfort is ignored
MCPSO based optimized operation model [19]	PSO, MCPSO	Convergence speed, environmental benefit	Increase system complexity
DSM in nearly zero energy buildings [20]	GA, EDE, TLBO	User comfort and energy consumption	PAR is neglected
Hybrid optimization for residential load [21]	BPSO, GA	Maximize user comfort, minimize electricity cost	PAR not considered
RSM for smart houses [22]	BPSO, RSM	Electricity cost and user comfort	PAR is neglected

System model. Energy management and end-user demand-side control are the two main goals of DSM, which increase its efficiency and dependability. Smart devices such as energy management controllers (EnMCs) and smart meters are installed in every smart home to facilitate consistent and reliable bidirectional communication between consumers and utilities. The EnMC receives data from sensors, storage devices, local generation, and all electrical equipment. Smart meter sends pricing signals to the EnMC after receiving them from the utility. After that, the EnMC organizes appliance data according to the utility's price signal. Smart meter and utilities can connect via wired protocols or wireless systems such as Z-Wave and ZigBee. All electric loads, EnMCs and smart meters interact over a home area network. This paper examined single and multiple homes equipped with 15 appliances. In the energy pricing model, the RTP tariff is used to generate an electricity bill. To achieve the aforementioned aims, operating time interval (OTI) of 5 min, 30 min and 1 hour are employed. A 1-hour time slot is broken into 12 equal-sized sub-time slots, each of which lasts 5 min. Because many appliances last less than an 1 hour, the remaining operating time of the appliance is squandered. As a result, a 5-min time interval saves power and makes the system more resilient than a 30-min or 1-hour OTI.

Load categorization. Load appliances are categorized according to their power consumption into 2 main classes: non-controllable appliances and base appliances. Figure 1 shows the model of the proposed system and Table 2 shows the parameters of all appliances. Burst load appliances are another name for non-controllable appliances. The time slots of these appliances can be adjusted to any available slot. It is impossible to change the equipment's overall running time or energy consumption pattern. These appliances can not be shut off once they are switched on. Examples of these items are a washing machine and a fabric dryer. Base appliances are also known as fixed appliances. The total operating duration and energy consumption pattern of these appliances cannot be altered. If the user wants to switch on these appliances at any time, they must do so during the specified time frame.

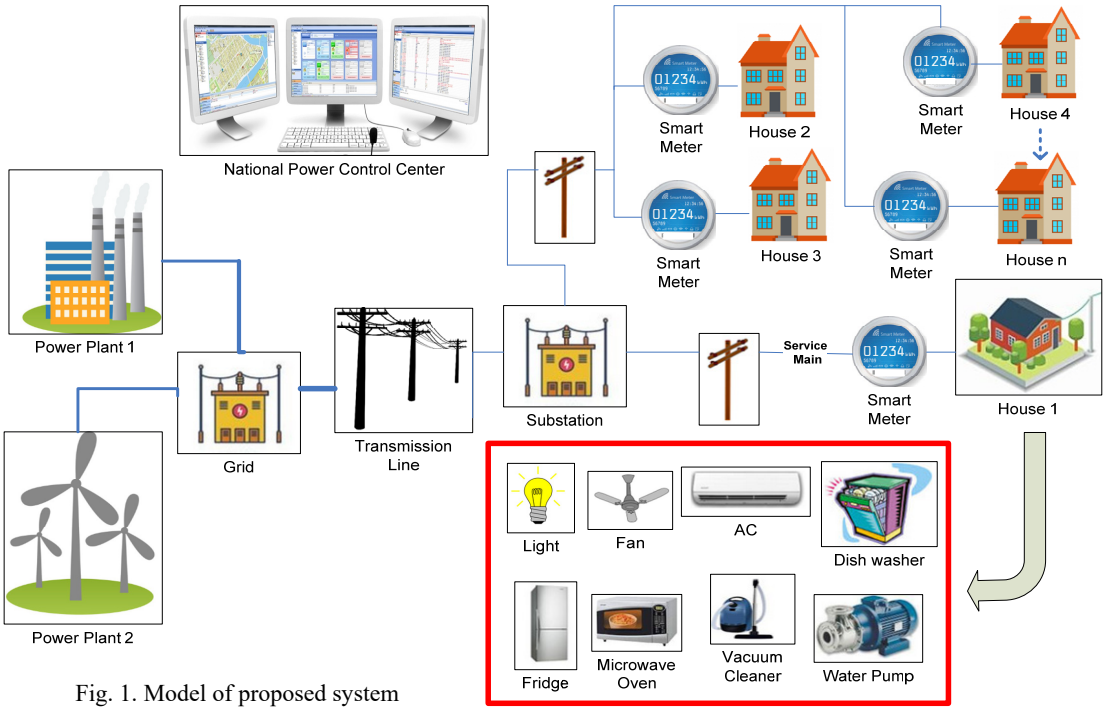

Fig. 1. Model of proposed system

Table 2

Parameters of appliances

Appliances	LOT*, slots	PR*, kW	Category
Washing machine	18	2	Non-controllable
Cloth dryer	10	2	Non-controllable
Dish washer	20	0.5	Non-controllable
Hair dryer	3	1.8	Base
Toaster	2	0.8	Base
Kettle	2	2	Base
Phone	288	0.005	Base
Computer	24	0.15	Base
Hair straighter	2	0.055	Base
Oven	13	2.4	Base
Cooker hood	13	0.225	Base
Iron	6	2.4	Base
Light	90	0.1	Base
Refrigerator	288	1.67	Base
Television	158	0.083	Base

*LOT – length of operation time (time slots); PR – power rating (kW).

Price model. Power prices are determined by the utility and power costs are calculated accordingly. Different dynamic methods are employed to reduce power costs and the PAR levels. These dynamic methods incentivize customers to shift large loads from peak to off-peak hours. Time-of-use, inclining block rate, critical peak pricing, day-ahead pricing and RTP are all included in dynamic pricing plans. In this study, RTP is used to calculate power bills. RTP-based power pricing can fluctuate as frequently as once per hour. Price signals in RTP may vary between time slots, whereas other pricing methods remain consistent for each time slot.

Mathematical formulation of the problem. The HEMS problem is formulated as a multi-objective optimization problem. The goal is to determine the optimal control of household appliances, energy storage units and distributed generation sources to minimize energy cost and PAR, while maintaining acceptable waiting time and maximizing user satisfaction.

The **objective function** can be expressed as a weighted sum of multiple objectives:

$$F_{\min} = \alpha_1 \cdot C_{tot} + \alpha_2 \cdot PAR + \alpha_3 \cdot W_t - \alpha_4 \cdot U_s, \quad (1)$$

where C_{tot} is the total energy cost; PAR is the peak-to-average ratio of power demand; W_t is the total waiting time, hrs; U_s is the user satisfaction index (0–1); α_1 – α_4 are the weighting coefficients representing the priority of each objectives.

The **cost of energy consumption** is calculated as:

$$C_{tot} = \sum_{t=1}^{T} \gamma(t) \cdot E_{grid}(t), \quad (2)$$

where $\gamma(t)$ is the electricity price at time t (time of use tariff); $E_{grid}(t)$ is the energy purchased from the grid at time t.

The **energy balance constraint** is expressed as:

$$\sum_{h1}^{H} P_h(t) = E_{grid}(t) + E_{DG}(t) + E_{bat}(t), \quad (3)$$

where $P_h(t)$ is the power demand of home appliance h at time t; $E_{grid}(t) + E_{DG}(t) + E_{bat}(t)$ is the combination of grid, local generation and storage.

PAR reduction. The PAR is defined as:

$$PAR = \frac{\max_t \left(\sum_{h1}^{H} P_h(t) \cdot x_h(t) \right)}{\frac{1}{T} \sum_{t=1}^{T} \left(\sum_{h1}^{H} P_h(t) \cdot x_h(t) \right)}, \quad (4)$$

where $x_h(t)$ is the binary control variable (ON/OFF status of appliance h).

Waiting time constraint. If an appliance h is deferred by d_h hours, then:

$$W_t = \sum_{h=1}^{H} d_h . \quad (5)$$

Proposed approaches. HSA. In this work, the heuristic algorithm HSA is applied to achieve the objectives. In 2001, this algorithm was proposed by Prof. Zong Woo Geem. The HSA is motivated by musicians' improvisations to establish harmony in their works [23]. It is based on 3 primary components: harmony memory, harmony memory consideration and pitch correction. Initially, a harmony memory is created with potential solutions. During each cycle, a new solution is generated by either selecting values from the harmony memory or generating new ones using

pitch adjustment and a randomization factor. New harmony is tested using a fitness function, and if it outperforms the poorest solution in the harmony memory, it replaces it. This iterative procedure is repeated until an optimal or satisfactory solution is found, making HSA suitable for addressing complex optimization issues [24].

Steps of HSA are next:

```
Initialize all the algorithm parameters
Generate starting harmoniousness memory
Measure the fitness of starting generated memory
for x = 1 : H do
    for itr = 1 : Maximum.iterations do
        Improvise new harmony vector newh
        for y = 1 : 12 do
            if rand() < HMCR then
                Choose value from harmoniousness memory
                if rand() < PAR then
                    Tune the value
                end if
            else
                Select a random value
            end if
        end for
    end for
    Perform selection process
    Compare newh with worst harmony Xworst
    if f(xnew) < f(xworst) then
        xworst = xnew
    else
        Keep the existing value
    end if
end for
```

FPA is inspired by the pollination process in flowering plants [25]. It uses 2 modes of pollination: global and local. In global pollination, solutions are updated by considering the best solution and a Lévy flight-based random walk. In local pollination, neighboring solutions are combined to create new candidate solutions. The transition between global and local pollination is controlled by a switch probability parameter. FPA mimics the natural foraging and pollination behaviors of insects to effectively explore and exploit the solution space, making it a robust approach for optimization tasks. The most recent nature-inspired algorithm is FPA, which is based on the pollination process of plants. Flowering plants' flower pollination technique led Xin-She Yang to develop FPA in 2012. FPA is primarily used to address both constrained and unconstrained optimization issues. The primary advantages of FPA that interest researchers are its processing speed, resilience and simplicity of modification based on requirements [26]. The 4 rules listed below are used for simplicity of reference.

1) Biotic and cross-pollination are considered global pollination processes; pollen is carried by pollinators in a manner consistent with Lévy flights.

2) Local pollination involves abiotic pollination and self-pollination.

3) Pollinators, like insects, contribute to the likelihood of reproduction based on the matching of two flowers.

4) The interplay of local and global pollination may be regulated by a switch probability p [0, 1], which is somewhat biased in favor of local pollination. The algorithm 2 depicts the entire FPA process.

Steps of FPA are next:

```
for x = 1 − population.size do
    for y = 1 − loads do
        Generate a random population
        Calculate F = fitness function
        if F()F(i−1)||load(t) < unscheduledload(t) then
            F(i) = F(i)
            if (va using (4) – (ha < ta) then
                Load is ON
            else
                wait until Low demand period (off-peak hours)
            end if
        else
            F(i) = F(i − 1)
        end if
    end for
end for
for z = 1 − MaxItr do
    Generate random flowers (population)
    for m = 1 : appliances do
        if rand > ProbabilitySwitch then
            use levy flight to update solution
        else
            select random population
            check simple bounds
        end if
    end for
    Evaluate new solution
    if Fnew < Fold then
        update the solution using new fitness values
    end update the global best
end Return best solution
```

HFPA is a hybrid optimization technique combining the strengths of HSA and FPA [27]. It utilizes the harmony memory concept of HSA to generate and refine solutions in the early phases and uses the global and local pollination concepts of FPA to make better use of the solution exploration and exploitation. Such hybridization will be used to strike a balance between convergence speed and solution space diversity. The incorporation of these 2 methodologies has resulted in better performance of HFPA in terms of computational efficiency and solution quality, and makes HFPA effective in dealing with complex optimization problems [28].

Steps of HFPA are next:

```
Initialize all the parameters
Generate initial harmoniousness memory
for x = 1 − MaxItr do
    Generate random flowers (population)
    for m = 1: appliances do
        if rand > P robabilitySwitch then
            use levy flight to update solution
        else
            select random population
            check simple bounds
        end if
    end for
    Evaluate new solution
    Perform selection
    Compare new solution with worst harmony
    if (xnew) < f(xworst) then
        xworst = xnew
    else
        Keep existing
    end if update the global best
end for Return best solution
```

The suggested hybrid algorithm HFPA employs FPA in initializing the population of n flowers or pollen

gametes with random solutions. A *d*-dimensional step vector *L* is drawn from a Lévy distribution, then the new solutions are compared to the worst harmony vectors.

MVO algorithm is inspired by such concepts as the multiverse theory [29]. It applies the theory of white holes, black holes and wormholes to explore and exploit the processes of optimization. White holes represent solutions that are being found and carry positive characteristics with the previous but black holes represent the substitution of unwanted solutions with better solutions. Wormholes lead to random modifications in solutions and this keeps the space of search diverse. It uses dynamic exploration and exploitation to dynamically balance between them to optimally converge upon the best solution and, therefore, it can be applied to a broad class of optimization problems [30].

Steps of MVO algorithm are next:

```
Initialize all parameters
Generate initial population of universes
Evaluate fitness of each universe
for i = 1 : T do
    for itr = 1 : Max.iterations do
    Sort universes based on fitness
    Normalize inflation rates
        for j = 1 : N do
            if rand() < WEP then
            Perform white hole tunneling
        else
            Perform wormhole existence
            probability adjustment
        end if
    end for
    end for
    Perform selection
    Compare new universe with worst universe
    Xworst
    if f(Xnew) < f(Xworst) then
        Xworst = Xnew
    else
        Keep existing
    end if
end for
```

CSA is a bio inspired optimization algorithm that emulates the collaborative foraging process of cuckoo birds [31]. The techniques employed by the algorithm include selection of nest, egg-laying area and finding of prey. Cuckoo eggs are solutions that might be good, and the algorithm repeats the process of replacing the old with a better one as it searches through the cuckoo eggs. It utilizes search mechanisms such as global and local search in maintaining diversity combined with speed in approaching convergence. The flexible characteristic of the method defines its applicability in addressing non-linear as well as multidimensional optimization [32].

Steps of CSA are next:

```
Initialize all parameters
Generate initial population
Evaluate fitness of each individual
for i = 1 : T do
    for itr = 1 : Max.iterations do
    Sort universes based on fitness
    Select the best individuals
        for j = 1 : N do
            if rand() < Pm then
            Perform mutation
        else
            Perform local search
        end if
    end for
    end for
    Perform selection
    Compare new universe with worst universe
    Xworst
    if f(Xnew) < f(Xworst) then
        Xworst = Xnew
    else
        Keep existing
    end if
end for
```

Simulation and results. This section evaluates the performance of the suggested approach using MATLAB simulations with the RTP scheme. The algorithm's efficacy is evaluated using measures such as power cost, energy usage, PAR reduction and user satisfaction. The simulation scenario includes single and multiple households, each with 15 appliances divided into 2 categories: non-controllable and base appliances.

Figure 2 depicts the power cost of the simulated algorithm for single and multiple homes, as determined during the scheduling process. It also shows the electricity cost of HAS, FPA, HFPA, MVO and CSA, which is less than the unplanned cost. The comparative data is provided in Table 3. The results demonstrate that the hybrid approach of HFPA and MVO outperforms than the other strategies in terms of cost in all scenarios.

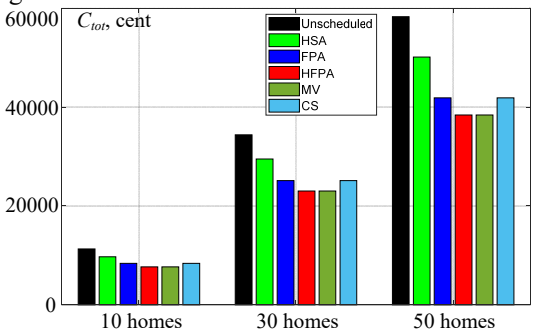

Fig. 2. Total cost against different OTIs

Table 3

Cost comparison of single home for different OTIs

OTI	Parameters	Unscheduled	HSA	FPA	HFPA	MVO	CSA
5-min	Cost, cent	71.09	66.577	65.14	61.647	63.134	64.98
	Difference	–	4.513	5.95	9.443	7.956	6.11
	Efficiency, %	–	6.34	8.36	13.28	11.19	8.59
30-min	Cost, cent	480.822	420.614	408.977	386.912	390.883	407.214
	Difference	–	60.207	71.844	93.909	89.939	73.608
	Efficiency, %	–	12.53	14.94	19.54	18.70	15.31
1-hour	Cost, cent	963.304	847.751	836.283	771.988	793.218	835.012
	Difference	–	115.552	127.021	191.313	170.086	128.292
	Efficiency, %	–	11.99	13.59	19.86	17.65	13.31

The reduction of PAR is beneficial to both utilities and consumers. During the scheduling process, if PAR increases, then the cost also increases, and if PAR is reduced, then the electricity cost decreases. The PAR performance of HSA, FPA, HFPA, MVO and CSA is listed in Table 4 for all OTIs. It is shown that PAR is reduced compared to the unscheduled case. Result shows (Fig. 3) that HFPA and MVO perform better in all OTIs compared to CSA, HSA and FPA.

Table 4 compares the PAR for different optimization techniques. HFPA stands out by significantly reducing PAR, particularly in the 30-min interval, where it achieves an efficiency improvement of 81.03 %. This demonstrates how HFPA reduces power consumption while maintaining system performance. The results complement this by showing the efficiency levels of the optimization techniques over time. It highlights that HFPA and MVO maintain higher efficiency across all time intervals, with particularly strong performance in the 1-hour interval. These results underscore the effectiveness of HFPA and MVO in reducing power consumption and ensuring high efficiency over extended periods.

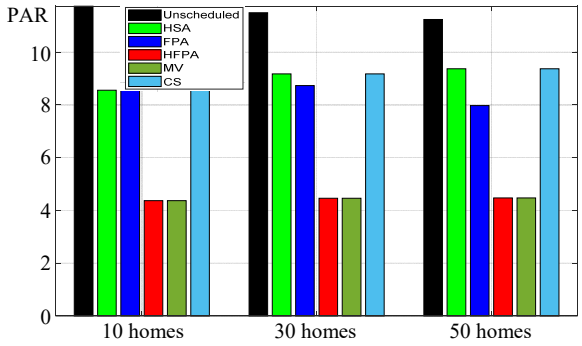

Fig. 3. PAR against different OTIs

Table 4

PAR comparison of single home for different OTIs

OTI	Parameters	Unscheduled	HSA	FPA	HFPA	MVO	CSA
5-min	PAR	16.204	7.8312	7.9717	3.4293	5.4567	7.6243
	Difference	–	8.3728	8.2323	12.7747	10.7473	8.5797
	Efficiency, %	–	51.67	50.8	78.83	66.32	52.94
30-min	PAR	14.421	6.2447	5.3035	2.7345	4.4155	5.0005
	Difference	–	8.1763	9.1175	11.6865	10.0055	9.4205
	Efficiency, %	–	56.69	63.22	81.03	69.38	65.32
1-hour	PAR	8.0991	5.2407	5.3035	2.7345	3.5535	5.1545
	Difference	–	2.8584	2.7956	5.3646	4.5456	2.9446
	Efficiency, %	–	35.29	34.51	66.23	56.12	36.36

The waiting time and electricity cost both affect user comfort. In this case, waiting time is used to gauge consumer comfort. Customers must use the most energy-efficient appliance schedule in order to reduce their power costs. Power costs and user comfort are a trade-off; if customers value comfort more than power costs, they will have to pay more for electricity. Power costs and user comfort are inversely related.

Figure 4 shows the average waiting time for HSA, FPA, HFPA, MVO and CSA. These results show that waiting time is reduced compared to unplanned cases. The results show that HFPA and MVO perform better in all OTIs than CSA, HSA, and FPA.

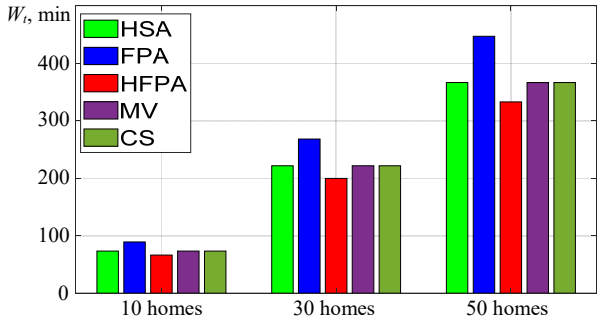

Fig. 4. The average waiting time for different OTIs

Table 5 compares the waiting times for each optimization technique across the 3 OTIs. HFPA achieves the lowest waiting times, particularly in the 1-hour interval, where the waiting time is reduced to just 7 min. This demonstrates HFPA's ability to enhance system responsiveness.

Table 5

Waiting time comparison of single home for different OTIs

Parameter	OTI	HSA	FPA	HFPA	MVO	CSA
Waiting time	5-min	115	110	102	105	108
	30-min	23	20	18	19	21
	1-hour	9	7.5	7	7.5	8.2

Comparison of techniques. HFPA emerges as the best choice because it offers excellent performance across all 3 criteria (cost, waiting time and PAR). It effectively handles the interdependencies between multiple homes, optimizing energy sharing and scheduling. Its hybrid nature makes it adaptable to multi-objective problems common in multi-home systems. The MVO is a close second because it performs well in dynamic, highly interconnected environments where energy demands fluctuate significantly. However, its computational complexity may be a limitation for very large-scale systems.

Figure 5 shows a comparison of the proposed algorithms for all constraints. Table 6 shows a comparison of algorithms for HEMS for multiple homes.

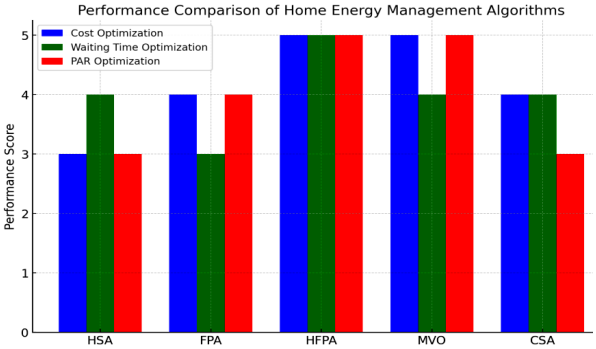

Fig. 5. Comparison of proposed algorithms for all constraints

Table 6

Comparison of algorithms for HEMS for multiple homes

Algorithm	Cost optimization	Waiting time optimization	PAR optimization	Strengths	Weaknesses	Suitability
HSA	Moderate	Good	Moderate	Simple algorithm, computationally efficient for small-scale systems	Limited global optimization capabilities, struggles with interdependencies between homes	Better for simpler, independent multi-home systems with less complex constraints
FPA	Good	Moderate	Good	Balances local and global optimization, effective for multiple objectives	May struggle with dynamic changes in load-sharing and inter-home dependencies	Suitable for moderately interconnected multi-home systems with predictable energy patterns
HFPA	Excellent	Excellent	Excellent	Combines the strengths of HSA and FPA, handles interdependencies effectively	Computationally demanding, requires more resources	Ideal for highly interconnected systems requiring robust optimization for cost, waiting time and PAR
MVO	Excellent	Good	Excellent	Excels in handling dynamic and interdependent systems, adaptable to changes in energy demand	High computational complexity, slower convergence for very large-scale systems	Suitable for complex and highly dynamic multi-home systems, especially with fluctuating demands
CSA	Good	Good	Moderate	Fast convergence, effective for systems with straightforward optimization needs	Less capable of handling complex interdependencies and dynamic energy management	Best for smaller-scale multi-home systems with limited interaction between homes

Conclusions. The introduction of smart grids has enabled considerable advances in energy system optimization, notably through the use of HEMS in smart homes. Effective energy management in these contexts requires accurate scheduling of smart appliances, a challenge addressed by ground breaking discoveries in DSM. DSM approaches have been effectively deployed in the residential, commercial and industrial sectors, proving their ability to balance consumer load profiles within grid networks.

This study investigates metaheuristic optimization methodologies for increasing energy efficiency in smart homes. The strategies studied include the HSA, FPA, HFPA, MVO and CSA. These solutions optimize energy use across multiple loads while using the RTP model to determine power bills. Simulations in MATLAB show that these strategies effectively reduce electricity bills and PAR. Compared to the unscheduled case, energy costs decreased by up to 19.86 % (HFPA), 19.54 % (HFPA, 30-min OTI), and 13.28 % (HFPA, 5-min OTI). The highest savings were achieved by the HFPA algorithm, consistently outperforming others. The PAR was reduced by up to 81.03 % (HFPA, 30-min OTI), 78.83 % (HFPA, 5-min OTI), and 66.23 % (HFPA, 1-hour OTI). This confirms effective load shifting and peak shaving. All algorithms maintained waiting times within acceptable limits. HFPA achieved the best results with only 102 min (5-min OTI), 18 min (30-min OTI), and 7 min (1-hour OTI), ensuring high user comfort.

The HFPA is the most successful of the proposed approaches, outperforming others in key criteria such as cost reduction, reduced waiting time, and enhanced PAR. Its hybrid formulation enables it to deal with the multi-objective attribute of energy management in multi-home systems by optimizing energy sharing as well as appliance schedules. The MVO is in second place and has an exceptional performance in the context of various dynamic and interconnected environments where energy requirements are highly volatile. But it can be considered computationally intensive to scale to the larger size.

The research shows that metaheuristic optimization methods can be used to enhance smart home energy management that would allow developing a more sustainable and efficient practice of energy consumption.

It is recommended that future research would concentrate on improvement and optimization of HFPA so it can be introduced at an even greater scale. It must also be combined with the machine learning and deep learning models to improve predictability and accuracy. The MVO is associated with greater complexity and hence, there is need to lower the degree of complexity of this algorithm in any follow up research. The proposed model should be combined with renewable energy resources in order to enhance sustainability.

Conflict of interest. The authors declare that they have no conflicts of interest.

REFERENCES

1. Peng Q., Liu W., Zhang Y., Zeng S., Graham B. Generation planning for power companies with hybrid production technologies under multiple renewable energy policies. *Renewable and Sustainable Energy Reviews*, 2023, vol. 176, art. no. 113209. doi: https://doi.org/10.1016/j.rser.2023.113209.

2. Bakare M.S., Abdulkarim A., Zeeshan M., Shuaibu A.N. A comprehensive overview on demand side energy management towards smart grids: challenges, solutions, and future direction. *Energy Informatics*, 2023, vol. 6, no. 1, art. no. 4. doi: https://doi.org/10.1186/s42162-023-00262-7.

3. Elazab R., Abdelnaby A.T., Ali A.A. Impacts of multiple demand-side management strategies on microgrids planning: a literature survey. *Clean Energy*, 2024, vol. 8, no. 1, pp. 36-54. doi: https://doi.org/10.1093/ce/zkad057.

4. Mateen A., Wasim M., Ahad A., Ashfaq T., Iqbal M., Ali A. Smart energy management system for minimizing electricity cost and peak to average ratio in residential areas with hybrid genetic flower pollination algorithm. *Alexandria Engineering Journal*, 2023, vol. 77, pp. 593-611. doi: https://doi.org/10.1016/j.aej.2023.06.053.

5. Ratshitanga M., Orumwense E.F., Krishnamurthy S., Melamu M. A Review of Demand-Side Resources in Active Distribution Systems: Communication Protocols, Smart Metering, Control, Automation, and Optimization. *Applied Sciences*, 2023, vol. 13, no. 23, art. no. 12573. doi: https://doi.org/10.3390/app132312573.

6. Marzband M., Ghazimirsaeid S.S., Uppal H., Fernando T. A real-time evaluation of energy management systems for smart hybrid home Microgrids. *Electric Power Systems Research*, 2017, vol. 143, pp. 624-633. doi: https://doi.org/10.1016/j.epsr.2016.10.054.
7. Zahra S.T., Khan R.U., Ullah M.F., Begum B., Anwar N. Simulation-based analysis of dynamic voltage restorer with sliding mode controller at optimal voltage for power quality enhancement in distribution system. *Electrical Engineering & Electromechanics*, 2022, no. 1, pp. 64-69. doi: https://doi.org/10.20998/2074-272X.2022.1.09.
8. Grechko O., Kulyk O. Current State and Future Prospects of Using SF6 Gas as an Insulation in the Electric Power Industry. *2024 IEEE 5th KhPI Week on Advanced Technology (KhPIWeek)*, 2024, pp. 1-6. doi: https://doi.org/10.1109/KhPIWeek61434.2024.10877987.
9. Tebbakh N., Labed D., Labed M.A. Optimal size and location of distributed generations in distribution networks using bald eagle search algorithm. *Electrical Engineering & Electromechanics*, 2022, no. 6, pp. 75-80. doi: https://doi.org/10.20998/2074-272X.2022.6.11.
10. Liu Y., Li H., Zhu J., Lin Y., Lei W. Multi-objective optimal scheduling of household appliances for demand side management using a hybrid heuristic algorithm. *Energy*, 2023, vol. 262, art. no. 125460. doi: https://doi.org/10.1016/j.energy.2022.125460.
11. Youssef H., Kamel S., Hassan M.H. Meta-heuristic-based home energy management system for optimizing smart appliance scheduling and electricity cost reduction in residential complexes. *Neural Computing and Applications*, 2024, vol. 36, no. 36, pp. 23077-23102. doi: https://doi.org/10.1007/s00521-024-10275-2.
12. Youssef H., Kamel S., Hassan M.H., Nasrat L., Jurado F. An improved bald eagle search optimization algorithm for optimal home energy management systems. *Soft Computing*, 2024, vol. 28, no. 2, pp. 1367-1390. doi: https://doi.org/10.1007/s00500-023-08328-0.
13. Mahmood A., Baig F., Alrajeh N., Qasim U., Khan Z., Javaid N. An Enhanced System Architecture for Optimized Demand Side Management in Smart Grid. *Applied Sciences*, 2016, vol. 6, no. 5, art. no. 122. doi: https://doi.org/10.3390/app6050122.
14. Logenthiran T., Srinivasan D., Vanessa K.W.M. Demand side management of smart grid: Load shifting and incentives. *Journal of Renewable and Sustainable Energy*, 2014, vol. 6, no. 3, art. no. 033136. doi: https://doi.org/10.1063/1.4885106.
15. El Mezdi K., El Magri A., Bahatti L. Advanced control and energy management algorithm for a multi-source microgrid incorporating renewable energy and electric vehicle integration. *Results in Engineering*, 2024, vol. 23, art. no. 102642. doi: https://doi.org/10.1016/j.rineng.2024.102642.
16. Ozturk Y., Senthilkumar D., Kumar S., Lee G. An Intelligent Home Energy Management System to Improve Demand Response. *IEEE Transactions on Smart Grid*, 2013, vol. 4, no. 2, pp. 694-701. doi: https://doi.org/10.1109/TSG.2012.2235088.
17. Salazar E.J., Samper M.E., Patiño H.D. Dynamic customer demand management: A reinforcement learning model based on real-time pricing and incentives. *Renewable Energy Focus*, 2023, vol. 46, pp. 39-56. doi: https://doi.org/10.1016/j.ref.2023.05.004.
18. Ogwumike C., Short M., Abugchem F. Heuristic Optimization of Consumer Electricity Costs Using a Generic Cost Model. *Energies*, 2015, vol. 9, no. 1, art. no. 6. doi: https://doi.org/10.3390/en9010006.
19. Wang F., Zhou L., Wang B., Wang Z., Shafie-Khah M., Catalao J.P.S. Modified chaos particle swarm optimization-based optimized operation model for stand-alone CCHP microgrid. *Applied Sciences*, 2017, vol. 7, no. 8, art. no. 754. doi: https://doi.org/10.3390/app7080754.
20. Silva B.N., Khan M., Wijesinghe R.E., Wijenayake U. Meta-heuristic optimization based cost efficient demand-side management for sustainable smart communities. *Energy and Buildings*, 2024, vol. 303, art. no. 113599. doi: https://doi.org/10.1016/j.enbuild.2023.113599.
21. Abdelhameed E.H., Abdelraheem S., Mohamed Y.S., Diab A.A.Z. Effective hybrid search technique based constraint mixed-integer programming for smart home residential load scheduling. *Scientific Reports*, 2023, vol. 13, no. 1, art. no. 21870. doi: https://doi.org/10.1038/s41598-023-48717-x.
22. Sharma O., Rathee G., Kerrache C.A., Herrera-Tapia J. Two-Stage Optimal Task Scheduling for Smart Home Environment Using Fog Computing Infrastructures. *Applied Sciences*, 2023, vol. 13, no. 5, art. no. 2939. doi: https://doi.org/10.3390/app13052939.
23. Ul Hassan C.A., Iqbal J., Ayub N., Hussain S., Alroobaea R., Ullah S.S. Smart Grid Energy Optimization and Scheduling Appliances Priority for Residential Buildings through Meta-Heuristic Hybrid Approaches. *Energies*, 2022, vol. 15, no. 5, art. no. 1752. doi: https://doi.org/10.3390/en15051752.
24. Irfan M., Ul Hassan C.A., Althobiani F., Ayub N., Khan R.J.U.H., Ghandourah E.I., Almas M.A., Ghonaim S.M., Shamji V.R., Rahman S. Power Scheduling with Max User Comfort in Smart Home: Performance Analysis and Tradeoffs. *Computer Systems Science and Engineering*, 2023, vol. 46, no. 2, pp. 1723-1740. doi: https://doi.org/10.32604/csse.2023.035141.
25. Laouafi F. Improved grey wolf optimizer for optimal reactive power dispatch with integration of wind and solar energy. *Electrical Engineering & Electromechanics*, 2025, no. 1, pp. 23-30. doi: https://doi.org/10.20998/2074-272X.2025.1.04.
26. Yu Y.H., Ong P., Wahab H.A. Intelligent optimization of a hybrid renewable energy system using an improved flower pollination algorithm. *International Journal of Environmental Science and Technology*, 2024, vol. 21, no. 5, pp. 5105-5126. doi: https://doi.org/10.1007/s13762-023-05354-1.
27. Daqaq F., Ouassaid M., Kamel S., Ellaia R., El-Naggar M.F. A novel chaotic flower pollination algorithm for function optimization and constrained optimal power flow considering renewable energy sources. *Frontiers in Energy Research*, 2022, vol. 10, art. no. 941705. doi: https://doi.org/10.3389/fenrg.2022.941705.
28. Dao T.-K., Nguyen T.-T., Nguyen V.-T., Nguyen T.-D. A Hybridized Flower Pollination Algorithm and Its Application on Microgrid Operations Planning. *Applied Sciences*, 2022, vol. 12, no. 13, art. no. 6487. doi: https://doi.org/10.3390/app12136487.
29. Kumari J.S., Abdul Nabi M. An Enhancement of Grid Integration in Renewable Energy Systems Using Multi- Objective Multi-Verse Optimization. *International Journal of Electrical and Computer Engineering Systems*, 2024, vol. 15, no. 10, pp. 885-895. doi: https://doi.org/10.32985/ijeces.15.10.7.
30. Grisales-Norena L.F., Sanin-Villa D., Montoya O.D. Optimal integration of PV generators and D-STATCOMs into the electrical distribution system to reduce the annual investment and operational cost: A multiverse optimization algorithm and matrix power flow approach. *E-Prime - Advances in Electrical Engineering, Electronics and Energy*, 2024, vol. 9, art. no. 100747. doi: https://doi.org/10.1016/j.prime.2024.100747.
31. Alouache B., Helaimi M., Djilali A.B., Gabbar H.A., Allouache H., Yahdou A. Optimal tuning of multi-stage PID controller for dynamic frequency control of microgrid system under climate change scenarios. *Electrical Engineering & Electromechanics*, 2025, no. 1, pp. 8-15. doi: https://doi.org/10.20998/2074-272X.2025.1.02.
32. Jasim A.M., Jasim B.H., Flah A., Bolshev V., Mihet-Popa L. A new optimized demand management system for smart grid-based residential buildings adopting renewable and storage energies. *Energy Reports*, 2023, vol. 9, pp. 4018-4035. doi: https://doi.org/10.1016/j.egyr.2023.03.038.

Received 27.08.2025
Accepted 25.11.2025
Published 02.03.2026

Mohsin Kamal[1], *MSc,*
Mian Farhan Ullah[1], *MSc,*
Naveed Anwar[2], *MSc, Lab Engineer,*
Aziza I. Hussein[2], *PhD, Professor,*
[1] Elementary and Secondary Education Department,
KPK, Pakistan.
[2] Department of Electrical and Computer Engineering,
Effat University, Jeddah, Saudi Arabia,
e-mail: naveanwar@effatuniversity.edu.sa (Corresponding Author)

How to cite this article:
Kamal M., Ullah M.F., Anwar N., Hussein A.I. Optimizing residential energy usage patterns in smart grids using hybrid metaheuristic techniques. *Electrical Engineering & Electromechanics*, 2026, no. 2, pp. 31-39. doi: https://doi.org/10.20998/2074-272X.2026.2.05

UDC 621.3.013 https://doi.org/10.20998/2074-272X.2026.2.06

B.I. Kuznetsov, A.S. Kutsenko, T.B. Nikitina, I.V. Bovdui, K.V. Chunikhin, V.V. Kolomiets

The methodology of multi objective design of active-passive shielding system for overhead power lines magnetic field in residential buildings space based on metaheuristic optimization method

Problem. *Most studies of power frequency magnetic field reduced to safe level in in residential buildings located near overhead power lines carried out based on passive or active electromagnetic shielding, but there is no methodology for designing active-passive systems that include active and solid or multi-circuit passive shields. The* ***goal*** *of the work is to develop the methodology of multi objective design of active-passive electromagnetic shielding system, consisting of active and solid self or multi-circuit passive parts to improve shielding efficiency of initial magnetic field in residential building edges generated by overhead power lines to sanitary standards level. This goal proposed to achieve based on metaheuristic optimization method* ***Methodology.*** *Multi objective design methodology of active-passive shielding system based on solution of the geometric inverse problem of magnetostatics for the resulting magnetic field generated by the transmission line wires, compensation windings of the active shielding system and a passive shield in the form of a solid or multi-loop shield. The geometric forward problem is solved based on solutions of Maxwell's equation for magnetic field three-dimensional model using the COMSOL Multiphysics software. The solution of the geometric inverse problem of magnetostatics is formulated as a minimax vector problem of nonlinear programming. The solution of the minimax vector problem of nonlinear programming is calculated based on the metaeristic optimization algorithm from Pareto optimal solutions taking into account binary preference relations.* ***Results.*** *During combined active and solid or multi-circuit passive shielding system design spatial arrangement coordinates of solid or multi-loop passive shield and compensating windings, as well as windings currents and phases of active shield calculated. New scientific results are theoretical and experimental studies of a designed combined active and of solid or multi-circuit passive shielding system efficiency for magnetic field created by overhead power lines.* ***Scientific novelty****. For the first time multi objective design methodology for combined active and solid or multi-circuit passive shielding system taking into account original field shielding effectiveness decrease in residential building* edges *for more effective reduction of industrial frequency magnetic field created by overhead power lines developed.* ***Practical value****. Practical recommendations for the reasonable choice of the coordinates of the spatial arrangement of compensation windings of the active shielding system and a passive shield in the form of a solid or multi-loop shield, as well as the currents and phases in the compensation windings, parameters of regulators of the open and closed controls of the two degrees of freedom active shielding system and parameters of positions of magnetic field sensors of the active shielding system for magnetic field generated by overhead power lines in residential building space are given. The possibility of reducing the initial magnetic field induction to the sanitary standards level shown.* References 48, figures 11.

Key words: **overhead power line, magnetic field, combined electromagnetic active and passive shielding system, design computer simulation, experimental research.**

Проблема*. Більшість досліджень по зниженню рівня магнітного поля промислової частоти в житлових будинках, що розташовані поблизу повітряних ліній електропередачі, до безпечного рівня, виконані на основі пасивних або активних засобів електромагнітного екранування, але відсутня методологія проєктування активно-пасивних систем, які включають активні та суцільні або багатоконтурні пасивні екрани.* ***Метою*** *роботи є розробка методології багатоцільового проєктування активно-пасивної системи електромагнітного екранування, що складається з активних та суцільних або багатоконтурних пасивних частин для підвищення ефективності екранування вихідного магнітного поля на краях житлових будівель, що генерується повітряними лініями електропередачі, до рівня санітарних норм. Досягти зазначеної мети пропонується на основі методу метаевристичної оптимізації.* ***Методика****. Багатоцільове проєктування активно-пасивної системи екранування базується на розв'язанні геометричної оберненої задачі магнітостатики для результуючого магнітного поля, що генерується проводами лінії електропередачі, компенсаційними обмотками активної системи екранування та пасивним екраном у вигляді суцільного або багатоконтурного екрану. Геометрична пряма задача обчислюється на основі розв'язків рівняння Максвелла для тривимірної моделі магнітного поля за допомогою програмного забезпечення COMSOL Multiphysics. Розв'язок геометричної оберненої задачі магнітостатики формулюється як мінімаксна векторна задача нелінійного програмування. Розв'язок мінімаксної векторної задачі нелінійного програмування розраховується на основі метаевристичного алгоритму оптимізації, що базується на оптимальних за Парето розв'язках з урахуванням бінарних співвідношень переваги.* ***Результати****. В процесі багатоцільового проєктування активно-пасивної системи електромагнітного екранування розраховано координати просторового розташування суцільного або багатоконтурного пасивного екрану та компенсаційних обмоток системи активного екранування, а також струм та фази компенсуючих обмоток системи активного екранування. Новими науковими результатами є теоретичні та експериментальні дослідження ефективності синтезованої комбінованої активної та суцільної, або багатоконтурної, пасивної електромагнітних екрануючих систем магнітного поля, що створюється повітряними лініями електропередачі.* ***Наукова новизна.*** *Вперше розроблено методологію багатоцільового проєктування комбінованої активної та суцільної, або багатоконтурної, пасивної системи екранування з урахуванням ефективності екранування результуючого магнітного поля на краях житлових будівель для більш ефективного зменшення магнітного поля промислової частоти, що створюється повітряними лініями електропередачі.* ***Практична значимість****. Надано практичні рекомендації щодо обґрунтованого вибору координат просторового розташування компенсаційних обмоток системи активного екранування та пасивного екрану у вигляді суцільного, або багатоконтурного, екрану, а також струмів та фаз в компенсаційних обмотках, параметрів регуляторів розімкнутого та замкнутого управління системи активного екранування з двома ступенями свободи та параметрів положень датчиків магнітного поля системи активного екранування для магнітного поля, що генерується повітряними лініями електропередачі в просторі житлової забудови. Показана можливість зниження індукції вихідного магнітного поля до рівня санітарних норм*. Бібл. 48, рис. 11.

Ключові слова: **повітряна лінія електропередачі, магнітне поле, система комбінованого електромагнітного активного та пасивного екранування, проєктування, комп'ютерне моделювання, експериментальні дослідження.**

Introduction. Operating high-voltage overhead power lines, located in residential areas of most developed countries of the world, are the main sources of power frequency magnetic fields, which massively affect the population and are more dangerous to health than electric fields. At the end of the 20th century, experts from the World Health Organization discovered the carcinogenic properties of the power frequency magnetic field with its weak but long-term effect on humans [1]. Therefore, over the past 20 years, sanitary standards for the maximum permissible level of power frequency of 50-60 Hz for the population have been actively implemented and constantly

strengthened in the world, and intensive development of methods for normalizing power frequency magnetic fields is being carried out [2, 3].

Calculations and the results of numerous experiments show, the maximum permissible level of induction of power frequency magnetic fields at the border of sanitary protection zones of operating overhead lines, which were previously determined only by the EP, can be exceeded by more than an order of magnitude [3–5]. This poses a threat to the health of hundreds of thousands of people living closer than 100 m from the overhead line.

Fig. 1. Residential buildings located close to power line

As an example, Fig. 1 shows residential buildings located close to power line. From an economic point of view, methods of shielding residential buildings from magnetic field overhead lines are more promising [6, 7]. The economic significance of the work lies in normalizing the level of the magnetic field of industrial frequency in existing residential buildings located near overhead power lines, without decommissioning or reconstructing already operating overhead lines. The social significance of the work lies in ensuring the protection of public health from the negative effects of the man-made magnetic field of industrial frequency and, accordingly, extending the life expectancy of the population of Ukraine.

However, at present, the problem of effective shielding of power frequency magnetic fields of overhead lines has not been sufficiently studied. Methods of passive (electromagnetic) shielding of power frequency magnetic fields with conductive plates, which are traditional and effective for power frequency magnetic fields, when used for shielding magnetic fields of power frequency 50-60 Hz, require increased metal capacity, which within the framework of economic feasibility limits their efficiency to the level of 2-3, which in some cases is insufficient [8, 9]. In addition, traditional passive electromagnetic shield are airtight for air and opaque for light, which creates a problem of shielding window openings of residential buildings.

Active shielding methods of power frequency magnetic fields can be provided higher efficiency of shielding of overhead power lines (up to 10) with lower metal content [10–13]. Their essence lies in the automatic formation in a closed structure using special windings of compensating power frequency magnetic fields with such a space-time structure, the superposition of which with the power frequency magnetic fields of the overhead power line in the protection zone is minimized to a safe level [14–16]. The technology of active shielding of power frequency magnetic fields of operating overhead power lines has been used for more than 10 years by most developed countries of the world, for example, the USA, Italy, Spain and Israel [17, 18].

However, methods and means of increasing the characteristics of both active and passive shielding systems of residential buildings for effective protection of their residents from the effects of overhead power lines remain undeveloped [19–26]. Also, the methods of active and passive shielding do not have a theoretical and experimental justification, and the criteria for their rational use depending on the design and localization of overhead power lines relative to the residential building have not been determined [26–28]. The idea of the research is to optimize the systems of active and passive shielding of overhead power lines in residential buildings depending on the spatial structure of the overhead power lines, which is determined by the design and localization of overhead power lines, as well as the use of transparent lattice electromagnetic shielding for residential buildings.

When designing combined electromagnetic shield, it is necessary to reduce the level of the initial magnetic field in the entire shielding space along the length, width and height of the residential building [29–31]. Therefore, it is necessary to use a three-dimensional model of the magnetic field. Moreover, the need to use passive shielding may be needed precisely at the edges of the residential building [32–34]. When designing combined electromagnetic shielding, it is necessary to take into account the inaccurate knowledge of the parameters of the initial magnetic field, as well as their change during operation, and therefore the designed system must be robust [35–37].

Therefore, the problem of designing combined electromagnetic shielding taking into account the uncertainties of the initial magnetic field model is reduced to solving a minimax vector optimization problem with constraints [38–40]. The components of the vector objective function are the values of the induction of the resulting magnetic field at the considered points of the shielding space. These components of the vector objective function are nonlinear nonconvex functions and contain a set of local extrema [41–43].

To solve such complex, multidimensional nonlinear and nonconvex optimization problems, metaheuristic group intelligence algorithms are widely used [31, 32].

The **goal** of the work is to develop the methodology of multi objective design of active-passive electromagnetic shielding system, consisting from active and solid or multi-circuit passive parts to improve shielding efficiency of initial magnetic field in residential building edges generated by overhead power lines to sanitary standards level. This goal proposed to achieve based on metaheuristic optimization method.

Definition of geometric forward magnetostatic problem for passive solid electromagnetic shield. The most widespread method of reducing the magnetic field level is electromagnetic shielding using a solid passive shield. The geometric forward problem of magnetostatics for solid passive electromagnetic shield is to calculate the secondary three-dimensional model of magnetic field generated by a solid passive electromagnetic shield placed in the original magnetic field. It is assumed that the coordinates of the spatial location, geometric dimensions and electrical parameters – electrical and magnetic conductivity of the solid passive electromagnetic shield are specified. Naturally, the original magnetic field is also considered specified.

To model electromagnetic processes in a solid passive electromagnetic shield, the COMSOL Multiphysics software is used to solve Maxwell's equations using the finite element method for three-dimensional models of the electromagnetic field in the following form.

Gauss's law for electric field

$$\nabla \cdot \boldsymbol{E} = \frac{\rho}{\varepsilon_0}; \quad (1)$$

Gauss's law for magnetism

$$\nabla \cdot \boldsymbol{B} = 0; \quad (2)$$

Faraday's law for electromagnetic induction

$$\nabla \times \boldsymbol{E} = -\frac{\partial \boldsymbol{B}}{\partial t}; \quad (3)$$

Ampere's loop law

$$\nabla \times \boldsymbol{B} = \mu_0 \boldsymbol{J} + \mu_0 \varepsilon_0 \frac{\partial \boldsymbol{E}}{\partial t}, \quad (4)$$

where vector $\boldsymbol{E}$ is electric field strength; vector $\boldsymbol{B}$ is magnetic flux density; vector $\boldsymbol{J}$ is current density; ρ is electric charge density.

To study the process of electromagnetic shielding of a three-phase power line through which a harmonic current flows in a steady state, the law of the total current in integral form, written in a quasi-stationary approximation in terms of complex amplitudes, was used:

$$\oint_l \boldsymbol{H}\,\mathrm{d}l = \int_S \gamma \boldsymbol{E}\,\mathrm{d}S + \int_S \boldsymbol{J}^{ext}\,\mathrm{d}S, \quad (5)$$

where $\boldsymbol{H}$, $\boldsymbol{E}$ – complex amplitudes of the intensity vectors of the magnetic and electric fields, respectively; $\boldsymbol{J}^{ext}$ – complex amplitude of the current density vector of external sources; γ – specific electrical conductivity; l – contour covering the integration surface S.

Equation (1) can be written in the form:

$$\oint_l \frac{1}{\mu} \mathrm{rot}\,\boldsymbol{A}^*\,\mathrm{d}l = -j\mu_0\omega \cdot \int_S \gamma \boldsymbol{A}^*\,\mathrm{d}S + \mu_0 \cdot \int_S \boldsymbol{J}^{ext}\,\mathrm{d}S, \quad (6)$$

where $\boldsymbol{A}^*$ is the vector magnetic potential; μ is the relative magnetic permeability; $\mu_0 = 4\pi \cdot 10^{-7}$ H/m is the magnetic constant; ω is the circular frequency.

The obtained equation describes the distribution of vector magnetic potential in the system «solid electromagnetic shield – current sources of magnetic field». The electromagnetic shield is given by its geometric parameters, relative magnetic permeability μ and specific electrical conductivity γ. For the external environment, we can set μ=1, γ=0. The system of current sources is described by the frequency ω and the current density distribution vector $\boldsymbol{J}^{ext}$. In this case, the current conductors are considered as current filaments.

Numerical modeling of electromagnetic processes in systems with extended current conductors and thin-walled open-circuited conductive shielding elements is based on the combined use of finite difference methods and absorbing boundary conditions, the division of the computational domain into a number of additional subdomains containing thin-walled elements, and the use of a non-uniform computational grid to calculate the field in the thickness of the shield walls with subsequent «stitching» of the solutions obtained in each subdomain [44, 45].

The computational domain contains current conductors, an electromagnetic shield and a protected area. Uniaxial well-matched layers are introduced at the boundaries of the computational domain: this additional medium occupies several cells of the computational grid and plays an auxiliary role, and its anisotropic parameters ensure fast and non-reflective attenuation of the electromagnetic field in it. Therefore, at its outer boundary, the value of the vector magnetic potential can be set equal to zero: $\boldsymbol{A}^* = 0$. The computational domain was divided into a number of additional subdomains, some of which contained thin-walled conductive elements. A rectangular grid was imposed in each subdomain, and the step inside the shielding elements was smaller. The solutions obtained in each subdomain were «stitched» at their boundaries [46].

Let us define the vector $\boldsymbol{X}_{pss}$ of the sought parameters of solid passive electromagnetic shield, the components of which are coordinates of the spatial location, geometric dimensions and electrical parameters – electrical and magnetic conductivity of the solid passive electromagnetic shield. Such three-dimensional numerical modeling allows us to calculate instantaneous value of a vector $\boldsymbol{B}_{pss}(\boldsymbol{X}_{pss}, P_i, t)$ of induction of the three-dimensional model of magnetic field generated by solid electromagnetic shield at the point P_i of the shielding space at the moment of time t. Therefore, the geometric forward problem of magnetostatics for a solid passive electromagnetic shield is solved.

Definition of geometric forward magnetostatic problem for multi-circuit passive electromagnetic shield. The geometric forward problem of magnetostatics for multi-circuit passive electromagnetic shield is to calculate the secondary three-dimensional model of magnetic field generated by a multi-circuit passive electromagnetic shield placed in the original magnetic field [26]. It is assumed that the coordinates of the spatial location, geometric dimensions and electrical parameters – electrical and magnetic conductivity of multi-circuit passive electromagnetic shield are specified. Naturally, the original magnetic field is also considered specified.

Multi-circuit passive shield consist of a set of aluminum wires that are interconnected in a certain way and form current circuit. In most cases, all the wires of the shield are connected in parallel. The wires are arranged parallel to each other and parallel to the overhead line, which provides the greatest shielding efficiency. The calculation of the magnetic field of multi-circuit passive shield can be carried out by analytical, semi-analytical or numerical methods.

For given initial magnetic field induction vector $\boldsymbol{B}_{Ra}(Q_i, \boldsymbol{X}_a, \boldsymbol{\delta}, t)$ as well as of geometric dimensions vector values $\boldsymbol{X}_p$ of multi-circuit passive contour shield, magnetic flux $\boldsymbol{\Phi}_l(\boldsymbol{X}_a, \boldsymbol{X}_p, \boldsymbol{\delta}, t)$ piercing contour l of multi-circuit passive shield calculated [26]

$$\boldsymbol{\Phi}_l\left(\boldsymbol{X}_a, \boldsymbol{X}_p, \boldsymbol{\delta}, t\right) = \int_S \boldsymbol{B}_{Ra}(\boldsymbol{X}_a, \boldsymbol{\delta}, t)\,\mathrm{d}S. \quad (7)$$

Current $\boldsymbol{I}_{Pl}(\boldsymbol{X}_a, \boldsymbol{X}_p, \boldsymbol{\delta}, t)$ in complex form, induced in circuit l of multi-circuit passive shield calculated according to Ohm law and in integral form of Faraday law [19]:

$$\boldsymbol{I}_{Pl}\left(\boldsymbol{X}_a, \boldsymbol{X}_p, \boldsymbol{\delta}, t\right) = -j\omega\boldsymbol{\Phi}(\boldsymbol{X}_a, \boldsymbol{X}_p, \boldsymbol{\delta}, t)/\ldots \\ \ldots/(\boldsymbol{R}_l(\boldsymbol{X}_p) + j\omega\boldsymbol{L}_l(\boldsymbol{X}_p)), \quad (8)$$

where $\boldsymbol{R}_l(\boldsymbol{X}_p)$ – active resistance and inductance $\boldsymbol{L}_l(\boldsymbol{X}_p)$ of circuit l of multi-circuit passive shield calculated for passive shield geometric dimensions vector values $\boldsymbol{X}_p$.

In the numerical method of calculating the three-dimensional model of the magnetic field of multi-circuit

passive shield, the coordinates of the spatial arrangement of the wires, the geometric dimensions of these wires and the electrical conductivity of the shield wires are given. The entire calculation area is divided into sub-areas, each of which is aluminum or air. During the calculation, discrete calculation mesh were superimposed, the types and sizes of which differed significantly according to the calculation sub-area. The presented model allows you to calculate the electric currents induced in the screen and, accordingly, find the three-dimensional model of of the shielded magnetic field distribution.

Let us define the vector $\boldsymbol{X}_{pcs}$ of the sought parameters of multi-circuit passive electromagnetic shield, the components of which are coordinates of the spatial location, geometric dimensions and electrical parameters – electrical and magnetic conductivity of multi-circuit passive electromagnetic shield. Such three-dimensional numerical modeling allows us to calculate instantaneous value of a vector $\boldsymbol{B}_{pcs}(\boldsymbol{X}_{pcs}, P_i, t)$ of induction of the three-dimensional model of magnetic field generated by multi-circuit electromagnetic shield at the point P_i of the shielding space at the moment of time t. Therefore, the geometric forward problem of magnetostatics for a multi-circuit passive electromagnetic shield is solved.

Definition of geometric forward magnetostatic problem for active quasi-static electromagnetic shield. Let's first consider a quasi-static formulation of the forward magnetostatic problem of current regulation in the compensation windings of an active shielding system. This direct problem involves calculating a three-dimensional model of the magnetic field generated by the compensation windings of an active shielding system. It is assumed that the spatial coordinates of these compensation windings of the active shielding system are specified, as are the instantaneous current values – the amplitudes and phases of the currents in these compensation windings of the active shielding system.

Three-dimensional model is calculated the magnetic field inside a residential building and represents the compensation windings of the active shielding system as a set of current conductors, while the influence of other elements is not taken into account. The general method of calculating the three-dimensional model of magnetic field based on the Biot-Savart law. The essence of the method is that the conductors are replaced by a broken line consisting of straight segments. A current $i(t)$ flows through each infinitely thin segment of the conductor with a dl length. According to the Biot-Savart law, the current $i(t)$ flowing through the segment dl generates a magnetic field with induction:

$$\mathrm{d}\boldsymbol{B}(t) = \frac{\mu_0 \mathrm{i}(t)}{4\pi R^3}(\mathrm{d}\boldsymbol{l} \times \boldsymbol{R}). \qquad (9)$$

Then we can calculate the magnetic field induction generated by the entire compensation winding.

$$\boldsymbol{B}(t) = \frac{\mu_0 \mathrm{i}(t)}{4\pi} \int_{-L}^{L} \frac{(\mathrm{d}\boldsymbol{l} \times \boldsymbol{R})}{R^3}, \qquad (10)$$

where it is assumed that the integration is carried out along a line segment $(-L,+L)$ along which the unit vector is directed.

Let us define the vector $\boldsymbol{X}_{aqs}$ of the sought geometric parameters of compensation windings of an active shielding system, the components of which are coordinates of the spatial location, geometric dimensions compensation windings of an active shielding system.

Let us define also the vector $\boldsymbol{I}_{aqs}$ of sought electric parameters of compensation windings of an active shielding system, the components of which are current in these compensation windings of an active shielding system.

Such three-dimensional numerical modeling allows us to calculate based on the Biot-Savart law (6) instantaneous value of a vector $\boldsymbol{B}_{aqs}(\boldsymbol{X}_{aqs}, \boldsymbol{I}_{aqs}, P_i, t)$ of induction of the three-dimensional model of magnetic field generated by active quasi-static electromagnetic shield at the point P_i of the shielding space at the moment of time t. Therefore, the geometric forward problem of magnetostatics for active quasi-static electromagnetic shield is solved.

Definition of geometric forward magnetostatic problem for magnetic field sensors positions of active electromagnetic shield. The active shielding system is a multi-channel dynamic automatic control system, the number of channels in which is determined by the number of compensation windings. This active shielding system is a two-degree-of-freedom system and simultaneously includes open and closed control loops. The forward objective of designing an active shielding system is to calculate the currents in the compensation windings of the active shielding system using magnetic field sensors. Moreover, to implement closed-loop control, the magnetic field sensors are installed within the shielding space.

The number of these magnetic field sensors is usually equal to the number of compensation windings in the active shielding system. To implement open-loop current control in the compensation windings of the active shielding system, the magnetic field sensor is installed outside the shielding space. Typically, to implement open current control loops in all compensation windings of the active shielding system, one magnetic field sensor is used, which is installed at a significant distance from the shielding space. In this case, it is assumed that the voltages at the outputs of the magnetic field sensors, which are used to implement open and closed loops for regulating currents in the compensation windings of the active shielding system, are specified.

The geometric forward magnetostatic problem for positions of magnetic field sensors of active electromagnetic shield is to calculate the output of the magnetic field sensors, which is necessary for implementing open and closed loop current control in the compensation windings of the active shielding system. In this case, it is naturally assumed that the spatial coordinates and spatial orientation angles of these magnetic field sensors are specified. Naturally, the magnetic field at the location of these magnetic field sensors is also assumed to be known.

Let's first consider definition of geometric forward magnetostatic problem for magnetic field sensors positions of active electromagnetic shield. We introduce the induction vector $\boldsymbol{B}_R(t)$ the components of which are induction vectors $\boldsymbol{B}_R(Q_i,t)$ of the resulting magnetic field at points Q_i of magnetic field sensors installed. We also introduce the unit vectors $\boldsymbol{\varphi}$ of the angular positions of the

magnetic field sensors and column vector $\boldsymbol{K}_M$ of the gain coefficients of the magnetic field sensor taking into account the number of turns of their measuring coils and the gains of the preamplifiers.

Then the vector $\boldsymbol{y}_s(t)$ of sensor output voltage will take the following form

$$\boldsymbol{y}_S(t) = \boldsymbol{B}_R(t) \otimes \varphi \otimes \boldsymbol{K}_M + \boldsymbol{w}(t), \qquad (11)$$

where the sign $\otimes$ denotes the tensor (Kronecker) product of the column vectors; $\boldsymbol{w}(t)$ is the magnetometer noise vector.

The components of the sensor output voltage vector $\boldsymbol{y}_s(t)$ are instantaneous values of projections of the components of the induction vectors $\boldsymbol{B}_R(Q_i, t)$ of the resulting magnetic field in sensors installed points Q_i on the components of unit vectors $\boldsymbol{\varphi}$ of the angular position of the magnetic field sensors taking into account the components of column vector $\boldsymbol{K}_M$ of the magnetic field sensor gain coefficients.

Let's define a vector $\boldsymbol{X}_{asp}$ of positions of magnetic field sensors for active dynamic electromagnetic shield, whose components are the vector of spatial coordinates Q_i and the vector of angular positions $\boldsymbol{\varphi}$ of the magnetic field sensor. Then, for a given vector $\boldsymbol{X}_{asp}$, based on (7), a geometric forward magnetostatic problem for magnetic field sensors positions of active electromagnetic shield can be solved – the vector of instantaneous values of the magnetic field sensor output voltages can be calculated.

Definition of forward problem for active dynamic electromagnetic shield. Let us now consider the forward problem for active dynamic electromagnetic shield of calculating the currents $\boldsymbol{I}_w(t)$ in the compensation windings of the active shielding system using a dynamic system with two degrees of freedom based on the output voltages $\boldsymbol{y}_s(t)$ of the magnetic field sensors.

Let us introduce the vector $\boldsymbol{X}_{ars}$, the components of which are the parameters of the open and closed controllers $\boldsymbol{R}(\boldsymbol{X}_{ars})$, with the help of which control with two degrees of freedom is implemented. Then, based on the vectors $\boldsymbol{y}_s(t)$ of instantaneous values of the output voltages of the magnetic field sensors using the regulators of the open and closed controls of the two degrees of freedom active shielding system, a vector $\boldsymbol{I}_w(t)$ of instantaneous values of the currents in the cleanliness windings can be calculated.

$$\boldsymbol{I}_w(t+1) = \boldsymbol{R}(\boldsymbol{X}_{ars})\boldsymbol{y}_S(t). \qquad (12)$$

Definition of geometric inverse magnetostatic problem for combined electromagnetic shield. The resulting magnetic field in the shielding space is a superposition of the original magnetic field generated by the transmission line wires and the combined electromagnetic shield. The combined electromagnetic shield includes the active shield windings and a passive solid or multi-circuit shield.

In most works devoted to the calculation of the electromagnetic field of power transmission lines, the sagging of the wires on the field distribution is not taken into account. The wires are assumed to be infinite, rectilinear and parallel to the earth's surface. The advantage of this approach is that it allows the problem of calculating the magnetic field to be considered in a two-dimensional setting. However, research results have shown that neglecting the effect of sagging when calculating the magnetic field can lead to an error of 45 %.

Therefore, when calculating the magnetic field of overhead power lines, we will take into account the sagging of the wires. It is assumed that the wires have the shape of a catenary line, and in this case the problem of calculating the magnetic field is three-dimensional.

Let us define the vector $\boldsymbol{X}_{ipl}$ of the parameters of overhead power lines, the components of which are are coordinates of the spatial location and geometric dimensions of overhead power lines wires as wel as vector $\boldsymbol{X}_{ipl}$ of amplitudes A_i and phases φ_i of currents in power transmission lines wires.

Currents in transmission lines exhibit daily, weekly, seasonal, and annual variations. Let's define the uncertainty vector $\boldsymbol{\delta}$ of the initial magnetic field generated by the transmission line. Then, the vector $\boldsymbol{B}_{ipl}(\boldsymbol{\delta}, P_i, t)$ of the instantaneous value at time t of the resulting magnetic space point P_i can be calculated as a three-dimensional model based on the Biot-Savart law (10).

Such three-dimensional numerical modeling allows us to calculate the distributions of the induction of the three-dimensional model of magnetic field generated by the transmission line wires, that is, to solve the geometric forward problem of magnetostatics for transmission line wires.

Let us first consider the problem of compensating for the initial magnetic field generated by the power transmission line wires using a combined shield in a quasi-static setting. For given vectors of parameters of a solid passive electromagnetic shield $\boldsymbol{X}_{pss}$, a multi-circuit passive electromagnetic shield $\boldsymbol{X}_{pcs}$ and geometric $\boldsymbol{X}_{aqs}$ and currents $\boldsymbol{I}_{aqs}$ parameters of compensation windings of an active shielding system in a quasi-stationary setting based on the solution of geometric forward problems, the instantaneous values of the magnetic field induction vectors $\boldsymbol{B}_{pss}(\boldsymbol{X}_{pss}, P_i, t)$ generated by solid passive electromagnetic shield vectors $\boldsymbol{B}_{pcs}(\boldsymbol{X}_{pcs}, P_i, t)$ generated by multi-circuit passive electromagnetic shield vectors $\boldsymbol{B}_{aqs}(\boldsymbol{X}_{aqs}, \boldsymbol{I}_{aqs}, P_i, t)$ generated by compensation windings of an active shielding system at the moment of time t in space point P_i can be calculated.

Let us introduce the vector $\boldsymbol{X}$ of the required parameters of the design of a combined shield, the components of which are vectors of parameters of a solid passive electromagnetic shield $\boldsymbol{X}_{pss}$, a multi-circuit passive electromagnetic shield $\boldsymbol{X}_{pcs}$ and geometric $\boldsymbol{X}_{aqs}$ and currents $\boldsymbol{I}_{aqs}$ parameters of compensation windings of an active shielding system in a quasi-stationary setting

$$\boldsymbol{X} = \left(\boldsymbol{X}_{pss}, \boldsymbol{X}_{pcs}, \boldsymbol{X}_{aqs}, \boldsymbol{I}_{aqs}\right). \qquad (13)$$

Then the instantaneous value of the vector $\boldsymbol{B}_R(\boldsymbol{X}, \boldsymbol{\delta}, P_i, t)$ of the resulting magnetic field induction is calculated as the following sum

$$\begin{aligned}\boldsymbol{B}_R(\boldsymbol{X}, \boldsymbol{\delta}, P_i, t) = \boldsymbol{B}_{ipl}(\boldsymbol{\delta}, P_i, t) + \boldsymbol{B}_{pss}\left(\boldsymbol{X}_{pss}, P_i, t\right) + \\ + \boldsymbol{B}_{pcs}\left(\boldsymbol{X}_{pcs}, P_i, t\right) + \boldsymbol{B}_{aqs}\left(\boldsymbol{X}_{aqs}, \boldsymbol{I}_{aqs}, P_i, t\right)\end{aligned} \qquad (14)$$

Let us now consider the problem of compensation of the initial magnetic field generated by the power transmission line wires using a combined shield in a dynamic setting taking into account the solution to the problem of spatial placement and angular position of magnetic field sensors, as well as the design of active

shielding system controllers as a dynamic system with two degrees of freedom. In contrast to the quasi-static formulation of the problem of designing a combined shield, when the currents in the compensation windings of the active shielding system are the desired parameters, in the dynamic formulation of the problem of designing a combined shield, when the currents in the compensation windings of the active shielding system are calculated using a dynamic system with two degrees of freedom.

For the given values of the vector $\boldsymbol{X}_{asp}$ of the sought parameters of the spatial and angular positions of the magnetic field sensors, the output voltages $\boldsymbol{y}_s(t)$ of the magnetic field sensors are calculated based on the solution of the geometric forward problem. Naturally, when calculating the output voltages of the magnetic field sensors, the calculated values of the vector $\boldsymbol{B}_R(Q_i, t)$ of resulting magnetic field at the installation points Q_i of the magnetic field sensors inside the shielding space are used to implement closed-loop control algorithms for the currents of the compensation windings of the active shielding system.

When calculating the output voltage $\boldsymbol{y}_s(t)$ of the initial magnetic field sensors, the calculated values of the initial magnetic field $\boldsymbol{B}_{ipl}(Q_i, t)$ at the installation points Q_i of the magnetic field sensor outside the shielding space are used to implement open-loop control algorithms for the currents of the compensation windings of the active shielding system. For the given values of the vector $\boldsymbol{X}_{ars}$ of the parameters of the active shielding system regulators, the vector $\boldsymbol{I}_w(t)$ of instantaneous values of the currents in the compensation windings of the active shielding system are calculated based on the calculated output voltages $\boldsymbol{y}_s(t)$ of the magnetic field sensors. Then, for the values of currents $\boldsymbol{I}_w(t)$ in the compensation windings of the active dynamic shielding system calculated in this way and for the given values of the vector $\boldsymbol{X}_{aqs}$ of the sought geometric parameters of compensation windings of an active shielding system, the value of instantaneous value of induction vector $\boldsymbol{B}_{ads}(\boldsymbol{X}_{aqs}, \boldsymbol{X}_{asp}, \boldsymbol{X}_{ars}, P_i, t)$ is calculated.

Then three-dimensional numerical modeling allows us to calculate based on the Biot-Savart law (10) instantaneous value of a vector $\boldsymbol{B}_{ads}(\boldsymbol{X}_{aqs}, \boldsymbol{X}_{asp}, \boldsymbol{X}_{ars}, P_i, t)$ of induction of the three-dimensional model of magnetic field generated by active dynamic electromagnetic shielding system at the point P_i of the shielding space at the moment of time t. Therefore, the geometric forward problem of magnetostatics for active dynamic electromagnetic shielding system is solved.

Let us introduce the vector $\boldsymbol{X}$ of the required parameters of the design of combined shield with dynamic electromagnetic shielding system, the components of which are vectors of parameters of a solid passive electromagnetic shield $\boldsymbol{X}_{pss}$, a multi-circuit passive electromagnetic shield $\boldsymbol{X}_{pcs}$, geometric parameters $\boldsymbol{X}_{aqs}$ of compensation windings of an active shielding system, positions $\boldsymbol{X}_{asp}$ of magnetic field sensors for active dynamic electromagnetic shield and regulator parameters $\boldsymbol{X}_{ars}$ of active dynamic electromagnetic shielding system

$$\boldsymbol{X} = \left(\boldsymbol{X}_{pss}, \boldsymbol{X}_{pcs}, \boldsymbol{X}_{aqs}, \boldsymbol{X}_{asp}, \boldsymbol{X}_{ars}\right). \qquad (15)$$

Then the instantaneous value of the vector $\boldsymbol{B}_R(\boldsymbol{X}, \boldsymbol{\delta}, P_i, t)$ of the resulting magnetic field induction is calculated as the following sum

$$\boldsymbol{B}_R(\boldsymbol{X}, \boldsymbol{\delta}, P_i, t) = \boldsymbol{B}_{ipl}(\boldsymbol{\delta}, P_i, t) + \boldsymbol{B}_{pss}\left(\boldsymbol{X}_{pss}, P_i, t\right) + \boldsymbol{B}_{pcs}\left(\boldsymbol{X}_{pcs}, P_i, t\right) + \boldsymbol{B}_{aqs}\left(\boldsymbol{X}_{aqs}, \boldsymbol{X}_{asp}, \boldsymbol{X}_{ars}, P_i, t\right). \qquad (16)$$

The requirements for the resulting magnetic field level apply not to the instantaneous value $\boldsymbol{B}_R(\boldsymbol{X}, \boldsymbol{\delta}, P_i, t)$ of the magnetic field induction vector, but to its effective value. Therefore, based on the instantaneous value $\boldsymbol{B}_R(\boldsymbol{X}, \boldsymbol{\delta}, P_i, t)$ of magnetic field induction vector we calculated effective value $\boldsymbol{B}_R(\boldsymbol{X}, \boldsymbol{\delta}, P_i)$ of resulting magnetic field induction in shielding space point P_i. A safe magnetic field level for habitation is usually regulated throughout the entire shielding space, so we introduce a vector $\boldsymbol{B}_R(\boldsymbol{X}, \boldsymbol{\delta})$ of effective magnetic field values. Its components are the effective magnetic field values $\boldsymbol{B}_R(\boldsymbol{X}, \boldsymbol{\delta}, P_i)$ at individual points P_i of the shielding space, covering the entire shielding space

$$\boldsymbol{B}_R(\boldsymbol{X}, \boldsymbol{\delta}) = \left(\boldsymbol{B}_R(\boldsymbol{X}, \boldsymbol{\delta}, P_1), \boldsymbol{B}_R(\boldsymbol{X}, \boldsymbol{\delta}, P_2), \ldots \boldsymbol{B}_R(\boldsymbol{X}, \boldsymbol{\delta}, P_n)\right)^T. \qquad (17)$$

Then the problem of designing a combined shield is reduced to solving a nonlinear minimax vector optimization problem $\boldsymbol{B}_R(\boldsymbol{X}, \boldsymbol{\delta})$. In the process of this problem solving it is necessary to minimize $\boldsymbol{B}_R(\boldsymbol{X}, \boldsymbol{\delta})$) (14) or (16) by the vector $\boldsymbol{X}$ (9) or (15) of sought parameters, but to maximize this same $\boldsymbol{B}_R(\boldsymbol{X}, \boldsymbol{\delta})$ by the vector $\boldsymbol{\delta}$ of uncertainty parameters.

Metaheuristic optimization algorithm. A distinctive feature of the nonlinear minimax vector optimization problem (15) or (17) is its multi-extremality, which is due to the nature of the original nonlinear functions. Furthermore, the scalar objective functions that are components of the vector objective function are antagonistic. This is due to the nature of the compensation of the initial magnetic field at a specific point in the shielding space. When minimizing the magnetic field level at a particular point in the shielding space, the magnetic field level at other points in the shielding space increases due to undercompensation or overcompensation of the original magnetic field using a combined electromagnetic shield.

To solve such complex, nonlinear and multidimensional optimization problems metaheuristic algorithms of group intelligence are widely used. From metaheuristic algorithms the most widely used are genetic optimization, particle swarm optimization (PSO), white whale optimization, gray wolf optimization, wind driven optimization, bacterial foraging optimization algorithm, binary particle swarm optimization, harmony search algorithm, flower pollination algorithm, harmony flower pollination algorithm, multiverse optimization algorithm, coco search algorithm and many other algorithms that model the group intelligence of the behavior of a swarm of living organisms. To improve computing capabilities, a combination of these metaheuristic algorithms is used, and these evolutionary algorithms of group intelligence are also used simultaneously with deterministic algorithms – sequential quadratic programming, Levenberg-Marquardt algorithms and many others.

Currently, it seems that various types of heuristic algorithms based on PSO are most widely used.

Consider calculated nonlinear minimax vector optimization problem based on PSO. Let's first look initial value of sought parameters vector $\boldsymbol{X}$ and external parametric perturbations vectors $\boldsymbol{\delta}$. for nonlinear minimax vector optimization problem calculated by PSO.

Nonlinear minimax vector optimization problem required parameters (17) desired parameters vectors $\boldsymbol{X}$ and uncertainties parameters vectors $\boldsymbol{\delta}$. It is necessary to minimize nonlinear minimax vector optimization problem (17) by parameters vectors $\boldsymbol{X}$ but maximize the same nonlinear minimax vector optimization problem by uncertainty parameters vector $\boldsymbol{\delta}$. Therefore, each particle i of swarm j included both position $x_{ij}(t)$, $\delta_{ij}(t)$ and velocity $v_{ij}(t)$, $u_{ij}(t)$ components for both required vector $\boldsymbol{X}$ and vector $\boldsymbol{\delta}$ calculated.

$$x_{ij}(t+1) = x_{ij}(t) + v_{ij}(t+1); \tag{18}$$

$$\delta_{ij}(t+1) = \delta_{ij}(t) + u_{ij}(t+1), \tag{19}$$

where

$$v_{ij}(t+1) = w_j v_{ij}(t) + c_{1j} r_{1j}(t) H\left(p_{1j} - \varepsilon_{1j}(t)\right)\left[y_{ij}(t) - \ldots \right.$$
$$\left. \ldots - {}_{ij}(t)\right] + c_{2j} r_{2j}(t) H\left(p_{2j} - \varepsilon_{2j}(t)\right)\left[y^*_j(t) - x_{ij}(t)\right]; \tag{20}$$

$$u_{ij}(t+1) = w_j u_{ij}(t) + c_{1j} r_{1j}(t) H\left(p_{1j} - \varepsilon_{1j}(t)\right)\left[z_{ij}(t) - \ldots \right.$$
$$\left. \ldots - \delta_{ij}(t)\right] + c_{2j} r_{2j}(t) H\left(p_{2j} - \varepsilon_{2j}(t)\right)\left[z^*_j(t) - \delta_{ij}(t)\right] \tag{21}$$

In fact, all varieties of PSO algorithms are implementations of random search algorithms of first-order order. In this case, the role of the derivative is played by the random direction in which the change in the objective function is greatest. It is well known that first-order methods are most effective when searching far from the optimum. As the optimum is approached, the rate of change of the objective function decreases, and consequently, the effectiveness of first-order methods declines. Furthermore, as the extremum is approached, zigzag movements are possible, with the extremum point jumping. In a nearly stationary region, second-order methods are more effective, using both first and second derivatives to find the extremum.

Let us consider a heuristic algorithm for random search based on a swarm of particle motion, which simultaneously uses the velocities and accelerations of particles – analogs of the first and second derivatives, calculated on the basis of random search [47]. Let us denote the initial values of the vectors $\boldsymbol{X}_{ij}(t)$ and $\boldsymbol{\delta}_{ij}(t)$, which are calculated using the PSO. Then the step $\boldsymbol{d}_{ijx}(t)$ of further changing the vector $\boldsymbol{X}_{ij}(t)$ is calculated as the solution of the problem of minimizing the quadratic objective function.

Minimize

$$\left\langle \boldsymbol{F}(\boldsymbol{X}_{ij}(t), \boldsymbol{\delta}_{ij}(t)) \right\rangle + 1/2 \boldsymbol{d}^T_{ijx}(t) \boldsymbol{H}_{ijx}(t) \boldsymbol{d}_{ijx}(t) + \ldots$$
$$\ldots + J^T_{ijx}(t) \boldsymbol{d}_{ijx}(t). \tag{22}$$

Also the step $\boldsymbol{d}_{ij\delta}(t)$ of further changing the vector $\boldsymbol{\delta}_{ij}(t)$ is calculated as the solution of the problem of maximizing the quadratic objective function.

Maximize

$$\left\langle \boldsymbol{F}(\boldsymbol{X}_{ij}(t), \boldsymbol{\delta}_{ij}(t)) \right\rangle + 1/2 \boldsymbol{d}^T_{ij\delta}(t) \boldsymbol{H}_{ij\delta}(t) \boldsymbol{d}_{ij\delta}(t) + \ldots$$
$$\ldots + J_{ij\delta}{}^T(t) \boldsymbol{d}_{ij\delta}(t). \tag{23}$$

In these both quadratic objective function (22), (23) the components of Jacobian matrices $\boldsymbol{J}_{ijx}(t)$, $\boldsymbol{J}_{ij\delta}(t)$ and Hessian matrices $\boldsymbol{H}_{ijx}(t)$, $\boldsymbol{H}_{ij\delta}(t)$, respectively, along vectors $\boldsymbol{X}_{ij}(t)$ and $\boldsymbol{\delta}_{ij}(t)$ calculated from velocities $v_{ij}(t)$, $u_{ij}(t)$ and accelerations $A_{ijx}(t)$, $A_{ij\delta}(t)$ of particle i of swarm j movement from $x_{ij}(t)$, $\delta_{ij}(t)$ positions.

Particles movement accelerations $A_{ijx}(t)$, $A_{ij\delta}(t)$ calculated based on velocities $v_{ij}(t)$, $u_{ij}(t)$ as

$$A_{ijx}(t+1) = v_{ij}(t+1) - v_{ij}(t); \tag{24}$$

$$A_{ij\delta}(t+1) = u_{ij}(t+1) - u_{ij}(t). \tag{25}$$

Then, to minimize nonlinear minimax vector optimization problem by $\boldsymbol{X}_{ij}(t)$ and to maximize nonlinear minimax vector optimization problem by $\delta_{ij}(t)$ step size optimal values $d_{ijx}(t)$ and $d_{ij\delta}(t)$ calculated as

$$A_{ijx}(t) d_{ijx}(t) + v_{ij}(t) = 0; \tag{26}$$

$$A_{ij\delta}(t) d_{ij\delta}(t) + u_{ij}(t) = 0. \tag{27}$$

And then particle motion calculated as

$$x_{ij}(t+1) = x_{ij}(t) + \alpha_{ijx}(t) d_{ijx}(t); \tag{28}$$

$$\delta_{ij}(t+1) = \delta_{ij}(t) + \alpha_{ij\delta}(t) d_{ij\delta}(t). \tag{29}$$

In conclusion, we note that to calculate the optimal values of the motion steps $\boldsymbol{d}_{ijx}(t)$ and $\boldsymbol{d}_{ij\delta}(t)$ to minimize the objective function (22) and maximize the objective function (23), it is necessary to calculate the inverse Hessian matrices $\boldsymbol{H}_{ijx}(t)$, $\boldsymbol{H}_{ij\delta}(t)$, respectively, along vectors $\boldsymbol{X}_{ij}(t)$ and $\boldsymbol{\delta}_{ij}(t)$. Random search of this matrices are calculated from velocities $v_{ij}(t)$, $u_{ij}(t)$ and accelerations $A_{ijx}(t)$, $A_{ij\delta}(t)$ of particle i of swarm j movement from $x_{ij}(t)$, $\delta_{ij}(t)$ positions. To improve computational efficiency, a stochastic analogue of the Levenberg-Marquardt algorithm is used. The step sizes are calculated as

$$\left\{ \boldsymbol{J}_{ijx}{}^T(t) \boldsymbol{J}_{ijx}(t) + \lambda_t diag\left[\boldsymbol{J}_{ijx}{}^T(t) \boldsymbol{J}_{ijx}(t) \right] \right\} \boldsymbol{d}_{ijx}(t) =$$
$$= -\boldsymbol{J}_{ijx}{}^T(t) \boldsymbol{F}(\boldsymbol{X}_{ij}(t), \boldsymbol{\delta}_{ij}(t); \tag{30}$$

$$\left\{ \boldsymbol{J}_{ij\delta}{}^T(t) \boldsymbol{J}_{ij\delta}(t) + \lambda_t diag\left[\boldsymbol{J}_{ij\delta}{}^T(t) \boldsymbol{J}_{ij\delta}(t) \right] \right\} \boldsymbol{d}_{ij\delta}(t) =$$
$$= -\boldsymbol{J}_{ij\delta}{}^T(t) \boldsymbol{F}(\boldsymbol{X}_{ij}(t), \boldsymbol{\delta}_{ij}(t). \tag{31}$$

In this case, there is no need to calculate the inverse Hessian matrix and particle motion calculated by (28, 29).

When nonlinear minimax vector optimization problem global optimum calculated from Pareto sets of optimal solutions it is necessary binary preference relations used [31, 32].

Simulation results. As an example, Fig. 2 shows three-dimensional magnetic field level distribution with combined shield with of a multi-circuit passive shield when only one passive shield is operating (*a*), when only one active shield is operating (*b*), and when a combined shield with a multi-circuit passive shield is operating (*c*). As can be seen from Fig. 2,*a*, when only one multi-loop passive shield is in operation, the level of induction in the shielding space is practically independent of the width of the passive shield. As can be seen from Fig. 2,*b*, when only one active shield is in operation, the level of induction in the shielding space is approximately 2–3 times lower than when only one multi-circuit passive shield is in operation. Moreover, the level of induction in the shielding space increases significantly at the edges of the shielding zone, which is due to the finite length of the compensation windings of the active shield. As can be seen from Fig. 2,*c*, when operating a combined shield with a multi-contour passive shield, the level of induction in the shielding space is practically independent of the width of the passive shield.

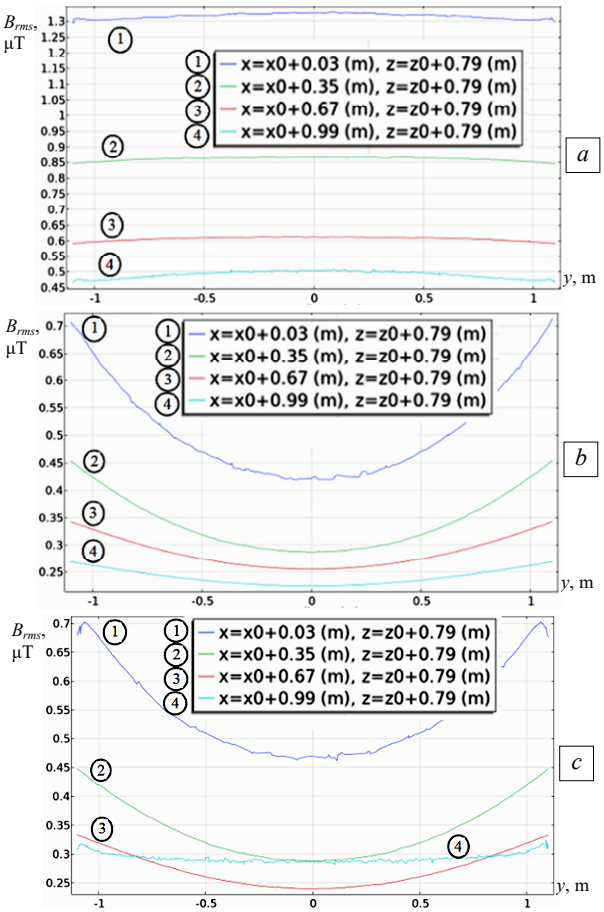

Fig. 2. Three-dimensional magnetic field level distribution with combined shield with multi-circuit passive shield

As a second example, Fig. 3 shows three-dimensional magnetic field level distribution with combined shield with solid passive shield when operating a combined shield with continuous passive shield without (*a*) and with side plates (*b*).

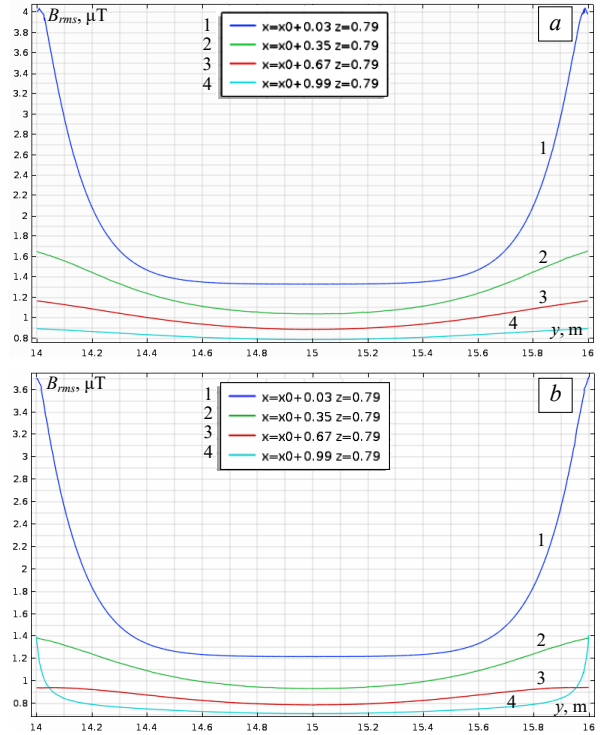

Fig. 3. Three-dimensional magnetic field level distribution with combined shield with solid passive shield

As follows from the comparison of these distributions of magnetic field induction, when using side plates from a continuous passive shield, the level of induction at the edges of the shielding space decreases compared to a continuous passive shield without side plates.

Experimental setup of a combined electromagnetic shielding systems. To conduct comprehensive experimental studies, an experimental setup of a combined electromagnetic shield was developed [48].

Figure 4 shows a solid passive shield without side plates. Figure 5 shows a solid passive shield with side plates on either side of the shield.

Figure 6 shows a multi-circuit passive shield.

Fig. 4. Solid passive shield without side plates

Fig. 5. Solid passive shield with side plates on either side of the shield

Fig. 6. Multi-circuit passive shield

Figure 7 shows the active shield compensation windings. This figure also shows magnetometers installed in the shielding space and designed to provide feedback on the resulting magnetic field. Figure 8 shows the power amplifiers for powering the active shield compensation windings. Figure 9 shows the electronic part of the control system for the active shield compensation windings.

Fig. 7. Active shield compensation windings

Fig. 8. Power amplifiers for powering the active shield compensation windings

Fig. 9. Control system electronic part for active shield compensation windings

Experimental studies results. Figure 10 shows experimentally measured three-dimensional magnetic field level distribution with combined shield with of a multi-circuit passive shield when only one passive shield is operating (*a*), when only one active shield is operating (*b*), and when a combined shield with a multi-circuit passive shield is operating (*c*). As can be seen from Fig. 10,*a*, when only one multi-loop passive shield is in operation, the level of induction in the shielding space is practically independent of the width of the passive shield. As can be seen from Fig. 10,*b*, when only one active shield is in operation, the level of induction in the shielding space is approximately 2–3 times lower than when only one multi-circuit passive shield is in operation. Moreover, the level of induction in the shielding space increases significantly at the edges of the shielding zone, which is due to the finite length of the compensation windings of the active shield. As can be seen from Fig. 10,*c*, when operating a combined shield with a multi-contour passive shield, the level of induction in the shielding space is practically independent of the width of the passive shield.

Figure 11 shows experimentally measured three dimensions magnetic field level distribution with combined shield with solid passive shield during operation of a combined shield with a continuous passive shield without (*a*) and with side plates (*b*).

How should these experimental distributed magnetic field inductions be compared, using side plates of a continuous passive screen, induction in the central part and at the edges of the screen, displacement of space compared to continuous passive light without side plates.

Based on the comparison of the experimentally measured three dimensions magnetic field level distribution (Fig. 10, 11) and the results of modeling three-dimensional magnetic field level distribution (Fig. 2, 3), we can conclude that experimentally measured induction levels values of magnetic field distribution coincide with calculated magnetic field distributions with 20 % accuracy.

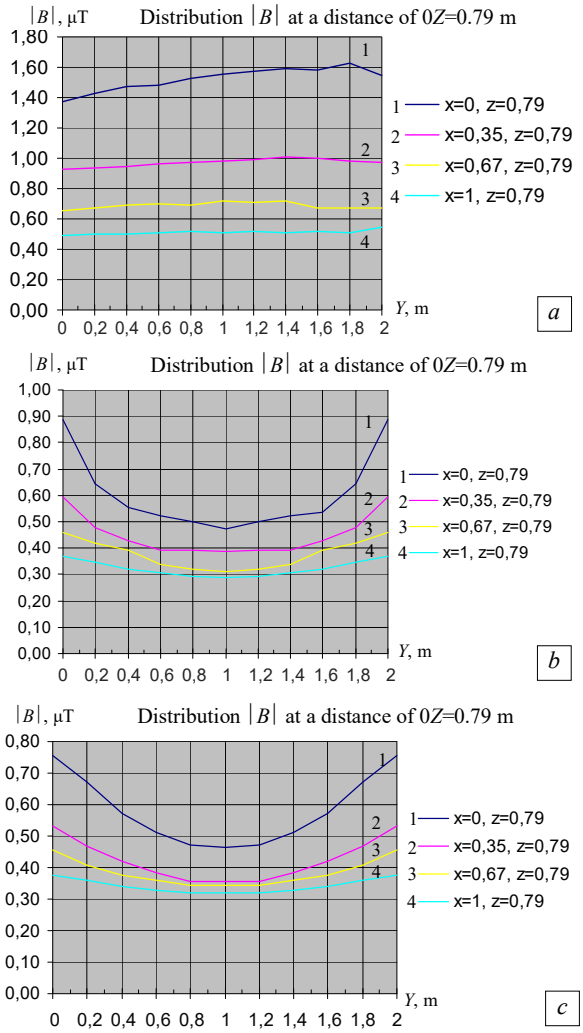

Fig. 10. Experimentally measured three dimensions magnetic field level distribution with combined shield with multi-circuit passive shield

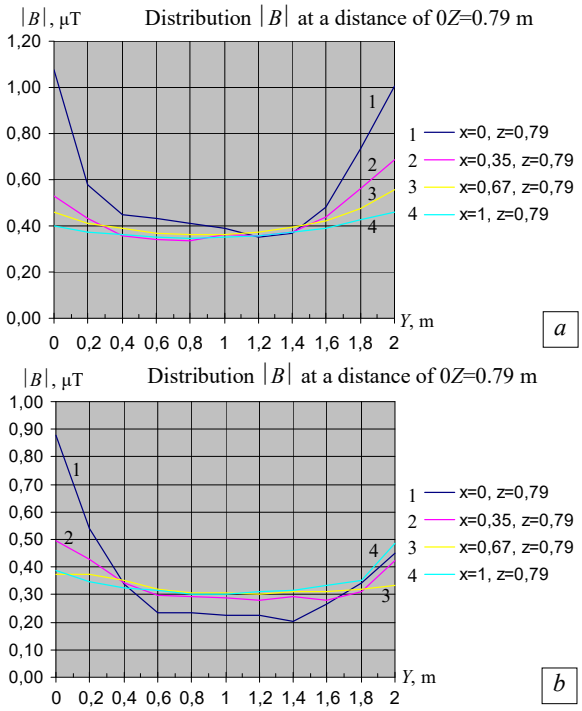

Fig. 11. Experimentally measured three dimensions magnetic field level distribution with combined shield with solid passive shield

Conclusions.

1. For the first time methodology of multi objective design of active-passive electromagnetic shielding system, consisting of active and solid self or multi-circuit passive parts, based on metaheuristic optimization algorithm developed, which allows to improve shielding efficiency of initial magnetic field in residential building edges generated by overhead power lines to sanitary standards level.

2. A new solution method for active-passive shielding system design developed based on solution of the geometric inverse problem of magnetostatics for the resulting magnetic field generated by the transmission line wires, which made it possible to calculate the coordinates of the spatial arrangement of compensation windings of the active shielding system and a passive shield in the form of a solid or multi-loop shield, as well as the currents and phases in the compensation windings, parameters of regulators of the open and closed controls of the two degrees of freedom active shielding system and parameters of positions of magnetic field sensors of the active shielding system.

3. A new solution method for geometric inverse problem based on minimax vector nonlinear programming problem is proposed. The geometric forward problem solved based on Maxwell's equation solutions for magnetic field three-dimensional model using the COMSOL Multiphysics software. The minimax vector nonlinear programming problem calculated based on the metaeristic optimization algorithm point from Pareto optimal solutions taking into account binary preference relations, which allows to reduce the computation time.

4. Results of theoretical and experimental studies of different types designed combined active and solid or multi-circuit passive shielding system efficiency for magnetic field created by overhead power lines are given. Results of experimental studies confirmed the correctness of the main theoretical principles. Experimentally measured induction levels values of resulting magnetic field distribution coincide with calculated magnetic field distributions with 20 % accuracy.

5. Practical recommendations for the reasonable choice of the coordinates of the spatial arrangement of compensation windings of the active shielding system and a passive shield in the form of a solid or multi-loop shield, as well as the currents and phases in the compensation windings, parameters of regulators of the open and closed controls of the two degrees of freedom active shielding system and parameters of positions of magnetic field sensors of the active shielding system for magnetic field generated by overhead power lines in residential building space are given.

6. It is planned to practically realization of developed methodology for the multi objective design of active-passive electromagnetic shielding systems of magnetic fields for residential buildings located near 110 kV overhead power transmission lines to normalize magnetic field level in real residential building.

Conflict of interest. The authors declare that they have no conflicts of interest.

REFERENCES

1. Sung H., Ferlay J., Siegel R.L., Laversanne M., Soerjomataram I., Jemal A., Bray F. Global Cancer Statistics 2020: GLOBOCAN Estimates of Incidence and Mortality Worldwide for 36 Cancers in 185 Countries. *CA: A Cancer Journal for Clinicians*, 2021, vol. 71, no. 3, pp. 209-249. doi: https://doi.org/10.3322/caac.21660.

2. *Directive 2013/35/EU of the European Parliament and of the Council of 26 June 2013 on the minimum health and safety requirements regarding the exposure of workers to the risks arising from physical agents (electromagnetic fields)*. Available at: http://data.europa.eu/eli/dir/2013/35/oj (Accessed 20 May 2025).

3. *The International EMF Project. Radiation & Environmental Health Protection of the Human Environment World Health Organization*. 1996. 2 p. Available at: https://www.who.int/initiatives/the-international-emf-project (Accessed 20 May 2025).

4. Rozov V.Y., Reutskiy S.Y., Pelevin D.Y., Kundius K.D. Magnetic field of electrical heating cable systems of the floors for residential premises. *Electrical Engineering & Electromechanics*, 2024, no. 5, pp. 48-57. doi: https://doi.org/10.20998/2074-272X.2024.5.07.

5. Rozov V.Y., Reutskiy S.Y., Kundius K.D. Protection of workers against the magnetic field of 330-750 kV overhead power lines when performing work without removing the voltage under load. *Electrical Engineering & Electromechanics*, 2024, no. 4, pp. 70-78. doi: https://doi.org/10.20998/2074-272X.2024.4.09.

6. Rozov V.Y., Pelevin D.Y., Kundius K.D. Simulation of the magnetic field in residential buildings with built-in substations based on a two-phase multi-dipole model of a three-phase current conductor. *Electrical Engineering & Electromechanics*, 2023, no. 5, pp. 87-93. doi: https://doi.org/10.20998/2074-272X.2023.5.13.

7. Rozov V.Y., Pelevin D.Y., Reutskiy S.Y., Kundius K.D., Vorushylo A.O. The complex influence of external and internal electricity networks on the magnetic field level in residential premises of buildings. *Electrical Engineering & Electromechanics*, 2025, no. 4, pp. 11-19. doi: https://doi.org/10.20998/2074-272X.2025.4.02.

8. Salceanu A., Paulet M., Alistar B.D., Asiminicesei O. Upon the contribution of image currents on the magnetic fields generated by overhead power lines. *2019 International Conference on Electromechanical and Energy Systems (SIELMEN)*. 2019. doi: https://doi.org/10.1109/sielmen.2019.8905880.

9. Del Pino Lopez J.C., Romero P.C. Influence of different types of magnetic shields on the thermal behavior and ampacity of underground power cables. *IEEE Transactions on Power Delivery*, Oct. 2011, vol. 26, no. 4, pp. 2659-2667. doi: https://doi.org/10.1109/tpwrd.2011.2158593.

10. Hasan G.T., Mutlaq A.H., Ali K.J. The Influence of the Mixed Electric Line Poles on the Distribution of Magnetic Field. *Indonesian Journal of Electrical Engineering and Informatics (IJEEI)*, 2022, vol. 10, no. 2, pp. 292-301. doi: https://doi.org/10.52549/ijeei.v10i2.3572.

11. Victoria Mary S., Pugazhendhi Sugumaran C. Investigation on magneto-thermal-structural coupled field effect of nano coated 230 kV busbar. *Physica Scripta*, 2020, vol. 95, no. 4, art. no. 045703. doi: https://doi.org/10.1088/1402-4896/ab6524.

12. Ippolito L., Siano P. Using multi-objective optimal power flow for reducing magnetic fields from power lines. *Electric Power Systems Research*, 2004, vol. 68, no. 2, pp. 93-101. doi: https://doi.org/10.1016/S0378-7796(03)00151-2.

13. Barsali S., Giglioli R., Poli D. Active shielding of overhead line magnetic field: Design and applications. *Electric Power Systems Research*, May 2014, vol. 110, pp. 55-63. doi: https://doi.org/10.1016/j.epsr.2014.01.005.

14. Bavastro D., Canova A., Freschi F., Giaccone L., Manca M. Magnetic field mitigation at power frequency: design principles and case studies. *IEEE Transactions on Industry Applications*, May 2015, vol. 51, no. 3, pp. 2009-2016. doi: https://doi.org/10.1109/tia.2014.2369813.

15. Beltran H., Fuster V., García M. Magnetic field reduction screening system for a magnetic field source used in industrial applications. *9 Congreso Hispano Luso de Ingeniería Eléctrica (9 CHLIE)*, 2005, pp. 84-99.

16. Bravo-Rodríguez J., Del-Pino-López J., Cruz-Romero P. A Survey on Optimization Techniques Applied to Magnetic Field Mitigation in Power Systems. *Energies*, 2019, vol. 12, no. 7, art. no. 1332. doi: https://doi.org/10.3390/en12071332.

17. Canova A., del-Pino-López J.C., Giaccone L., Manca M. Active Shielding System for ELF Magnetic Fields. *IEEE Transactions on Magnetics*, March 2015, vol. 51, no. 3, pp. 1-4. doi: https://doi.org/10.1109/tmag.2014.2354515.

18. Canova A., Giaccone L. Real-time optimization of active loops for the magnetic field minimization. *International Journal of Applied Electromagnetics and Mechanics*, Feb. 2018, vol. 56, pp. 97-106. doi: https://doi.org/10.3233/jae-172286.

19. Canova A., Giaccone L., Cirimele V. Active and passive shield for aerial power lines. *Proc. of the 25th International Conference on Electricity Distribution (CIRED 2019)*, paper no. 1096.

20. Houicher S.-E., Djekidel R., Bessidek S.A. Optimized passive and active shielding of magnetic induction generated by ultra-high-voltage overhead power lines. *International Journal of Electrical and Computer Engineering (IJECE)*, 2025, vol. 15, no. 6, pp. 5144-5161. doi: https://doi.org/10.11591/ijece.v15i6.pp5144-5161.

21. Meng Q., Wang Z., Lin Q., Ju D., Liang X., Xian D. Theoretical Analysis of a Magnetic Shielding System Combining Active and Passive Modes. *Nanomaterials*, 2024, vol. 14, no. 6, art. no. 538. doi: https://doi.org/10.3390/nano14060538.

22. Cruz P., Izquierdo C., Burgos M., Ferrer L.F., Soto F., Llanos C., Pacheco J.D. Magnetic field mitigation in power lines with passive and active loops. *CIGRE Session Materials*, 2002, reference 36-107.

23. Radwan R.M., Abdel-Salam M., Samy M.M., Mahdy A.M. Passive and active shielding of magnetic fields underneath overhead transmission lines theory versus experiment. *17th International Middle East Power Systems Conference*, 2015. pp. 1-10.
24. Radwan R., Abdel-Salam M., Mahdy A., Samy M. Laboratory Validation of Calculations of Magnetic Field Mitigation Underneath Transmission Lines Using Passive and Active Shield Wires. *Innovative Systems Design and Engineering*, 2011, vol. 2, no. 4, pp. 218-232.
25. Ziolkowski M., Gratkowski S. Active, passive and dynamic shielding of static and low frequency magnetic fields. *15th International Symposium on Theoretical Engineering*, 2009, pp. 370-374.
26. Grinchenko V.S. Mitigation of three-phase power line magnetic field by grid electromagnetic shield. *Technical Electrodynamics*, 2018, no. 4, pp. 29-32. (Ukr). doi: https://doi.org/10.15407/techned2018.04.029.
27. Celozzi S. Active compensation and partial shields for the power-frequency magnetic field reduction. *2002 IEEE International Symposium on Electromagnetic Compatibility*, Minneapolis, MN, USA, 2002, vol. 1, pp. 222-226. doi: https://doi.org/10.1109/isemc.2002.1032478.
28. Celozzi S., Garzia F. Active shielding for power-frequency magnetic field reduction using genetic algorithms optimization. *IEE Proceedings - Science, Measurement and Technology*, 2004, vol. 151, no. 1, pp. 2-7. doi: https://doi.org/10.1049/ip-smt:20040002.
29. Celozzi S., Garzia F. Magnetic field reduction by means of active shielding techniques. *WIT Transactions on Biomedicine and Health*, 2003, vol. 7, pp. 79-89. doi: https://doi.org/10.2495/ehr030091.
30. Martynenko G. Analytical Method of the Analysis of Electromagnetic Circuits of Active Magnetic Bearings for Searching Energy and Forces Taking into Account Control Law. *2020 IEEE KhPI Week on Advanced Technology (KhPIWeek)*, 2020, pp. 86-91. doi: https://doi.org/10.1109/KhPIWeek51551.2020.9250138.
31. Popov A., Tserne E., Volosyuk V., Zhyla S., Pavlikov V., Ruzhentsev N., Dergachov K., Havrylenko O., Shmatko O., Averyanova Y., Ostroumov I., Kuzmenko N., Sushchenko O., Zaliskyi M., Solomentsev O., Kuznetsov B., Nikitina T. Invariant Polarization Signatures for Recognition of Hydrometeors by Airborne Weather Radars. *Computational Science and Its Applications – ICCSA 2023. Lecture Notes in Computer Science*, 2023, vol. 13956, pp. 201-217. doi: https://doi.org/10.1007/978-3-031-36805-9_14.
32. Sushchenko O., Averyanova Y., Ostroumov I., Kuzmenko N., Zaliskyi M., Solomentsev O., Kuznetsov B., Nikitina T., Havrylenko O., Popov A., Volosyuk V., Shmatko O., Ruzhentsev N., Zhyla S., Pavlikov V., Dergachov K., Tserne E. Algorithms for Design of Robust Stabilization Systems. *Computational Science and Its Applications – ICCSA 2022. ICCSA 2022. Lecture Notes in Computer Science*, 2022, vol. 13375, pp. 198-213. doi: https://doi.org/10.1007/978-3-031-10522-7_15.
33. Ostroverkhov M., Chumack V., Monakhov E., Ponomarev A. Hybrid Excited Synchronous Generator for Microhydropower Unit. *2019 IEEE 6th International Conference on Energy Smart Systems (ESS)*, Kyiv, Ukraine, 2019, pp. 219-222. doi: https://doi.org/10.1109/ess.2019.8764202.
34. Ostroverkhov M., Chumack V., Monakhov E. Ouput Voltage Stabilization Process Simulation in Generator with Hybrid Excitation at Variable Drive Speed. *2019 IEEE 2nd Ukraine Conference on Electrical and Computer Engineering (UKRCON)*, Lviv, Ukraine, 2019, pp. 310-313. doi: https://doi.org/10.1109/ukrcon.2019.8879781.
35. Tytiuk V., Chornyi O., Baranovskaya M., Serhiienko S., Zachepa I., Tsvirkun L., Kuznetsov V., Tryputen N. Synthesis of a fractional-order $PI^{\lambda}D^{\mu}$-controller for a closed system of switched reluctance motor control. *Eastern-European Journal of Enterprise Technologies*, 2019, no. 2 (98), pp. 35-42. doi: https://doi.org/10.15587/1729-4061.2019.160946.
36. Shchur I., Turkovskyi V. Comparative Study of Brushless DC Motor Drives with Different Configurations of Modular Multilevel Cascaded Converters. *2020 IEEE 15th International Conference on Advanced Trends in Radioelectronics, Telecommunications and Computer Engineering (TCSET)*, Lviv-Slavske, Ukraine, 2020, pp. 447-451. doi: https://doi.org/10.1109/tcset49122.2020.235473.
37. Volosyuk V., Zhyla S., Pavlikov V., Ruzhentsev N., Tserne E., Popov A., Shmatko O., Dergachov K., Havrylenko O., Ostroumov I., Kuzmenko N., Sushchenko O., Averyanova Yu., Zaliskyi M., Solomentsev O., Kuznetsov B., Nikitina T. Optimal Method for Polarization Selection of Stationary Objects Against the Background of the Earth's Surface. *International Journal of Electronics and Telecommunications*, 2022, vol. 68, no. 1, pp. 83-89. doi: https://doi.org/10.24425/ijet.2022.139852.
38. Halchenko V., Trembovetska R., Bazilo C., Tychkova N. Computer Simulation of the Process of Profiles Measuring of Objects Electrophysical Parameters by Surface Eddy Current Probes. *Lecture Notes on Data Engineering and Communications Technologies*, 2023, vol. 178, pp. 411-424. doi: https://doi.org/10.1007/978-3-031-35467-0_25.
39. Halchenko V., Bacherikov D., Filimonov S., Filimonova N. Improvement of a Linear Screw Piezo Motor Design for Use in Accurate Liquid Dosing Assembly. *Smart Technologies in Urban Engineering. STUE 2022. Lecture Notes in Networks and Systems*, 2023, vol. 536, pp. 237-247. doi: https://doi.org/10.1007/978-3-031-20141-7_22.
40. Maksymenko-Sheiko K.V., Sheiko T.I., Lisin D.O., Petrenko N.D. Mathematical and Computer Modeling of the Forms of Multi-Zone Fuel Elements with Plates. *Journal of Mechanical Engineering*, 2022, vol. 25, no. 4, pp. 32-38. doi: https://doi.org/10.15407/pmach2022.04.032.
41. Hontarovskyi P.P., Smetankina N.V., Ugrimov S.V., Garmash N.H., Melezhyk I.I. Computational Studies of the Thermal Stress State of Multilayer Glazing with Electric Heating. *Journal of Mechanical Engineering*, 2022, vol. 25, no. 1, pp. 14-21. doi: https://doi.org/10.15407/pmach2022.02.014.
42. Kostikov A.O., Zevin L.I., Krol H.H., Vorontsova A.L. The Optimal Correcting the Power Value of a Nuclear Power Plant Power Unit Reactor in the Event of Equipment Failures. *Journal of Mechanical Engineering*, 2022, vol. 25, no. 3, pp. 40-45. doi: https://doi.org/10.15407/pmach2022.03.040.
43. Rusanov A.V., Subotin V.H., Khoryev O.M., Bykov Y.A., Korotaiev P.O., Ahibalov Y.S. Effect of 3D Shape of Pump-Turbine Runner Blade on Flow Characteristics in Turbine Mode. *Journal of Mechanical Engineering*, 2022, vol. 25, no. 4, pp. 6-14. doi: https://doi.org/10.15407/pmach2022.04.006.
44. Kurennov S., Smetankina N., Pavlikov V., Dvoretskaya D., Radchenko V. Mathematical Model of the Stress State of the Antenna Radome Joint with the Load-Bearing Edging of the Skin Cutout. *Lecture Notes in Networks and Systems*, 2022, vol. 305, pp. 287-295. doi: https://doi.org/10.1007/978-3-030-83368-8_28.
45. Kurennov S., Smetankina N. Stress-Strain State of a Double Lap Joint of Circular Form. Axisymmetric Model. *Lecture Notes in Networks and Systems*, 2022, vol 367 LNNS, pp. 36-46. doi: https://doi.org/10.1007/978-3-030-94259-5_4.
46. Smetankina N., Merkulova A., Merkulov D., Misiura S., Misiura I. Modelling Thermal Stresses in Laminated Aircraft Elements of a Complex Form with Account of Heat Sources. *Lecture Notes in Networks and Systems*, 2023, vol. 534 LNNS, pp. 233-246. doi: https://doi.org/10.1007/978-3-031-15944-2_22.
47. Hashim F.A., Hussain K., Houssein E.H., Mabrouk M.S., Al-Atabany W. Archimedes optimization algorithm: a new metaheuristic algorithm for solving optimization problems. *Applied Intelligence*, 2021, vol. 51, no. 3, pp. 1531-1551. doi: https://doi.org/10.1007/s10489-020-01893-z.
48. Baranov M.I., Rozov V.Y., Sokol Y.I. To the 100th anniversary of the National Academy of Sciences of Ukraine – the cradle of domestic science and technology. *Electrical Engineering & Electromechanics*, 2018, no. 5, pp. 3-11. doi: https://doi.org/10.20998/2074-272X.2018.5.01.

Received 13.09.2025
Accepted 29.11.2025
Published 02.03.2026

B.I. Kuznetsov[1], *Doctor of Technical Science, Professor,*
A.S. Kutsenko[2], *Doctor of Technical Science, Professor*
T.B. Nikitina[3], *Doctor of Technical Science, Professor,*
I.V. Bovdui[1], *PhD, Senior Research Scientist,*
K.V. Chunikhin[1], *PhD, Senior Research Scientist,*
V.V. Kolomiets[3], *PhD, Assistant Professor,*
[1] Anatolii Pidhornyi Institute of Power Machines and Systems of the National Academy of Sciences of Ukraine,
2/10, Komunalnykiv Str., Kharkiv, 61046, Ukraine,
e-mail: kuznetsov.boris.i@gmail.com (Corresponding Author)
[2] National Technical University «Kharkiv Polytechnic Institute»,
2, Kyrpychova Str., Kharkiv, 61002, Ukraine.
[3] Bakhmut Education Research and Professional Pedagogical Institute V.N. Karazin Kharkiv National University,
9a, Nosakov Str., Bakhmut, Donetsk Region, 84511, Ukraine.

How to cite this article:
Kuznetsov B.I., Kutsenko A.S., Nikitina T.B., Bovdui I.V., Chunikhin K.V., Kolomiets V.V. The methodology of multi objective design of active-passive shielding system for overhead power lines magnetic field in residential buildings space based on metaheuristic optimization method. *Electrical Engineering & Electromechanics*, 2026, no. 2, pp. 40-50. doi: https://doi.org/10.20998/2074-272X.2026.2.06

UDC 621.314 https://doi.org/10.20998/2074-272X.2026.2.07

I.I. Alnaib, A.N. Alsammak

Intelligent unified power quality conditioner based photovoltaic to improve grid reliability and mitigate power quality issues

Problem. *Electrical distribution networks are plagued by power quality problems, which have a negative impact on sensitive electrical loads. These problems include reactive current, low power factor on the load side, and voltage harmonics, voltage sags and voltage swells on the grid voltage side. To address these issues, a unified power quality conditioner (UPQC) that combines shunt and series compensators is suggested. The* ***goal*** *of the work is to implement a UPQC integrated with a photovoltaic (PV) system to mitigate power quality problems in the power system, and boosting the grid supply through power injection from the PV system.* ***Methodology.*** *One of the less complex and effective ways to improve the grid's voltage quality is by using the unit vector template generation (UVTG) strategy as the composition technique (UPQC-P) through the UPQC series compensator. The synchronous reference frame (SRF) strategy through the UPQC shunt compensator to improve the current quality on the load side is used. To further optimize the SRF strategy, it is used the snake optimization (SO) to find the optimal values for the PI controller's parameters.* ***Results.*** *The UPQC-PV is used to mitigation the power quality issues in the grid and loads by UVTG and SRF techniques in series and shunt compensators, respectively.* ***Scientific novelty****. The composition technique (UPQC-P) through a series compensator and uses the SO for tuning the PI controller in the shunt compensator.* ***Practical value.*** *This study reduces the total harmonic distortion (THD) in the load voltage to 0.57 %, while the THD in the grid voltage remains at 10 %. It restores the load voltage to its reference value of 230 V during voltage sags (down to 161 V) and swells (up to 300 V) in the grid. Additionally, it mitigates the low power factor on the load side (0.707 lagging) to achieve a unity power factor in grid current, balances the unbalanced load current to a balanced grid current, and enhances grid stability by injecting power from the PV system into the grid.* References 33, table 3, figures 7.

Key words: **power quality, unified power quality conditioner, unit vector template generation, synchronous reference frame strategy, photovoltaic system.**

Проблема*. Розподільні електромережі страждають від проблем якості електроенергії, які негативно впливають на чутливі електричні навантаження. Ці проблеми включають реактивний струм, низький коефіцієнт потужності на стороні навантаження, а також гармоніки напруги, зниження та стрибки напруги на стороні напруги мережі. Для вирішення цих проблем пропонується єдиний стабілізатор якості електроенергії (UPQC), який поєднує шунтуючі та послідовні компенсатори.* ***Метою*** *роботи є впровадження UPQC, інтегрованого з фотоелектричною (PV) системою, для зменшення проблем якості електроенергії в енергосистемі та підвищення потужності мережі шляхом подачі енергії в мережу.* ***Методика****. Одним з менш складних та ефективних способів покращення якості напруги мережі є використання стратегії генерації шаблонів одиничних векторів (UVTG) як методу композиції (UPQC-P) за допомогою послідовного компенсатора UPQC. Використовується стратегія синхронної системи відліку (SRF) через компенсатор шунту UPQC для покращення якості струму на стороні навантаження. Для подальшої оптимізації стратегії SRF використовується оптимізацію типу «змійка» (SO), щоб знайти оптимальні значення параметрів ПІ-регулятора.* ***Результати****. Метод UPQC-PV використовується для зменшення проблем із якістю електроенергії в мережі та навантаженнях за допомогою методів UVTG та SRF у послідовних та шунтуючих компенсаторах відповідно.* ***Наукова новизна****. Метод композиції (UPQC-P) використовує послідовний компенсатор та використовує SO для налаштування ПІ-регулятора в шунтуючому компенсаторі.* ***Практична значимість*** *полягає у зменшенні загального коефіцієнта гармонійних спотворень (THD) у напрузі навантаження до 0,57 %, тоді як THD у напрузі мережі залишається на рівні 10 %, а також відновлення напруги навантаження до опорного значення 230 В під час зменшення (до 161 В) та зростань (до 300 В) напруги в мережі. Крім того, отримано зменшення низького коефіцієнта потужності на стороні навантаження (затримка 0,707) для досягнення одиничного коефіцієнта потужності в струмі мережі, вирівняння незбалансованого струму навантаження до збалансованого струму мережі та підвищення стабільності мережі шляхом введення енергії з PV системи в мережу.* Бібл. 33, табл. 3, рис. 7.

Ключові слова: **якість електроенергії, уніфікований стабілізатор якості електроенергії, генерація шаблону одиничного вектора, стратегія синхронної системи відліку, фотоелектрична система.**

Introduction. The primary goals of electrical distribution networks are to ensure a constant power flow from the grid and to provide consumers with a pure sinusoidal voltage and frequency [1]. Distribution networks have recently faced challenges with power quality, including imbalanced loads, harmonic load currents, and high reactive power consumption [2]. Additionally, these devices do not protect the customer's load end from surges, dips, fluctuations, imbalances, or voltage swells in the grid. To prevent power quality defects from activating their protective mechanisms, critical loads including medical devices and financial facilities that use uninterruptible power supplies require constant, sinusoidal, balanced voltages with a steady frequency and magnitude [3, 4]. This results in a financial loss due to decreased efficiency, time, quality, and consumer satisfaction [5]. The best solution for addressing voltage and current quality issues for sensitive loads seems to be a sort of robust, reliable device called a unified power quality conditioner (UPQC). One answer to many power quality issues is the UPQC, which combines shunt and series compensators [6]. The shunt component of the UPQC, connected in parallel to the load, delivers reactive power compensation, load unbalancing, and harmonic mitigation resulting from nonlinear loads. The series component of the UPQC, which is interconnected between the grid and the load, addresses issues related to sag, swell, variations, imbalance, and harmonic voltage in the grid [7].

The goal of the work is to implement a UPQC integrated with a photovoltaic (PV) system to mitigate power quality problems in the power system, and boosting the grid supply through power injection from the PV system.

Review of the literature. In 1998, Fujita and Akagi implemented the earliest use of UPQC utilizing a series active power filter (APF) and a shunt APF with an integrated DC link [8]. Subsequent years saw additional researchers examining the UPQC and developing various topologies, mathematical models, and control methodologies for it. The research article employs a single-phase UPQC to mitigate power quality challenges in grid-connected solar systems, including voltage sags and swells, as well as linear and nonlinear loads. The system employs a unit vector template generation (UVTG) control algorithm in both the shunt and series

inverters of the UPQC, utilizing a phase-locked loop (PLL) and the composition technique (UPQC-P) to enhance voltage and current quality [9]. The article presents an effective sizing methodology for a solar PV based on UPQC with distributed generation (UPQC-DG), which mitigates power quality concerns such as voltage sags and swells and reactive nonlinear loads while decreasing the supply current across all operational conditions through the PV system. The method employs an enhanced power angle control (PAC) technique utilizing nonlinear programming methods to equilibrate the reactive power load between series and shunt converters, the composition technique (UPQC-S) in the series converter, and the synchronous reference frame (SRF) theory in the shunt converter [10]. The study suggests improving the solar PV-based UPQC-DG to address power quality challenges, such as voltage sags and swells, reactive nonlinear loads, and to offer reactive power assistance to the grid. The system regulates load reactive electricity and exports it to the grid systematically. The control methodology integrates the composition approach (UPQC-S) within the series converter alongside PAC and SRF theory in the shunt converter. A PI controller manages reactive power flow, whereas the PAC approach allocates the reactive power load between series and shunt APFs to diminish the total rating [11]. This research examines the UPQC-PV's role in delivering regulated electricity and preserving power quality. The system utilises an adaptive notch filter-based instantaneous symmetrical component controller for series compensation of voltage sags and swells, the composition technique (UPQC-P), and a moving average filter employing an adaptive hyperbolic tangent function controller for shunt compensation to regulate current supply in case of nonlinear loads. Simulations validate the system's effectiveness, showing a significant reduction in total harmonic distortion (THD) from 33.45 % to 2.45 % [12]. This article describes a system that includes a standalone hydro turbine-driven permanent magnet synchronous generator that supplies sensitive and nonlinear loads through a UPQC-based energy storage system. The UPQC mitigates harmonic voltage supply and current quality problems, including reactive power compensation and harmonic removal, while modifying the load, incorporating series (the composition technique UPQC-P) and shunt compensators [13]. This research introduces a unified framework for adaptive and variable phase angle control in single-phase UPQC, employing the practical optimized-Volt-Ampere (VA) loading operational strategy and the universal flexible control method (the composition technique UPQC-S). The proposed approach can systematically and iteratively determine the optimal phase angle across different power ratings and various grid disturbances. This technique employs a gradual alteration of the phase angle to mitigate its impact on sensitive loads. A comparison with the UPQC-P approach revealed a reduction in VA loading with the proposed technique [14]. This paper proposes an operation scheme for the UPQC under VA capacity constraints using hierarchical optimization. The approach contains 3 optimization objectives:

1) reducing load voltage deviation;
2) improving the power factor of the power grid;
3) minimizing the total apparent power of the UPQC (the compositional approach UPQC-S) [15].

The research seeks to improve power quality in grid-connected renewable energy systems (PV-wind) with nonlinear loads. The study examines the deployment of the UPQC, which consists of a series of components utilizing the UVTG strategy and a shunt component employing the SRF algorithm. APFs are linked by a DC connection to alleviate harmonic distortions and voltage imbalances (sag and swell) referred to as the composition technique (UPQC-P) [16]. This article defines the Volterra expansion filter using the least mean square (LMS) and least mean square/fourth (LMS/F) control algorithms on UPQC. Additionally, a non dominated sorting genetic algorithm-II optimization method is employed to determine the PI controller gains within the Volterra LMS/F control algorithms. Voltage source disturbances are (sag, harmonic and unbalance), and 3-phase nonlinear loads. A zigzag transformer is applied on the load side to mitigate neutral current when the load configuration is a 3-phase system. Given that the UPQC circuit configuration is 3-phase 3-wire, the composition technique (UPQC-P) [17]. This paper discusses the treatment of power quality issues, including sag, swell, and nonlinear loads, through a UPQC-PV using the PAC strategy in the series converter, The composition technique (UPQC-S) and a shunt converter utilizing SRF strategy, alongside the optimization of PI controller parameters in the shunt converter via particle swarm optimization to enhance the stability and performance of the DC link voltage under varying operational conditions [18]. The study introduces a method that reduces demand on load voltage sensors and source current sensors in managing the series and parallel components of the UPQC device. The line voltage for 2 phases of the load was measured, and the 3rd phase was inferred, along with the source current. PV system was integrated with the UPQC device to enhance power quality and increase the reliability of the source by reducing the active power delivered to the load. The study examines system disturbances, including harmonics, asymmetrical voltage sags and swells (unbalance), nonlinear loads, and unbalanced loads by removing one of the load phases. The primary drawback of this paper is that, in instances of voltage imbalance in one phase, not only is the voltage of the unbalanced phase compensated, but the voltages of the remaining healthy phases are also compensated. Additionally, algorithms for maximizing power from the PV system are not employed, as it is directly connected to the UPQC device. The composition technique (UPQC-P) and 3-phase 3-wire type UPQC [19]. This paper proposes a method for implementing a variable leaky LMS adaptive compensation strategy as a replacement to a low-pass filter for tracking the fundamental component of current and voltage signals in the control of shunt and series inverters of the UPQC-PV, addressing power quality issues such as voltage sags, swells, and both balanced and unbalanced non-linear loads. The limitation of this technique depends on the estimation method employed. The approach is complex and challenging to calculate its optimal values. Furthermore, strategies designed to optimize power extraction from the solar system are not utilized, as it is directly linked to the UPQC device. The composition method (UPQC-P) and the 3-phase 3-wire type UPQC [20].

UPQC system configuration. Series and shunt compensators are integrated in UPQC-PV (Fig. 1). The 3-phase, 4-wire UPQC's power circuit consists of 2 voltage source inverters (VSIs) connected by a shared DC link capacitor at the DC bus. At its core, it consists [21, 22]:

1) The series compensator, situated between the grid supply and the load, serves as both a dynamic voltage restorer and a series compensator within the UPQC. This compensator work is to return the load voltage to its reference value while keeping the voltage at the consumer load unaffected by issues with the grid voltage.

2) The shunt compensators, also known as distribution compensators (DSTATCOMs) in the UPQC framework, are inverters that are linked in parallel with the load. Their purpose is to improve the current quality and reduce the unbalanced load current.

3) A UPQC consists of several passive components. These components include an AC coupling inductor to connect the 2 VSIs to the grid, a DC-link capacitor (also referred to as a DC bus capacitor) to supply DC voltage to the VSIs, and LC filters to minimize switching ripples in the outputs of the shunt and series compensators.

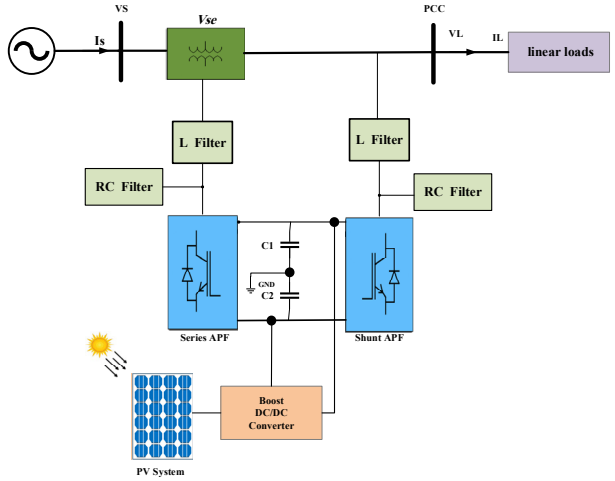

Fig. 1. Configuration of the UPQC-PV

Control technique for UPQC. Control strategy of series compensator. This section ensures that the load voltage meets the necessary values and is free of power quality issues by addressing voltage quality concerns related to sag, swell, and harmonics in the source voltage. An approach called UVTG is put into action by the control circuit. A PLL is used to produce the phase angle (ωt) at the source voltage's fundamental frequency. It then generates 3-phase signals at the same frequency, free of power quality concerns, and compares them to the load voltage. Afterwards, pulse width modulation (PWM) is used to generate the series inverter circuit's gate signals [23]. The UPQC series compensator (Fig. 2) is responsible for delivering load voltages free of distortion.

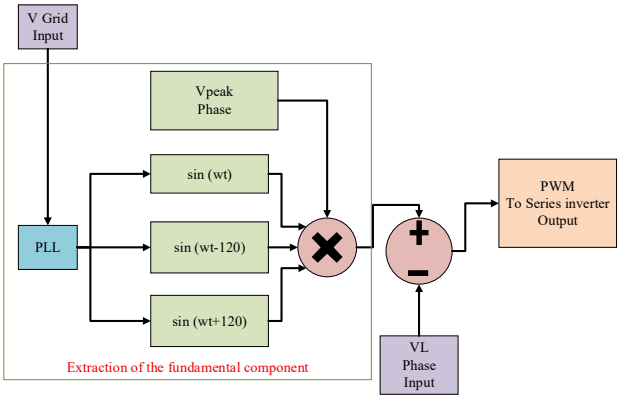

Fig. 2. The control circuit of series compensator in UPQC-based UVTG technique

Control strategy of the shunt compensator (DSTATCOM). This section addresses quality issues in the current source, specifically concerning low power factor and reactive power as well as imbalances resulting from uneven loads on the load side. The system regulates the DC link voltage via a PI controller [24], with its parameters optimized using the snake optimization (SO) algorithm to achieve optimal performance in the source current. Figure 3, which depicts the SRF theory, shows how to generate the reference current signal using the SRF method, moreover a $dq0$ frame is used to alter the load currents from an abc frame. After that, any harmonics in the I_d component are filtered out using the low pass filter (LPF). After that, it becomes the I_d fundamental, and then, to get the harmonic numbers, we subtract this component from the initial I_d value. After that, the PI controller's output signal is integrated with the value [25]. To generate the 3-phase source's fundamental frequency, use a PLL. By contrasting the reference currents with the 3-phase shunt compensator's output current, this technique uses hysteresis to produce gate signals for the shunt compensator [26].

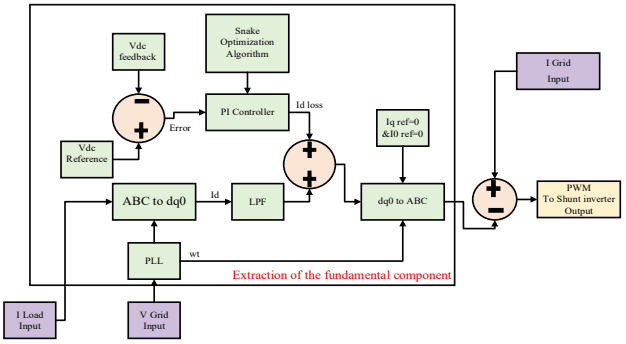

Fig. 3. The control circuit of shunt compensator in UPQC-based SRF technique

PV system control. To optimize solar power systems, the perturb and observe (P&O) algorithm makes incremental changes to the system and then monitors the impact of those changes on the system's power production. To find the best perturbation direction for the highest power, it compares the current and past power levels. To maximize the benefits of a solar system, boost converters are utilized by increasing the output voltage of the PV panel to the level necessary for the UPQC to operate with the minimal number of PV panels [27]. Using the maximum power point tracking approach, which is based on the P&O algorithm, is a prominent way to enhance the efficiency of UPQC. The P-V characteristics of PV panels as they are exposed to solar radiation are shown in Fig. 4.

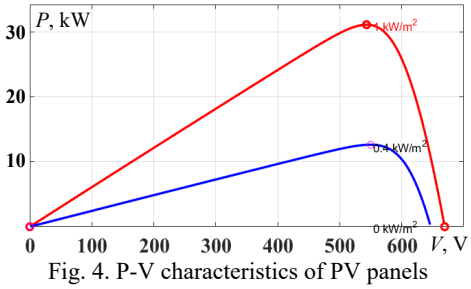

Fig. 4. P-V characteristics of PV panels

Figure 5 shows the flowchart of the P&O algorithm to find the maximum power under the influence of solar radiation and heat directed at the PV panels.

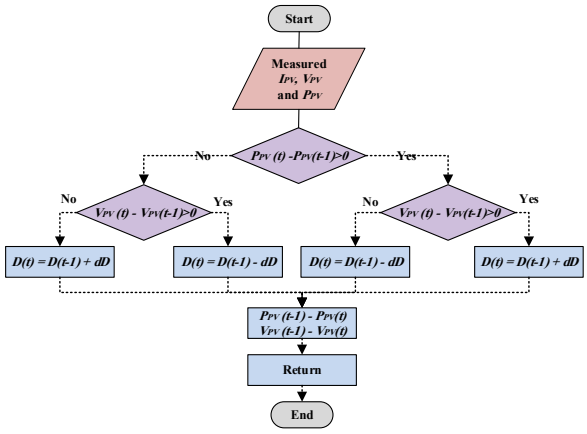

Fig. 5. The flowchart of P&O algorithm

Snake optimization. Snake reproductive behavior is affected by variables such as temperature and food accessibility. Mating often transpires in late spring and early summer when temperatures are moderate. When food is plentiful, male snakes vie for the attention of females. The female determines the suitability of a partner, and upon copulation, she deposits her eggs in a nest or burrow and departs after hatching [28]. The SO method is derived from the reproductive behavior of snakes. It functions in 2 stages: exploration and exploitation. In the absence of food and freezing temperatures during exploration, the snake seeks sustenance. In exploitation, the serpent prioritizes efficiency, adjusting according to food supply and temperature. When food is accessible and temperatures are elevated, the snake consumes it. Mating occurs under simultaneous conditions of food and cold, characterized by 2 modes: a competitive mode, in which males vie for females, and a mating mode, wherein pairs copulate depending on food availability. Upon mating, the female may deposit eggs that subsequently hatch into baby snakes [29].The mathematical model and technique are elucidated in depth in the following sections:

1) *Initialization* [30–32]: before beginning the optimization process, SO, like other metheuristic algorithms, creates a uniformly distributed, randomly generated population. The following equation can be used to find the initial population:

$$x_i = x_{\min} + r\cdot(x_{\max} - x_{\min}), \quad (1)$$

where x_i is the position of i^{th} individual; r is the random number between 0 and 1; $x_{\max}$, $x_{\min}$ are the lower and upper bounds of the problem respectively.

Assuming there are n_m males and n_f females in the swarm, after initialization the swarm will be divided into 2 equal groups. In order to assess each group, we can define food and temperature using (2) for temperature *Temp* and (3) – for food quantity Q:

$$Temp = \exp(-t / T); \quad (2)$$

$$Q = c_1\cdot\exp[(t-T) / T]; \quad (3)$$

where t, T are the current and maximum iteration times, respectively; c_1 is the constant equal to 0.5.

2) *Exploration phase* (no food) [30–32]: if the value of Q is less than the threshold (where the threshold is 0.25), the snakes will update their position relative to any randomly chosen position in their search for food. To model the exploration phase, the following equation is used:

$$x_{i,m}(t+1) = x_{rand,m}(t) \pm c_2\cdot a_m\cdot[(x_{\max} - x_{\min})\cdot rand - x_{\min}]; \quad (4)$$

$$x_{i,f}(t+1) = x_{rand,f}(t) \pm c_2\cdot a_f\cdot[(x_{\max} - x_{\min})\cdot rand - x_{\min}]; \quad (5)$$

where a_m, a_f are the individuals' respective food-finding capacities; *rand* is the random number between 0 and 1; c_2 is the constant equal to 0.05 [30–32].

3) *Exploitation phase* (food exists) [30–32]: the food is available if the quantity exceeds the threshold value 0.6. After that, the snakes will start to feel the temperature. Only when the temperature drops below 0.6 will the snakes start eating what's already there. The process is illustrated below:

$$x_{i,j}(t+1) = x_{food} \pm c_3\cdot Temp\cdot rand\cdot[x_{food} - x_{i,j}(t)], \quad (6)$$

where $x_{i,j}$ is the position of individual (male or female); x_{food} is the position of the best individuals; c_3 is the constant equal to 2.

SO was used in this work to find the best parameters for PI controller [33] in UPQC by the objective function by integral error.

$$IAE = \int_0^t |e(t)| \mathrm{d}t \, . \quad (7)$$

Table 1 explains the parameters of SO algorithm.

Table 1

The parameters of SO algorithm

Parameters	Values
Number of variables	K_P, K_I
Minimum desirable	[0, 0]
Maximum desirable	[50, 50]
Population size and iteration number	20, 50

Results and simulation. A right-shunt UPQC configuration with 3 phases and 4 wires was modeled in the MATLAB/Simulink program. The power system and UPQC parameters are listed in Table 2.

Table 2

The power system parameters

Parameters	Value
Grid voltage V, V	400
Grid frequency f, Hz	50
3 phase balance load P, kW, Q, kVAr	20 20
3 phase unbalance load P_{abc}, kW, Q_{abc}, kVAr	6, 7, 8 6, 7, 8
PI parameter for balance load K_P, K_I	0.6925 12.2467
PI parameter for unbalance load K_P, K_I	0.6234 22
DC link voltage V_{dc}, V	800
DC link capacitor C_1, mF, C_2, mF	4 4
Shunt inductance L_{sh}, mH	3
Shunt filter capacitance C_{sh}, μF, filter resistance R, Ω	600 6
Series inductance L_{se}, mH	30
Series filter capacitance C_{se}, μF, filter resistance R, Ω	150 6
Rated power P, kW	29.6
Open-circuit voltage V_{oc}, V	47.8
Short-circuit current I_{sc}, A	10.17
Voltage at maximum power V_{mp}, V	38.8
Current at maximum power I_{mp}, A	9.54
Number of cells in parallel	6
Number of cells in series	14
Boost converter inductance L, mH	0.35
Boost converter capacitance C, μF	220

The line-to-line voltage of the grid is 400 V, so the phase voltage is 230 V. The instances of mitigating power quality issues through the UPQC are categorized as follows.

1) the voltage quality issues in the grid (sag, swell and harmonics). Figure 6 shows all cases of the power quality issues in grid voltage and load side.

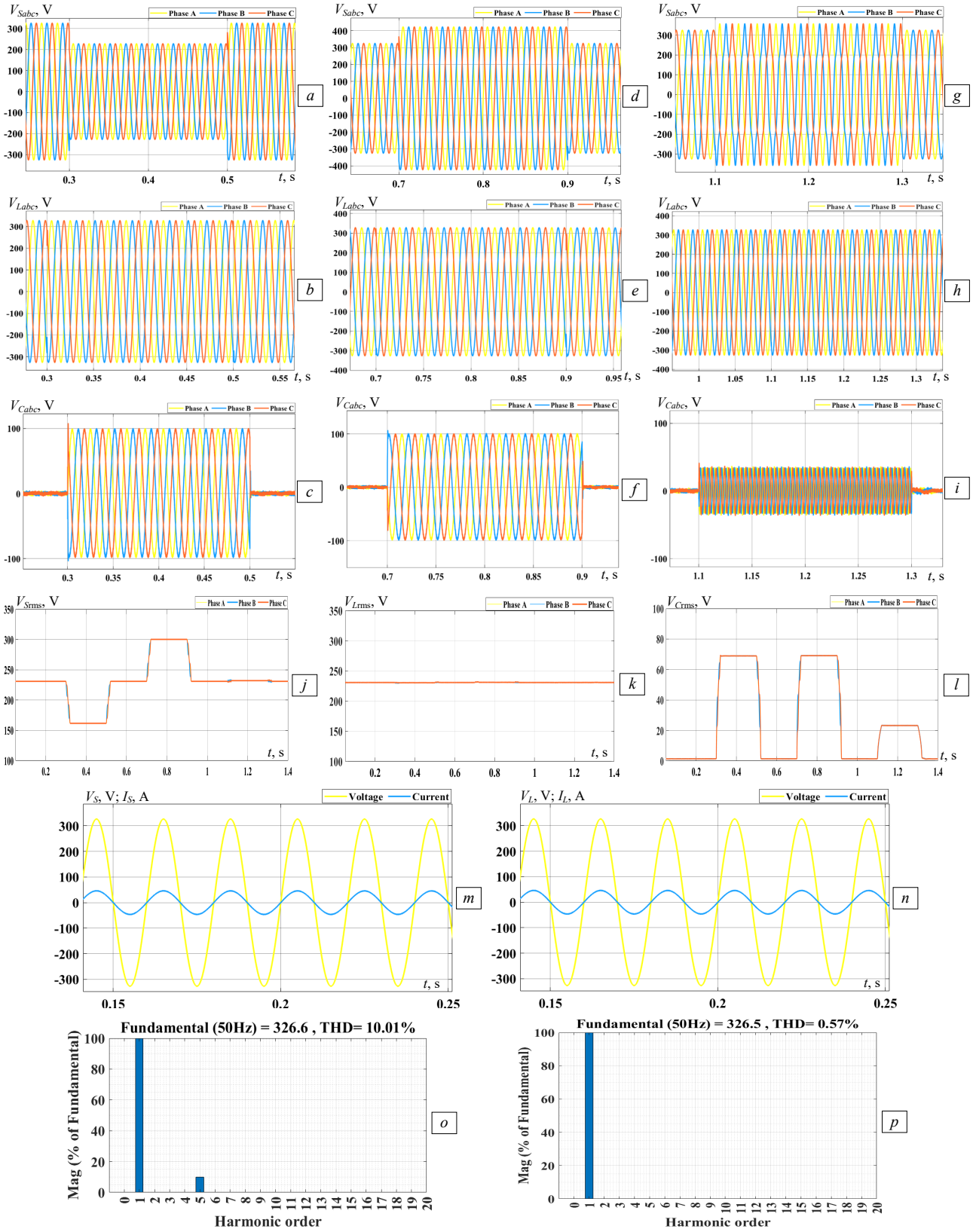

Fig. 6. All cases of the power quality issues in grid voltage and load side: *a* – sag grid voltage; *b* – voltage injected by series part of UPQC; *c* – load voltage; *d* – swell grid voltage; *e* – load voltage; *f* – voltage injected by series part of UPQC; *g* – harmonics grid voltage; *h* – load voltage; *i* – voltage injected by series part of UPQC; *j* – RMS grid voltage; *k* – RMS load voltage; *l* – RMS voltage injected by series part of UPQC; *m* – grid waveforms of voltage and current; *n* – load waveforms of voltage and current; *o* – THD of grid voltage; *p* – THD of load voltage after mitigation by UPQC

The UVTG technique in series UPQC to mitigate the voltage quality issues under voltage sag (30 % p.u) of the grid voltage between (0.3–0.5) s in Fig. 6,*a* and the phase RMS voltage grid is 161 V (Fig. 6,*j*), voltage swell (30 % p.u) of the grid voltage between (0.7–0.9) s in Fig. 6,*d* and the RMS phase voltage grid is 300 V (Fig. 6,*j*) and distorted grid voltage by harmonic 5th order (0.1 p.u of the fundamental grid voltage, zero degree) during (1.1–1.3) s in Fig. 6,*g*. The series part of UPQC works to solve the problems of the voltage source by injecting a voltage in series between the grid and load side so that when a sag occurs, it injects a voltage with the same percentage of the decrease but in phase with the grid voltage in Fig. 6,*c* so that the load voltage is constant and is not affected by the reduction of the grid voltage in Fig. 6,*b*. Similarly, when a swell in the grid voltage occurs, it injects a voltage in series with the same value as the swell but in the opposite phase of the grid voltage in Fig. 6,*f*. When a distortion occurs in the grid voltage, the UPQC works to inject a voltage that contains harmonics in the opposite phase of the harmonics present in the voltage grid in Fig. 6,*i*, resulting in a THD of 10 % in the grid voltage in Fig. 6,*o*. The THD in load voltage decreased after the injection process via the series part to 0.57 % in Fig. 6,*p*. Thus, the load voltage always remains constant in value from the reference value and a pure sinusoidal form, free of voltage problems in the source in Fig. 6,*b*,*e*,*h*. And a control mechanism utilizing the SRF *d*-*q* methodology in a shunt part of UPQC were employed to address current quality concerns. Balanced reactive load is 20 kVAr and power factor in load side is 0.707 in Fig. 6,*n* along with the control techniques employed for shunt part the SRF uses adjusted PI control parameters optimized by the SO algorithm to mitigation the reactive power in grid current the power factor unity for all phase in Fig. 6,*m*.

2) The current quality issues in the load (unbalance load and reactive power compensations). In this part explain the integration of a PV system enhances the functionality of the UPQC system by increasing reliability and reducing grid losses by Fig. 7.

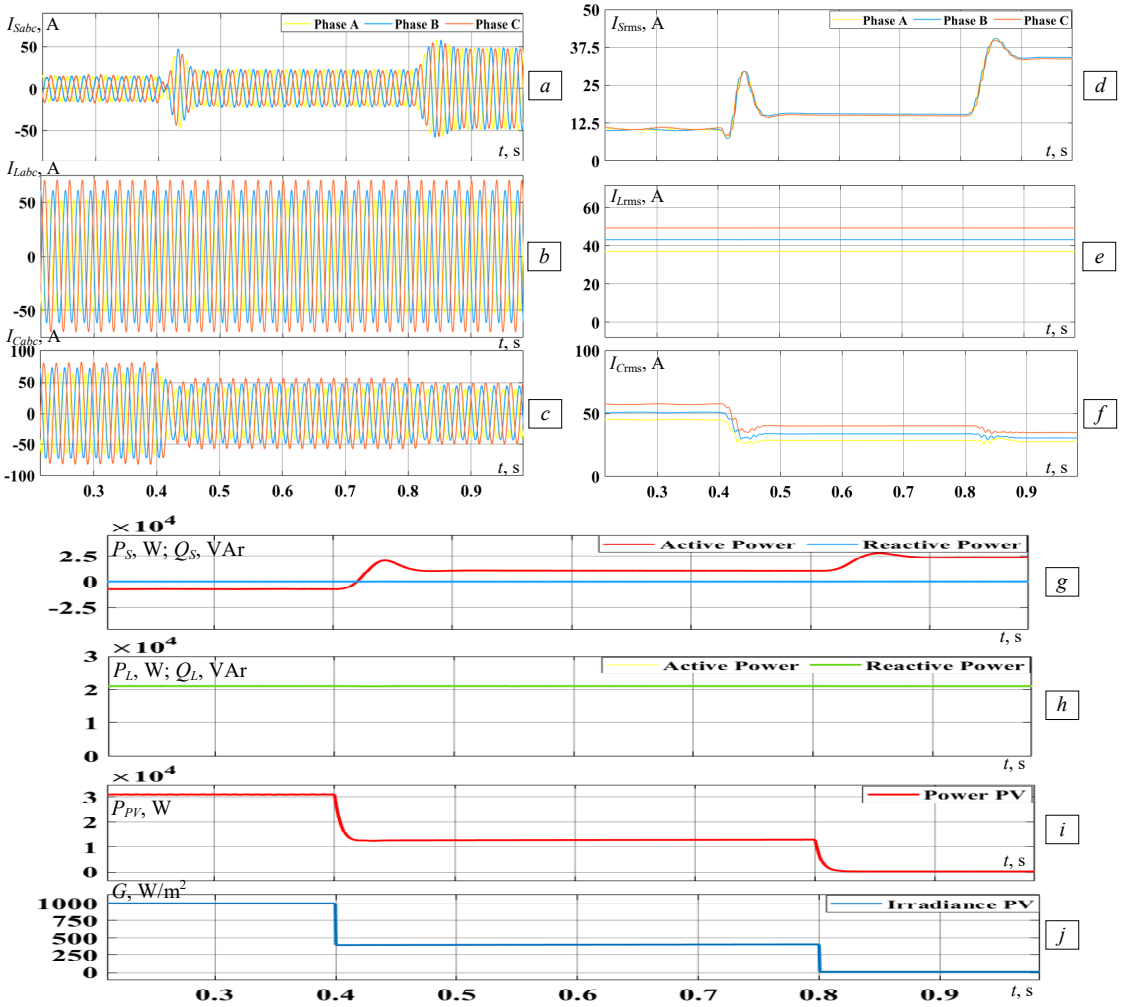

Fig. 7. All modes of the current quality issues in grid and load side: *a* – waveform grid current; *b* – waveform unbalance load current; *c* – current injected by shunt part of UPQC; *d* – RMS grid current; *e* – RMS of unbalance load current; *f* – RMS current injected by shunt part of UPQC; *g* – total active and reactive power of grid; *h* – total active and reactive power of load; *i* – total active PV power; *j* – solar radiation

The system operates in 3 distinct modes, depending on the ratio of the total active power of the load capacity to the active power of the PV generation capacity, based on the variation of the irradiance directed at the PV with the temperature factor on the cells at 25 °C, as follows.

Mode 1 (the active power of the PV system is greater than the active power of the load).

In this mode, the PV system generates an active power of 31 kW. In contrast, the total active power of the load is 21 kW. This occurs when the solar radiation

intensity incident on the solar cells is 1000 W/m^2. Consequently, the solar cells provide electricity to meet the demand of the load, while the surplus energy is sent into the grid. Consequently, the grid is fortified with electrical power, thereby improving its stability.

Mode 2 (the active power of the PV system is less than the active power of the load).

In this mode, the PV system generates an active power of 12.6 kW. In contrast, the total active power of the load is 21 kW. This occurs when the solar radiation intensity incident on the solar cells is 400 W/m^2. Consequently, the solar cells provide part of the electricity to meet the load demand; in this mode, no surplus energy is sent to the grid.

Mode 3 (the PV system does not generate any active power). This occurs when the solar radiation intensity incident on the solar cells is 0 W/m^2. Therefore, the grid has to supply the total load demand.

In all modes, the imbalanced currents and reactive power are compensated on the grid side because the imbalanced load and power factors are 0.707 lagging in all phases. Table 3 explains the characteristics of connected the PV to UPQC to mitigation the current quality issues in load.

Table 3

All modes by integration of UPQC-PV

Parameters	Mode 1	Mode 2	Mode 3
Duration T, s	0–0.4	0.4–0.8	0.8–1
RMS grid current I_{abc}, A	10.2 10.6 10.62	15 15.38 15.4	33.4 33.85 33.88
RMS load current I_{abc}, A	37 43.2 49.4	37 43.2 49.4	37 43.2 49.4
Grid power P_{abc} kW, Q_{abc} kVAr	7.3, 0	10, 0	23.6 0
Load power P_{abc} kW, Q_{abc} kVAr	6, 7, 8 6, 7, 8	6, 7, 8 6, 7, 8	6, 7, 8 6, 7, 8
PV power P_{PV}, kW	31	12.6	0

Conclusions. Using UPQC integrated with a PV system to mitigate power quality problems in the power system and boost the grid supply through power injection from the PV system, the proposed work improves the electrical power quality supplied to sensitive electrical loads, which is a result of power quality problems in the grid system. Utilizing the UVTG strategy as the composition methodology (UPQC-P) through the UPQC series compensator is a straightforward and efficient method to enhance the voltage quality of the grid. To enhance the load side current quality, implement the SRF technique via the UPQC shunt compensator. In order to fine-tune the SRF strategy even further, we determine the best values for the parameters of the PI controller using SO. While the grid voltage maintains a THD of 10 %, this study brings the load voltage down to 0.57 %. Whenever the grid voltage drops below 161 V or rises above 300 V, it brings the load voltage back up to its reference value of 230 V. Achieving a unity power factor in grid current, balancing the imbalanced load current to a balanced grid current, and enhancing grid stability by injecting power from the PV system are all additional benefits. It also mitigates the low power factor on the load side (0.707 lagging).

Acknowledgements. The authors would like to sincerely thank the Electrical Engineering Department, College of Engineering, University of Mosul for the tremendous help they provided during this work.

Conflict of interest. The authors declare that there is no conflict of interest.

REFERENCES

1. Eristi B., Eristi H. Classification of Power Quality Disturbances in Solar PV Integrated Power System Based on a Hybrid Deep Learning Approach. *International Transactions on Electrical Energy Systems*, 2022, vol. 2022, art. no. 8519379. doi: https://doi.org/10.1155/2022/8519379.

2. Manohara M., Muthukaruppasamy S., Dharmaprakash R., Sendilkumar S., Dattatreya Bharadwaj D., Parimalasundar E. Power quality enhancement of grid-integrated solar photovoltaic system with unified power quality conditioner. *Electrical Engineering & Electromechanics*, 2024, no. 6, pp. 44-48. doi: https://doi.org/10.20998/2074-272X.2024.6.06.

3. Ravi T., Kumar K.S., Dhanamjayulu C., Khan B., Rajalakshmi K. Analysis and mitigation of PQ disturbances in grid connected system using fuzzy logic based IUPQC. *Scientific Reports*, 2023, vol. 13, no. 1, art. no. 22425. doi: https://doi.org/10.1038/s41598-023-49042-z.

4. Alnaib I.I., Mohammed K.K., Alsammak A.N.B. A Comparative Analysis of Different Optimization Algorithms for Optimal System Reconfiguration to Improve the Radial Distribution Network in Iraq. *Lecture Notes in Electrical Engineering*, 2025, vol. 1294, pp. 383-397. doi: https://doi.org/10.1007/978-981-97-9037-1_27.

5. Samanta I.S., Mohanty S., Parida S.M., Rout P.K., Panda S., Bajaj M., Blazek V., Prokop L., Misak S. Artificial intelligence and machine learning techniques for power quality event classification: a focused review and future insights. *Results in Engineering*, 2025, vol. 25, art. no. 103873. doi: https://doi.org/10.1016/j.rineng.2024.103873.

6. Alajrash B.H., Salem M., Swadi M., Senjyu T., Kamarol M., Motahhir S. A comprehensive review of FACTS devices in modern power systems: Addressing power quality, optimal placement, and stability with renewable energy penetration. *Energy Reports*, 2024, vol. 11, pp. 5350-5371. doi: https://doi.org/10.1016/j.egyr.2024.05.011.

7. Qasim A.Y., Tahir F.R., Alsammak A.N.B. Improving Power Quality in Distribution Systems Using UPQC: An Overview. *Journal Europeen des Systemes Automatises*, 2024, vol. 57, no. 2, pp. 311-322. doi: https://doi.org/10.18280/jesa.570201.

8. Fujita H., Akagi H. The unified power quality conditioner: the integration of series- and shunt-active filters. *IEEE Transactions on Power Electronics*, 1998, vol. 13, no. 2, pp. 315-322. doi: https://doi.org/10.1109/63.662847.

9. Poongothai S., Srinath S. Power quality enhancement in solar power with grid connected system using UPQC. *Microprocessors and Microsystems*, 2020, vol. 79, art. no. 103300. doi: https://doi.org/10.1016/j.micpro.2020.103300.

10. Patel A., Yadav S.K., Mathur H.D., Bhanot S., Bansal R.C. Optimum sizing of PV based UPQC-DG with improved power angle control. *Electric Power Systems Research*, 2020, vol. 182, art. no. 106259. doi: https://doi.org/10.1016/j.epsr.2020.106259.

11. Patel A., Yadav S.K., Mathur H.D. Utilizing UPQC-DG to export reactive power to grid with power angle control method. *Electric Power Systems Research*, 2022, vol. 209, art. no. 107944. doi: https://doi.org/10.1016/j.epsr.2022.107944.

12. Dash S.K., Ray P.K., Ray P. Implementation of adaptive control strategies for PV system integrated unified conditioner for optimal power quality regulation. *Results in Engineering*, 2025, vol. 26, art. no. 105122. doi: https://doi.org/10.1016/j.rineng.2025.105122.

13. Sanjenbam C.D., Singh B. Modified Adaptive Filter Based UPQC for Battery Supported Hydro Driven PMSG System. *IEEE*

Transactions on Industrial Informatics, 2023, vol. 19, no. 7, pp. 8018-8028. doi: https://doi.org/10.1109/TII.2022.3215950.
14. Li Z., Yang R., Zhou Y., Wang C., Wang Z. A Unified Framework for Adaptive and Flexible Phase Angle Regulation in Single-Phase UPQC. *IEEE Transactions on Power Electronics*, 2025, vol. 40, no. 9, pp. 12779-12793. doi: https://doi.org/10.1109/TPEL.2025.3564527.
15. Han J., Li X., Sun Y., Luo D., Huang S. Optimal operation of UPQC under VA capacity constraints based on hierarchical optimization. *International Journal of Electrical Power & Energy Systems*, 2020, vol. 122, art. no. 106168. doi: https://doi.org/10.1016/j.ijepes.2020.106168.
16. Reguieg Z., Bouyakoub I., Mehedi F. Harmonic mitigation in grid-integrated renewable energy systems with nonlinear loads. *Energy*, 2025, vol. 324, art. no. 135882. doi: https://doi.org/10.1016/j.energy.2025.135882.
17. Alam S.J., Arya S.R. Volterra LMS/F Based Control Algorithm for UPQC With Multi-Objective Optimized PI Controller Gains. *IEEE Journal of Emerging and Selected Topics in Power Electronics*, 2023, vol. 11, no. 4, pp. 4368-4376. doi: https://doi.org/10.1109/JESTPE.2022.3146210.
18. Yadav S.K., Patel A., Mathur H.D. PSO-Based Online PI Tuning of UPQC-DG in Real-Time. *IEEE Open Journal of Power Electronics*, 2024, vol. 5, pp. 1419-1431. doi: https://doi.org/10.1109/OJPEL.2024.3445719.
19. Sanjenbam C.D., Singh B., Shah P. Reduced Voltage Sensors Based UPQC Tied Solar PV System Enabling Power Quality Improvement. *IEEE Transactions on Energy Conversion*, 2023, vol. 38, no. 1, pp. 392-403. doi: https://doi.org/10.1109/TEC.2022.3197408.
20. Ray P., Ray P.K., Dash S.K. Power Quality Enhancement and Power Flow Analysis of a PV Integrated UPQC System in a Distribution Network. *IEEE Transactions on Industry Applications*, 2022, vol. 58, no. 1, pp. 201-211. doi: https://doi.org/10.1109/TIA.2021.3131404.
21. Heenkenda A., Elsanabary A., Seyedmahmoudian M., Mekhilef S., Stojcevski A., Aziz N.F.A. Unified Power Quality Conditioners Based Different Structural Arrangements: A Comprehensive Review. *IEEE Access*, 2023, vol. 11, pp. 43435-43457. doi: https://doi.org/10.1109/ACCESS.2023.3269855.
22. Sai Sarita N.C., Suresh Reddy S., Sujatha P. Control strategies for power quality enrichment in Distribution network using UPQC. *Materials Today: Proceedings*, 2023, vol. 80, pp. 2872-2882. doi: https://doi.org/10.1016/j.matpr.2021.07.053.
23. Alnaib I.I., Alsammak A.N. Reduce Multiple Power Quality Issues with UPQC by Using UVTG and PQ Current Control Techniques Based on Snake Optimization. *Lecture Notes in Electrical Engineering*, 2025, vol. 1294, pp. 35-48. doi: https://doi.org/10.1007/978-981-97-9037-1_4.
24. Alnaib I.I., Alsammak A.N., Mohammed K.K. Brushless DC motor drive with optimal fractional-order sliding-mode control based on a genetic algorithm. *Electrical Engineering & Electromechanics*, 2025, no. 2, pp. 19-23. doi: https://doi.org/10.20998/2074-272X.2025.2.03.
25. Boudechiche G., Aissa O., Sarra M., Griche I. Solar shunt active power filter based on optimized direct power control strategy with disturbance rejection principle. *Electrical Engineering & Electromechanics*, 2024, no. 3, pp. 72-80. doi: https://doi.org/10.20998/2074-272X.2024.3.10.
26. Alnaib I.I., Alsammak A.N. Utilize UPQC to Reduce Power Quality Issues by SRF Control Strategies Based on Snake Optimization. *Lecture Notes in Electrical Engineering*, 2025, vol. 1294, pp. 49-62. doi: https://doi.org/10.1007/978-981-97-9037-1_5.
27. Bousnoubra C., Djeghader Y., Belila H. Contribution of using a photovoltaic unified power quality conditioner in power quality improvement. *Electrical Engineering & Electromechanics*, 2024, no. 4, pp. 42-47. doi: https://doi.org/10.20998/2074-272X.2024.4.05.
28. Ghamari S.M., Hajihosseini M., Habibi D., Aziz A. Design of an Adaptive Robust PI Controller for DC/DC Boost Converter Using Reinforcement-Learning Technique and Snake Optimization Algorithm. *IEEE Access*, 2024, vol. 12, pp. 141814-141829. doi: https://doi.org/10.1109/ACCESS.2024.3440580.
29. Hashim F.A., Hussien A.G. Snake Optimizer: A novel meta-heuristic optimization algorithm. *Knowledge-Based Systems*, 2022, vol. 242, art. no. 108320. doi: https://doi.org/10.1016/j.knosys.2022.108320.
30. Zheng K., Liu H., Li B. Improved Snake Optimization Algorithm for Global Optimization and Engineering Applications. *Scientific Reports*, 2025, vol. 15, no. 1, art. no. 18171. doi: https://doi.org/10.1038/s41598-025-01299-2.
31. Ghamari S.M., Molaee H., Ghahramani M., Habibi D., Aziz A. Design of an Improved Robust Fractional-Order PID Controller for Buck–Boost Converter using Snake Optimization Algorithm. *IET Control Theory & Applications*, 2025, vol. 19, no. 1, art. no. e70008. doi: https://doi.org/10.1049/cth2.70008.
32. Mohammadi F., Kaffash A., Donyagozashteh Z., Marasi M., Tavakoli M. Design of a novel robust adaptive backstepping controller optimized by snake algorithm for buck-boost converter. *IET Control Theory & Applications*, 2025, vol. 19, no. 1, art. no. e12770. doi: https://doi.org/10.1049/cth2.12770.
33. Alnaib I.I., Alsammak A.N. Optimization of fractional PI controller parameters for enhanced induction motor speed control via indirect field-oriented control. *Electrical Engineering & Electromechanics*, 2025, no. 1, pp. 3-7. doi: https://doi.org/10.20998/2074-272X.2025.1.01.

Received 26.07.2025
Accepted 08.10.2025
Published 02.03.2026

I.I. Alnaib [1], *MSc., Lecturer,*
A.N. Alsammak [1], *PhD, Professor,*
[1] Electrical Engineering Department,
College of Engineering, University of Mosul, Iraq,
e-mail: ibrahim-85353@uomosul.edu.iq (Corresponding Author);
ahmed_alsammak@uomosul.edu.iq

How to cite this article:
Alnaib I.I., Alsammak A.N. Intelligent unified power quality conditioner based photovoltaic to improve grid reliability and mitigate power quality issues. *Electrical Engineering & Electromechanics*, 2026, no. 2, pp. 51-58. doi: https://doi.org/10.20998/2074-272X.2026.2.07

UDC 621.314 https://doi.org/10.20998/2074-272X.2026.2.08

M. Naidji, A.E. Toubal Maamar, M. Boudour, A. Garmat, A. Aissa-Bokhtache

Comparative analysis of numerical, evolutionary and metaheuristic methods for experimental implementation of selective harmonic elimination in a five-level emerging inverter

Introduction. *Multilevel inverters (MLIs) are widely used in renewable energy conversion and high-performance power applications due to their ability to generate output voltages with low harmonic distortion and reduced switching stress. Selective harmonic elimination (SHE) remains one of the most effective modulation strategies for suppressing low-order harmonics; however, its practical implementation relies on solving nonlinear transcendental equations that often require robust and efficient computational methods.* ***Problem.*** *Determining optimal switching angles for SHE in MLIs remains a challenging optimization problem because of the nonlinear, non-convex nature of the governing equations and the need to simultaneously preserve the fundamental voltage component while eliminating selected harmonics. The choice of an appropriate numerical or optimization-based solution method directly affects computational efficiency, robustness, and practical implementability. The* ***goal*** *of the work is the reducing harmonic distortion of output voltage and determining optimal switching angles of a single-phase 5-level inverter using the Newton-Raphson (NR) method, particle swarm optimization (PSO) and genetic algorithm (GA).* ***Methodology.*** *The operating principle and harmonic model of the inverter are first established using Fourier series analysis. The SHE problem is formulated as a system of nonlinear equations subject to ordering constraints. The NR method is used as a fast numerical solver, while PSO and GA are employed as evolutionary and metaheuristic optimization techniques capable of handling non-convex search spaces. All algorithms are implemented in MATLAB/Simulink over a range of modulation indices. Experimental validation is carried out using an Arduino Mega 2560-based prototype, where the optimized switching patterns are executed in real time and the output voltage is analyzed using oscilloscope and harmonic measurement tools.* ***Results.*** *The three approaches converge to identical switching-angle solutions over the investigated modulation range, confirming the consistency of the formulation. Simulation results demonstrate effective elimination of the 3rd harmonic and its multiples, with the total harmonic distortion of the output voltage decreasing from 28.42 % at M = 0.55, f = 1 kHz to 14.88 % at M = 0.55, f = 10 kHz. In terms of computational efficiency, NR-SHE achieves the shortest execution time (0.516 s), while PSO-SHE (10.237 s) and GA-SHE (23.289 s) require longer computation. Experimental waveforms and harmonic spectra closely match the simulation results, validating the proposed approach.* ***Scientific novelty.*** *This work provides a unified comparative analysis of numerical, evolutionary and metaheuristic methods for SHE applied to a 5-level emerging inverter with a reduced switch count (6 switches instead of 8 in a conventional 5-level H-bridge). In addition, it demonstrates the feasibility of executing SHE-based modulation schemes on a low-cost Arduino microcontroller.* ***Practical value.*** *The presented results offer practical guidance for selecting suitable computational methods for SHE in MLIs and confirm that efficient harmonic control can be achieved using inexpensive embedded platforms. The findings are relevant for research, prototyping and educational applications in industrial electronics and power conversion systems.* References 21, tables 5, figures 12.

Key words: **emerging multilevel inverter, genetic algorithm, Newton-Raphson algorithm, particle swarm optimization, selective harmonic elimination.**

Вступ. *Багаторівневі інвертори (MLIs) широко використовуються в системах перетворення відновлюваної енергії та високопродуктивних енергетичних системах завдяки їхній здатності генерувати вихідну напругу з низьким рівнем гармонік та зменшеним напругою перемикання. Вибіркове усунення гармонік (SHE) залишається однією з найефективніших стратегій модуляції для зменшення гармонік нижчого порядку; однак її практична реалізація залежить від розв'язання нелінійних трансцендентних рівнянь, які часто вимагають надійних та ефективних обчислювальних методів.* ***Проблема***. *Визначення оптимальних кутів перемикання для SHE в MLIs залишається складною задачею оптимізації через нелінійний, неопуклий характер керівних рівнянь та необхідність одночасного збереження основної складової напруги при усуненні вибраних гармонік. Вибір відповідного числового або оптимізаційного методу розв'язання безпосередньо впливає на обчислювальну ефективність, надійність та практичну реалізованість.* ***Метою*** *роботи є зменшення гармонійних спотворень вихідної напруги та визначення оптимальних кутів перемикання однофазного 5-рівневого інвертора за допомогою методу Ньютона-Рафсона (NR), оптимізації рою частинок (PSO) та генетичного алгоритму (GA).* ***Методика***. *Принцип роботи та гармонічна модель інвертора спочатку встановлюються за допомогою аналізу рядів Фур'є. Задачу SHE сформульовано як систему нелінійних рівнянь з обмеженнями на впорядкування. Метод NR використовується як швидкий числовий розв'язувач, тоді як PSO та GA використовуються як еволюційні та метаевристичні методи оптимізації, здатні обробляти неопуклі простори пошуку. Всі алгоритми реалізовані в MATLAB/Simulink для діапазону індексів модуляції. Експериментальна перевірка проводиться з використанням прототипу на базі Arduino Mega 2560, де оптимізовані шаблони перемикання виконуються в режимі реального часу, а вихідна напруга аналізується за допомогою осцилографа та інструментів вимірювання гармонік.* ***Результати***. *Три підходи сходяться до ідентичних рішень кута перемикання в досліджуваному діапазоні модуляції, що підтверджує узгодженість формулювання. Результати моделювання демонструють ефективне усунення 3-ї гармоніки та її кратних, при цьому загальне гармонічне спотворення вихідної напруги зменшується з 28,42 % при M = 0.55, f = 1 кГц до 14,88 % при M = 0.55, f = 10 кГц. З точки зору обчислювальної ефективності, NR-SHE досягає найкоротшого часу виконання (0,516 с), тоді як PSO-SHE (10,237 с) та GA-SHE (23,289 с) вимагають довших обчислень. Експериментальні форми хвиль та гармонічні спектри точно відповідають результатам моделювання, що підтверджує запропонований підхід.* ***Наукова новизна***. *Ця робота надає уніфікований порівняльний аналіз числових, еволюційних та метаевристичних методів для SHE, застосованих до нового 5-рівневого інвертора зі зменшеною кількістю перемикачів (6 перемикачів замість 8-ми у звичайному 5-рівневому H-мості). Крім того, вона демонструє можливість виконання схем модуляції на основі SHE на недорогому мікроконтролері Arduino.* ***Практична значимість***. *Представлені результати пропонують практичні рекомендації щодо вибору відповідних обчислювальних методів для SHE в MLI та підтверджують, що ефективного гармонічного контролю можна досягти за допомогою недорогих вбудованих платформ. Результати є актуальними для досліджень, прототипування та освітніх застосувань у промисловій електроніці та системах перетворення енергії.* Бібл. 21, табл. 5, рис. 12.

Ключові слова: **новий багаторівневий інвертор, генетичний алгоритм, алгоритм Ньютона-Рафсона, оптимізація рою частинок, вибіркове усунення гармонік.**

Introduction. Since multilevel inverters (MLIs) can produce high-voltage outputs with improved power quality, they have become a hot topic in power electronics research [1]. Distributed generation systems, grid-connected renewable energies and multilevel resonant inverters make heavy use of these converters [2].

Review of recent publications demonstrates that, there are primarily 2 types of MLIs: traditional and new.

Topologies commonly used in inverters include the neutral-point-clamped, the flying-capacitor and the cascaded H-bridge [3]. Inverters with an uneven number of levels, inverters with fewer components, inverters with soft switches, and MLIs with a single source are all examples of recent advances [4]. The simplicity of control requirements, low total standing voltage, minimal switching losses, and cost-effectiveness of emerging topologies as compared to traditional designs are attracting attention [5]. There are 2 main types of modulation when it comes to generating gating signals for converter semiconductor devices. One type is high-switching frequency modulation, which includes techniques like sinusoidal pulse width modulation, and space vector pulse width modulation [6, 7]. On the other hand, fundamental-frequency modulation includes methods like selective harmonic elimination (SHE), optimal switching angle modulation, and nearest-level modulation [8]. The fundamental-frequency modulation is becoming more pragmatic because the advancements in digital control hardware as digital signal processors, field-programmable gate arrays and embedded controllers [9].

To put SHE into action, the best switching angles must be determined by solving nonlinear transcendental equations. Various methods, including algebraic approaches, numerical techniques, and metaheuristic and evolutionary algorithms, are employed to generate solutions [10]. Metaeuristic methods are great at finding good approximations when optimization problems are hard. Some algorithms that could be mentioned in this context are genetic algorithm (GA); flower pollination algorithm; gravitational search algorithm; grey wolf optimizer; artificial neural networks; particle swarm optimization (PSO); artificial bee colony; ant colony optimization; bald eagle search; salp swarm algorithm; wild horse optimization algorithm; and generalized pattern search [11–14].

The **goal** of this work is the reducing harmonic distortion of output voltage and determining optimal switching angles of a single-phase 5-level inverter using the Newton-Raphson (NR) method, particle swarm optimization and genetic algorithms. By providing a comparative perspective on numerical, metaheuristic and evolutionary techniques for solving the SHE problem, the findings offer practical guidance for selecting appropriate optimization methods and demonstrate that emerging multilevel topologies can be efficiently controlled using accessible, low-cost embedded platforms.

The key benefits of the proposed study are simplicity and low-cost implementation of the system. By covering the principles, applications and benefits of Arduino-based controlled inverters, this research seeks to be a reference for students and engineers interested in developing converter applications using this kind of open-source technology. Furthermore, the comparative analysis between a numerical method, metaheuristic algorithm and evolutionary algorithm presents valuable information to select the appropriate algorithm for harmonic elimination in MLIs.

Description of the MLI system. The basic architecture of the single-phase 5-level inverter is given in Fig. 1. The circuit comprises 2 DC sources, 6 electronic switches and resistor load. In a full switching period (T), the inverter has 12 switching transitions, where the switches operate periodically by complementary mode (S_1, S_2), (S_3, S_4) and (S_5, S_6), hence we can set (S_a, S_b, S_c) = = (S_1, S_3, S_5) to suggest the following switching system:

$$V_0 = \begin{cases} 0 & \xrightarrow{\text{if}} (S_a, S_b) = (0,0) \text{or} (1,1); \\ -V_{dc} & \xrightarrow{\text{if}} (S_a, S_b, S_c) = (0,1,0); \\ +V_{dc} & \xrightarrow{\text{if}} (S_a, S_b, S_c) = (1,0,0); \\ -2V_{dc} & \xrightarrow{\text{if}} (S_a, S_b, S_c) = (0,1,1); \\ +2V_{dc} & \xrightarrow{\text{if}} (S_a, S_b, S_c) = (1,0,1). \end{cases} \quad (1)$$

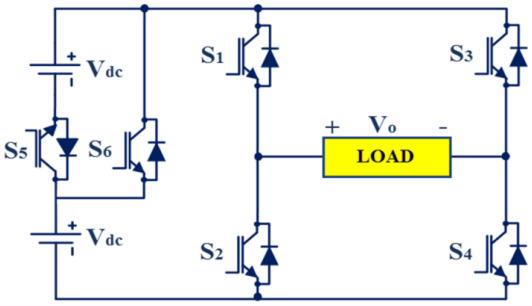

Fig. 1. Topology of the 5-level emerging inverter

By using equal power V_{dc} sources and appropriate switching modes, the inverter can generate 5-levels of output voltage (V_0): 0, $-V_{dc}$, $+V_{dc}$, $-2V_{dc}$ and $+2V_{dc}$ (Fig. 2).

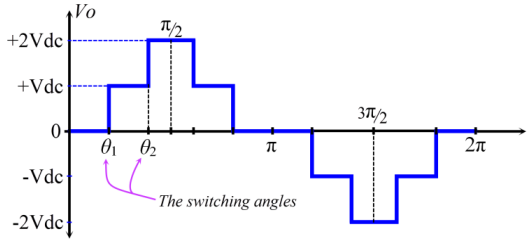

Fig. 2. The output voltage of the 5-level emerging inverter

Mathematical description of the harmonic problem. Harmonics refer to sine wave voltages or currents that occur at integer multiples of the fundamental frequency of the network. When harmonics combine with the fundamental sine wave voltage or current, they cause distortion in the energy waveform. These additional frequencies can lead to various issues in electrical systems, including overheating of equipment and distortion of power quality. To keep networks running smoothly and reliably, it's important to understand and deal with harmonics. If the total harmonic distortion (THD) is 0, it means that there are no harmonics in the electrical network. THD is the ratio of the RMS value of the harmonics in a signal (voltage or current) to the RMS value at the fundamental frequency.

The harmonics manifest as «lines» referred to as the spectrum. Harmonics beyond the 30th rank are often disregarded. The symmetry of output voltage waveforms leads to the near-elimination of even-order harmonics (e.g., the 2nd, 4th, 6th, and beyond). Consequently, these even harmonics are generally considered negligible. In contrast, odd-order harmonics (such as the 3rd, 5th, 7th, and beyond) frequently manifest in electrical grids and are therefore the primary focus of harmonic mitigation studies [5, 15]. The mathematical basis behind these signals was developed by J. Fourier. His seminal work proved that any complex signal which is periodic and piecewise-continuous can be resolved into a series of simple sinusoidal waves, called harmonics [10]. Via the Fourier series, this decomposition enables a powerful analytical method. It permits the engineer to analyze each harmonic component separately and then use the principle of superposition to determine the signal's behavior.

The standard trigonometric representation of the Fourier series for the output voltage $V_0(t)$ is:

$$V_0(t) = \frac{a_0}{2} + \sum_{n=1}^{\infty}\left[a_n \cos(n\omega_0 t) + b_n \sin(n\omega_0 t)\right], \quad (2)$$

where $\omega_0 = 2\pi/T$ is the fundamental angular frequency; $a_0 = 0$ is the DC component; a_n, b_n are the Fourier coefficients: $a_n = 0$, while b_n is determined as:

$$b_n = \frac{2}{T}\int_0^T V_0(t)\sin(n\omega_0 t)\mathrm{d}t\,. \quad (3)$$

By integrating $V_0(t)$ over [0, 2π] and performing standard algebraic simplifications, Eq. (3) is reformulated as:

$$b_n = \frac{4V}{n\pi}\left(\cos(n\theta_1) + \cos(n\theta_2)\right). \quad (4)$$

where θ_1, θ_2 are the switching angles.

Substituting (4) into (2) yields the expression for the inverter output voltage $V_0(t)$ as:

$$V_0(t) = \sum_{n=1}^{\infty}\left(\frac{4V}{n\pi}\left(\cos(n\theta_1) + \cos(n\theta_2)\right)\right)\sin(n\omega_0 t)\,. \quad (5)$$

For n=1, the output voltage of inverter $V_0(t)$ can be calculated by the fundamental harmonic h_1:

$$h_1 = \frac{4V}{\pi}\left(\cos(\theta_1) + \cos(\theta_2)\right). \quad (6)$$

The 3rd harmonic h_3 is defined as:

$$h_3 = \frac{4V}{3\pi}\left(\cos(3\theta_1) + \cos(3\theta_2)\right). \quad (7)$$

Following the analysis technique described in [16, 17], the optimal switching angles can be computed. This computation involves finding the solution of (8):

$$\begin{cases} 0 = \left(\cos(3\theta_1) + \cos(3\theta_2)\right), \\ M = \dfrac{1}{k}\left(\cos(\theta_1) + \cos(\theta_2)\right), \end{cases} \quad (8)$$

where k is the number of angles; M is the modulation index:

$$M = \frac{\pi h_1}{4 \cdot k \cdot V}\,. \quad (9)$$

It is also important that the best angles meet the conditions as:

$$0 < \theta_1 < \theta_2 < \pi/2\,. \quad (10)$$

The next sections explain and analyze the suggested 3 optimization-based methods (NR, PSO, and GA) for solving the SHE problem. The objective is to find the best switching angles that meet the basic voltage requirements and eliminate the 3rd harmonic with its multiples.

Solving the SHE problem with Newton-Raphson (NR) algorithm. The NR approach, one of the beneficial numerical methods, can be used to compute and solve the set of transcendental nonlinear equations [18]. An initial estimate is made at the start of this iteration process, which eventually converges to the solution. The switching angles' initial approximation values are:

$$\theta^j = [\theta_1^j;\ \theta_2^j].$$

The nonlinear system is represented in matrix form:

$$F\left(\theta^j\right) = \begin{pmatrix} \cos\left(3\theta_1^j\right) & \cos\left(3\theta_2^j\right) \\ \cos\left(\theta_1^j\right) & \cos\left(\theta_2^j\right) \end{pmatrix}, \quad (11)$$

where:

$$F\left(\theta^j\right) = Z;\quad Z = \begin{pmatrix} 0 \\ \pi h_1/(4 \cdot V) \end{pmatrix}.$$

The derivative of the nonlinear system (11) is computed as:

$$\left[\frac{\partial F(\theta)}{\partial \theta}\right]^j = \begin{pmatrix} -3\sin\left(3\theta_1^j\right) & -3\sin\left(3\theta_2^j\right) \\ -\sin\left(\theta_1^j\right) & -\sin\left(\theta_2^j\right) \end{pmatrix}. \quad (12)$$

The steps for executing the NR algorithm for our study are as follows.

1) Set the initial values of θ^j when $j = 0$.

$$\theta^j = [\theta_1^j;\ \theta_2^j].$$

2) Compute the value of:

$$F(\theta^0) = F^0.$$

3) Linearizing the system around θ^0 :

$$F^0 + \left[\frac{\partial F(\theta)}{\partial \theta}\right]^0 \mathrm{d}\theta^0 = Z\,.$$

Such as:

$$\mathrm{d}\theta^0 = [\mathrm{d}\theta_1{}^0;\ \mathrm{d}\theta_2{}^0].$$

4) Compute $\mathrm{d}\theta^0$ utilizing the subsequent equation:

$$\mathrm{d}\theta^0 = \left(\mathrm{inv}\left[\frac{\partial F(\theta)}{\partial \theta}\right]^0\right)\left(Z - F^0\right).$$

5) Adjust the initial values

$$\theta^{j+1} = \theta^j + \mathrm{d}\theta^j.$$

6) The algorithm continues the prior steps for each equation until the required level of accuracy is achieved for $\mathrm{d}\theta^j$. The solutions of the equation must adhere to the constraint in (10).

Solving the SHE problem with PSO algorithm. An objective function in optimization is essential for eliminating undesirable harmonics while maintaining the fundamental component at its designated magnitude. Consequently, (13) establishes the objective function:

$$F(\theta_1,\theta_2) = \left(\sum_{n=1}^{2}\cos(\theta_n) - k \cdot M\right)^2 + \left(\sum_{n=1}^{2}\cos(3\theta_n)\right)^2. \quad (13)$$

The optimal angles are established through the minimization of (13), subject to the constraints of (10). The primary issue is the nonlinearity of (8); thus, the PSO algorithm is utilized to address this challenge. Algorithm 1 below illustrates the pseudocode of PSO. The PSO algorithm consists of 3 components: 1) initial parameters; 2) assess the objective function; 3) particles' mobility involves updating their position and velocity.

Algorithm 1: PSO pseudocode

Input: objective function $F(\theta_1, \theta_2)$; swarm size N; iterations number N_{Iter}; acceleration constants c_1, c_2; minimum and maximum inertia weights $w_{\min}$, $w_{\max}$.
Output: optimal switching angles (θ_1, θ_2), a solution vector $G_{best} = (\theta_1, \theta_2)$ that minimizes $F(\theta_1, \theta_2)$.
1: ***Initialize:***
2: $i_{ter} \leftarrow 0$
3: **for** each particle $i = 1$ **to** N **do**
4: Initialize position X_i randomly in search space [0, π/2].
5: Initialize velocity V_i to 0.
6: Evaluate fitness: $P^i_{best} \leftarrow F(X_i)$.
7: Set personal best: $P_i \leftarrow X_i$.
8: **end for**
9: Find global best: $G_{best} \leftarrow$ argmin $F(P_i)$
10: ***Optimization Loop:***
11: **while** i_{ter} < max Iter **do**
12: **for** each particle $i = 1$ **to** N **do**
13: // update velocity and position

14: $V_{i+1} = ([V_i \cdot w] + [c_1 \cdot r_1 \cdot (P_{best} - X_i)]) + [c_2 \cdot r_2 \cdot (G_{best} - X_i)])$
15: $X_i \leftarrow X_i + V_i$
16: // apply position constraints: $0 < \theta_1 < \theta_2 < \pi/2$
17: **if** X_i violates constraints **then**
18: re-initialize X_i
19: **end if**
20: // Evaluate and update bests
21: **if** $F(X_i) < F(P_i)$ **then**
22: $P_i \leftarrow X_i$
23: **if** $F(P_i) < F(G_{best})$ **then**
24: $G_{best} \leftarrow P_i$
25: **end if**
26: **end if**
27: **end for**
28: $i_{ter} \leftarrow i_{ter} + 1$
29: **end while**
30: return G_{best}

In the PSO model, the search process is carried out by a population of interacting agents, referred to as particles. Each particle represents a candidate solution encoded as a parameter vector, and its motion within the search domain is governed by its velocity V_i and position X_i, both of which are initialized randomly. The initial position of a particle is considered its personal best P_{best}. After initialization, the quality of each particle is evaluated through the objective (fitness) function.

The global best solution G_{best} is identified by selecting the particle with the lowest fitness value among the swarm. Particle trajectories in the D-dimensional search space are updated based on 3 main components: the inertia weight, which regulates exploration; the cognitive term reflecting each particle's historical best performance P_{best}, and the social term guided by G_{best}. The velocity update for the (V_{i+1}) iteration follows the formulation given in (14), and the subsequent position update (X_{i+1}) is obtained using (15) [5]:

$$V_{i+1} = ([V_i \cdot w] + [c_1 \cdot r_1 \cdot (P_{best} - X_i)]) + [c_2 \cdot r_2 \cdot (G_{best} - X_i)]); \quad (14)$$

$$X_{i+1} = X_i + V_{i+1}. \quad (15)$$

The inertia weight is calculated as:

$$w = w_{\max} - j \cdot [(w_{\max} - w_{\min}) / N_{Iter}]. \quad (16)$$

Table 1 shows the setting of the PSO algorithm [5]. It is established in the literature that no definitive procedure or guideline exists for determining the parameters of metaheuristic algorithms. The parameter settings for metaheuristic optimization algorithms represent an optimization task in its own right. These parameters are typically tuned empirically or adapted dynamically to balance exploration and exploitation. The parameters typically recommended by researchers are $c_1 = c_2 = 2.05$, $w_{\min} = 0.4$, $w_{\max} = 0.9$. The literature review provides insight into the parameters that are nearly suitable. Additionally, the user may experiment with the parameters and analyze the outcomes, like we did in this study.

Table 1

The setting of PSO algorithm

Parameter	Symbol	Value
Swarm size	N	40
Iterations number	N_{Iter}	100
Number of variables	θ_1, θ_2, M	3
Limit intervals	θ_1 θ_2 M	$\theta_1 \in [0, 90]$ $\theta_2 \in [0, 90]$ $M \in [0.45, 0.85]$
The acceleration coefficients	c_1, c_2	2.05
Minimum inertia weight	$w_{\min}$	0.4
Maximum inertia weight	$w_{\max}$	0.9

Solving the SHE problem with GA algorithm. GA was first introduced as a model inspired by biological evolution. When set up adequately in a data space, GA is an effective method to solve optimization problems [19]. Optimization is the process of finding the best solution to a problem while keeping in mind a number of factors related to the system's properties and limitations. The genetic approach is employed to minimize (13) under the constraint of (10), allows for the determination of the optimal commutation angles. Algorithm 2 illustrates the GA pseudocode, delineating the method into 5 specific steps: 1) population initialization; 2) objective function evaluation; 3) selection; 4) crossover; 5) mutation.

Algorithm 2: GA pseudocode

Input: objective function $F(\theta_1, \theta_2)$. Population size. Maximum generations. Chromosome 3 (M, θ_1, θ_2) is the quantity of variables. Search spaces are the intervals limit. Encoding is binary with 10 bits per variable. Crossover type and its probability. Mutation type and its probability.
Output: optimal switching angles (θ_1, θ_2), the best individual that minimizes $F(\theta_1, \theta_2)$.
1: ***Initialize:***
2: g ← 0 // Initialize generation counter.
3: Initialize $P(g)$ // Randomly generate initial population of N chromosomes.
4: **for** each chromosome i in $P(g)$ **do**
5: Decode chromosome to real values: (θ_1^i, θ_2^i, M^i).
6: Evaluate fitness: $F_i \leftarrow F(\theta_1^i, \theta_2^i)$.
7: **end for**
8: Find best individual: ***Best*** ← argmin$F(P(g))$.
9: ***Optimization Loop:***
10: **while** $g < G_{\max}$ **do**
11: // Step 1: Selection (roulette wheel).
12: Create mating pool M_p by selecting N parents from $P(g)$ with probability proportional to fitness.
13: // Step 2: Crossover (random, $P_c = 1$).
14: **for** each pair of parents in M_p **do**
15: Perform random single-point crossover to produce two offspring.
16: Add offspring to offspring population $P_{offspring}$.
17: **end for**
18: // Step 3: Mutation (random, $P_m = 0.05$).
19: **for** each chromosome in $P_{offspring}$ **do**
20: **for** each bit in the chromosome **do**
21: **if** rand() < P_m **then**
22: Flip the bit (0→1 or 1→0).
23: **end if**
24: **end for**
25: **end for**
26: // Form new generation & evaluate.
27: $P(g+1) \leftarrow P_{offspring}$ // new generation replaces the old.
28: **for** each chromosome i in $P(g+1)$ **do**
29: Decode chromosome to real values: (θ_1^i, θ_2^i, M^i).
30: Evaluate fitness: $F_i \leftarrow F(\theta_1^i, \theta_2^i)$.
31: **end for**
32: // Update best solution
33: *CurrentBest* ← argmin$F(P(g+1))$.
34: **if** $F($*CurrentBest*$) < F($***Best***$)$ **then**
35: ***Best*** ← *CurrentBest*.
36: **end if**
37: $g \leftarrow g + 1$
38: **end while**
39: return ***Best***.

By using random processes to make new generations of solutions, the best one is chosen from a group of possible solutions. This method depends on 3 operators: selection, crossover and mutation, which are applied to the current population in order and repeated until a stopping point is reached [20].

The parameters of the GA are shown in Table 2. It is well-known in the literature that there is no method or rule for setting the parameters of metaheuristic algorithms. The found of these settings is, in fact, a problem on their own. It is possible to determine the range of optimum values by a literature review. Additionally, users can vary the parameters and compare the results, similar to the approach taken in this study.

Table 2

The parameters of the GA

Parameter	Value
Size of the population	50
Number of generations	100
Quantity of variables	3 (M, θ_1, θ_2)
Intervals limit	$\theta_1 \in [0, 90]$
	$\theta_2 \in [0, 90]$
	$M \in [0.1, 0.85]$
Number's length in binary	10
Selection	Roulette
Crossover	Random
Probability of crossover	100 %
Mutation	Random
Probability of mutation	5 %

Results discussion. The simulations were performed using the MATLAB/Simulink environment to execute the optimization algorithms. Figure 3 presents the switching angles θ_1 and θ_2 obtained using the NR, GA and PSO algorithms. As shown, all 3 methods converge to identical solutions for both switching angles over the modulation index M range 0.45–0.85. Therefore, we can primarily focus on the differences in implementation complexity and computational efficiency when evaluating these algorithms.

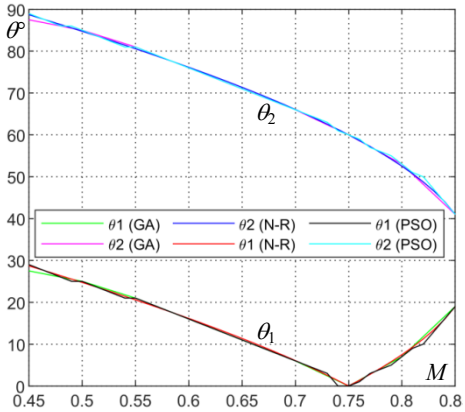

Fig. 3. The angles θ_1 and θ_2 versus M using the 3 algorithms

To demonstrate the effectiveness of the discussed SHE modulation technique and the proposed system, we performed 3 tests using different values of M for comparison purposes. In these tests 2 DC sources of 15 V are used. Table 3 displays the parameter settings in each of the 3 cases.

Table 3

Parameter settings to test the 5-level inverter

Test	Setting
Case 1	f = 1 kHz, M = 0.55, θ_1 = 21°, θ_2 = 81°
Case 2	f = 5 kHz, M = 0.65, θ_1 = 11°, θ_2 = 71°
Case 3	f = 10 kHz, M = 0.85, θ_1 = 19°, θ_2 = 41°

Simulation results. Figure 4 shows the simulation output voltage of the 5-level emerging inverter using SHE modulation in the 3 cases, and Fig. 5 – the simulation harmonic spectrum in this cases.

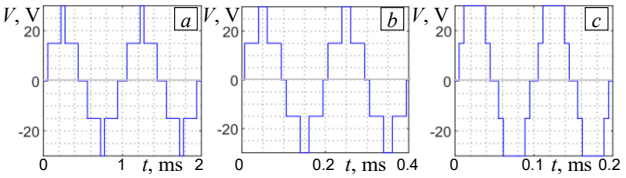

Fig. 4. The simulation output voltage of the 5-level inverter using SHE modulation: *a* – case 1; *b* – case 2; *c* – case 3

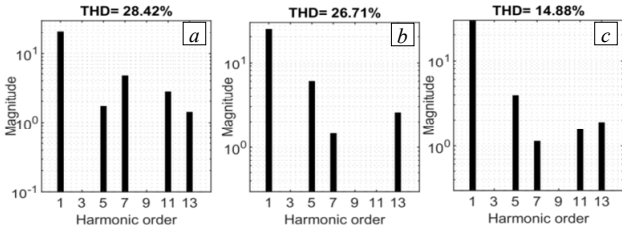

Fig. 5. The simulation harmonic spectrum of the inverter's output voltage: *a* – case 1; *b* – case 2; *c* – case 3

Across all 3 operating conditions, the 3rd harmonic and its multiples are effectively suppressed, confirming the success of the harmonic elimination strategy. In terms of overall distortion, the THD_v of the output voltage is 28.42 % in case 1. This value decreases to 26.71 % in case 2 and is further reduced to 14.88 % in case 3, demonstrating a progressive improvement in waveform quality.

Experimental results. To validate the simulation results, experimental tests were conducted using an experimental prototype. Figure 6 shows photo of the experimental setup. An Arduino Mega 2560 chip is used to execute the SHE modulation code and generate the suitable gating signals. The harmonic spectrums are extracted using digital oscilloscope. The fluke power quality analyzer is used to measure the THD_v values.

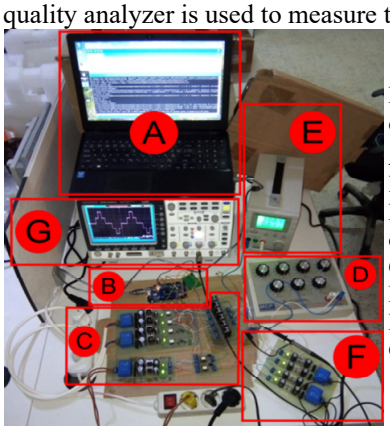

Fig. 6. Photo of the experimental setup:
A – PC with Arduino IDE software
B – Arduino Mega 2560 chip
C – 5-level inverter
D – resistive load
E, F – power supplies
G – oscilloscope

Figure 7 depicts the experimental output voltage of the 5-level emerging inverter using SHE modulation in case 1. Their associated harmonic spectrum is given in Fig. 8. The waveform results agree perfectly with the simulation results shown in Fig. 4,*a* and Fig. 5,*a*.

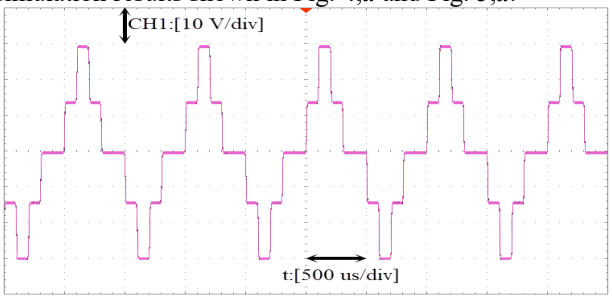

Fig. 7. The experimental output voltage of the 5-level inverter using SHE modulation in case 1

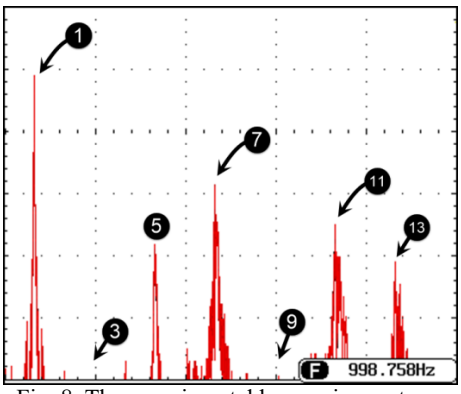

Fig. 8. The experimental harmonic spectrum of the 5-level output voltage in case 1

Figure 9 depicts the experimental output voltage of the 5-level inverter using SHE modulation in case 2. Their associated harmonic spectrum is shown in Fig. 10. The waveform results agree perfectly with the simulation results shown in Fig. 4,*b* and Fig. 5,*b*.

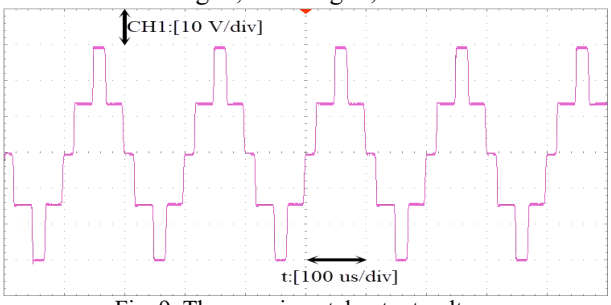

Fig. 9. The experimental output voltage of the 5-level inverter using SHE modulation in case 2

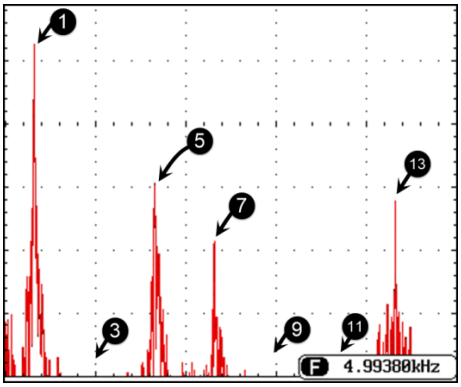

Fig. 10. The experimental harmonic spectrum of the 5-level output voltage in case 2

Figure 11 displays the experimental output voltage of the 5-level inverter using SHE modulation in case 3. Their associated harmonic spectrum is given in Fig. 12. The waveform results agree perfectly with the simulation results shown in Fig. 4,*c* and Fig. 5,*c*.

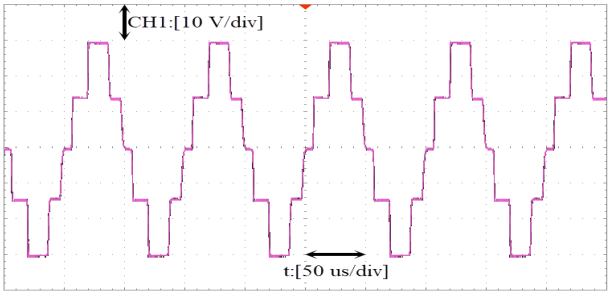

Fig. 11. The experimental output voltage of the 5-level inverter using SHE modulation in case 3

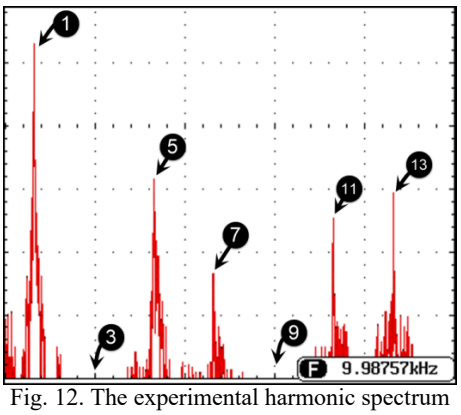

Fig. 12. The experimental harmonic spectrum of the 5-level output voltage in case 3

Comparison of results. Figure 4 presents the simulated phase-voltage of the 5-level inverter for all 3 cases, while Fig. 7, 9, 11 show the corresponding measurements obtained from the experimental prototype. A comparison between both sets of results indicates a strong agreement, confirming the accuracy of the simulation model. Likewise, the harmonic analyses of the output voltage in all 3 cases exhibit close correspondence between the simulated and experimental spectra, as summarized in Table 4. In each operating condition, the 3rd harmonic and its multiples are effectively eliminated. These outcomes were achieved using a relatively simple implementation method, and the observed performance is consistent with results previously reported in [5, 21].

Table 4

THD_v comparison

Test	Simulation THD_v, %	Experimental THD_v, %
Case 1	28.42	29.7
Case 2	26.71	27.2
Case 3	14.88	15.1

Table 5 details the computation time necessary for finding the switching angles in each approach. The PSO-SHE necessitates 10.237 s, but the NR-SHE requires merely 0.516 s. The GA-SHE operates at a sluggish pace, necessitating 23.289 s.

Table 5

The execution time of the 3 algorithms

Method	The execution time, s
NR-SHE	0.516
PSO-SHE	10.237
GA-SHE	23.289

In fact, all 3 methods are able to produce valid switching angles for the SHE problem. However, their performances are significantly different regarding execution time, complexity, and interpretability. The NR method is the most rapid and computationally efficient approach due to the use of a deterministic numerical scheme. Indeed, its main advantage is that the associated solution process is fully interpretable: it naturally yields clear convergence behavior based on the Jacobian and nonlinear equations. However, NR requires a good initial guess and may fail to converge for some values of the modulation index, hence limiting its robustness.

On the other hand, PSO and GA are metaheuristic algorithms that search globally within the solution space. No starting values are needed which are close to the final solution. Therefore, they are more robust on problematic or multi-modal harmonic equations. However, metaheuristic methods behave like «black box» optimizers. Therefore,

from an analytical point of view, they do not supply any insight in how the solution is reached, whereas their internal search dynamics are less interpretable than in NR methods. In general, the execution times are longer and parameters require careful tuning.

Overall, while the NR method is attractive because of its speed and interpretability, PSO and GA offer superior flexibility and robustness, especially when the harmonic elimination problem becomes highly nonlinear.

Conclusions.

1. This work focused on reducing output voltage harmonic distortion and determining optimal switching angles for a single-phase 5-level emerging inverter using 3 approaches: numerical (NR), evolutionary (GA) and metaheuristic (PSO). All approaches successfully achieved harmonic reduction and converged to the same switching angle solutions across the tested modulation indices, confirming the validity of the mathematical formulation and the reliability of the optimization process.

2. Simulation results showed that the 3rd harmonic and its multiples were effectively eliminated for all operating conditions. THD of the output voltage reduced progressively with frequency and modulation indices, decreasing from 28.42 % at (M = 0.55, f = 1 kHz) to 14.88 % at (M = 0.55, f = 10 kHz). These results demonstrate the effectiveness of SHE in reducing harmonic distortion and enhancing waveform quality in reduced-switch 5-level inverter topologies.

3. Numerical results show clear performance differences among the 3 methods. NR-SHE is the fastest (0.516 s) due to its deterministic structure, while PSO-SHE (10.237 s) and GA-SHE (23.289 s) require significantly longer times because of their search mechanisms. Thus, NR offers the best computational efficiency, whereas PSO and GA provide higher robustness for complex or highly nonlinear modulation indices. Methodologically, NR is interpretable and offers predictable convergence but depends on a good initial guess. In contrast, PSO and GA require no initial solution and explore the search space, improving robustness at the expense of longer execution times and less transparency in how the solution is obtained.

4. An Arduino Mega 2560 platform was employed to implement the optimized switching patterns, highlighting the feasibility of using low-cost open-source hardware for experimental validation and educational purposes. The measured waveforms and harmonic spectra closely matched the simulation results, thereby confirming the accuracy of the discussed numerical, evolutionary, and metaheuristic methods, as well as the practical reliability of the proposed inverter design.

5. The future works will focus on the integration of hybrid optimization schemes that combine the speed of deterministic methods with the global search capability of metaheuristics, enabling faster computation of switching angles while maintaining robustness against nonlinearities. Additionally, extending the inverter topology to higher-level or modular multilevel configurations may yield improved output waveform quality and reduced harmonic content. Implementing the optimization and control algorithms on high performance embedded platforms such as digital signal processors, field-programmable gate arrays processors can further accelerate computation time. Finally, this work opens pathways for applying the proposed approach to related energy conversion systems, including alternative converter structures and renewable energy based applications. Future studies may integrate photovoltaic, wind or hybrid solar-wind sources to develop sustainable, high performance power electronic systems optimized for modern energy infrastructures.

Conflict of interest. The authors declare that they have no conflicts of interest.

REFERENCES

1. Priyanka G., Surya Kumari J., Lenine D., Srinivasa Varma P., Sneha Madhuri S., Chandu V. MATLAB-Simulink environment based power quality improvement in photovoltaic system using multilevel inverter. *Electrical Engineering & Electromechanics*, 2023, no. 2, pp. 43-48. doi: https://doi.org/10.20998/2074-272X.2023.2.07.

2. Aishwarya V. A single-phase reduced switch 21-level asymmetrical multilevel inverter topology for renewable energy systems. *Electrical Engineering*, 2025, vol. 107, no. 6, pp. 7417-7436. doi: https://doi.org/10.1007/s00202-024-02936-1.

3. Toubal Maamar A.E., Helaimi M., Taleb R. Analysis, Simulation and Experimental Validation of High Frequency DC/AC Multilevel Inverter. *Przegląd Elektrotechniczny*, 2020, vol. 1, no. 8, pp. 16-19, https://doi.org/10.15199/48.2020.08.03.

4. Elamri O., Toubal Maamar A.E., Oukassi A., El Bahir L. Nonlinear Backstepping Controller for Current Control of Grid-Connected Five-Level Inverter. *Revista Politécnica*, 2024, vol. 54, no. 2, pp. 85-96. doi: https://doi.org/10.33333/rp.vol54n2.08.

5. Toubal Maamar A.E. Analysis and experimental validation of selective harmonic elimination in single-phase five-level inverter using particle swarm optimization algorithm. *Electronics Journal*, 2022, vol. 26, no. 2, pp. 65-72. doi: https://doi.org/10.53314/ELS2226065M.

6. Elamri O., Toubal Maamar A.E., Oukassi A., El Kharki A., Hammoudi A., Mekhilef S. SVPWM-Based Control of a Three-Phase Five-Level NPC Inverter for Grid-Connected Solar Power System. *2025 5th International Conference on Innovative Research in Applied Science, Engineering and Technology (IRASET)*, 2025, pp. 1-6. doi: https://doi.org/10.1109/IRASET64571.2025.11008300.

7. Feyrouz Abdelgoui R., Taleb R., Bentaallah A., Chabni F. Harmonic Elimination in Uniform Step Nine-Level Inverter Using Differential Evolution: Experimental Validation. *Electronics Journal*, 2021, vol. 25, no. 1, pp. 31-36. doi: https://doi.org/10.53314/ELS2125031A.

8. Parimalasundar E., Muthukaruppasamy S., Dharmaprakash R., Suresh K. Performance investigations of five-level reduced switches count H-bridge multilevel inverter. *Electrical Engineering & Electromechanics*, 2023, no. 6, pp. 58-62. doi: https://doi.org/10.20998/2074-272X.2023.6.10.

9. Mohamed O., Jalil A., Bouazza E.M., Yassine L., Mohamed B. Study and realization of a single-phase solar inverter with harmonics rejection. *Advances in Science, Technology & Innovation,* 2024, pp. 59-65. doi: https://doi.org/10.1007/978-3-031-51796-9_7.

10. Toubal Maamar A.E., Helaimi M., Taleb R., Mouloudj H., Elamri O., Gadoum A. Mathematical Analysis of N-R Algorithm for Experimental Implementation of SHEPWM Control on Single-phase Inverter. *International Journal of Engineering Trends and Technology*, 2020, vol. 68, no. 2, pp. 9-16. doi: https://doi.org/10.14445/22315381/IJETT-V68I2P202.

11. Hamadneh T., Batiha B., Gharib G.M., Montazeri Z., Dehghani M., Aribowo W., Noori H.M., Jawad R.K., Ibraheem I.K., Eguchi K. Revolution Optimization Algorithm: A New Human-based Metaheuristic Algorithm for Solving Optimization Problems. *International Journal of Intelligent Engineering and*

Systems, 2025, vol. 18, no. 2, pp. 520-531. doi: https://doi.org/10.22266/ijies2025.0331.38.
12. Ebrahimi F., Wndarko N.A., Gunawan A.I. Wild horse optimization algorithm implementation in 7-level packed U-cell multilevel inverter to mitigate total harmonic distortion. *Electrical Engineering & Electromechanics*, 2024, no. 5, pp. 34-40. doi: https://doi.org/10.20998/2074-272X.2024.5.05.
13. Hamadneh T., Batiha B., Gharib G.M., Montazeri Z., Dehghani M., Aribowo W., Zalzala A.M., Jawad R.K., Ahmed M.A., Ibraheem I.K., Eguchi K. Perfumer Optimization Algorithm: A Novel Human-Inspired Metaheuristic for Solving Optimization Tasks. *International Journal of Intelligent Engineering and Systems*, 2025, vol. 18, no. 4, pp. 633-643. doi: https://doi.org/10.22266/ijies2025.0531.41.
14. Keek J., Loh S., Wong Y., Woo X., Lee W. Genetic Algorithms and Particle Swarm Optimization for Interference Minimization in Mobile Network Channel Assignment Problem. *International Journal of Intelligent Engineering and Systems*, 2021, vol. 14, no. 4, pp. 276-288. doi: https://doi.org/10.22266/ijies2021.0831.25.
15. Subramanian N., Stonier A.A. A Comprehensive Review on Selective Harmonic Elimination Techniques and Its Permissible Standards in Electrical Systems. *IEEE Access*, 2024, vol. 12, pp. 141966-141998. doi: https://doi.org/10.1109/ACCESS.2024.3436079.
16. Memon M.A., Siddique M.D., Mekhilef S., Mubin M. Asynchronous Particle Swarm Optimization-Genetic Algorithm (APSO-GA) Based Selective Harmonic Elimination in a Cascaded H-Bridge Multilevel Inverter. *IEEE Transactions on Industrial Electronics*, 2022, vol. 69, no. 2, pp. 1477-1487. doi: https://doi.org/10.1109/TIE.2021.3060645.
17. Buccella C., Cecati C., Cimoroni M.G., Kulothungan G., Edpuganti A., Rathore A.K. A Selective Harmonic Elimination Method for Five-Level Converters for Distributed Generation. *IEEE Journal of Emerging and Selected Topics in Power Electronics*, 2017, vol. 5, no. 2, pp. 775-783. doi: https://doi.org/10.1109/JESTPE.2017.2688726.
18. Djafer L., Taleb R., Toubal Maamar A.E., Mehedi F., Mostefaoui S.A., Rekmouche H. Analysis and Experimental Implementation of SHEPWM based on Newton-Raphson Algorithm on Three-Phase Inverter using Dspace 1104. *2023 2nd International Conference on Electronics, Energy and Measurement (IC2EM)*, 2023, pp. 1-6. doi: https://doi.org/10.1109/IC2EM59347.2023.10419389.
19. Yang X.-S. Genetic Algorithms. *Nature-Inspired Optimization Algorithms*, 2021, pp. 91-100. doi: https://doi.org/10.1016/B978-0-12-821986-7.00013-5.
20. Swayamsiddha S. Bio-inspired algorithms: principles, implementation, and applications to wireless communication. *Nature-Inspired Computation and Swarm Intelligence*, 2020, pp. 49-63. doi: https://doi.org/10.1016/B978-0-12-819714-1.00013-0.
21. Djafer L., Taleb R., Mehedi F. Dspace implementation of real-time selective harmonics elimination technique using modified carrier on three phase inverter. *Electrical Engineering & Electromechanics*, 2024, no. 5, pp. 28-33. doi: https://doi.org/10.20998/2074-272X.2024.5.04.

Received 21.08.2025
Accepted 28.10.2025
Published 02.03.2026

M. Naidji[1]*, PhD, Associate Professor,*
A.E. Toubal Maamar[2]*, PhD, Associate Professor,*
M. Boudour[3]*, PhD, Professor,*
A. Garmat[2,4]*, PhD, Associate Professor,*
A. Aissa-Bokhtache[5]*, PhD, Associate Professor,*
[1] Laboratory of Electrical Engineering (LGE),
Department of Electrical Engineering, University of M'Sila, Algeria,
e-mail: mourad.naidji@univ-msila.dz (Corresponding Author)
[2] Laboratoire Ingénierie des Systèmes et Télécommunications (LIST),
Department of Electrical Systems Engineering,
Faculty of Technology,
University of M'hamed Bougara of Boumerdes, Algeria,
e-mail: a.toubalmaamar@univ-boumerdes.dz
[3] Department of Electrical Engineering,
University of Sciences & Technology Houari Boumediene, Algeria,
e-mail: mboudour@usthb.dz
[4] Faculty of Science and Technology, University of Djelfa, Algeria,
e-mail: a.garmat@univ-djelfa.dz
[5] Laboratoire Génie Electrique et Energies Renouvelables (LGEER),
Electrical Engineering Department,
Hassiba Benbouali University of Chlef, Algeria,
e-mail: a.aissabokhtache@univ-chlef.dz

How to cite this article:
Naidji M., Toubal Maamar A.E., Boudour M., Garmat A., Aissa-Bokhtache A. Comparative analysis of numerical, evolutionary and metaheuristic methods for experimental implementation of selective harmonic elimination in a five-level emerging inverter. *Electrical Engineering & Electromechanics*, 2026, no. 2, pp. 59-66. doi: https://doi.org/10.20998/2074-272X.2026.2.08

UDC 621.313 https://doi.org/10.20998/2074-272X.2026.2.09

A. Nayli, S. Guizani, F. Ben Ammar

Normal and degraded operation of the open-end winding induction machine fed by 2-level inverters in cascading

Introduction. *The machine-converter system is a prevalent and essential configuration, widely used not only in variable-speed industrial drive applications, but also in high-tech transportation and power fields.* ***Problem.*** *Conventional drive systems, particularly those supplied by standard 2-level inverters, face major challenges regarding the enhancement of their dynamic performance and drive availability. To overcome these limitations, a solution involves utilizing the open-end stator winding induction machine associated with cascaded 2-level inverter topologies. The* ***goal*** *of this work is to improve the availability of the drive system by increasing its degrees of freedom through the association of an open-end winding induction machine by two cascaded 2-level inverters.* ***Methodology.*** *The mathematical modeling of this machine is presented and validated using MATLAB/Simulink. To evaluate the machine's performance, it is first powered by two cascaded 2-level inverters and subsequently by three cascaded 2-level inverters. Following this initial evaluation, the machine is then fed by two cascaded 2-level inverters operating in degraded mode. This analysis features different failure configurations, and the specific operational conditions that must be respected.* ***Results.*** *This topology enhances dynamic performances and enables effective power segmentation as well as a degraded mode operation. These benefits are confirmed by the simulation results. The* ***scientific novelty*** *is based on demonstrating the effectiveness of degraded mode control, which gives the machine-cascaded inverters topology a superior advantage in terms of reliability and performances.* ***Practical value.*** *This topology provides a highly reliable and fault-tolerant drive solution, ensuring better performance during normal operation and better availability after an inverter failure.* References 15, tables 1, figures 24.

Key words: **open-end winding induction machine, cascaded 2-level inverters, degraded mode, power segmentation.**

Вступ. *Система «машина-перетворювач» є поширеною та важливою конфігурацією, що широко використовується не тільки в системах приводу з регульованою швидкістю в промисловості, а й у високотехнологічних транспортних та енергетичних галузях.* ***Проблема***. *Традиційні системи приводу, особливо ті, які живляться від стандартних дворівневих інверторів, стикаються із серйозними проблемами щодо підвищення їх динамічних характеристик та доступності приводу. Для подолання цих обмежень пропонується рішення, що включає використання асинхронної машини з відкритою статорною обмоткою в поєднанні з каскадними дворівневими інверторними топологіями.* ***Мета*** *роботи – підвищення доступності системи приводу за рахунок збільшення її ступенів свободи шляхом з'єднання асинхронної машини з відкритою обмоткою з двома каскадними дворівневими інверторами.* ***Методика***. *Математична модель цієї машини розроблена та перевірена за допомогою MATLAB/Simulink. Для оцінки продуктивності машини спочатку живлять її від двох каскадних дворівневих інверторів, а потім від трьох каскадних дворівневих інверторів. Після початкової оцінки машина живиться від двох каскадно з'єднаних дворівневих інверторів, що працюють у режимі зниженої потужності. Цей аналіз включає різні зміни відмов і конкретні умови експлуатації, яких необхідно дотримуватися.* ***Результати***. *Дана топологія підвищує динамічні характеристики та забезпечує ефективне сегментування потужності, а також роботу в режимі зниженої потужності. Ці переваги підтверджуються результатами моделювання.* ***Наукова новизна*** *ґрунтується на демонстрації ефективності управління в режимі зниженої потужності, що дає топології «машина-каскадні інвертори» значну перевагу з погляду надійності та продуктивності.* ***Практична цінність***. *Дана топологія забезпечує високонадійне та відмовостійке рішення для приводу, гарантуючи кращу продуктивність у нормальному режимі роботи та кращу доступність після відмови інвертора.* Бібл. 15, табл. 1, рис. 24.

Ключові слова: **асинхронна машина з відкритою обмоткою, каскадні дворівневі інвертори, режим зі зниженою потужністю, сегментація потужності.**

Introduction. In order to satisfy the demands for reliability, availability and dynamic performance of the drive system across various industrial domains [1–3], power segmentation at the level of the machines is often used [4–6]. This approach specifically allows for the optimization of electrical system performance by simultaneously increasing reliability, modularity, scalability and reconfigurability, while also ensuring better cost control; ultimately, adopting this strategy yields cleaner power waveforms and minimizes stress on power semiconductor devices, thereby substantially enhancing the overall efficiency and durability of the drive system. Consequently, several lines of research have focused on inverter structures such as 2-level cascaded inverters and various other multilevel topologies [7, 8] as well as on machine structures including multiphase machines [9, 10], double-star machines, where each star is supplied by its own 3-phase voltage source inverter [11–13], this architecture substantially enhances the drive system's reliability, providing multiple degrees of redundancy [4]. Another machine structure is the open-end winding induction machine (OEWIM), where each end is supplied by its own 3-phase voltage source inverter [5, 14, 15].

The **goal** of this work is to improve the availability of the drive system by increasing its degrees of freedom through the association of an open-end winding induction machine by two cascaded 2-level inverters.

The structure of the work is next. In the first part, the mathematical modeling of the proposed OEWIM is presented and implemented in the MATLAB/Simulink. In the second part, the OEWIM is fed by cascaded 2-level inverter structures based on a pulse width modulation (PWM) strategy. The various results obtained concerning the speed, torque, stator current, the voltage between phases of the cascaded inverters and the machine, the total harmonic distortion (THD) of the voltage and the torque ripple are shown. The final part of this work presents the machine's degraded mode performance across 4 specific inverter failure configurations, utilizing two cascaded 2-level inverters. Successfully conducting this study requires strict adherence to predefined operational constraints unique to each configuration.

Modeling of the OEWIM. As shown in Fig. 1, the design of the OEWIM allows for a dual-inverter supply configuration.

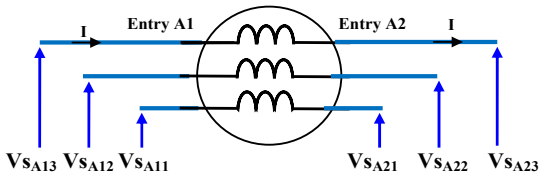

Fig. 1. The design of o the OEWIM

The following state equations describe the mathematical flux model in the (d, q) reference frame:

$$\begin{cases} \dfrac{\mathrm{d}X(t)}{\mathrm{d}t} = [\boldsymbol{A}]\cdot[\boldsymbol{X}(t)] + [\boldsymbol{B}]\cdot\boldsymbol{U}(t); \\ \boldsymbol{Y}(t) = [\boldsymbol{C}]\cdot\boldsymbol{X}(t), \end{cases} \tag{1}$$

where the state vector:

$$\boldsymbol{X}(t) = [\boldsymbol{\Phi}] = \begin{bmatrix} \Phi_{\mathrm{sd}} & \Phi_{\mathrm{sq}} & \Phi_{\mathrm{rd}} & \Phi_{\mathrm{rq}} \end{bmatrix}^T;$$

the control vector:

$$\boldsymbol{U}(t) = U_1(t) - U_2(t) = \begin{bmatrix} V_{\mathrm{sd1}} - V_{\mathrm{sd2}} & V_{\mathrm{sq1}} - V_{\mathrm{sq2}} \end{bmatrix}^T;$$

the output vector:

$$\boldsymbol{Y}(t) = [\boldsymbol{I}] = \begin{bmatrix} I_{\mathrm{sd}} & I_{\mathrm{sq}} & I_{\mathrm{rd}} & I_{\mathrm{rq}} \end{bmatrix}^T.$$

The equation of current vector is:

$$[\boldsymbol{I}] = [\boldsymbol{L}]^{-1}[\boldsymbol{\Phi}]. \tag{2}$$

The matrices [$\boldsymbol{A}$], [$\boldsymbol{B}$] and [$\boldsymbol{C}$] are:

$$[\boldsymbol{A}] = \begin{bmatrix} -\dfrac{1}{\sigma\tau_s} & \omega_{dq} & \dfrac{L_m}{\sigma\tau_s L_r} & 0 \\ -\omega_{dq} & -\dfrac{1}{\sigma\tau_s} & 0 & \dfrac{L_m}{\sigma\tau_s L_r} \\ \dfrac{L_m}{\sigma\tau_r L_s} & 0 & -\dfrac{1}{\sigma\tau_r} & \omega_{dq}-\omega \\ 0 & \dfrac{L_m}{\sigma\tau_r L_s} & -(\omega_{dq}-\omega) & -\dfrac{1}{\sigma\tau_r} \end{bmatrix}; \tag{3}$$

$$[\boldsymbol{B}] = \begin{bmatrix} 1 & 0 & 0 & 0 \\ 0 & 1 & 0 & 0 \\ 0 & 0 & 1 & 0 \\ 0 & 0 & 0 & 1 \end{bmatrix}; \tag{4}$$

$$[\boldsymbol{C}] = [\boldsymbol{L}]^{-1} = \begin{bmatrix} \dfrac{1}{\sigma L_s} & 0 & \dfrac{-L_m}{\sigma L_s L_r} & 0 \\ 0 & \dfrac{1}{\sigma L_s} & 0 & \dfrac{-L_m}{\sigma L_s L_r} \\ \dfrac{-L_m}{\sigma L_r L_s} & 0 & \dfrac{1}{\sigma L_r} & 0 \\ 0 & \dfrac{-L_m}{\sigma L_r L_s} & 0 & \dfrac{1}{\sigma L_r} \end{bmatrix}, \tag{5}$$

where $\tau_s = L_s/R_s$, $\tau_r = L_r/R_r$ are the constants of time for stator and rotor; R_s, R_r are the resistances of stator and rotor; L_s, L_r are the inductances of stator and rotor; $\sigma = 1 - (L_m^2/L_s{\cdot}L_r)$ is the coefficient of dispersion of Blondel; L_m is the mutual inductance between stator and rotor.

The mechanical equation governing the drive and the electromagnetic torque T_{em} is:

$$T_{em} - T_r = j\frac{\mathrm{d}\omega}{\mathrm{d}t} + f\omega; \tag{6}$$

$$T_{em} - T_r = \frac{3}{2}p\left(\psi_{s\alpha}I_{s\beta} - \psi_{s\beta}I_{s\alpha}\right), \tag{7}$$

where T_r is the load torque; f is the frequency; ω is the angular frequency; p is the number of pairs of poles; $\psi_{s\alpha}$, $\psi_{s\beta}$, $I_{s\alpha}$, $I_{s\beta}$ are the flux linkages and the stator currents in the (α, β) reference frame.

Supply of the OEWIM by two cascaded 2-level inverters. The OEWIM is fed by two cascaded 2-level inverters based on PWM, with each inverter drawing power from a quarter of the DC-link voltage (E/4) (Fig. 2).

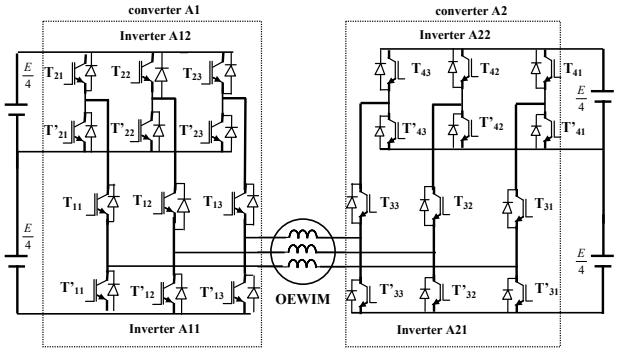

Fig. 2. Supply the OEWIM by two cascaded 2-level inverters

The evolution of the stator currents, speed and torque is shown in Fig. 3, illustrating the transient and steady-state modes during normal operation. The load torque is the type $k\omega^2$.

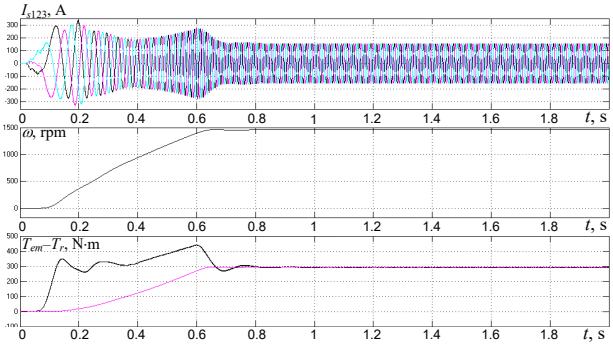

Fig. 3. Evolution of the stator currents, speed and torque

Figure 4 provides an enlarged view of the torque under steady-state conditions.

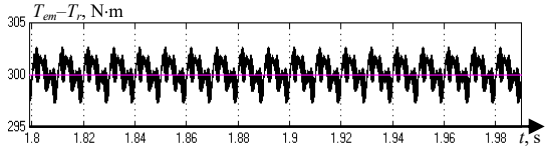

Fig. 4. Enlarged view of the torque

The torque ripple is calculated as:

$$\Delta T_{\mathrm{em}} = \frac{302.65 - 300}{300}\cdot 100\% = 0.88\%.$$

Figure 5 shows the compound voltages in the steady-state regime during normal operation. Specifically, the voltages at stator input A1 (U_1=Vs_{11}–Vs_{12}) of converter A1 and at input A2 (U_2=Vs_{21}–Vs_{22}) of converter A2 are shown. The machine phase-to-phase voltage U_{A}, which is given by the difference U_{A}=U_1–U_2, features 5 voltage levels.

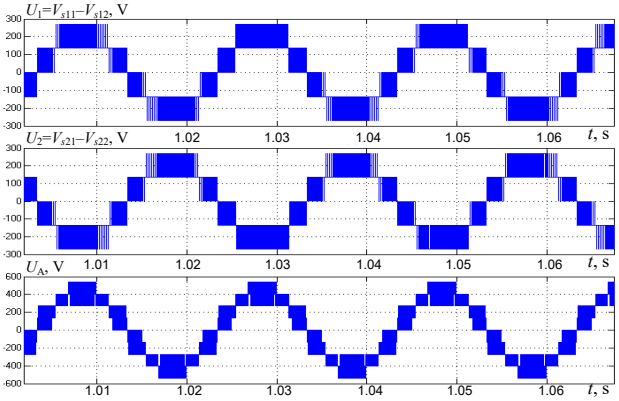

Fig. 5. Compound voltages at the terminals of the two cascaded 2-level inverters and the machine

THD of the voltage across the machine terminals is 24.99 % (Fig. 6).

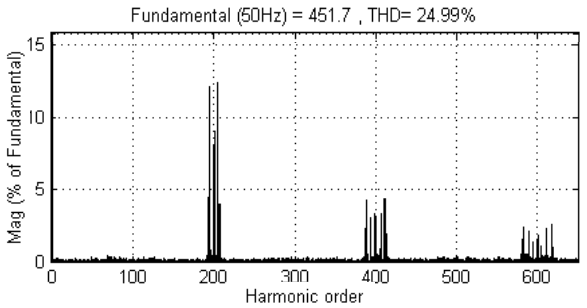

Fig. 6. THD of the machine voltage

The use of cascaded 2-level inverters to power the machine significantly increases the phase-to-phase voltage level from 3 to 5 levels when compared to conventional converters with the same machine. This configuration also substantially improves the voltage THD and doubles the bandwidth relative to a classic induction machine [4].

Supply of the OEWIM by three cascaded 2-level inverters. As illustrated in Fig. 7, the OEWIM is powered by three cascaded 2-level inverters. Crucially, each inverter is supplied by a dedicated DC source equivalent to 1/6 of the total DC-link voltage (E/6).

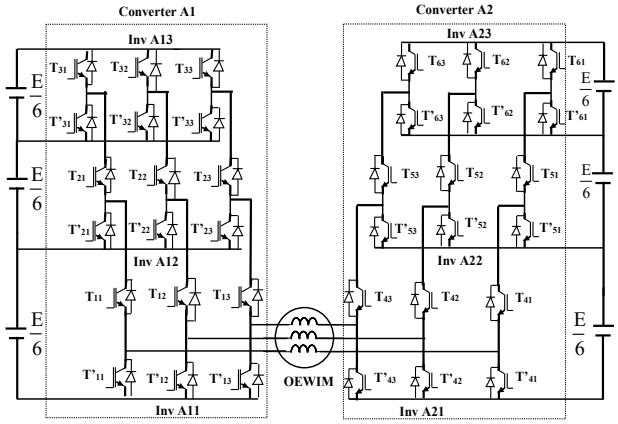

Fig. 7. Supply the OEWIM by three cascaded 2-level inverters

Figure 8 provides an enlarged view of the torque under steady-state conditions.

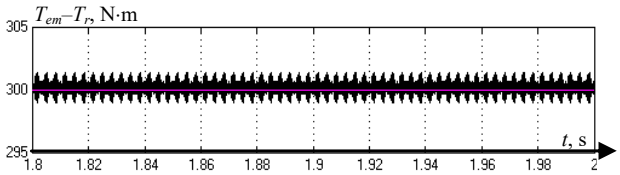

Fig. 8. Enlarged view of the torque

The steady-state torque ripple was calculated as follows: $\Delta T_{\text{em}} = \dfrac{301.35 - 300}{300} \cdot 100\% = 0.45\%$

Figure 9 shows a detailed visualization of the compound voltages in the steady-state regime during normal operation. It clearly differentiates the 4-level voltage waveform observed at the converter terminals from the 7-level voltage waveform observed at the machine terminals.

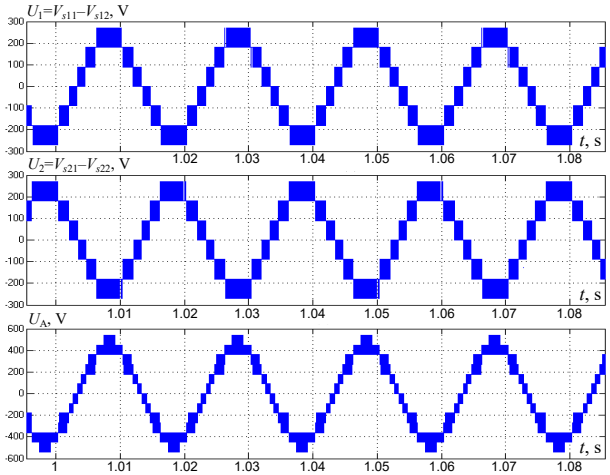

Fig. 9. Compound voltages at the terminals of the three cascaded 2-level inverters and the machine

THD of the voltage across the machine terminals is 15.07 % (Fig. 10).

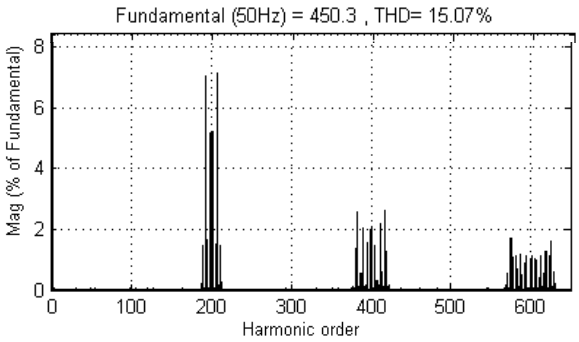

Fig. 10. THD of the machine voltage

The performance characteristics for different cascaded converters are detailed in Table 1. Specifically, the table reports the voltage levels at converter A1, A2 and OEWIM terminals, the voltage harmonic distortion rate and the steady-state torque ripple.

Table 1

Different results of THD and torque ripple

Voltage levels			THD of the voltage, %	ΔT_{em}, %
Inverter A1	Inverter A2	Machine N		
3	3	5	24.99	0.88
4	4	7	15.07	0.45

The integration of cascaded 2-level inverters with the OEWIM configuration delivers substantial performance enhancements across the drive system. Chief among these is the ability to increase the phase-to-phase voltage resolution from 5 to 7 levels, depending on the cascaded inverter topology employed. This voltage resolution directly translates into quantifiable improvements in signal quality. The voltage THD is drastically reduced from 24.99 % to 15.07 %, and the torque quality is improved, decreasing from 0.88 % to 0.45 %.

Degraded mode operation for the OEWIM fed by two cascaded 2-level inverters. Our focus is the degraded-mode operation of the OEWIM, which is powered by two 3-level converter systems. As each system comprises two cascaded 2-level inverters, we investigate 4 potential fault configurations by considering

only failures within the converter feeding input A1, given the operational symmetry with input A2. These 4 configurations stem from the fault location (upper or lower stage) in each of the 2 cascaded inverters. The specific operational constraints for each configuration must be adhered to throughout the study.

Sizing inverters. Accurate sizing of cascaded 2-level inverters is a prerequisite for proposing a mitigation strategy during degraded-mode operation. This section demonstrates the relevant sizing criteria based on the configuration of two cascaded 2-level inverters (Fig. 11).

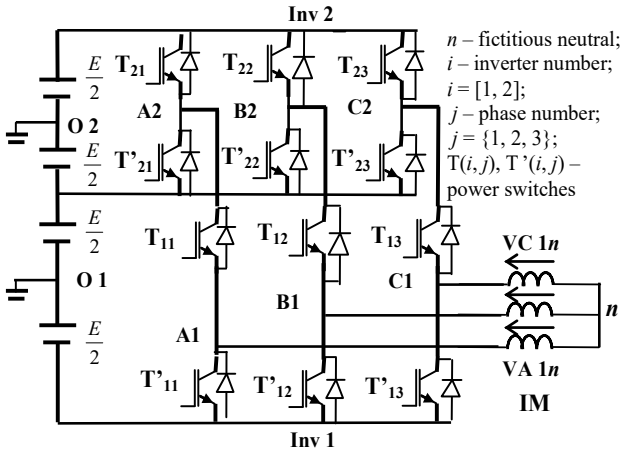

Fig. 11. Induction machine fed by two cascaded 2-level inverters

As shown in Fig. 11, the DC bus voltage for each inverter is denoted by E. This allows us to define the relation as follows. For inverter 2:

$$V_{\mathrm{T'_{21}}} = \frac{E}{2} + V_{\mathrm{A2O2}} = \frac{E}{2} + \frac{E}{2} = E\,. \qquad (8)$$

For inverter 1:

$$V_{\mathrm{T'_{11}}} = \frac{3E}{2} + V_{\mathrm{A2O2}} = \frac{3E}{2} + \frac{E}{2} = 2E\,. \qquad (9)$$

In this configuration, the OEWIM is sized for a power P. Since the machine is powered at each input by two cascaded 2-level inverters, the required sizing is:

- inverters Inv A11 and Inv A21 are rated for a power $P/2$;
- inverters Inv A12 and Inv A22 are rated for $P/4$.

Different configurations. We consider the failures of the converter A1 (the behavior is identical for failures of the converter A2). Only one fault is considered at a time. Four configurations 1–4 are possible.

Configuration 1. In the 1st configuration (Fig. 12) we consider an open circuit of one of the switches: T_{11} or T_{12} or T_{13} of the inverter A11 (following a short circuit). The control must act so that the 3 switches T_{11}, T_{12} and T_{13} are in state 0 and the switches T'_{11}, T'_{12} and T'_{13} are in state 1. We will thus have a star coupling of the input A1 of the machine.

This is the operation of the classic induction machine powered by converter A2. The machine must operate at reduced speed and therefore there are no conditions on the sizing of the inverters:

- 70 % of the nominal speed for $T_r = k\omega^2$;
- 50 % of the nominal speed for $T_r = k\omega$.

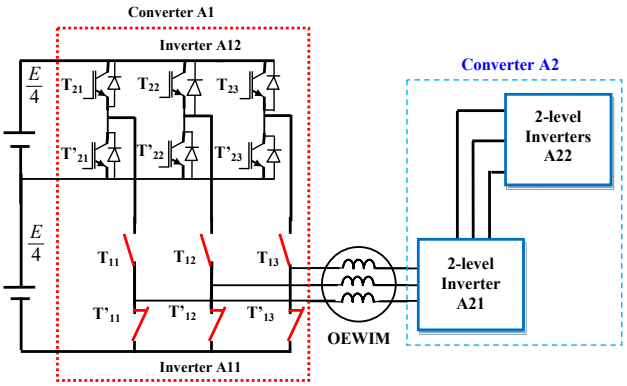

Fig. 12. Supply the OEWIM by cascaded 2-level inverters for the configuration 1

The provided figures illustrate the simulated operation of an OEWIM powered by two cascaded 3-phase inverters. The simulation is designed to show the machine's behavior before and after a fault that occurs at t = 1.2 s in inverter A11. The system has a load torque defined by the equation $T_r = k\omega^2$. This particular characteristic necessitates a control strategy that intentionally commands the machine's speed to drop to 70 % of its nominal value following the fault. As shown in Fig. 13, this speed reduction is imposed at the moment of the fault, which effectively reducing the required torque to manage the load and allowing the machine to operate safely despite the inverter failure.

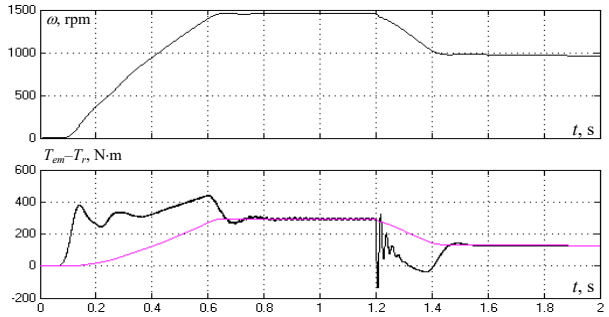

Fig. 13. Evolution of speed and torque for the configuration 1

Figure 14 shows the evolution of the stator currents before and after the failure in the inverter A11, which occurs alongside a reduction in speed.

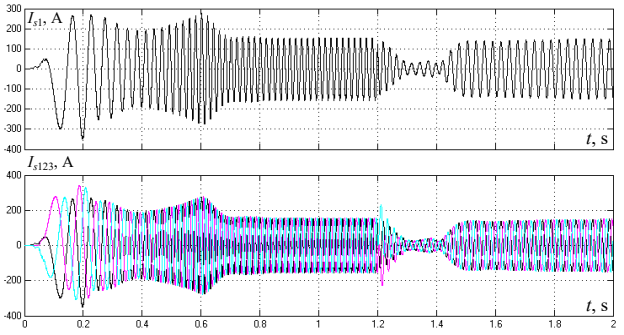

Fig. 14. Evolution of stator current for configuration 1

Figure 15 shows the evolution of the machine and inverter voltages, covering the regimes before and after the failure that occurred within inverter A11. A zoomed visualization is included to accurately capture the immediate dynamic response of the system to the fault.

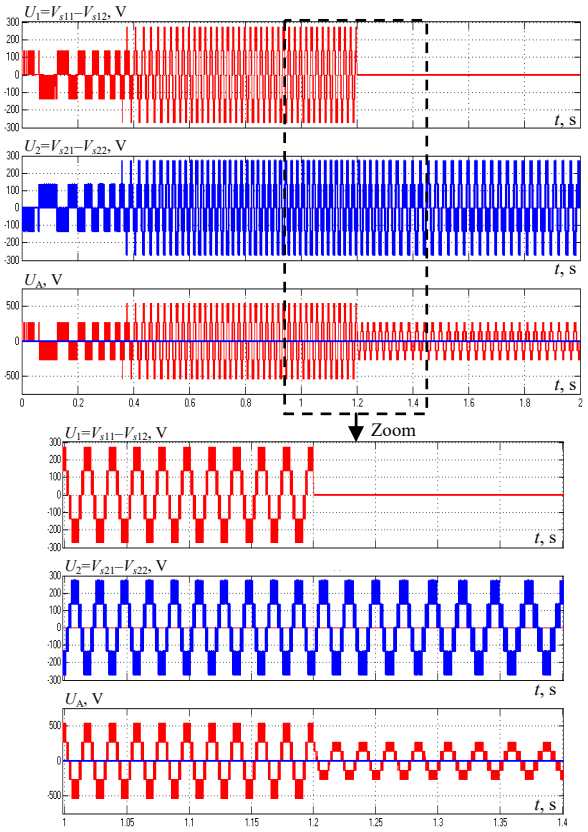

Fig. 15. Evolution of the machine and inverter voltages for configuration 1

Configuration 2. In the 2nd configuration (Fig. 16) we consider an open circuit in one of the switches of inverter A11 (T'_{11}, T'_{12}, or T'_{13}). Following a short circuit event, the control system must act to force the affected switches (T'_{11}, T'_{12}, and T'_{13}) to state 0 and their complementary switches (T_{11}, T_{12}, and T_{13}) to state 1. For this configuration, the machine is powered through its input 2 and exclusively by the A12 inverter. Following the failure of inverter A11, the OEWIM shifts into a fault-tolerant mode where it is supplied only by the remaining inverters (A12, A21 and A22). This operational change means the machine is now fed by the sum of 3 continuous DC buses, resulting in a total DC-link voltage $3E/4$. This constrained voltage supply directly limits the maximum operational speed the machine can achieve while delivering the required load torque. Consequently, the machine must operate at a reduced maximum speed: this speed is 86 % of the nominal value for quadratic load torque $T_r = k\omega^2$, or is further restricted to 75 % of the nominal speed for linear load torque $T_r = k\omega$.

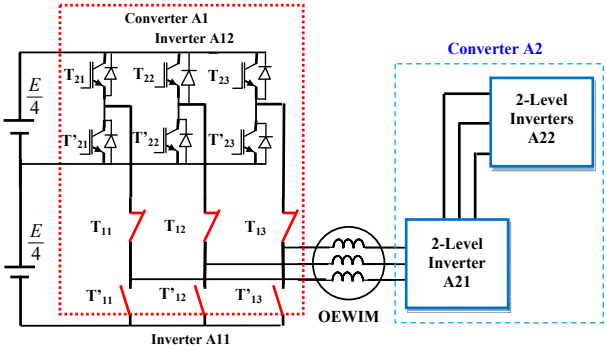

Fig. 16. Supply the OEWIM by cascaded 2-level inverters for configuration 2

Figure 17 presents the evolution of speed and torque with a speed reduction to 86 % of the nominal speed to maintain the operating current for $T_r = k\omega^2$.

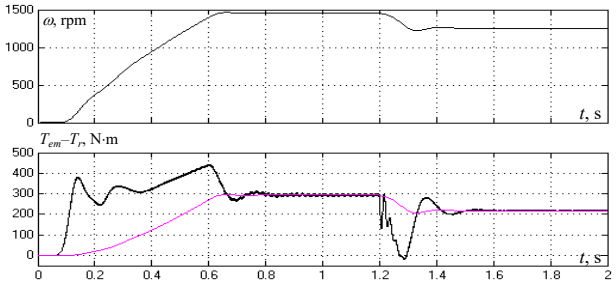

Fig. 17. Evolution of speed and torque for configuration 2

Figure 18 shows the evolution of the stator currents during an event accompanied by a reduction in speed.

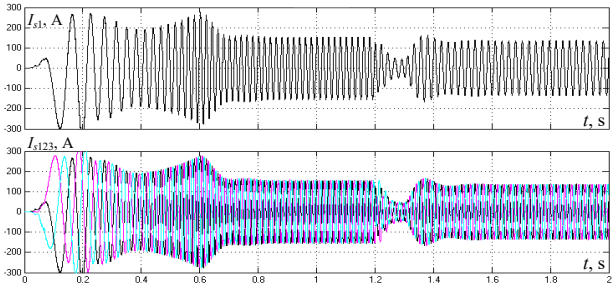

Fig. 18. Evolution of stator current for configuration 2

Figure 19 shows the evolution of the machine and inverter voltages in both normal and degraded operating modes. A zoomed visualization provides a detailed view to better capture the immediate impact of the fault that occurred at t = 1.2 s in inverter A11.

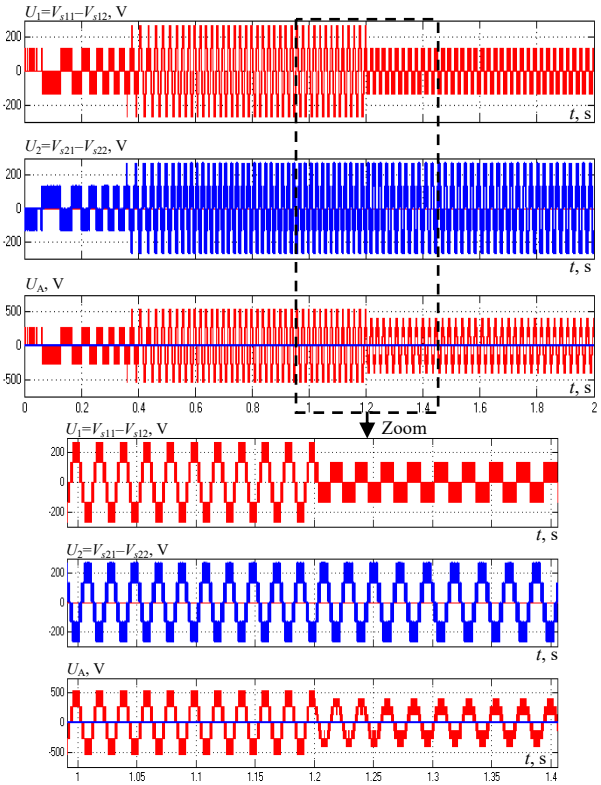

Fig. 19. Evolution of the machine and inverter voltages for configuration 2

Configuration 3. For the 3rd configuration (Fig. 20) we consider an open-circuit fault on one of the switches (T_{21}, T_{22}, or T_{23}) of inverter A12. The control system must then act by ensuring that the 3 switches (T_{11}, T_{12}, and T_{13}) are set to state 0 and switches (T'_{21}, T'_{22}, and T'_{23}) are set to state 1. The input A1 of the machine is powered by only inverter A11. We will have the same power supply conditions as in the 2nd configuration, where the power supply to input A1 is provided solely by inverter A12. Moreover, in both cases, the DC bus voltage at input A1 is $E/4$, the results are then identical to those obtained in the 2nd configuration.

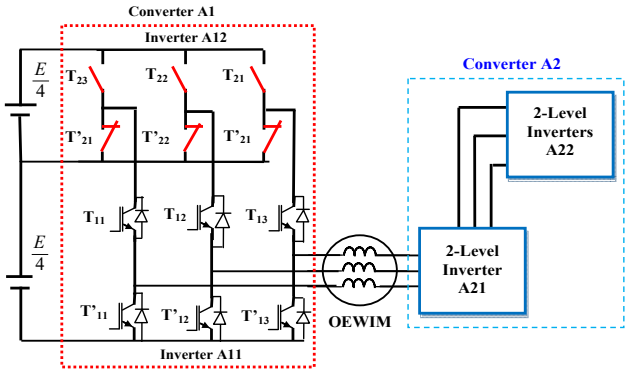

Fig. 20. Supply the OEWIM by cascaded 2-level inverters for the configuration 3

Configuration 4. The 4th configuration involves an open-circuit fault on switch (T'_{21}, T'_{22}, or T'_{23}) of inverter A12. Consequently, the control sets switches (T'_{21}, T'_{22} and T'_{23}) to state 0 and switches (T_{21}, T_{22}, and T_{23}) to state 1 (Fig. 21). Since the DC bus voltage at input A1 is now $E/2$, the machine operates at nominal speed. No operating conditions need to be imposed on inverter A11, as it is sized for half of the nominal power.

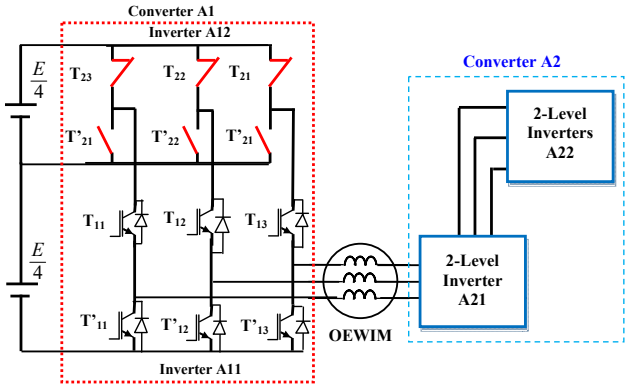

Fig. 21. Supply the OEWIM by cascaded 2-level inverters for configuration 4

The evolution of the speed and torque after the inverter A11 failure is shown in Fig. 22. The results display the state before and after the fault at t = 1.2 s, maintaining 100 % of the nominal speed with a load torque of $T_r = k\omega^2$.

Figure 23 shows the evolution of the stator currents before and after the failure of inverter A12, demonstrating that the stator current magnitude remains unchanged (or similar) despite the fault.

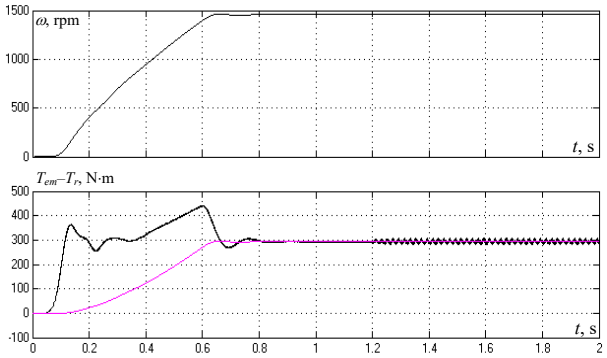

Fig. 22. Evolution of the speed and torque for configuration 4

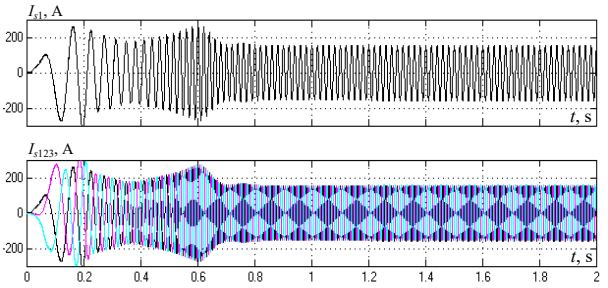

Fig. 23. Evolution of stator current for configuration 4

The evolution of the machine and inverter voltages before and after a failure in inverter A11 at t = 1.2 s is shown in Fig. 24. This event occurred while the DC bus voltage at input A1 is $E/2$. A zoomed view provides a detailed visualization to better capture the immediate impact of the fault.

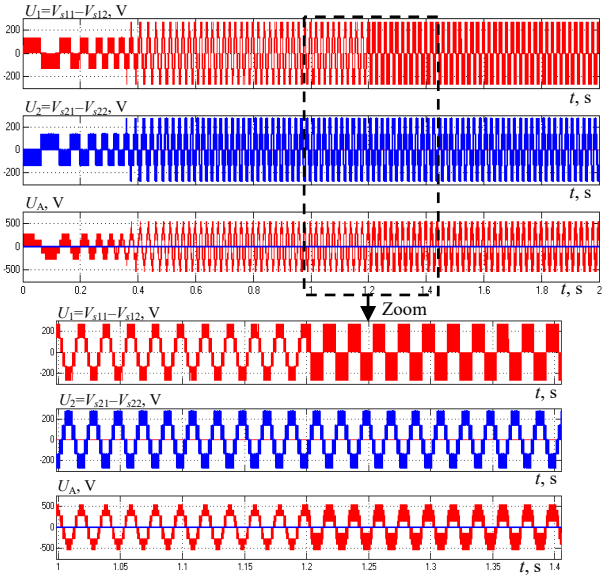

Fig. 24. Evolution of the machine and inverter voltages for configuration 4

The characteristics of the machine, which has a nominal power P = 45 kW, are defined by: nominal speed of 1450 rpm, stator resistance R_s = 150 mΩ, rotor resistance R_r = 46 mΩ, stator inductance L_s = 17.9 mH, rotor inductance L_r = 18.6 mH, mutual inductance L_m = 17.2 mH.

Conclusions. The association of the OEWIM with cascaded 2-level inverter structures offers benefits in both operating modes. In normal mode, it improves dynamic performances. In degraded mode, it enhances the system's reliability, availability, and safety because the failure of a single inverter does not stop the motor.

The OEWIM mathematical model was derived and simulated using the MATLAB/Simulink. The results obtained allowed us to draw the following conclusions: for the normal operation, supplying the machine with cascaded 2-level inverter structures offers several advantages. These include a higher output voltage level (increasing from 5 levels with two cascaded inverters to 7 levels with three cascaded inverters), a significant decrease in voltage THD (falling from 24.99 % to 15.07 % for the same configurations, respectively) and enhanced torque quality (improving from 0.88 % to 0.45 %). The different degraded mode operating configurations for the OEWIM were investigated with the analysis of the switch failure in one of the two cascaded 2-level inverters. Four configurations are then detailed, along with the operational constraints necessary for each scenario. The resulting simulations confirmed the control strategy's efficacy and underscore the importance of this inverter-machine topology for guaranteeing system service continuity. Furthermore, the system configuration successfully balances the power segmentation capabilities and service continuity achieved by using cascaded two-level inverters with the machine. Moreover, the use of cascaded 2-level inverters to feed the machine makes it possible to withstand a second inverter fault, consequently enhancing the drive system's reliability.

Conflict of interest. The authors declare that they have no conflicts of interest.

REFERENCES

1. Nemouchi B., Rezgui S.E., Benalla H., Nebti K. Fractional-based iterative learning-optimal model predictive control of speed induction motor regulation for electric vehicles application. *Electrical Engineering & Electromechanics*, 2024, no. 5, pp. 14-19. doi: https://doi.org/10.20998/2074-272X.2024.5.02.

2. Chaib Ras A., Bouzerara R., Bouzeria H. An adaptive controller for power quality control in high speed railway with electric locomotives with asynchronous traction motors. *Electrical Engineering & Electromechanics*, 2024, no. 2, pp. 23-30. doi: https://doi.org/10.20998/2074-272X.2024.2.04.

3. Senani F., Rahab A., Benalla H. Performance evaluation and analysis by simulation for sliding mode control with speed regulation of permanent magnet synchronous motor drives in electric vehicles. *Electrical Engineering & Electromechanics*, 2025, no. 5, pp. 43-48. doi: https://doi.org/10.20998/2074-272X.2025.5.06.

4. Guizani S., Nayli A., Ben Ammar F. Comparison between star winding and open-end winding induction machines. *Electrical Engineering*, 2016, vol. 98, no. 3, pp. 219-232. doi: https://doi.org/10.1007/s00202-016-0359-4.

5. Guizani S., Nayli A., Ben Ammar F. Fault-tolerant control of a double star induction machine operating in active redundancy. *Electrical Engineering & Electromechanics*, 2025, no. 6, pp. 27-31. doi: https://doi.org/10.20998/2074-272X.2025.6.04.

6. Nayli A., Guizani S., Ben Ammar F. Experimental analysis for star and open-end stator winding structures of IM. *Power Electronics and Drives*, 2025, vol. 10, no. 1, pp. 271-286. doi: https://doi.org/10.2478/pead-2025-0019.

7. Ebrahimi F., Wndarko N.A., Gunawan A.I. Wild horse optimization algorithm implementation in 7-level packed U-cell multilevel inverter to mitigate total harmonic distortion. *Electrical Engineering & Electromechanics*, 2024, no. 5, pp. 34-40. doi: https://doi.org/10.20998/2074-272X.2024.5.05.

8. Benboukous M., Bahri H., Talea M., Bour M., Abdouni K. Comparative analysis of principal modulation techniques for modular multilevel converter and a modified reduced switching frequency algorithm for nearest level pulse width modulation. *Electrical Engineering & Electromechanics*, 2025, no. 4, pp. 26-34. doi: https://doi.org/10.20998/2074-272X.2025.4.04.

9. Sun J., Zheng Z., Li C., Wang K., Li Y. Optimal Fault-Tolerant Control of Multiphase Drives Under Open-Phase/Open-Switch Faults Based on DC Current Injection. *IEEE Transactions on Power Electronics*, 2022, vol. 37, no. 5, pp. 5928-5936. doi: https://doi.org/10.1109/TPEL.2021.3135280.

10. Abdelwanis M.I., Zaky A.A. Maximum power point tracking in a perovskite solar pumping system with a six-phase induction motor. *Revue Roumaine des Sciences Techniques Serie Electrotechnique et Energetique*, 2024, vol. 69, no. 1, pp. 15-20. doi: https://doi.org/10.59277/RRST-EE.2024.1.3.

11. Chaabane H., Khodja D.E., Chakroune S., Hadji D. Model reference adaptive backstepping control of double star induction machine with extended Kalman sensorless control. *Electrical Engineering & Electromechanics*, 2022, no. 4, pp. 3-11. doi: https://doi.org/10.20998/2074-272X.2022.4.01.

12. L'Hadj Said M., Ali Moussa M., Bessaad T. Control of an autonomous wind energy conversion system based on doubly fed induction generator supplying a non-linear load. *Electrical Engineering & Electromechanics*, 2025, no. 4, pp. 3-10. doi: https://doi.org/10.20998/2074-272X.2025.4.01.

13. Darsouni Z., Rezgui S.E., Benalla H., Rebahi F., Boumendjel M.A.M. Ensuring service continuity in electric vehicles with vector control and linear quadratic regulator for dual star induction motors. *Electrical Engineering & Electromechanics*, 2025, no. 2, pp. 24-30. doi: https://doi.org/10.20998/2074-272X.2025.2.04.

14. Zerdani M., Ardjoun S.A.E.M., Chafouk H., Denai M. Experimental Investigation of Decoupled Discontinuous PWM Strategies in Open-End Winding Induction Motor Supplied by a Common DC-Link. *IEEE Journal of Emerging and Selected Topics in Power Electronics*, 2023, vol. 11, no. 3, pp. 3087-3096. doi: https://doi.org/10.1109/JESTPE.2023.3258799.

15. Yu Z., Chen Y., Zhao J., Zhang X., Zhou X. Alternate Subhexagonal Center Dual-Inverter PWM Scheme for Open-End Winding DC-Biased-VRM Drive Using Adjustable Zero Voltage Vector With Dead-Time Effect Compensation. *IEEE Transactions on Transportation Electrification*, 2025, vol. 11, no. 3, pp. 7322-7333. doi: https://doi.org/10.1109/TTE.2025.3526609.

Received 13.08.2025
Accepted 09.11.2025
Published 02.03.2026

A. Nayli [1,3], *Doctor of Electrical Engineering,*
S. Guizani [2,3], *Professor of Electrical Engineering,*
F. Ben Ammar [3], *Professor of Electrical Engineering,*
[1] University of Gafsa, IPEIG, Tunisia,
e-mail: abdelmonoem.nayli@gmail.com (Corresponding Author)
[2] University of El Manar, IPEIEM, Tunisia.
[3] MMA Laboratory, INSAT, University of Carthage, Tunisia.

How to cite this article:
Nayli A., Guizani S., Ben Ammar F. Normal and degraded operation of the open-end winding induction machine fed by 2-level inverters in cascading. *Electrical Engineering & Electromechanics*, 2026, no. 2, pp. 67-73. doi: https://doi.org/10.20998/2074-272X.2026.2.09

UDC 621.314 https://doi.org/10.20998/2074-272X.2026.2.10

N.T. Vinh, D.T. Anh

Bidirectional DC/AC converter for flexible distributed energy integration into AC microgrids

Introduction. *This work focuses on the development of microgrids in remote areas, islands and regions frequently affected by natural disasters, particularly in Vietnam and other island countries in Asia.* ***Problem.*** *The converters perform direct and isolated energy conversion to AC or DC microgrids, which are distributed grids that integrate various distributed energy sources, including renewable energy such as wind power, solar power and others. To enable the system to operate continuously providing stable power, improving the efficiency and effectiveness of distributed power sources by providing a suitable circuit design to limit losses on the main switches and the number of switches and passive components in the converter is minimal. The* ***goal*** *is to develop the internal structure of a boost DC converter into a multi-port converter connected to the storage system and the AC microgrid under the condition of reducing the main switching losses with the condition of intermittent charging of the storage system during the operating period of the solar power source.* ***Methodology.*** *The study uses the switching adjustment method and modeling simulated to analyze the operating conditions adapted to the application system.* ***Results.*** *Analytical expressions were derived for calculating currents, voltages, losses on components, main switches, and conventional switches. The influence of storage circuit switching on reducing losses in the main switch is shown for the operating cases.* ***Scientific novelty.*** *Using the developed simulation model, new expressions were derived that allow us to establish operational dependencies that reveal the relationships between the parameters of the storage device's switching components. These dependencies determine the efficiency and performance of the operational function, meeting the requirements of the microgrid system.* ***Practical value.*** *Enhance the efficiency of utilizing distributed energy sources and improve the conversion efficiency of flexible operation converters for AC or DC microgrids in the power system.* References 30, tables 2, figures 22.
Key words: **boost DC/DC converter, battery, DC/DC full bridge, bidirectional DC/DC and DC/AC converters.**

Вступ. *Робота присвячена розробці мікромереж у віддалених районах, на островах і в регіонах, часто схильних до стихійних лих, зокрема у В'єтнамі та інших острівних країнах Азії.* ***Проблема***. *Перетворювачі здійснюють пряме та ізольоване перетворення енергії в АС або DC мікромережі, які є розподіленими мережами, що інтегрують різні розподілені джерела енергії, включаючи відновлювані джерела, такі як вітрова, сонячна енергія тощо. Для забезпечення безперервної роботи системи та стабільного електропостачання необхідно підвищити ефективність розподілених джерел енергії за рахунок відповідної схемотехніки, що обмежує втрати на головних перемикачах, а також мінімізувати кількість перемикачів та пасивних компонентів у перетворювачі.* ***Мета*** *полягає в розробці внутрішньої структури підвищувального DC перетворювача в багатопортовий перетворювач, підключений до системи накопичення енергії і АС мікромережі, за умови зниження втрат на головних перемикачах і періодичної зарядки системи накопичення енергії протягом періоду роботи сонячного джерела енергії.* ***Методика***. *У роботі використовується метод регулювання перемикання та моделювання для аналізу умов експлуатації, адаптованих до системи застосування.* ***Результати***. *Отримані аналітичні вирази для розрахунку струмів, напруг, втрат на компонентах, головних та звичайних перемикачах. Для різних режимів роботи показано вплив перемикання кіл накопичувача на зниження втрат у головному вимикачі.* ***Наукова новизна***. *За допомогою розробленої імітаційної моделі отримано нові вирази, що дозволяють встановити операційні залежності, які розкривають взаємозв'язки між параметрами комутаційних компонентів накопичувача. Ці залежності визначають ефективність та продуктивність операційного режиму, що відповідає вимогам мікромережевої системи.* ***Практична значимість***. *Підвищення ефективності використання розподілених джерел енергії та покращення коефіцієнта перетворення гнучких перетворювачів для АС або DC мікромереж в енергосистемі.* Бібл. 30, табл. 2, рис. 22.
Ключові слова: **підвищувальний DC/DC перетворювач, батарея акумуляторів, повний DC/DC міст, двонаправені DC/DC і DC/AC перетворювачі.**

Introduction. A comprehensive overview of the micro-AC grid multi-port converter topology has been presented in [1–5]. In recent years, our society has caused numerous negative environmental impacts through the intensive use of traditional energy sources. In addition, the deterioration of the distribution system and the increasing demand for electrical energy has made this concern evident. Although there have been many promising developments in energy decentralization using renewable energy sources in recent years [6]. The increasing penetration of renewable energy sources into the conventional AC grid may cause other problems such as voltage and frequency instability [7].

To address these issues, concepts such as microgrids, minigrids and smart grids for future distribution systems have been researched and put into practice. The microgrid concept was initially proposed in [8]. Its operating principle involves aggregating multiple micropower sources and loads into a system-like model that includes these components and enables either stand-alone or grid-connected operation [9]. Therefore, to optimize the grid appropriately using both AC and DC hybrid systems in the ongoing and future smart grid, typical hybrid microgrid architecture is proposed to reduce the number of power converters in standalone AC or DC systems and to promote the interconnection of different AC and DC sources and loads as a multi-energy system. In this architecture, power routers aim to minimize losses in power distribution [10], energy management for hybrid microgrids using conventional transformers is an inflexible constraint for operations [11–13]. In contrast to AC or DC power grids, the control, system management and operation of hybrid microgrids are more complex. This structure can provide the following contents:

1) Hybrid microgrids can flexibly supply power loads from both DC and AC subgrids, thus system reliability can be improved by feasible alternative power sources [14].

2) Each DC source can be easily connected to the DC line by simply adjusting the DC voltage to limit the starting current.

3) System costs and losses are reduced because some power conversion stages are eliminated for both DC source and load components.

4) The system can be expanded more easily because DC converters can be installed in parallel.

In hybrid renewable energy systems, components such as unidirectional AC/DC converters are used to connect sources to the grid, sources to stored energy, or to perform a single operating function in one direction only. Bidirectional converters handle one load and are capable of connecting two AC and DC grids. DC/DC converters

are employed for DC grids, and multi-output DC/DC converters serve different loads [15–18], the literature has some limitations in the existing multi-port converter topologies, and further research is needed in this area. Renewable energy-based power systems may use dual-input single-output converters [19]. The solar power system, which includes a DC/AC converter, has many components that limit the conversion efficiency [20]. Similarly, portable devices also utilize dual-input single-output converters [21]. For low input voltages corresponding to renewable energy sources there is a family of three-switched multi-input DC/DC converters [22]. The DC/DC converter can work with low voltage sources [23]. Dual-port, multi-output DC/DC converter converts energy in one direction [24, 25]. Later, many other topologies were derived from this basic series of converters [26, 27]. Multi-input and multi-output converters [28] are often used for hybridization between renewable energy sources and electric vehicles for higher efficiency, lower cost and higher reliability. With different current, voltage characteristics are proposed in the DC/DC converter [29] has many components that destabilize the energy conversion. In this topology, the voltage stress on the switch is reduced by increasing the output voltage level.

The converter structure proposed in this work is implemented in a system with a block diagram (Fig. 1). This system can operate to meet different voltage parameter requirements and integrate several distributed power sources to handle changing loads. Sources can be used independently or simultaneously with this structure if connected in parallel with the DC line connected right inside the DC/DC phase conversion converter with simple, low-volume switching components.

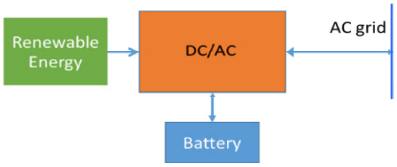

Fig. 1. Schematic diagram of a microgrid system using a DC/DC/AC converter

The advantages of the proposed topology over the topologies in the cited papers are:

- it can connect multiple input sources or a single input source at the same time;
- it can power multiple loads with different voltage levels;
- in addition to providing regulated output power to the load, this converter can harvest maximum power from input sources.

The **goal** is to develop the internal structure of a boost DC converter into a multi-port converter connected to the storage system and the AC microgrid under the condition of reducing the main switching losses with the condition of intermittent charging of the storage system during the operating period of the solar power source. The new topology assimilates multiple renewable energy sources and powers multiple loads with different output levels. Energy is converted in two directions for each stage and case, according to the requirements of the source and load.

Proposed converter operating case. The proposed converter is designed to provide an AC load output and to receive input from the AC grid and a renewable energy source, such as distributed energy, in each operating case. This converter is developed by integrating boost converters, buck-boost bidirectional converters, and H-bridges. Figure 2 shows the circuit diagram of this combination.

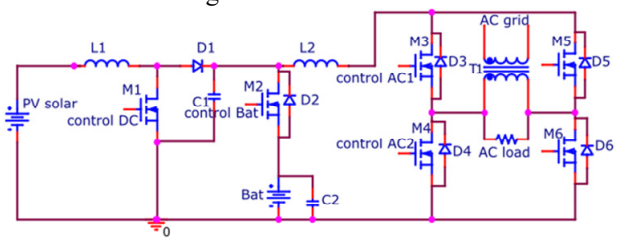

Fig. 2. Proposed DC/DC/AC converter combining power source, DC load, AC load, storage system and AC microgrid

The converter is linked by wind power or solar battery in this paper using solar power, a storage system port denoted by Bat (could be an electric vehicle-EV) and an output load port is AC grid. Two independent inductors with inductances L1 and L2 facilitate energy exchange in 2 basic boost converters, which include an electronic switch M1 connected to a PV source. In this structure, it is possible to add more energy sources to the circuit by connecting additional boost circuits in parallel to the input point of the energy storage circuit. Furthermore, L2 is connected to an H-bridge circuit to enable bidirectional operation. The converter is equipped with 6 power electronic switches: M1 and M2, as well as the switch group M3–M6. These switches can be controlled independently, and each power switch group can be adjusted based on the converter's operating conditions. The switches are the main elements that convert energy from the inverter ports: PV sources, storage systems, AC, DC loads and microgrids. M1 is responsible for efficient energy conversion from a PV power source. Diode D2 is responsible for maximum energy transfer to AC and DC loads, M2 converts energy taken from PV power source and AC grid.

To analyze the proposed converter, certain assumptions are made, as follows:

- all switches ideally conduct reverse blocking;
- all connected renewable energy sources are assumed to supply DC voltages at their maximum power points.

The following are the possible cases that can be described according to the different input and output operations of this new converter. Each case of this converter operating in a steady state will be analyzed independently in the following sections.

**Case* 1. In the first case of the converter shown in Fig. 3, energy from solar renewable sources supplies power to the storage system. Additionally, it can feed the DC load, which is sourced from VC1, as well as the loads at the AC supply grid, including the AC source and other loads. The accumulator system is charged during the conversion. The converter is implemented based on the DC/DC circuit principles of boost, buck, and H-bridge. A single-phase H-bridge is connected to the AC supply grid. The H-bridge circuit is connected to the AC grid via transformer T1, as shown in Fig. 3. The circuit connected to the storage system acts as a buffer circuit for the DC/DC converter at the key switch M1, helping to consume the leakage energy of the coil L1. The voltage to the DC/AC converter is limited by the voltage on the Bat storage system:

$$U_{C1} = U_{pv}\frac{1}{1-d_1}; \tag{1}$$

$$U_{Bat} = U_{C1}d_2, \tag{2}$$

where d_1, d_2 are the duty cycle of M1 and M2 respectively; U_{C1} is the output voltage of DC/DC converter stage.

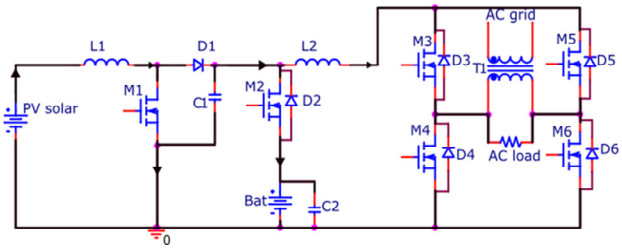

Fig. 3. Schematic diagram in case 1

This mode of operation can be applied when multiple distributed energy sources are available, and maximum power can be obtained with the addition of Boost converters. In addition to boosting the power to the load, the excess energy can be stored for later use. When the Bat is charging in this mode and M2 will control the Bat charging voltage and will close when the Bat is fully charged, or the input voltage increases to a certain value. The transfer of energy from the source to the load depends on the control strategy used to generate gate signals that control the input and output switches. This strategy is based on the availability of the input source, the load conditions, and the status of storage devices.

The voltage across the main switches M1 and M2 is:

$$U_{M1} = U_{D1} + \frac{U_{pv}}{1-d_1}; \tag{3}$$

$$U_{M2} = \frac{U_{pv}}{1-d_1} - U_{Bat}. \tag{4}$$

Current M1 is expressed as:

$$i_{M1} = \frac{(u_{pv} - u_{M1})d_1}{L1} + i_0, \tag{5}$$

where i_0 is the initial operating current of the converter.

When M2 has d_2 operating to conduct current, the current through switch M2 is:

$$i_{M2} = i_{D1} - i_{C1}. \tag{6}$$

Conduction loss power is:

$$P_{condMOSFET} = U_{DS\_M1} \cdot I_{DSM1} + r_{M1} \cdot I^2_{DS\_M1} + \ldots$$
$$\ldots + U_{DS\_M6} \cdot i_{DS\_M6} + r_{M1} \cdot I^2_{DS\_M6}, \tag{7}$$

where U_{DS} is the junction voltage when the MOSFET switch is turn-on; I_{DS} is the drain-to-source current of the MOSFET.

Power loss during switching is:

$$P_{loss\_sw} = f_{sw} \cdot (W_{on} + W_{off}), \tag{8}$$

where W_{on}, W_{off} are the energy dissipation during turn-on and turn-off times, respectively [30]; f_{sw} is the switching frequency of switches M1 and M2.

Conduction loss power of diode D1 is:

$$P_{loss\_D1} = f_{sw} \cdot V_{D1} \cdot I_{D1}, \tag{9}$$

where V_{D1}, I_{D1} are the voltage, current of D1 during the time for current to pass.

Power losses of LC component in the converter are:

$$P_{L1} = R_{L1} \cdot I^2_{L1rms}; \tag{10}$$

$$P_{L2} = R_{L2} \cdot I^2_{L2rms}; \tag{11}$$

$$P_{C1} = R_{C1} \cdot I^2_{C1rms}, \tag{12}$$

where R_{L1}, R_{L2}, R_{C1} are the internal resistances of coils L1, L2, C1; I^2_{L1rms}, I^2_{L2rms}, I^2_{C1rms} are the effective currents through coils L1, L2, C1.

Total power loss in the converter in case 1 is:

$$P_{loss\_case1} = P_{condMOSFET} + P_{loss\_sw} + \\ + P_{loss\_D1} + P_{L1} + P_{L2} + P_{C1}. \tag{13}$$

In which d_1 and d_2 are the opening times of M1 and M2, respectively, and they have different values to ensure that the output voltage of bridge H is stable. As a result, the opening time of M2 (d_2) is delayed compared to that of M1 (d_1). As expression (1) we see an advantage of this circuit is that the opening time of the locks is always less than 1/2 of the working cycle of the converter.

Bat is charged with current when the switch M2 is active and if the PV source voltage is less than Bat voltage then the PV supply diagram is considered to be inactive. This is also a value to set the working threshold for the PV source to supply to the load.

**Case* 2. Figure 4 shows the schematic diagram for case 2. The required AC and DC load power is supplied so that the storage system will temporarily suspend the charging state. The charging circuit of lock M2 does not operate. Due to many reasons such as the energy from the PV source not being enough to meet the load (cloudy weather), the AC and DC load increasing, or the storage system is fully charged. The converter operates according to the DC/DC boost circuit principle combined with the H-bridge. The switches M1 and M3–M6 work on the DC/DC boost converter and the DC/AC H-bridge circuit (converting energy to the AC grid).

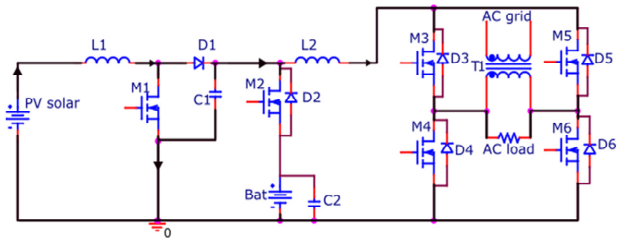

Fig. 4. Schematic diagram in case 2

**Case* 3. In case 3 (Fig. 5) AC and DC loads are supplied from PV power source and storage system. In this case, PV power source reduces capacity, the load increases, and the AC grid is at a high load time, so the storage system generates additional energy to supply the load. At this time, the circuit has M1 active, D2 active, and M3–M6 active.

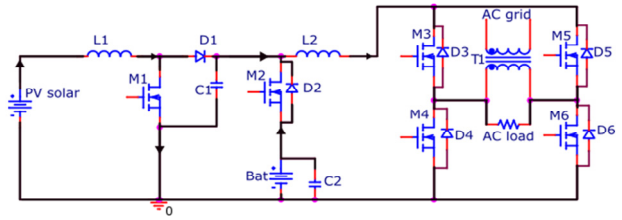

Fig. 5. Schematic diagram in case 3

**Case* 4. Case 4 operations (Fig. 6) the Bat storage source energy supplies the load and the AC grid, the switch M1 is not working, the PV energy source is not working because of the weather at night. M2 is not working, and the energy is transmitted through D2 and L2 to the H-bridge circuit. In this case, the microgrid load is used under priority conditions because of the limited energy source from the storage system.

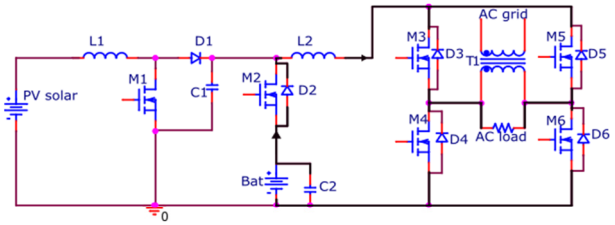

Fig. 6. Schematic diagram in case 4

**Case 5*. Case 5 operations (Fig. 7) excess solar energy is supplied to the DC load. Meanwhile, the AC load receives sufficient and surplus energy from the AC grid. As a result, the energy from PV sources and the AC grid becomes redundant, leading to the accumulation system being charged from both sources. This case arises when distributed energy sources are built locally close to each other in an area. The circuit operates in this case as follows: M1, M2 and M3–M6 operate according to the Boost principle and H-bridge circuit.

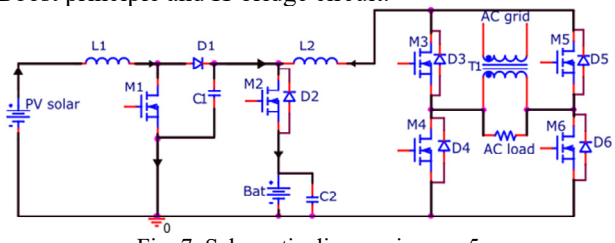

Fig. 7. Schematic diagram in case 5

**Case* 6. This case of the converter system assumes that the AC grid power source is sufficient and has surplus power to supply the AC load, leading to the converter operating independently of the AC grid. The PV power source supplies Bat storage and the DC load if any. The converter operates as a DC/DC boost in which M1 and M2 are active, and the H-bridge circuit is inactive. The PV power is always used thoroughly and efficiently. The operation of case 6 is depicted in Fig. 8.

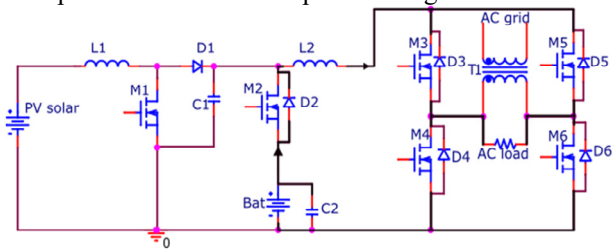

Fig. 8. Schematic diagram in case 6

**Case* 7. Figure 9 describes this case of the converter assuming that renewable energy sources stop producing energy (wind sources need to stop operating or maintenance due to natural disasters or weather, solar energy sources at night). In addition, the load-side energy source connected to the AC grid system is connected to another source of energy with excess energy; then the energy is converted from the AC grid to the DC load and the Bat storage system through M3–M6 and M2 locks in operation.

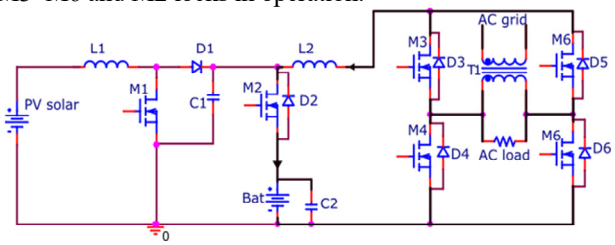

Fig. 9. Schematic diagram in case 7

In the seven working cases, case 1, case 3 and case 5, the main switches M1, M2, and the common switch H-bridge in the proposed converter perform full operation. These cases all demonstrate the loss limitation process for the main switch M1 when there is a storage connection circuit. The stress voltage on switch M1 is limited to a maximum of the rated voltage on the battery. The regulating switches in the converter play a crucial role in managing operations for real-world scenarios. They account for the requirements of each load and the capacity of the regulating sources, ensuring the optimal use of renewable energy from the AC microgrid and PV distributed sources connected to the storage system. The flexible DC/DC/AC converter proposed has the following highlights:

1. There are 7 cases to convert energy to optimize electric energy from renewable energy sources, storage systems, and energy sources from the grid. Flexibly adjust sources and loads according to the priority conditions of the load (electricity customers). Increase the stability of the continuous power supply for the load (when there is a power outage due to incidents or natural disasters). For converters [1–5], which only perform certain functions for identifying the maximum point of the distributed energy source supplied to the load, the load depends on the capacity of the source or storage system. Additionally, the system does not utilize coordination from energy sources in the AC microgrid.

2. In the principal circuit, multiple sources can be connected by placing the connection structures in parallel with the connection point of capacitor C1 (Fig. 2). This method allows for many distributed input sources to pass through the proposed converter without altering its internal structure. However, this approach may complicate the control system. In contrast, converters described in [26, 27] are limited to only one or two input sources.

3. The converter limits the stress voltage on the switch M1 when adjusting the charging mode for the appropriate storage system when the right time the switch M1 changes state from open to closed, the switch M2 opens for a period of time shorter than the closing time of the switch M1 to dissipate the leakage energy of the coil L1.

Control engineering. In this converter, there are 6 electronic switches to control with the cases analyzed in the above section described as Fig. 10 using the PWM technique for main switches M1, M2 and SPWM for the H-bridge.

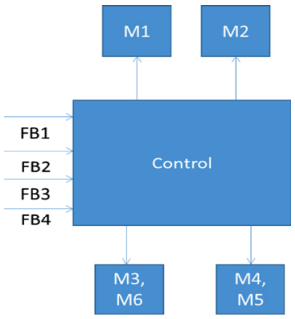

Fig. 10. Control block diagram for mixed-source DC/DC/AC converter

Each case of control mode will be implemented differently with the goal that the output voltage connected to the H-bridge circuit of the converter is almost stable and finds the largest power points from renewable energy sources and storage systems. Therefore, the control circuit has current and voltage feedback loops and uses the

maximum power point finding method for the converter. From specific terminals such as current and voltage on Bat; current and voltage on AC and DC loads; current and voltage on PV source and AC grid to determine the energy status of the terminals connected to the converter. From those parameters to give control commands according to the operating cases of the converter in accordance with the goal of optimal use of energy from the PV source.

**Case 1 – PV supplies energy to Bat, AC, DC loads, and AC grid.* The control mode for this case has the following basic components and requirements for the control circuit:

1) Implement the algorithm to find the maximum power point for the 2 mixed energy sources;

2) Adjust the output voltage to stabilize the load or connect to the AC grid and DC grid;

3) Implement the charging mode control for Bat. Switches M1 and M2 perform control using a PWM control technique along with controlling switches M3–M6 according to the feedback signal from the storage system and the AC microgrid output current and voltage to perform appropriate control.

**Case 2 – PV supplies energy to AC grid, DC and AC loads.* In the converter, the energy feedback signal on the Bat is full or needs to supply power to the AC or DC load, leading to the control circuit for the charging circuit for the Bat not working and stopping charging from the renewable energy source and only supplying power to the AC grid through the H-bridge DC/AC converter. Pulse width modulation for the switch M1 is calculated as the formula in the basic boost converter so that the voltage to the H-circuit is stable.

**Case 3 – PV and Bat supply power to AC, DC loads, and AC grid.* This mode is intended for the power source to the AC grid and DC load to be supplied from PV and Bat solar power. The feedback signal from the feedback loops confirms to modulate the pulse width for the electronic switch M1, M3–M6 is calculated as the formula in the basic boost converter and H-bridge.

**Case 4 – Bat supplies power to AC grid.* This mode is intended for the power source to the AC grid to be supported from the Bat source when it is dark, and the PV renewable source is no longer generating electricity. There is essentially an independent DC/AC conversion circuit from Bat to the AC load. The feedback signal is confirmed to be sent back to control the M3–M6 switches to operate as a DC/AC circuit.

**Case 5 – PV energy and AC grid supply the AC and DC storage and load systems together*. At this time, PV energy generates well (DC load decreases), AC grid has excess energy (AC load decreases). There are essentially 2 DC/DC and AC/DC conversion circuits. Feedback signals from the feedback loops make control decisions for the M1, M2, and M3–M6 switches according to the corresponding principle as the circuit above.

**Case 6 – PV source supplies energy to Bat.* Converter works independently of the AC grid, the AC load demand is fully supplied from the AC grid. Besides, the PV source is still generating electricity, the Bat is not fully charged yet. The control signal will command M1 and M2 to operate.

**Case 7 – AC grid supplies power to Bat.* This mode is intended to supply power to Bat from the AC grid when there are no renewable energy sources. This situation will arise when Bat is fully discharged or under-powered. Control signal for switches M2 and M3–M6 AC/DC H-bridge circuit.

Simulation results. The proposed converter model discussed above is simulated using Orcad software corresponding to the operating cases. The simulation model is based on the actual operating situation of the system when the converter is connected and to verify the analytical results obtained in this section. The parameters used for simulation study are predetermined and are presented in Table 1. The input voltage corresponds to the voltage level of small renewable energy sources such as solar panels, fuel cells and small wind turbines. The output voltage is designed to power low power electronic devices, and the output voltage is designed to charge a 200 V Bat storage battery. The performance of the converter under different operating conditions in open-loop and closed-loop systems is evaluated and discussed in this section.

Table 1

System parameters for simulation studies

Parameter	Value
PV source voltage, V	75–180
Battery voltage, VDC	200
AC grid, AC load	220 V, 50 Hz
DC load, V	250
Inductance L1, L2, μH	10
Load capacitance, μF	10
Electronic switch	MOSFET
DC/DC switching frequency, kHz	50
DC/AC switching frequency, kHz	30

Simulation for case 1. The simulation model for the converter is shown in Fig. 2. In this model, the input source varies with the environmental changes, so in addition to supplying power to the load, additional power is stored.

The proposed inverter operating mode involves 3 components, i.e., PV source, Bat and AC, DC load. This mode will operate during the day when PV source is good. The aim of this mode is to utilize maximum power from PV and can connect a wind source to supply power to AC load and storage. This objective needs to be achieved while ensuring maximum power point tracking of PV source.

Figure 11,*a* shows the reverse breakdown voltage value of 240 V for the M1 and M2 switches at the V(M1:2) probe, from which we can get the parameter value to select the appropriate electronic switch for the circuit. In the M1 voltage graph, an image of the parasitic parameter of the MOSFET is seen during the off period, this effect increases the actual loss of the MOSFET. The output voltage of the load is close to 250–400 VDC at the V(L2) probe. Current through the components L1, M1, M2 in Fig. 11,*a*, the current values through the inductance components L1 at the PV power source.

Figure 11,*b* shows the total power values at the sources and the loads in the whole system. We can see the sources at the loads, including the 2nd and 3rd measuring terminals. From the values, we can simply calculate the efficiency of the conversion system in this case when changing the input power value.

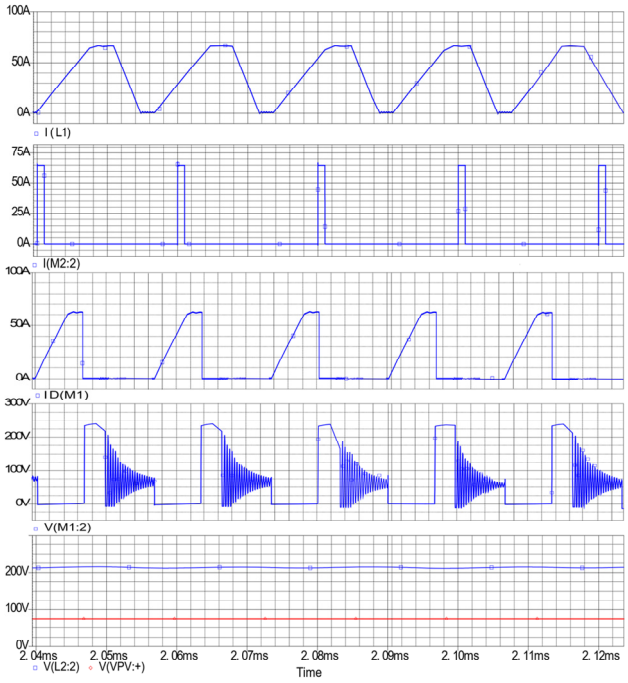

a

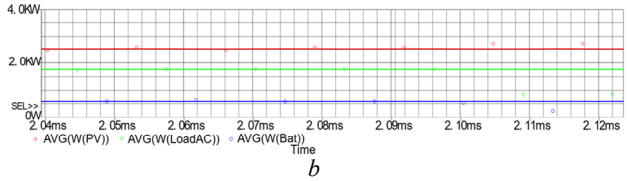

b

Fig. 11. Graph during case 1 operation:
a – current and voltage diagrams of the elements in the circuit;
b – active power of PV input and AC load

Simulation for case 2. This case involves 2 components – PV source and AC load. From Fig. 12,*a* it is observed that the reverse voltage on M1 is the same as in case 1, but the load decreases due to no power supply to Bat, so it is necessary to adjust the control pulse width for M1 to decrease. Figure 12,*a* results of measuring the current value through the load and through the M1, L1 switches compared to scenario 1. Figure 12,*b* shows the power value of two PV source components and AC load. The energy part at the load value is determined by the PV input voltage parameter of 75 V.

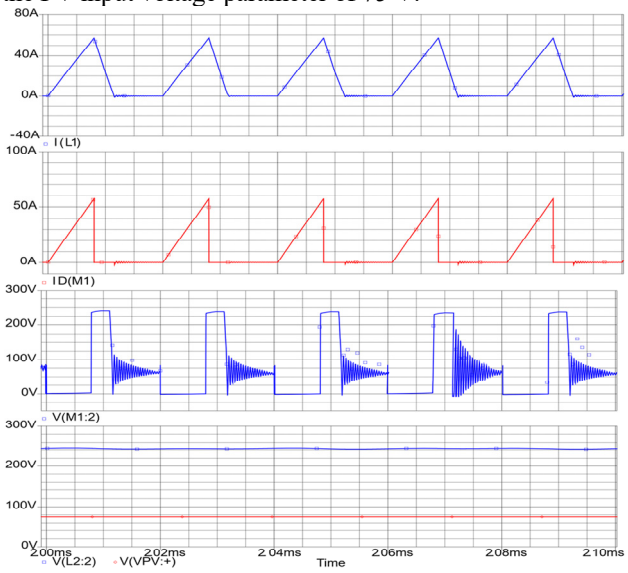

a

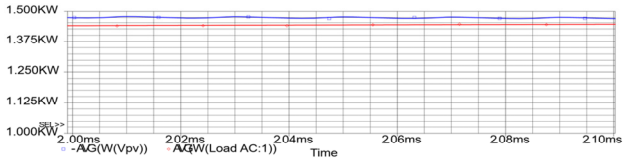

b

Fig. 12. *a* – current and voltage diagrams of the elements in the circuit; *b* – active power of PV input and AC load in case 2

Simulation for case 3. This mode is active when the battery is fully charged as well as when the PV still gets enough light to produce electricity. The purpose is to supplement the energy from storage to the load at AC and DC. From Fig. 13,*a* we have the simulation diagram of the conversion system in this case, this implies that the control for this mode is active, and it is verified.

Figure 13,*b* shows the power measurement results of 3 components in the power supply circuit of the Bat power supply.

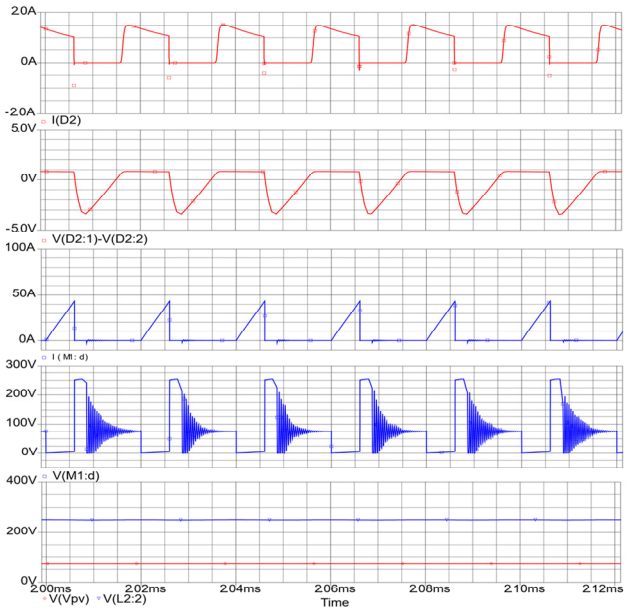

a

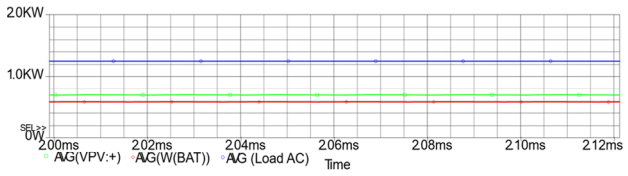

b

Fig. 13. *a* – simulation diagram of case 3; *b* – power on 3 ports

Simulation for case 4. Similarly, in this case, Fig. 14 illustrates the measurement results of the battery storage power supplied to the AC load, as well as the current and voltage patterns of the circuit elements during the energy conversion process. With this energy source, it is possible to provide partial stabilization for the entire system when there is a shortage of energy in the AC microgrid.

Simulation for case 5. The power measurement results of the storage and AC load supplied by PV energy source and AC grid are shown in Fig. 15. With this energy source it can provide partial stabilization for the storage system as well as the load side that is reducing the power flow.

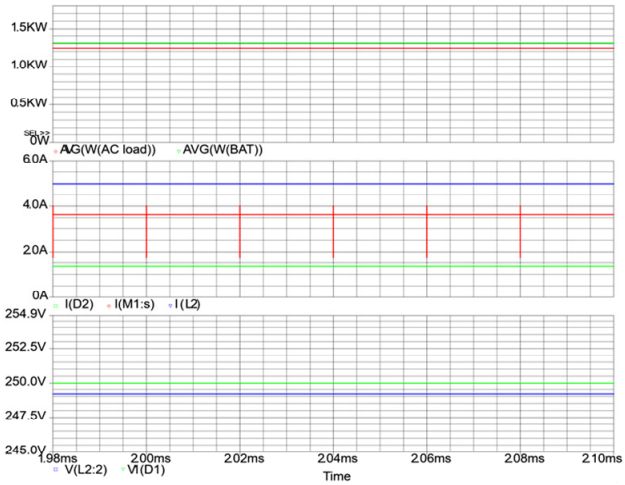

Fig. 14. Simulation activity graph of case 4

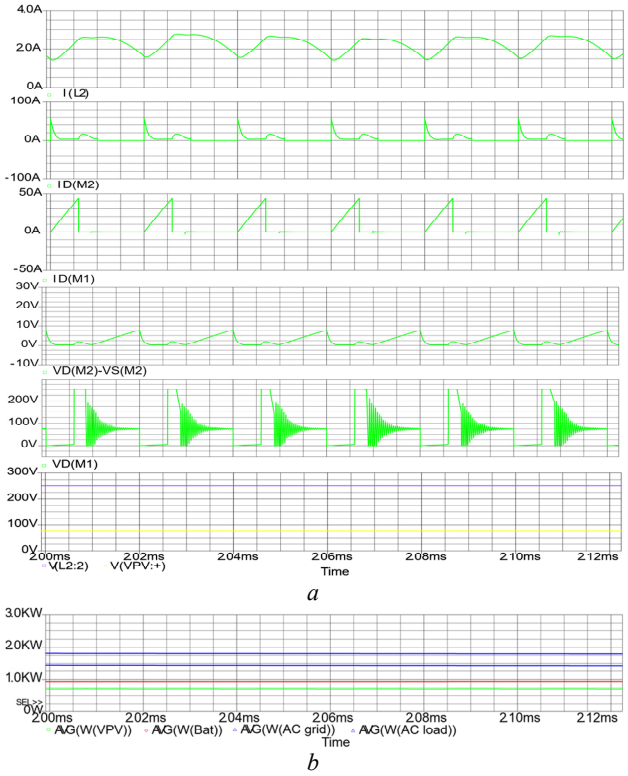

a

b

Fig. 15. Single-input (*a*), dual-output (*b*) power graph in case 5

Simulation for case 6. Figure 16,*a* shows the voltage and current values on the elements M1, M2, and L1, the input voltage for the storage system. Figure 16,*b* shows the input and output power values to determine the efficiency of this conversion process.

Simulation for case 7. In 7 case H-bridge circuits are working, the current and voltage signals on elements M2 and L2 are shown in Fig. 17,*a*. Figure 17,*b* shows the power values of the AC load, AC grid and Bat.

Figure 18 shows the simulation results of the performance of the DC/DC/AC converter with different power values for each specific case, the maximum working power is 2500 W, PV voltage is 75 V. The voltage change of the power supply input is shown in some cases with PV power supply.

When the load demand energy changes at the AC microgrid, it affects the energy conversion process from the energy source supplied from PV with each mode of increasing or decreasing the energy consumption, the change time is 5–10 ms to reach the change value when decreasing as shown in Fig. 18. The fluctuation amplitude is about 10 % compared to the new change value.

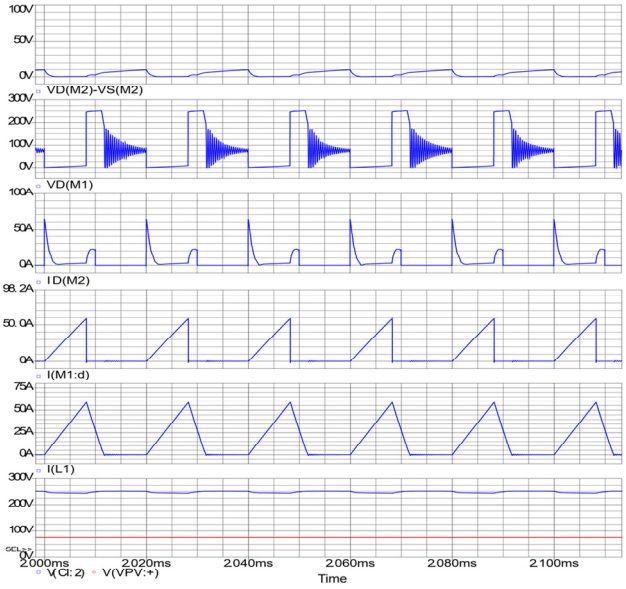

a

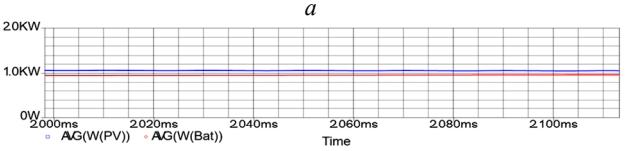

b

Fig. 16. *a* – voltage-consistent signal; *b* – input and output power values

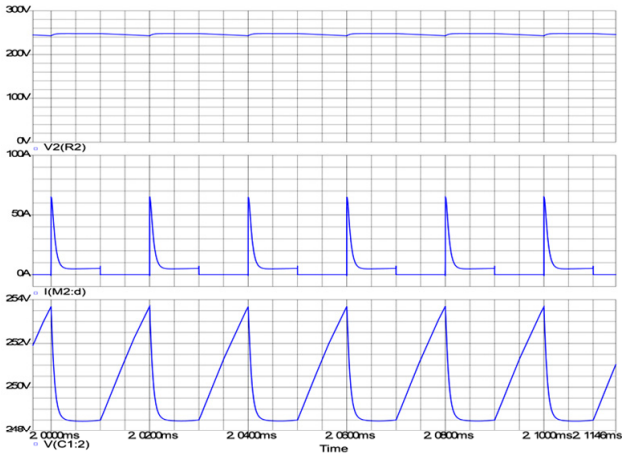

a

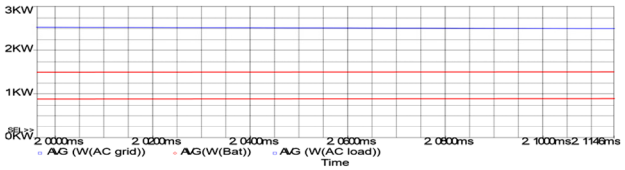

b

Fig. 17. *a* – simulated current, voltage; *b* – gate power in case 7

Figure 19,*a* cases 1, 2, 3, 5, 6 show the power efficiency for the specific cases, where the higher efficiency value is in cases 2 and 3 near 96.9 % at 500 W operating power. The low efficiency value is near 94.2 % at 2500 W operating power in case 6 in the converter. Figure 19,*b* depicts the overall efficiency of the converter for the 7 cases.

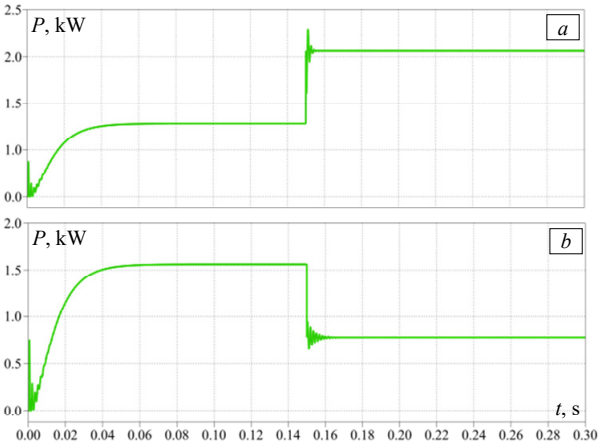

Fig. 18. AC load at $t = 0.15$ s for case 1:
a – AC load increase 610 W; *b* – AC load decrease 750 W

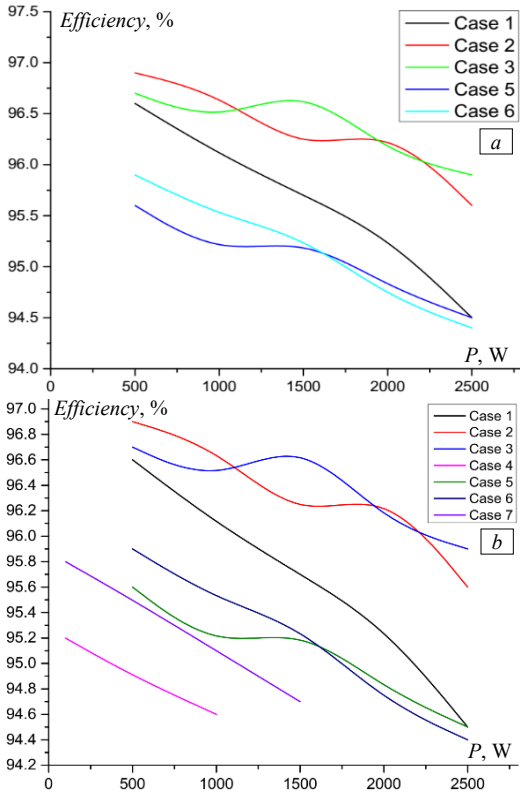

Fig. 19. Simulation results of the performance of the converter operation cases (*a*) related to the operation of PV sources (5 cases); *b* – all cases (7 cases)

Experimental results. Figure 20 shows the experimental DC/DC/AC converter at the following parameters: input voltage value 75–180 VDC; AC load capacity 500–2500 W.

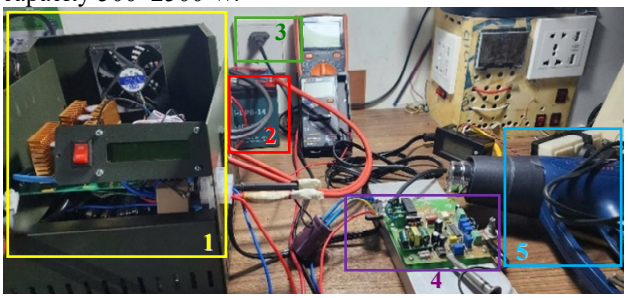

Fig. 20. Experimental image of flexible converter:
1 – converter; 2 – storage; 3 – single-phase AC grid;
4 – DC source; 5 – single-phase AC load

Table 2 shows the input and output parameters of the converter at the ports.

Table 2

Experimental parameters

DC/DC boost input voltage, VDC	75–180
DC/DC boost output voltage, VDC	250
Inductances L1, L2, μH	10
Bat capacitor, μF	10
Boost circuit output capacitor, μF	10
Diodes D1, D2	Mur1560
MOSFET switch M1	IRF740
MOSFET switch M2	IRFP640N
MOSFET switches M3–M6	IRF340
DC load, Ω	500
AC output voltage, V	220±3 %
AC input voltage, VDC	200–350
AC load frequency, Hz	50±0.5 %

Figure 21 shows the experimental operation modes with the largest power value change of 2500 W, the input voltage from the PV source is 75–180 V, voltage on the DC bus is 398–399 VDC can be connected to DC microgrid, the values are displayed on the voltage and power meters.

Figure 21 shows the output voltage waveform of the load under varying load conditions. The actual output voltage is a sinusoidal waveform with a frequency of 50 Hz, in harmony with the AC grid, as shown in Fig. 21,*a*.

Figure 21,*b* – the voltage from the PV source is 75 V working with the AC load capacity of more than 1000 W and the DC voltage at DC load 399 VDC.

Figure 21,*c* – the voltage from the PV source is more than 110 V working with the AC load capacity of more than 1500 W.

Figure 21,*d* – the voltage from the PV source is 75 V working with the AC load capacity of more than 2000 W.

Figure 21,*e* – the voltage from the PV source is more than 180 V working with the AC load capacity of more than 2000 W.

Figure 21,*f* – the voltage from the PV source is 110 V working with the AC load capacity of more than 2500 W.

Experimental results are given for some typical cases in the 7 operating cases of the converter. The simulated and calculated efficiency is determined at different power values with the maximum value of 2500 W (Fig. 19). It has been studied in different load capacities and operating modes with different functions of the proposed converter. The average efficiency when powered by PV power source is close to 96.2 % corresponding to power 500 W, the efficiency at 2500 W power is close to 94.5 % (Fig. 22). The average efficiency when powered from the system storage (cases 2 and 4) is 96 %. For example, there is only one mode, such as DC/DC (case 6 is 95.8 %) and DC/AC (efficiency above 95 % [15, 16]). According to the experimental results, the average efficiency of the designed converter in working with different modes is close to 95.3 % with a maximum power of 2500 W.

Figure 22 shows the experimental and simulated average performance of the converter with a difference of almost 1 % in value. This difference is basically consistent with the actual performance during the experiment because the loss values of the components in the device, the quality of the electronic components, and the quality of the printed circuit board will be larger in the

simulation. The experimental performance of the proposed converter is larger than that of the references [15, 16] with a load operating mode of less than 2500 W.

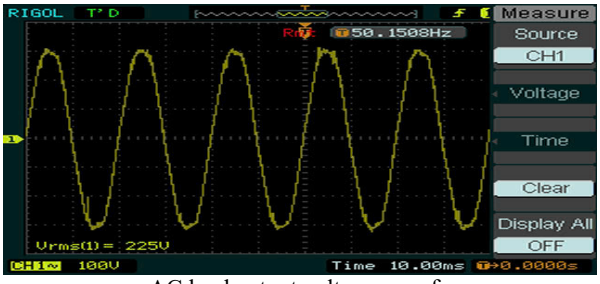

a – AC load output voltage waveforms

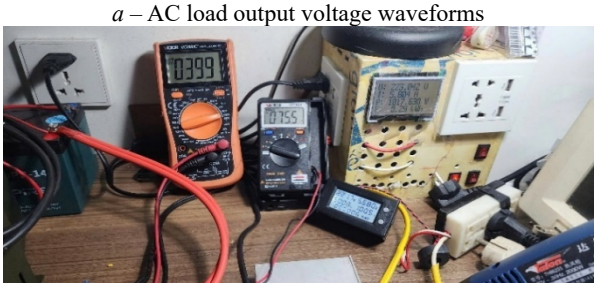

b – AC load near 1000 W

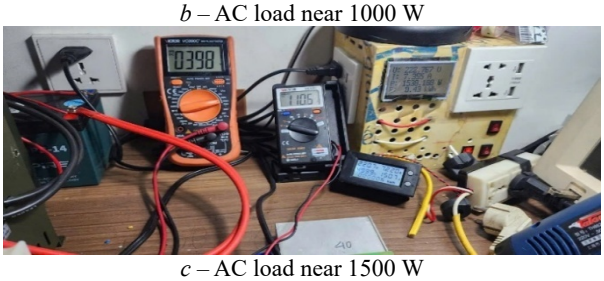

c – AC load near 1500 W

d – AC load near 1500 W

e – AC load near 2000 W

f – AC load near 2500 W

Fig. 21. AC load power values change

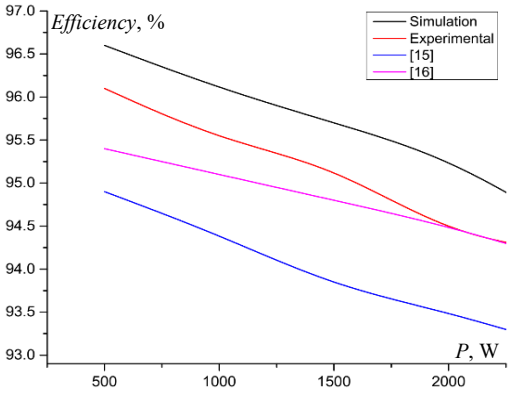

Fig. 22. Converter performance compared with references

Conclusions. The article is devoted to a multifunctional DC/AC bidirectional converter with three different independent ports, flexible operation with 7 cases, application for AC microgrids and distributed energy sources. The operating case results demonstrate 94.5 % efficiency of the converter when implemented in the system. The power circuit design creates a snubber at the storage system to limit the stress voltage on the main switch connected to the renewable energy source.

This study shows that the snubber parameters used for charging the energy storage system with recovery affect the performance, cost and design of DC/DC/AC converters in power generation and energy conversion systems.

The experimental converter basically corresponds to the simulation design and is capable of operating flexibly for systems with microgrids that can be connected to the distribution grid or work independently.

The presented research has shown the possibility of developing high-frequency non-isolated DC/DC/AC converters with low-cost performance and shows a feasible method to study new systems in the non-isolated DC/DC/AC converter family.

This solution converter increases the stability of the current grid in the Vietnamese power system. Improves the efficiency of using renewable energy sources (or distributed energy sources) contributes to national energy security.

Acknowledgments. The research team would like to thank the Science and technology project code 08-2025-HV-KTDT1 of the Posts and Telecommunications Institute of Technology Hanoi, Vietnam.

Conflict of interest. The authors declare that they have no conflicts of interest.

REFERENCES

1. Sindhuja R., Padma S. Bipolar DC output fed grounded DC-AC converter for photovoltaic application. *Electrical Engineering & Electromechanics*, 2023, no. 2, pp. 57-62. doi: https://doi.org/10.20998/2074-272X.2023.2.09.

2. Khan S.A., Islam M.R., Guo Y., Zhu J. A New Isolated Multi-Port Converter With Multi-Directional Power Flow Capabilities for Smart Electric Vehicle Charging Stations. *IEEE Transactions on Applied Superconductivity*, 2019, vol. 29, no. 2, pp. 1-4. doi: https://doi.org/10.1109/TASC.2019.2895526.

3. Alotaibi S., Darwish A. Modular Multilevel Converters for Large-Scale Grid-Connected Photovoltaic Systems: A Review. *Energies*, 2021, vol. 14, no. 19, art. no. 6213. doi: https://doi.org/10.3390/en14196213.

4. Murugan S., Jaishankar M., Premkumar K. Hybrid DC–AC Microgrid Energy Management System Using an Artificial Gorilla Troops Optimizer Optimized Neural Network. *Energies*, 2022, vol. 15, no. 21, art. no. 8187. doi: https://doi.org/10.3390/en15218187.

5. Aryani D.R., Adi F.S., Kim J.-S., Song H. An improved model-based interlink converter control design in hybrid AC/DC microgrids. *Energy Reports*, 2022, vol. 8, pp. 520-531. doi: https://doi.org/10.1016/j.egyr.2022.10.146.
6. Østergaard P.A., Duic N., Noorollahi Y., Kalogirou S.A. Recent advances in renewable energy technology for the energy transition. *Renewable Energy*, 2021, vol. 179, pp. 877-884. doi: https://doi.org/10.1016/j.renene.2021.07.111.
7. Adajah Y.Y., Thomas S., Haruna M.S., Anaza S.O. Distributed Generation (DG): A Review. *2021 1st International Conference on Multidisciplinary Engineering and Applied Science (ICMEAS)*, 2021, pp. 1-5. doi: https://doi.org/10.1109/ICMEAS52683.2021.9692353.
8. Lasseter R.H. MicroGrids. *2002 IEEE Power Engineering Society Winter Meeting. Conference Proceedings*, 2002, vol. 1, pp. 305-308. doi: https://doi.org/10.1109/PESW.2002.985003.
9. Uddin M., Mo H., Dong D., Elsawah S., Zhu J., Guerrero J.M. Microgrids: A review, outstanding issues and future trends. *Energy Strategy Reviews*, 2023, vol. 49, art. no. 101127. doi: https://doi.org/10.1016/j.esr.2023.101127.
10. Zhang D., Zhang Z., Ren Q., Tang Y., Chen X., Li Z. Research on application mode of HYBRID microgrid AC-DC microgrid in large industrial enterprise Park based on energy Router. *2022 China International Conference on Electricity Distribution (CICED)*, 2022, pp. 1715-1721. doi: https://doi.org/10.1109/CICED56215.2022.9929073.
11. Qu Z., Shi Z., Wang Y., Abu-Siada A., Chong Z., Dong H. Energy Management Strategy of AC/DC Hybrid Microgrid Based on Solid-State Transformer. *IEEE Access*, 2022, vol. 10, pp. 20633-20642. doi: https://doi.org/10.1109/ACCESS.2022.3149522.
12. Sarwar S., Kirli D., Merlin M.M.C., Kiprakis A.E. Major Challenges towards Energy Management and Power Sharing in a Hybrid AC/DC Microgrid: A Review. *Energies*, 2022, vol. 15, no. 23, art. no. 8851. doi: https://doi.org/10.3390/en15238851.
13. Li Z., Xie X., Cheng Z., Zhi C., Si J. A novel two-stage energy management of hybrid AC/DC microgrid considering frequency security constraints. *International Journal of Electrical Power & Energy Systems*, 2023, vol. 146, art. no. 108768. doi: https://doi.org/10.1016/j.ijepes.2022.108768.
14. Ayat Y., Badoud A.E., Mekhilef S., Gassab S. Energy management based on a fuzzy controller of a photovoltaic/fuel cell/Li-ion battery/supercapacitor for unpredictable, fluctuating, high-dynamic three-phase AC load. *Electrical Engineering & Electromechanics*, 2023, no. 3, pp. 66-75. doi: https://doi.org/10.20998/2074-272X.2023.3.10.
15. Suriyan K., Vennila C., Sentamilselvi M., Adhikary P., Karpoora S.K., Madhu M.C., Madhusudhana C.S., Badari N.K. A novel reconfigurable hybrid DC-AC home technique with renewable energy resources and converters. *International Journal of Sustainable Engineering*, 2023, vol. 16, no. 1, pp. 285-301. doi: https://doi.org/10.1080/19397038.2023.2205872.
16. Dharmasena S., Olowu T.O., Sarwat A.I. Bidirectional AC/DC Converter Topologies: A Review. *2019 SoutheastCon*, 2019, pp. 1-5. doi: https://doi.org/10.1109/SoutheastCon42311.2019.9020287.
17. Saafan A.A., Khadkikar V., El Moursi M.S., Zeineldin H.H. A New Multiport DC-DC Converter for DC Microgrid Applications. *2021 IEEE Industry Applications Society Annual Meeting (IAS)*, 2021, pp. 1-7. doi: https://doi.org/10.1109/IAS48185.2021.9677403.
18. Litrán S.P., Durán E., Semião J., Díaz-Martín C. Multiple-Output DC–DC Converters: Applications and Solutions. *Electronics*, 2022, vol. 11, no. 8, art. no. 1258. doi: https://doi.org/10.3390/electronics11081258.
19. Danyali S., Moradkhani A., Abdulhussein A.O., Shirkhani M., Dadvand Z. A novel multi-input medium-gain DC-DC boost converter with soft-switching performance. *International Journal of Electrical Power & Energy Systems*, 2024, vol. 155, art. no. 109629. doi: https://doi.org/10.1016/j.ijepes.2023.109629.
20. Vinh N.T. Bidirectional converter connecting the energy storage system to the DC and AC grid. *International Energy Journal*, 2023, vol. 23, no. 3, p. 141-154.
21. Vinh V.T., Vinh N.T., Dai L.V. Partly-Isolated DC-DC Converter for DC Bus Battery-PV Solar Energy System. *GMSARN International Journal*, 2022, vol. 16, no. 3, pp. 267-272.
22. Sabhi K., Talea M., Bahri H., Dani S. Integrating dual active bridge DC-DC converters: a novel energy management approach for hybrid renewable energy systems. *Electrical Engineering & Electromechanics*, 2025, no. 2, pp. 39-47. doi: https://doi.org/10.20998/2074-272X.2025.2.06.
23. Benazza B., Bendaoud A., Slimani H., Benaissa M., Flitti M., Zeghoudi A. Experimental study of electromagnetic disturbances in common and differential modes in a circuit based on two DC/DC boost static converter in parallel. *Electrical Engineering & Electromechanics*, 2023, no. 4, pp. 35-39. doi: https://doi.org/10.20998/2074-272X.2023.4.05.
24. Baazouzi K., Bensalah A.D., Drid S., Chrifi-Alaoui L. Passivity voltage based control of the boost power converter used in photovoltaic system. *Electrical Engineering & Electromechanics*, 2022, no. 2, pp. 11-17. doi: https://doi.org/10.20998/2074-272X.2022.2.02.
25. Puppala S., Singh P.P., Potnuru D. Advancements in Multiple Input Multiple Output DC-DC Converters for Efficient DC Microgrid Integration: A Scientometric Analysis. *2024 International Conference on Smart Systems for Applications in Electrical Sciences (ICSSES)*, 2024, pp. 1-6. doi: https://doi.org/10.1109/ICSSES62373.2024.10561353.
26. Al-Ameedee H.A.H., Delshad M., Shalash N.A., Fani B. Soft-Switched Non-Isolated Double-Input High Step-Up Converter With Low Input Current Ripple. *IET Power Electronics*, 2025, vol. 18, no. 1, art. no. e70051. doi: https://doi.org/10.1049/pel2.70051.
27. Themozhi G., Srinivasan K., Arun Srinivas T., Prabha A. Analysis of suitable converter for the implementation of drive system in solar photovoltaic panels. *Electrical Engineering & Electromechanics*, 2024, no. 1, pp. 17-22. doi: https://doi.org/10.20998/2074-272X.2024.1.03.
28. Carrijo de Oliveira R., Tofoli F.L., Silva de Morais A. Novel Isolated Multiple-Input, Multiple-Output Multidirectional Converter for Modern Low-Voltage DC Power Distribution Architectures. *Sustainability*, 2023, vol. 15, no. 5, art. no. 4582. doi: https://doi.org/10.3390/su15054582.
29. Maalandish M., Hosseini S.H., Sabahi M., Rostami N., Khooban M. High step-up multi input–multi output DC–DC converter with high controllability for battery charger/EV applications. *IET Power Electronics*, 2023, vol. 16, no. 15, pp. 2606-2623. doi: https://doi.org/10.1049/pel2.12587.
30. Zhu B., Liu C., Guo D., Kong L., Cai G., Sun H., Shao X. AC Voltage Synthesis Using Arbitrary Two-Phase Voltages: Frequency, Phase, and Amplitude Modulation for Direct AC–AC Power Conversion. *IEEE Transactions on Power Electronics*, 2022, vol. 37, no. 10, pp. 11855-11864. doi: https://doi.org/10.1109/TPEL.2022.3176398.

Received 24.08.2025
Accepted 07.11.2025
Published 02.03.2026

N.T. Vinh[1]*, PhD,*
D.T. Anh[2]*, MSc Student,*
[1] Faculty of Electronic Engineering I,
Posts and Telecommunications Institute of Technology,
Hanoi, Vietnam,
e-mail: vinhnt@ptit.edu.vn (Corresponding Author)
[2] College of Agricultural Mechanics, Vietnam,
e-mail: tuanhbx@cam.edu.vn

How to cite this article:
Vinh N.T., Anh D.T. Bidirectional DC/AC converter for flexible distributed energy integration into AC microgrids. *Electrical Engineering & Electromechanics*, 2026, no. 2, pp. 74-83. doi: https://doi.org/10.20998/2074-272X.2026.2.10

UDC 621.315 https://doi.org/10.20998/2074-272X.2026.2.11

M. Rihan, A. Ghazzaly, A.A. Ebnalwaled, A.H. Fahmy, L.S. Nasrat

Influence of zinc oxide nanoparticles on flashover voltage of unsaturated polyester resin-based composites for electrical insulators

Introduction. *Polyester-based composites are increasingly used in electrical applications for their insulation, mechanical, and thermal properties. Nanofillers have shown promise in enhancing the properties of polymer-based composites.* ***Goal.*** *This study aims to improve the flashover voltage of unsaturated polyester resin (UPR)-based composites by incorporating zinc oxide (ZnO) nanoparticles.* ***Methodology.*** *UPR/ZnO nanocomposites were prepared with various ZnO nanofiller ratios (0 %, 1 %, 3 %, 5 %, and 7 % by weight) with different sample lengths (0.5, 1.5, 2, and 2.5 cm). The flashover voltage was measured for the pure UPR sample and each composition of the studied filler ratios at various sample lengths. X-ray diffraction analysis was performed. A curve-fitting method was applied to estimate the flashover voltage of UPR/ZnO nanocomposites containing intermediate filler ratios between those experimentally tested.* ***Results.*** *Incorporation of ZnO nanofillers significantly enhanced the flashover voltage of polyester-based nanocomposites. The pure UPR sample exhibited the lowest flashover voltage, whereas the composite with 7 wt.% ZnO nanofiller demonstrated the highest. Notably, increasing the sample length further improved flashover voltage.* ***Scientific novelty.*** *This study examines the influence of ZnO nanoparticles on the flashover voltage of UPR-based composites.* ***Practical value.*** *The obtained findings can contribute to the development of polyester-based nanocomposite insulators with enhanced flashover voltage.* References 26, tables 3, figures 6.
Key words: **unsaturated polyester resin, zinc oxide, filler, nanocomposites, flashover voltage, curve fitting technique**.

Вступ. *Композити на основі поліестеру все частіше використовуються в електротехніці завдяки своїм ізоляційним, механічним та тепловим властивостям. Нанонаповнювачі виявилися перспективними для покращення властивостей композитів на основі полімерів.* ***Мета***. *Це дослідження спрямоване на підвищення напруги пробою композитів на основі ненасиченої поліефірної смоли (UPR) шляхом включаючи наночастинок оксиду цинку (ZnO).* ***Методика***. *Нанокомпозити UPR/ZnO були виготовлені з різними масовими частками нанонаповнювача ZnO (0 %, 1 %, 3 %, 5 % та 7 % за масою) з різною довжиною зразків (0.5, 1.5, 2 та 2.5 см). Напругу пробою вимірювали для чистого зразка UPR та кожної композиції з досліджуваними концентраціями наповнювача при різній довжині зразків. Було проведено рентгенівський дифракційний аналіз. Метод апроксимації кривих було застосовано для оцінки напруги пробою нанокомпозитів UPR/ZnO з проміжними концентраціями наповнювача між експериментально дослідженими.* ***Результати***. *Включення нанонаповнювачів ZnO суттєво підвищило напругу пробою поліефірних нанокомпозитів. Чистий зразок UPR продемонстрував найнижчу напругу пробою, тоді як композит із 7 мас.% нанонаповнювача ZnO показав найвищу. Примітно, що збільшення довжини зразка додатково підвищувало напругу пробою.* ***Наукова новизна***. *У дослідженні розглянуто вплив наночастинок ZnO на напругу пробою композитів на основі UPR.* ***Практична значимість***. *Отримані результати можуть сприяти розробці поліефірних нанокомпозитних ізоляторів із підвищеною напругою пробою.* Бібл. 26, табл. 3, рис. 6.
Ключові слова: **ненасичена поліефірна смола, оксид цинку, наповнювач, нанокомпозити, напруга пробою, метод апроксимації кривої.**

Introduction. Insulators are crucial to the safety and reliability of power networks [1, 2]. As power systems continue to evolve to meet increasing energy demands and incorporate renewable energy sources [3–8], the selection of suitable insulation materials becomes critical to ensuring high performance and long-term reliability [9–12].

Traditional insulation materials such as ceramic, glass, and porcelain have been widely used since the late 1880s due to their high electrical resistance and dielectric properties. However, these materials exhibit several drawbacks, including fragility, brittleness, high weight, susceptibility to environmental factors, complex manufacturing processes, high production costs, aging effects, and, in the case of porcelain, water absorption [13].

To address these challenges, researchers have investigated polymeric-based insulators [14]. These polymeric-based insulators offer significant advantages over conventional ceramic insulators, including enhanced hydrophobicity, lighter structures that facilitate easier installation, and greater resistance to environmental degradation [15, 16].

Unsaturated polyester resins (UPRs). UPRs are widely used in electrical insulation due to their excellent physical properties, ease of processing, and cost-effectiveness. Upon curing, these resins form a solid structure with outstanding durability and mechanical strength [17–19].

Micro- and nanoscale inorganic fillers are widely used to enhance the performance of polymeric materials. Their incorporation improves mechanical strength [20], thermal stability, and dielectric properties, making polymeric-based composites highly suitable for advanced electrical insulation applications [13, 21, 22].

Goal. This study aims to improve the flashover voltage of unsaturated polyester resin (UPR)-based composites by incorporating zinc oxide (ZnO) nanoparticles.

UPR/ZnO nanocomposite samples were fabricated with different ZnO ratios (0 %, 1 %, 3 %, 5 %, and 7 % by weight), and their flashover voltages were measured for samples with various lengths (0.5, 1.5, 2, and 2.5 cm).

X-ray diffraction (XRD) was used to characterize the structural properties of the prepared samples.

A curve-fitting approach was employed to predict the flashover voltage of UPR/ZnO nanocomposites with intermediate filler ratios between the studied filler ratios.

Materials. The following materials were used:

- UPR, supplied by Egyptian British Co.
- ZnO nanoparticles, obtained from Nano Tech Egypt, with an average particle size of 30±5 nm.
- Ethyl alcohol (70 %), used as a reactive diluent.
- Methyl ethyl ketone peroxide (MEKP), which served as the hardener and was utilized as an initiator

agent. It has a density of 1.18±0.005 g/cm^3 and a viscosity of 23–25 mPa·s.

- Cobalt naphthenate, used as an accelerator.

To ensure accurate composition ratios, all weight measurements for UPR and ZnO were performed using a Sartorius analytical balance with a precision of 0.1 mg.

Preparation of pure UPR samples. UPR was dissolved in 70 % ethyl alcohol using a magnetic stirrer for 8 min. Subsequently, MEKP was added as an initiator, and the mixture was stirred for an additional 8 min. Cobalt naphthenate was added as an accelerator to initiate the curing process of the polyester resin before reinforcement. The mixture was stirred to ensure homogeneous distribution of the catalyst and initiator within the matrix, without any filler. The samples were molded into cylindrical rods (1.5 cm diameter) with lengths of 0.5 cm, 1.5 cm, and 2 cm at an ambient temperature of 25 °C [17].

Preparation of the UPR/ZnO nanocomposite samples. UPR/ZnO nanocomposites with various ZnO nanoparticle ratios were prepared by first dispersing ZnO nanoparticles in ethanol. This dispersion was subjected to ultrasonic vibration at 1500±50 rpm for 30 min, while also using mechanical agitation. ZnO nanoparticles were added to the UPR matrix at weight fractions of 1 %, 3 %, 5 %, and 7 %, relative to the total composite weight. After this, UPR and the initiator (MEKP) were gradually added to the solution. The mixture was then stirred vigorously for 10 min. Then, the accelerator (cobalt naphthenate) was added, and the mixture was stirred further to ensure even dispersion of ZnO throughout the resin. The resulting compositions were poured into cylindrical plastic molds with lengths of 0.5 cm, 1.5 cm, and 2 cm and a fixed diameter of 1.5 cm. After curing, the samples were prepared for each testing technique [17]. Preliminary trials showed that ZnO ratios above 7 wt.% caused a significant increase in viscosity. This made casting difficult and hindered uniform dispersion due to nanoparticle agglomeration.

The curing process was carried out at ambient temperature (~ 25 °C) using 1 wt.% MEKP and 0.5 wt.% cobalt naphthenate. No significant mass loss was detected before or after curing (< 0.1 %). This indicates that no low-molecular-weight decomposition products were released during the crosslinking process.

UPR weight ratios and ZnO nanofiller weight ratios, and the corresponding sample names are listed in Table 1.

Table 1

UPR weight ratios and ZnO nanofiller weight ratios, and the corresponding sample names

Sample name	% ratio of UPR by weight	% ratio of ZnO nanofiller by weight
P (Pure UPR)	100 %	0
Z1	99 %	1 %
Z3	97 %	3 %
Z5	95 %	5 %
Z7	93 %	7 %

XRD analysis. X-ray Diffraction (XRD) analysis was performed to assess the dispersibility of ZnO nanoparticles in the different prepared samples. XRD analysis was performed using an EMMAO 143 X-ray diffractometer (GBC, Australia) with a Bragg's angle (2θ) scanning range of 0°–80°. The XRD patterns of pure polyester, ZnO nanoparticles, and UPR/ZnO nanocomposites are shown in Fig. 1.

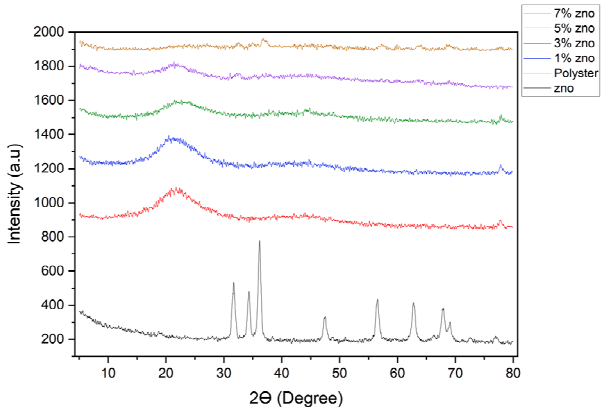

Fig. 1. XRD of pure polyester, ZnO nanoparticles and UPR/ZnO nanocomposites

According to Fig. 1, the presence of crystalline ZnO was confirmed by reflections at 2θ angles of 31.8°, 34.4°, 36.3°, 47.5°, 56.6°, and 62.8° [23]. The pure polyester intensity peak at 22.66° decreased as the ZnO content increased, indicating a uniform dispersion of ZnO nanoparticles [24, 25].

Flashover test. The flashover test is a critical method for evaluating the electrical properties of materials, particularly for outdoor insulators [15]. This test provides key characteristics of the studied UPR/ZnO nanocomposites, assessing their ability to withstand applied voltages.

Testing apparatus for flashover voltage. The AC flashover voltage test was performed using a high-voltage (HV) transformer (Terco HV 9105), which operates at 100 kV, 5 kVA, and 50 Hz. The voltage applied to the transformer's primary winding was regulated using a variac (0–250 V) controlled by a smooth control panel. Two electrodes were securely fixed on the samples, ensuring parallel alignment without defects. The transformer's LV side incorporated a safety circuit to disconnect the supply and prevent excessive current during flashover. The tests were conducted in the HV laboratory at Aswan University. To protect the HV transformer from high current surges during flashover, a 2.8 MΩ resistor was connected in series with the secondary winding of the transformer. The schematic diagram of the implemented flashover test platform is illustrated in Fig. 2 [26].

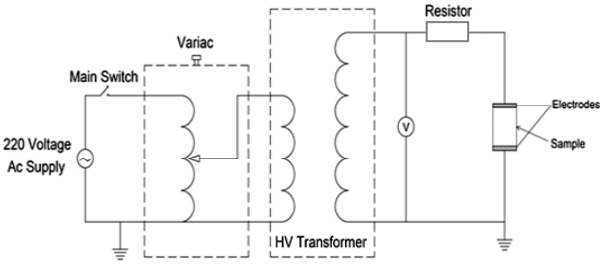

Fig. 2. Schematic diagram of flashover voltage test platform

Results and discussion. Flashover voltage measurements were conducted on the studied samples, with different sample lengths (0.5 cm, 1.5 cm, 2 cm, and

2.5 cm), at room temperature (25 °C) under normal dry weather conditions. The AC voltage increased steadily at 0.5 kV/s until breakdown occurred. Each sample was tested 10 times to ensure accuracy; the mean flashover voltages were calculated and listed in Table 2.

Table 2

Mean flashover voltage for the studied samples with different lengths

Sample	Sample length			
	0.5 cm	1.5 cm	2 cm	2.5 cm
	Mean flashover voltage, kV			
P	7.379	27.692	34.482	40.097
Z1	7.386	28.463	35.647	41.113
Z3	8.011	30.163	37.613	43.960
Z5	9.124	32.051	39.764	46.048
Z7	12.000	35.752	43.350	47.928

For all samples with different lengths, results showed that the flashover voltage increased directly with the increase in the ratio of ZnO filler. Sample Z7 exhibited the highest flashover voltage, whereas pure polyester had the lowest value. Additionally, the results showed that the flashover voltage increased directly with the increase in sample length.

For samples 0.5 cm in length, sample Z7 achieved an improvement in the flashover voltage of 62.624 % over pure polyester. For samples 1.5 cm in length, Z7 achieved an improvement in flashover voltage of 29.1 % compared to pure polyester.

For samples 2 cm in length, sample Z7 achieved an improvement in flashover voltage of 25.72 % compared to pure polyester. For samples of 2.5 cm in length, Z7 achieved an improvement in the flashover voltage of 25.72 % compared to pure polyester.

Curve fitting and flashover voltage prediction. Accurate prediction of flashover voltage for UPR/ZnO nanocomposites is essential due to the high cost of raw materials. To address this, 3rd- and 4th-degree polynomial regressions were implemented using MATLAB to estimate the flashover voltage of UPR/ZnO nanocomposites with intermediate ZnO ratios between the studied ratios, which were not prepared. These models were developed using the experimental results of the studied samples with various weight ratios of ZnO nanoparticles (0 %, 1 %, 3 %, 5 %, and 7 %) across four lengths (0.5, 1.5, 2, and 2.5 cm). Based on the root mean square error (RMSE) criterion, the 4th-degree polynomial showed the optimal fit, providing the highest accuracy and minimal deviation across all sample dimensions.

Flashover voltage of UPR/ZnO nanocomposites for various samples by the curve fitting technique. The following 4th-degree polynomial equation represents the best curve-fitting model for the dataset:

$$y = P_1 X^4 + P_2 X^3 + P_3 X^2 + P_4 X + P_5, \qquad (1)$$

where y is the flashover voltage; X is the percentage ratio of the ZnO nanofiller; $P_1 - P_5$ are the coefficients. Detailed results for each sample length are next.

Flashover voltage of 0.5 cm length samples. *Mathematical model*: coefficients of (1) would be: P_1= 0.0049613095, P_2= –0.0528184524, P_3 = 0.248610119, P_4= –0.1937529762, P_5= 7.379.
Statistical indicators: RMSE = 0.0 kV, R^2 = 1.0.

Figure 3 shows that the fitted curve accurately represents the flashover voltage data for the samples of 0.5 cm in length.

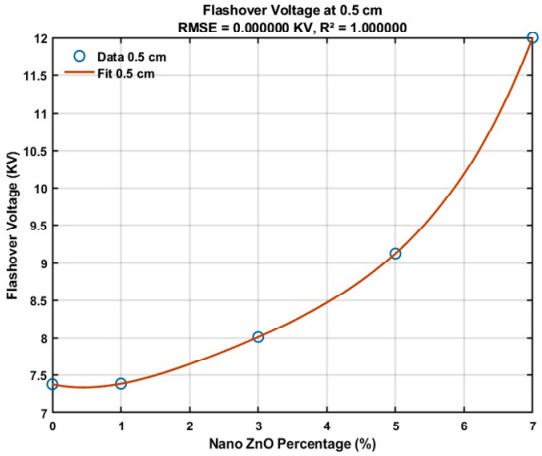

Fig. 3. Fitted curve results for the flashover voltage versus various weight percentages of nano ZnO filler for 0.5 cm length samples

Flashover voltage of 1.5 cm length samples. *Mathematical model*: coefficients of (1) would be: P_1= 0.0049172619, P_2 = –0.0448220238, P_3 = 0.1416970238, P_4 = –0.6692077381, P_5 = 27.692.
Statistical indicators: RMSE = 0.0 kV, R^2 = 1.0.

Figure 4 shows that the fitted curve accurately represents the flashover voltage data for the samples of 1.5 cm in length.

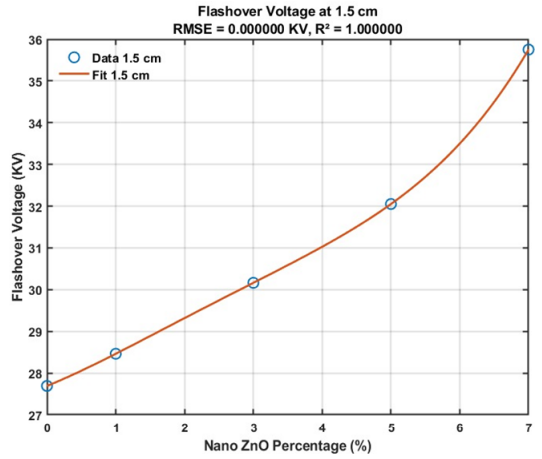

Fig. 4. Fitted curve results for the flashover voltage versus various weight percentages of nano ZnO filler for 1.5 cm length samples

Flashover voltage of 2 cm length samples. *Mathematical model*: coefficients of (1) would be: P_1= 0.0013261905, P_2 = 0.004822619, P_3 = – 0.097197619, P_4 = 1.2560488095, P_5 = 34.482.
Statistical indicators: RMSE = 0.0 kV, R^2 = 1.0.

Figure 5 shows that the fitted curve accurately represents the flashover voltage data for the samples of 2 cm in length.

Flashover voltage of 2.5 cm length samples. *Mathematical model*: coefficients of Eq. (1) would be: P_1= 0.0082315476, P_2= – 0.1202255952, P_3= 0.5097255952, P_4 = 0.6182684524, P_5 = 40.097.
Statistical indicators: RMSE = 0.0 kV, R^2 = 1.0.

Figure 6 shows that the fitted curve accurately represents the flashover voltage data for the samples of 2.5 cm in length.

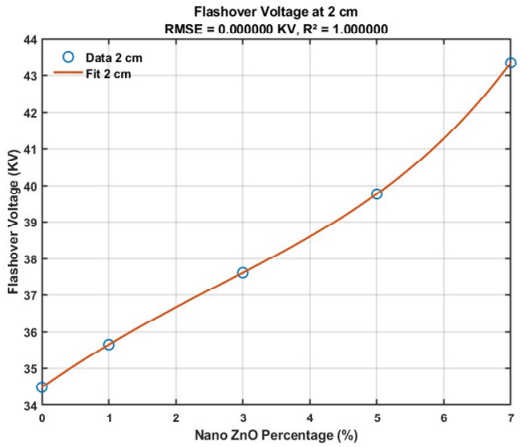

Fig. 5. Fitted curve results for the flashover voltage versus various weight percentages of nano ZnO filler for 2 cm length samples

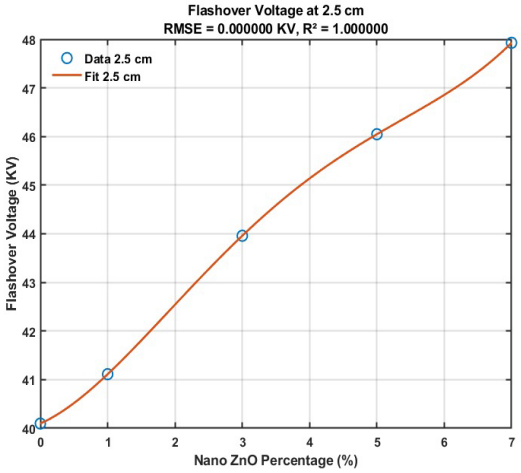

Fig. 6. Fitted curve results for the flashover voltage versus various weight percentages of nano ZnO filler for 2.5 cm length samples

Prediction of flashover voltage. Using the best-fit equations obtained from the curve-fitting technique, the prediction of flashover voltage for unmanufactured samples with intermediate ratios of nano ZnO filler (in the range of 0 % to 7 % by weight) is presented in Table 3.

Table 3

Predicted flashover voltage for several intermediate ZnO nanofiller ratios

Sample length, cm	% ratio of ZnO nanofiller by weight	Predicted flashover voltage, kV
0.5	2	7.643
1.5	2	29.317
2.0	4	38.599
2.5	6	46.856

Conclusions. This study investigated the impact of incorporating ZnO nanofiller on the flashover voltage of unsaturated polyester resin (UPR)-based nanocomposites. To evaluate the effect of ZnO, UPR/ZnO nanocomposites were prepared with different ZnO nanofiller ratios (0 %, 1 %, 3 %, 5 %, and 7 % by weight) and various sample lengths (0.5, 1.5, 2, and 2.5 cm). Experimental trials indicated that preparing UPR/ZnO nanocomposites with ZnO contents exceeding 7 wt.% was extremely challenging due to the significant increase in viscosity, which hindered proper casting and promoted filler agglomeration. XRD analysis confirmed the successful incorporation and adequate dispersion of the ZnO nanofiller within the polymer matrix. Flashover voltage measurements were conducted under identical dry conditions to ensure consistency. A curve-fitting approach based on 3rd- and 4th-degree polynomial regressions was implemented to predict the flashover voltage of unprepared UPR/ZnO nanocomposites of intermediate ZnO ratios between the studied ratios. Based on the RMSE criterion, the fourth-degree polynomial model provided the highest prediction accuracy with minimal deviation. The key findings can be summarized as follows:

1. Pure polyester exhibits the lowest flashover voltage among all tested samples.
2. Incorporation of nano-ZnO filler significantly enhanced the flashover voltage of UPR/ZnO-based nanocomposites.
3. Flashover voltage increased proportionally with increasing ZnO filler content up to 7 wt.%.
4. UPR/ZnO composites containing 7 wt.% nano ZnO filler demonstrated the highest flashover voltage among all the prepared samples for all sample lengths.
5. Flashover voltage increased with increasing sample length.
6. The polynomial regression model proved to be an effective predictive tool, minimizing the need for additional costly experimental investigations.

Conflict of interest. The authors declare that they have no conflicts of interest.

REFERENCES

1. Ahmed Z., Nasrat L.S., Rihan M. The effect of SiO_2 microparticle concentration on the electrical and thermal properties of silicone rubber for electrical insulation applications. *Electrical Engineering & Electromechanics*, 2025, no. 3, pp. 84-89. doi: https://doi.org/10.20998/2074-272X.2025.3.12.

2. Salem A.A., Lau K.Y., Abdul-Malek Z., Zhou W., Al-Ameri S., Al-Gailani S.A., Rahman R.A. Investigation of High Voltage Polymeric Insulators Performance under Wet Pollution. *Polymers*, 2022, vol. 14, no. 6, art. no. 1236. doi: https://doi.org/10.3390/polym14061236.

3. Salama H.S., Magdy G., Bakeer A., Alghamdi T.A.H., Alenezi M., Rihan M. An adaptive coordination control solution to boost frequency stability for a hybrid distributed generation system. *PLOS One*, 2025, vol. 20, no. 5, art. no. e0321657. doi: https://doi.org/10.1371/journal.pone.0321657.

4. Rihan M., Sayed A., Abdel-Rahman A.B., Ebeed M., Alghamdi T.A.H., Salama H.S. An artificial gorilla troops optimizer for stochastic unit commitment problem solution incorporating solar, wind, and load uncertainties. *PLOS ONE*, 2024, vol. 19, no. 7, art. no. e0305329. doi: https://doi.org/10.1371/journal.pone.0305329.

5. Hassan Q., Algburi S., Sameen A.Z., Salman H.M., Jaszczur M. A review of hybrid renewable energy systems: Solar and wind-powered solutions: Challenges, opportunities, and policy implications. *Results in Engineering*, 2023, vol. 20, art. no. 101621. doi: https://doi.org/10.1016/j.rineng.2023.101621.

6. Ebeed M., Elnaka M., Khan N.H., Jamal R., Abdel-Rahman A.B., Jurado F., Kamel, S., Rihan M. An enhanced weighted mean of vectors optimizer: addressing combined heat and power economic dispatch with system losses and valve point loading effect. *Neural Computing and Applications*, 2025, vol. 37, no. 1, pp. 16643-16675. doi: https://doi.org/10.1007/s00521-025-11245-y.

7. Holechek J.L., Geli H.M.E., Sawalhah M.N., Valdez R. A Global Assessment: Can Renewable Energy Replace Fossil Fuels by 2050? *Sustainability*, 2022, vol. 14, no. 8, art. no. 4792. doi: https://doi.org/10.3390/su14084792.

8. Rihan M., Nasrallah M., Hasanin B., El-Shahat A. A Proposed Controllable Crowbar for a Brushless Doubly-Fed Reluctance Generator, a Grid-Integrated Wind Turbine. *Energies*, 2022, vol. 15, no. 11, art. no. 3894. doi: https://doi.org/10.3390/en15113894.
9. Bezprozvannych G.V., Moskvitin Y.S., Kostiukov I.O., Grechko O.M. Dielectric parameters of phase and belt paper impregnated insulation of power cables. *Electrical Engineering & Electromechanics*, 2025, no. 2, pp. 69-78. doi: https://doi.org/10.20998/2074-272X.2025.2.09.
10. El Sherkawy E., Nasrat L.S., Rihan M. The effect of thermal ageing on electrical and mechanical properties of thermoplastic nanocomposite insulation of power high-voltage cables. *Electrical Engineering & Electromechanics*, 2024, no. 3, pp. 66-71. doi: https://doi.org/10.20998/2074-272X.2024.3.09.
11. Gaska K., Xu X., Gubanski S., Kádár R. Electrical, Mechanical, and Thermal Properties of LDPE Graphene Nanoplatelets Composites Produced by Means of Melt Extrusion Process. *Polymers*, 2017, vol. 9, no. 1, art. no. 11. doi: https://doi.org/10.3390/polym9010011.
12. Grechko O., Kulyk O. Current State and Future Prospects of Using SF6 Gas as an Insulation in the Electric Power Industry. *2024 IEEE 5th KhPI Week on Advanced Technology (KhPIWeek)*, 2024, pp. 1-6. doi: https://doi.org/10.1109/KhPIWeek61434.2024.10877987.
13. Musa A.A., Bello A., Adams S.M., Onwualu A.P., Anye V.C., Bello K.A., Obianyo I.I. Nano-Enhanced Polymer Composite Materials: A Review of Current Advancements and Challenges. *Polymers*, 2025, vol. 17, no. 7, art. no. 893. doi: https://doi.org/10.3390/polym17070893.
14. Mousavi S.R., Estaji S., Kiaei H., Mansourian-Tabaei M., Nouranian S., Jafari S.H., Ruckdäschel H., Arjmand M., Khonakdar H.A. A review of electrical and thermal conductivities of epoxy resin systems reinforced with carbon nanotubes and graphene-based nanoparticles. *Polymer Testing*, 2022, vol. 112, art. no. 107645. doi: https://doi.org/10.1016/j.polymertesting.2022.107645.
15. Nazir M.T., Khalid A., Akram S., Mishra P., Kabir I.I., Yeoh G.H., Phung B.T., Wong K.L. Electrical tracking, erosion and flammability resistance of high voltage outdoor composite insulation: Research, innovation and future outlook. *Materials Science & Engineering. R, Reports*, 2023, vol. 156, art. no. 100757. doi: https://doi.org/10.1016/j.mser.2023.100757.
16. Saleem M.Z., Akbar M. Review of the Performance of High-Voltage Composite Insulators. *Polymers*, 2022, vol. 14, no. 3, art. no. 431. doi: https://doi.org/10.3390/polym14030431.
17. Chen H., Tian X., Liu J. Unsaturated Polyester Resin Nanocomposites Containing ZnO Modified with Oleic Acid Activated by N,N′-Carbonyldiimidazole. *Polymers*, 2018, vol. 10, no. 4, art. no. 362. doi: https://doi.org/10.3390/polym10040362.
18. Pączkowski P., Sigareva N.V., Gorelov B.M., Terets M.I., Sementsov Y.I., Kartel M.T., Gawdzik B. The Influence of Carbon Nanotubes on the Physical and Chemical Properties of Nanocomposites Based on Unsaturated Polyester Resin. *Nanomaterials*, 2023, vol. 13, no. 23, art. no. 2981. doi: https://doi.org/10.3390/nano13232981.
19. Ramakrishnan T., Gift M.D.M., Chitradevi S., Jegan R., Jose, P.S.H., Nagaraja H.N., Sharma R., Selvakumar P., Hailegiorgis S.M. Study of Numerous Resins Used in Polymer Matrix Composite Materials. *Advances in Materials Science and Engineering*, 2022, vol. 2022, art. no. 1088926. doi: https://doi.org/10.1155/2022/1088926.
20. Ali H., Ali S., Ali K., Ullah S., Ismail P.M., Humayun M., Zeng C. Impact of the nanoparticle incorporation in enhancing mechanical properties of polymers. *Results in Engineering*, 2025, vol. 27, art. no. 106151. doi: https://doi.org/10.1016/j.rineng.2025.106151.
21. Haque S.M., Ardila-Rey J.A., Umar Y., Mas'ud A.A., Muhammad-Sukki F., Jume B.H., Rahman H., Bani N.A. Application and Suitability of Polymeric Materials as Insulators in Electrical Equipment. *Energies*, 2021, vol. 14, no. 10, art. no. 2758. doi: https://doi.org/10.3390/en14102758.
22. Rahman M.M., Khan K.H., Parvez M.M.H., Irizarry N., Uddin M.N. Polymer Nanocomposites with Optimized Nanoparticle Dispersion and Enhanced Functionalities for Industrial Applications. *Processes*, 2025, vol. 13, no. 4, art. no. 994. doi: https://doi.org/10.3390/pr13040994.
23. Franco-Urquiza E.A., May-Crespo J.F., Escalante Velázquez C.A., Pérez Mora R., González García P. Thermal Degradation Kinetics of ZnO/polyester Nanocomposites. *Polymers*, 2020, vol. 12, no. 8, art. no. 1753. doi: https://doi.org/10.3390/polym12081753.
24. Dan S., Gu H., Tan J., Zhang B., Zhang Q. Transparent epoxy/TiO 2 optical hybrid films with tunable refractive index prepared via a simple and efficient way. *Progress in Organic Coatings*, 2018, vol. 120, pp. 252-259. doi: https://doi.org/10.1016/j.porgcoat.2018.02.017.
25. Nallusamy S. Characterization of Epoxy Composites with TiO2 Additives and E-Glass Fibers as Reinforcement Agent. *Journal of Nano Research*, 2016, vol. 40, pp. 99-104. doi: https://doi.org/10.4028/www.scientific.net/JNanoR.40.99.
26. Salem A.A., Abd-Rahman R., Ishak M.T. Bin Lau K.Y., Abdul-Malek Z., Al-Ameri S., Al-Gailani S.A., Ghoneim S.S.M. Influence of contamination distribution in characterizing the flashover phenomenon on outdoor insulator. *Ain Shams Engineering Journal*, 2023, vol. 14, no. 12, art. no. 102249. doi: https://doi.org/10.1016/j.asej.2023.102249.

Received 08.04.2025
Accepted 06.10.2025
Published 02.03.2026

Mahmoud Rihan [1], *Associate Professor,*
Abdelhameid Ghazzaly [2], *PhD Student,*
Khaled Ebnalwaled [3], *Professor,*
Ahlam Hassan Fahmy [1], *MSc Student,*
Loai Saad Nasrat [2], *Professor,*
[1] Electrical Engineering Department, Faculty of Engineering, Qena University, Qena, Egypt,
e-mail: mahmoudrihan@eng.svu.edu.eg (Corresponding Author)
[2] Electrical Engineering Department, Faculty of Engineering, Aswan University, Aswan, Egypt.
[3] Physics Department, Faculty of Science, Qena University, Qena, Egypt.

How to cite this article:
Rihan M., Ghazzaly A., Ebnalwaled A.A., Fahmy A.H., Nasrat L.S. Influence of zinc oxide nanoparticles on flashover voltage of unsaturated polyester resin-based composites for electrical insulators. *Electrical Engineering & Electromechanics*, 2026, no. 2, pp. 84-88. doi: https://doi.org/10.20998/2074-272X.2026.2.11

UDC 621.315.23 https://doi.org/10.20998/2074-272X.2026.2.12

O. Tkachenko, U. Pyrohova, V. Grinchenko

Highly accurate approximation for sheath currents in high-voltage three-phase cable line

Introduction. *This study focuses on sheath currents in high-voltage single-core XLPE-insulated power cables with solid bonding. The analysis covers flat and trefoil three-phase cable lines. Sheath current calculation is essential for evaluating thermal conditions, losses, and overall cable performance.* ***Problem.*** *The regulatory documents of the Ministry of Energy of Ukraine provide formulas for sheath currents. We examine them by comparing with verified analytical solutions and find significant discrepancies in a wide range of typical parameters of high-voltage three-phase cable line. So the formulas in the current regulatory document have a narrow range of applicability, and the engineering calculations based on them may lead to significant inaccuracies and incorrect decisions.* ***Goal.*** *The paper aims to develop novel formulas for the RMS values of sheath currents in high-voltage three-phase cable lines with flat and trefoil arrangements of power cables, ensuring the accuracy required for engineering calculations across a wide range of cable line parameters.* ***Methodology.*** *This study is grounded on the previously developed and experimentally verified analytical model and corresponding formulas for calculating sheath currents and cable line magnetic field. These verified formulas for sheath currents are too cumbersome, so an approximation technique is used to find compact ones.* ***Results.*** *A novel approximation for sheath current in the flat cable line is developed. The discrepancy between the approximation and the verified formulas is within 5 %. Additionally, a new form of the formula for sheath current in the trefoil cable line is proposed.* ***Scientific novelty****. To perform the approximation, an original quality index is proposed. It is derived from the heat output of metal sheaths of cables.* ***Practical value.*** *The developed approximation for sheath current can be directly applied to the design of high-voltage cable lines, the analysis of the operating modes, and the control of the compliance of existing cable lines with actual operating conditions.* References 20, table 1, figures 4.
Keywords: **metal sheath, cable line, single-core cable, solid bonding, regulatory document.**

Вступ. *В роботі розглянуто струми в екранах одножильних силових кабелів високої напруги, з ізоляцією зі зшитого поліетилену (XLPE), при заземленні з обох кінців. Аналіз охоплює кабельні лінії змінного струму з розташуванням кабелів за схемами «у площині» та «у трикутник». Розрахунок струму в екранах є важливим при оцінці теплового стану, втрат та режиму роботи кабельної лінії.* ***Проблема.*** *Нормативні документи Міністерства енергетики України містять співвідношення для розрахунку струмів в екранах. Аналіз цих співвідношень шляхом порівняння з верифікованими аналітичними формулами показав значну розбіжність у широкому діапазоні типових параметрів трифазної кабельної лінії високої напруги. Відповідно, співвідношення в чинних нормативних документах мають вузький діапазон застосовності, а їх використання для інженерних розрахунків може призвести до значних неточностей та хибних висновків.* ***Метою*** *роботи є розробка нових наближених співвідношень для розрахунку діючих значень струмів у екранах кабелів трифазних кабельних ліній високої напруги, прокладених за схемами «у площині» та «у трикутник», задля забезпечення необхідної точності у широкому діапазоні параметрів кабельної лінії.* ***Методологія.*** *Дослідження ґрунтується на раніше розробленій авторами та експериментально верифікованій аналітичній моделі та відповідних співвідношеннях для розрахунку струмів в екранах, та магнітного поля трифазної кабельної лінії. Оскільки зазначені співвідношення для струмів є занадто громіздкими, тому для знаходження компактного співвідношення використовується апроксимація.* ***Результати.*** *Розроблено нове наближене співвідношення для розрахунку струму в екранах кабельної лінії з розташуванням кабелів «у площині». Розбіжність між наближенням та верифікованими формулами становить до 5 %. Крім того, запропоновано нову форму співвідношення для розрахунку струму в екранах кабельної лінії з розташуванням кабелів «у трикутник».* ***Наукова новизна.*** *Для виконання апроксимації запропоновано оригінальний показник якості, який визначається величинами теплової дії струмів в екранах кабелів.* ***Практична значимість.*** *Розроблене наближене співвідношення для розрахунку струму в екранах може бути безпосередньо застосоване при проєктуванні трифазних кабельних ліній високої напруги, аналізі режимів їхньої роботи та контролі відповідності існуючих кабельних ліній фактичним умовам експлуатації.* Бібл. 20, табл. 1, рис. 4.
Ключові слова: **екран, кабельна лінія, одножильний кабель, заземлення з обох кінців, нормативний документ.**

Introduction. The most advanced means of electrical energy transmission in urban areas are underground high-voltage three-phase cable line. A typical cable line consists of three single-core XLPE-insulated power cables. The main structural elements of these cables are an aluminum or copper conductor, XLPE insulation, and a copper sheath (Fig. 1). The metal sheath provides a uniform electric field in the insulation layer.

The Ukrainian industry uses the regulatory document [1]. According to them, the metal sheaths of cables require earthing. For this, sheaths are bonded and earthed at one or several points. Typically, there are three types of bonding: single-point bonding, cross-bonding, and solid bonding. Other types of bonding are discussed in [2], but they are not commonly used.

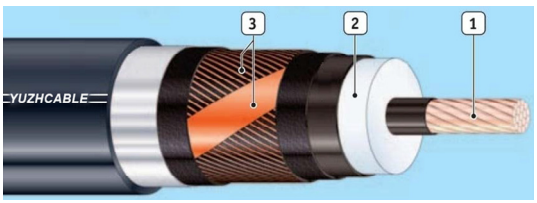

Fig. 1. Single-core XLPE-insulated power cable: 1 – aluminum or copper conductor, 2 – XLPE insulation, 3 – copper sheath

Single-point bonding is the simplest way. In this case, the metal sheaths of cables are solidly bonded together and earthed at only one point along an elementary section of cable line. The single-point bonding provides no circulating sheath currents and consequently no heating in sheaths. But sheaths are earthed only once. Thus, the cables have zero electric potential only at the earthing point. And additional protective devices are required for installation at each elementary section.

To implement the cross-bonding, the cable line length is divided into three approximately equal sections, and the metal sheaths in consecutive sections are cross-connected. As a result, there are no longitudinal sheath currents. However, this type of bonding is not widespread because of its relative complexity and high cost.

Solid bonding of high-voltage power cables is the most common one. All metal sheaths are electrically bonded together and earthed at two points: at the beginning and at the end of the cable line. Solid bonding ensures the absence of impulse overvoltage and does not require additional protective devices. Moreover, the cable metal sheaths form closed loops with induced longitudinal currents [3–6]. Thus, the magnetic field of induced currents

decreases the total magnetic field of the cable line. This effect contributes to the solution of magnetic ecology problems [7–11]. But currents in the sheaths can disrupt the thermal regime of the cable line and reduce its capacity.

The transmission capacity is determined by the temperature of the cable conductor. This temperature can be determined by numerical simulation of the cable line thermal field [12–14] or by using the standard IEC 60287 [15]. IEC 60287 is applicable in most cases, and numerical simulation has almost no constraints when a specific case is under study. However, to simulate the cable line thermal field, the RMS values of sheath currents are required.

The analytical formulas for calculating sheath currents provided in the regulatory document [1] are compact. However, the analysis below demonstrates that they have a narrow range of applicability, and calculations based on them may lead to significant inaccuracies.

Solid bonding is studied in [16], and a compact formula for sheath current is proposed. It is derived via algebraic manipulation of the known formulas for metal sheath losses in the standard IEC 60287 [15]. While mathematically valid, it obscures the physical interpretation and lacks experimental or numerical verification. In contrast, this paper presents an alternative approach that gives a novel verified approximation for a flat cable line.

The paper aims to develop novel formulas for the RMS values of sheath currents in high-voltage three-phase cable lines with flat and trefoil arrangements of power cables, ensuring the accuracy required for engineering calculations across a wide range of cable line parameters.

Verified formulas for sheath currents. The reduction of cable line magnetic field in the case of solid bonding is studied in [17]. As a result, the analytical model of the cable line magnetic field and the corresponding formulas for sheath currents are developed and experimentally verified. The following natural assumptions are used in [17]: the distribution of the induced current is uniform within each metal sheath, and the sheath thickness is much smaller than the cable radius. The discrepancy between calculations carried out according to [17] and experimental results from [18] is within 5 %.

Analytical formulas for the phasors of sheath currents are represented in [17]. To obtain the formulas for the RMS values of the sheath currents, we compute the modulus of the current phasors and divide by $\sqrt{2}$. Furthermore, the currents can be conveniently described with only two dimensionless parameters of the cable line:

$$Q = \frac{\mu_0 \omega}{2\pi R}, \quad \Delta = \frac{s}{d}, \tag{1}$$

where ω=2π·50 rad/s is the angular frequency of current; R is the DC resistance of a cable sheath unit length, Ω/m; s is the distance between axes of adjacent cables, m; d is the metal sheath diameter, m; μ_0 is the vacuum permeability.

Parameters Q and Δ vary within specific ranges related to the high-voltage cable line. Namely, the parameter Δ varies from 1 to 10, and Q varies from 0.1 to 0.5. The minimum of Δ occurs for closely laid cables, and the junction zone of cables exhibits maxima of Δ. The parameter Q is inversely proportional to DC resistance R. Table 1 shows the Q values for typical high-voltage power cables from [19].

Table 1

Parameter Q for a typical high-voltage single-core XLPE-insulated power cables

No.	Metal sheath cross-section S, mm^2	Metal sheath DC resistance R 10^{-3}, Ω/m	Q
1	35	0.524	0.12
2	50	0.387	0.16
3	70	0.268	0.23
4	95	0.193	0.33
5	120	0.153	0.41
6	150	0.124	0.51

We consider two types of arrangements of solidly bonded high-voltage power cables. In the case of the trefoil arrangement, the RMS values of sheath currents are equal and have the following form:

$$I_{sh} = I \cdot \sqrt{\frac{Q^2 \ln^2 2\Delta}{1 + Q^2 \ln^2 2\Delta}}. \tag{2}$$

In case of the flat arrangement, when currents in conductors form a positive sequence set, we get the following formulas for the RMS values of sheath currents:

$$I_{sh1} = I \cdot \sqrt{\frac{\left(Q \cdot \ln 4\Delta \cdot \ln 4\Delta^3 + \sqrt{3} \cdot \ln 2\right)^2 + \ln^2 32\Delta^3}{\left(Q \cdot \ln 4\Delta \cdot \ln 4\Delta^3 - \frac{3}{Q}\right)^2 + 4 \cdot \ln^2 16\Delta^3}};$$

$$I_{sh2} = I \cdot \sqrt{\frac{Q^2 \cdot \ln^2 4\Delta^3}{9 + Q^2 \cdot \ln^2 4\Delta^3}}; \tag{3}$$

$$I_{sh3} = I \cdot \sqrt{\frac{\left(Q \cdot \ln 4\Delta \cdot \ln 4\Delta^3 - \sqrt{3} \cdot \ln 2\right)^2 + \ln^2 32\Delta^3}{\left(Q \cdot \ln 4\Delta \cdot \ln 4\Delta^3 - \frac{3}{Q}\right)^2 + 4 \cdot \ln^2 16\Delta^3}},$$

where I is the RMS value of current in the conductors of the cables.

If the flat cable line has negative-sequence current, then the right sides of the first and the third formulas in (3) are swapped.

Note that the difference between formulas (2), (3) and their original forms from [17] is due to the difference in the definition of the dimensionless parameter Δ. Here we use the metal sheath diameter in the denominator. At the same time, the sheath radius is used as the denominator in [17].

Thus, we get verified formulas (2) and (3) for sheath currents within the accepted assumptions. Formula (2) is sufficiently compact for a trefoil cable line. But we treat formulas (3) as too cumbersome for a flat cable line.

Sheath current in trefoil cable line. The regulatory document [1] provides the following formula for sheath current in a trefoil cable line when its power cables are solidly bonded:

$$I_{sh}^{reg} = I \cdot \sqrt{\frac{0.0019}{R_{70}^2 + 0.0019}}, \tag{4}$$

where R_{70} is a DC resistance of the metal sheath per one kilometer length at a temperature of 70 °C, Ω/km.

We express (4) in terms of Q and obtain the following formula for the sheath current:

$$I_{sh}^{reg} = I \cdot \sqrt{\frac{4.75 \cdot Q^2}{\pi^2 + 4.75 \cdot Q^2}}. \tag{5}$$

To examine (4), (5) and to compare them with the verified analytical formula (2), we use the original quality index ε derived from the heat output of sheaths of power cables. It shows the discrepancy in the total heat output of sheaths when different formulas for sheath current are used. As the sheath heat output $W = I_{sh}^2 \cdot R$, then

$$\varepsilon = \left| 1 - \frac{3 \cdot \left(I_{sh}^{reg} \right)^2}{3 \cdot I_{sh}^2} \right| \cdot 100\% = \left| 1 - \frac{\left(I_{sh}^{reg} \right)^2}{I_{sh}^2} \right| \cdot 100\%, \quad (6)$$

where the numerator is calculated via (4) or (5), and the denominator is calculated via (2).

The factor 3 in the numerator and denominator of (6) indicates the number of cables.

Figure 2,*a* shows that the quality index ε weakly depends on parameter Q, and Fig. 2,*b* – significant dependence on parameter Δ. Particularly, ε rapidly rises from 0 to 60 % with the growth of Δ from 1 to 1.5. So the formula (4) has a narrow range of applicability when Δ is close to 1. But in general, it is not appropriate for engineering calculations. In contrast, the formula (2) is accurate and compact for engineering calculations of sheath current in a trefoil cable line.

Note that the value Δ=1.1 from Fig. 2,*a* refers to the cables laid in direct contact. The value Δ=2.2 refers to the cable spacing equal to one cable diameter. And according to the regulatory document [20], the value Δ=4.4 represents the maximum permissible cable spacing along the cable route.

Sheath current in flat cable line. Here, we calculate the sheath current in the flat cable line by analogy with our calculations for the trefoil one.

The regulatory document [1] provides the following formula for sheath current in a flat cable line when its power cables are solidly bonded:

$$I_{sh}^{reg} = I \cdot \sqrt{0.75 \cdot \frac{0.017}{R_{70}^2 + 0.017} + 0.25 \cdot \frac{0.01}{R_{70}^2 + 0.01}}. \quad (7)$$

We express (7) in terms of Q and get the following:

$$I_{sh}^{reg} = I \cdot \sqrt{0.75 \cdot \frac{42.5 \cdot Q^2}{\pi^2 + 42.5 \cdot Q^2} + 0.25 \cdot \frac{25 \cdot Q^2}{\pi^2 + 25 \cdot Q^2}}. \quad (8)$$

Then we examine (7), (8) by evaluating the discrepancy between the total heat output of the sheaths. The quality index ε is as follows for the flat cable line:

$$\varepsilon = \left| 1 - \frac{3 \cdot \left(I_{sh}^{reg} \right)^2}{I_{sh1}^2 + I_{sh2}^2 + I_{sh3}^2} \right| \cdot 100\%, \quad (9)$$

where the sheath current is calculated via (8) in the nominator and via (3) in the denominator.

Figure 3 shows the dependences of the quality index ε on the parameters Δ and Q. Figure 3,*a* shows that ε is approximately 20 % and does not depend on Q when Δ=2.2 only. In contrast, ε changes significantly with Q at other values of Δ. Figure 3,*b* shows that the quality index ε rapidly falls from 100 % to 20 % as the parameter Δ increases from 1.5 to 2.2. The quality index ε takes appropriate values in the range 0–20 % only when Δ lies in the narrow range from 2.2 to 4. And ε is about zero when Δ is about 2.8.

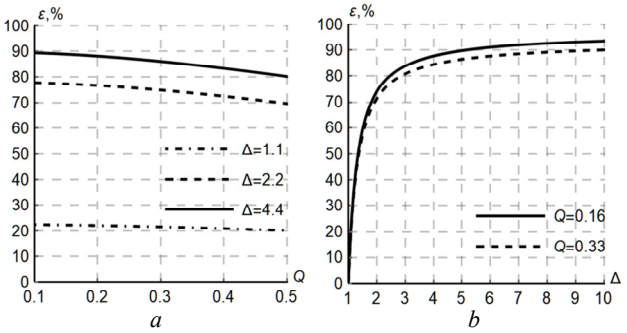

Fig. 2. Quality analysis of the regulatory formula for sheath current in the trefoil cable line

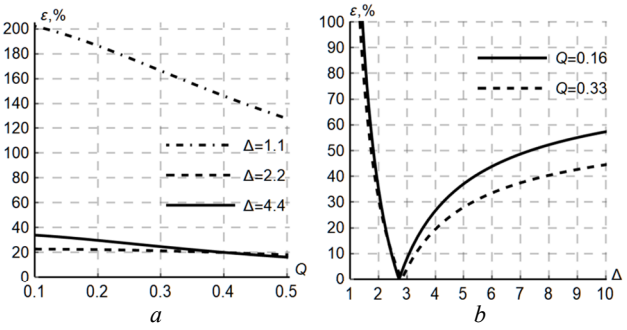

Fig. 3. Quality analysis of the regulatory formula for sheath current in the flat cable line

So the formula in regulatory document [1] has a narrow range of applicability, and the engineering calculations based on it may lead to significant inaccuracies and incorrect decisions.

To develop an accurate approximation for sheath current in a flat cable line, we use the following form based on (2):

$$I_{sh}^{approx} = I \cdot F(Q, \Delta) \cdot \sqrt{\frac{Q^2 \ln^2(2.52 \cdot \Delta)}{1 + Q^2 \ln^2(2.52 \cdot \Delta)}}, \quad (10)$$

where $F(Q, \Delta)$ is a non-dimensional correcting coefficient, and $2.52 \cdot \Delta$ is a geometrical mean value of three pairwise distances between cables.

In definition (9), we substitute I_{sh}^{reg} with (10) and find the unknown function $F(Q, \Delta)$ by minimizing the quality index ε under the constraints that Q varies from 0.1 to 0.5 and Δ varies from 1 to 10. Thus, we obtain the following novel approximation:

$$I_{sh}^{approx} = I \cdot \sqrt{\frac{Q^2 \ln^2(2.52 \cdot \Delta)}{1 + Q^2 \ln^2(2.52 \cdot \Delta)}} \times \times \left(1 + \frac{0.05 - 0.3Q}{\Delta} + \frac{0.1 + 0.075Q}{\Delta^2} \right). \quad (11)$$

To find the discrepancy between the approximation (11) and the verified formulas (3), we substitute I_{sh}^{reg} with (10) in the definition (9) and analyze the quality index ε in Fig. 4. It shows that ε is less than 3 %. And it is less than the 5 % error of analytical model used to find formulas (2) and (3).

Thus, the proposed formulas (2) and (11) are directly applicable to the design of high-voltage cable lines, the analysis of operating modes, and the assessment of compliance with actual operating conditions.

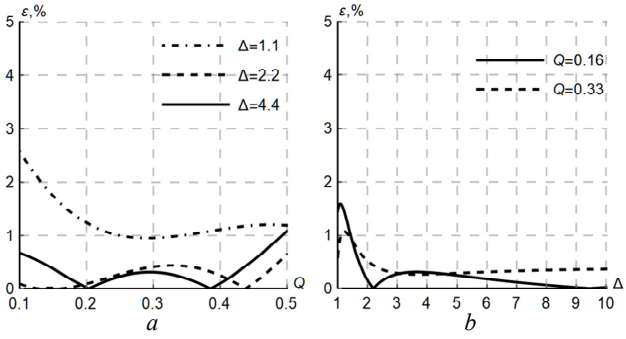

Fig. 4. Quality analysis of the novel approximation for sheath current in the flat cable line

Conclusions. This paper demonstrates that the formulas for calculating the RMS values of sheath currents in high-voltage three-phase cable line, as recommended by the regulatory documents of the Ministry of Energy of Ukraine when sheaths are solidly bonded, have narrow ranges of applicability. And the engineering calculations based on them may lead to significant inaccuracies and incorrect decisions.

A novel approximate formula for calculating the RMS values of sheath current in the flat cable line is developed. The approximation error is within 5 %. Additionally, the new form of the formula for the trefoil cable line is proposed. These formulas for calculating sheath currents cover the entire range of parameters of high-voltage cable lines.

The developed formulas are recommended for use in revising the regulatory documents of the Ministry of Energy of Ukraine that govern the calculation of sheath currents in cable lines with solidly bonded sheaths.

Acknowledgment. This work was supported by projects 0122U000178 and 0123U103031 funded by the National Academy of Sciences of Ukraine. It was endorsed by the seminar of section «Scientific Foundations of Energy Development Forecasting» held at GEI NASU in April, 2025.

Conflict of interest. The authors declare that they have no conflicts of interest.

REFERENCES

1. *Electrical installation regulations.* Kharkiv, Fort Publ., 2017. 760 p. (Ukr).

2. Mahdipour M., Akbari A., Khalilzadeh M., Werle P. Impact of different bonding methods on high voltage cable shield induced voltage and current in normal and fault conditions. *2017 Iranian Conference on Electrical Engineering*, pp. 1308–1312. doi: https://doi.org/10.1109/IranianCEE.2017.7985244.

3. Lunca E., Vornicu S., Săleanu A. Numerical and analytical analysis of the low-frequency magnetic fields generated by three-phase underground power cables with solid bonding. *Applied Sciences*, 2023, vol. 13, no. 10, art. no. 6328. doi: https://doi.org/10.3390/app13106328.

4. Lunca E., Vornicu S., Salceanu A. Numerical modelling of the magnetic fields generated by underground power cables with two-point bonded shields. *25th IMEKO TC-4 International Symposium on Measurement of Electrical Quantities*, 2022, pp. 221–226. doi: https://doi.org/10.21014/tc4-2022.41.

5. Cao J., Chen J., Ye Z., Lian J., Tan X., Zhang W. Research on optimization of high voltage cable circulating current suppression based on short circuit current guidance. *2023 5th Asia Energy and Electrical Engineering Symposium*, pp. 274–282. doi: https://doi.org/10.1109/AEEES56888.2023.10114368.

6. Bezprozvannych G.V., Kostiukov I.A. A calculation model for determination of impedance of power high voltage single-core cables with polymer insulation. *Electrical Engineering & Electromechanics*, 2021, no. 3, pp. 47–51. doi: https://doi.org/10.20998/2074-272X.2021.3.08.

7. Grinchenko V., Tkachenko O., Bilan T. Review of passive loop systems for normalization of high-voltage cable line magnetic field. *System Research in Energy*, 2022, no. 2(71), pp. 73–84. doi: https://doi.org/10.15407/srenergy2022.02.073.

8. Bravo-Rodriguez J.C., del-Pino-Lopez J.C., Cruz-Romero P.A survey on optimization techniques applied to magnetic field mitigation in power systems. *Energies*, 2019, vol. 12, no. 7, art. no. 1332. doi: https://doi.org/10.3390/en12071332.

9. Canova A., Giaccone L., Lavecchia G., Ribaldone P. Passive mitigation of stray magnetic fields generated by underground power lines. *2017 IEEE International Conference on Environment and Electrical Engineering and 2017 IEEE Industrial and Commercial Power Systems Europe*, pp. 1–5. doi: https://doi.org/10.1109/EEEIC.2017.7977522.

10. Rozov V.Yu., Reutskiy S.Yu., Pelevin D.Ye., Kundius K.D. Magnetic field of electrical heating cable systems of the floors for residential premises. *Electrical Engineering & Electromechanics*, 2024, no. 5, pp. 48–57. doi: https://doi.org/10.20998/2074-272X.2024.5.07.

11. Rozov V.Yu., Pelevin D.Ye., Reutskiy S.Yu., Kundius K.D., Vorushylo A.O. The complex influence of external and internal electricity networks on the magnetic field level in residential premises of buildings. *Electrical Engineering & Electromechanics*, 2025, no. 4, pp. 3–11. doi: https://doi.org/10.20998/2074-272X.2025.4.01.

12. Rerak M., Ocłon P. The effect of soil and cable backfill thermal conductivity on the temperature distribution in underground cable system. *4th Scientific and Technical Conference on Modern Technologies and Energy Systems*, 2017, pp. 1–6. doi: https://doi.org/10.1051/e3sconf/20171302004.

13. Sun Yu Xiao, Wang Qing Zhen, Meng Nan Xiang, Ju Zhu. A new method to cable performance assessment. *Advanced Materials Research*, 2012, vol. 446, pp. 450–453. doi: https://doi.org/10.4028/www.scientific.net/AMR.446-449.450.

14. Hwang Chang-Chou, Jiang Yi-Hsuan. Extensions to the finite element method for thermal analysis of underground cable systems. *Electric Power Systems Research*, 2003, vol. 64, no. 2, pp. 159–164. doi: https://doi.org/10.1016/S0378-7796(02)00192-X.

15. *Electric Cables – Calculation of Current Rating – Part 1: Current rating equations (100 % load factor) and calculation of losses, Section 1: General*. IEC Standard IEC-60287-1-1, 2006.

16. Antonets T., Buinyi R., Vorushylo A., Gai O., Tkachenko O. About power and electrical energy losses in single-core cable screens. *Power Engineering: Economics, Technique, Ecology*, 2025, no. 2, pp. 51–61. (Ukr). doi: https://doi.org/10.20535/1813-5420.2.2025.327189.

17. Rozov V., Grinchenko V., Tkachenko O., Yerisov A. Analytical Calculation of Magnetic Field Shielding Factor for Cable Line with Two-Point Bonded Shields. *2018 IEEE 17th International Conference on Mathematical Methods in Electromagnetic Theory (MMET)*, 2018, pp. 358–361. doi: https://doi.org/10.1109/MMET.2018.8460425.

18. Rozov V.Yu., Kvytsynskyi A.A., Dobrodeyev P.N., Grinchenko V.S., Erisov A.V., Tkachenko A.O. Study of the magnetic field of three phase lines of single core power cables with two-end bonding of their shields. *Electrical Engineering & Electromechanics*, 2015, no. 4, pp. 56–61. doi: https://doi.org/10.20998/2074-272X.2015.4.11.

19. *Guidelines for the Selection, Installation, Laying, Testing, and Operation of Cables with Insulation made of Cross-Linked Polyethylene for Voltage 45/150 kV*. PJSC Yuzhkabel Works, Kharkiv, Ukraine, 2014. (Ukr).

20. *SOU-N MEV 40.1-37471933-49:2011. Design of cable lines up to 330 kV. Guideline (in the edition of the order of the Minenergvugillya dated January 26, 2017, no. 82).* Kyiv, Minenergvugillya Ukraine Publ., 2017. 168 p. (Ukr).

Received 08.09.2025
Accepted 22.11.2025
Published 02.03.2026

O. Tkachenko[1], *PhD, Senior Researcher,*
U. Pyrohova, Independent Researcher,
V. Grinchenko[2], *PhD, Senior Researcher,*
[1] Anatolii Pidhornyi Institute of Power Machines and Systems of the National Academy of Sciences of Ukraine,
2/10, Komunalnykiv Str., Kharkiv, 61046, Ukraine.
[2] General Energy Institute of National Academy of Sciences of Ukraine,
172, Antonovycha Str., Kyiv, 03150, Ukraine
e-mail: oleksandr.tk7@gmail.com (Corresponding Author)

How to cite this article:
Tkachenko O., Pyrohova U., Grinchenko V. Highly accurate approximation for sheath currents in high-voltage three-phase cable line. *Electrical Engineering & Electromechanics*, 2026, no. 2, pp. 89-92. doi: https://doi.org/10.20998/2074-272X.2026.2.12

Матеріали приймаються за адресою:
Кафедра "Електричні апарати", НТУ "ХПІ", вул. Кирпичева, 2, м. Харків, 61002, Україна
Електронні варіанти матеріалів по e-mail: a.m.grechko@gmail.com

Довідки за телефонами: +38 067 359 46 96 Гречко Олександр Михайлович

Передплатний індекс: 01216